Ph.D. thesis

Magnetoelectric multiferroics: From static via dynamic magnetoelectric effect to nonlinear light-matter interaction

Jakub Vít
Czech Technical University in Prague
Institute of Physics, Czech Academy of Sciences
Budapest University of Technology and Economics

Supervisors:

Dr. Stanislav Kamba
Institute of Physics, Czech Academy of Sciences

Dr. Sándor Bordács
Budapest University of Technology and Economics

(2022)

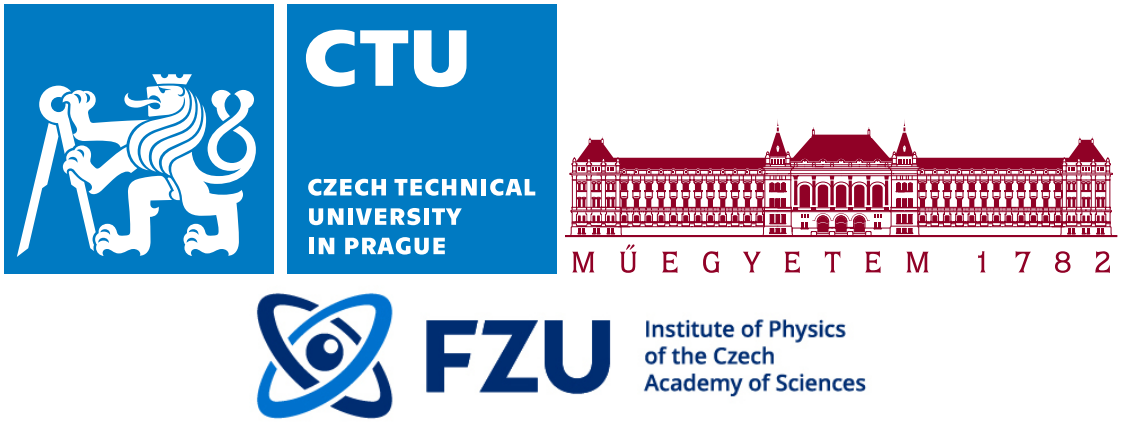

Abstract

Magnetoelectric and multiferroic materials are promising building blocks for energy-efficient memory devices as they allow electric-field control of the magnetic order. In this thesis, I focused on the dynamic magnetoelectric effect, which gives rise to electric-dipole-active magnon excitations and non-reciprocal light absorption. I studied the spin excitations of several magnetoelectric and multiferroic compounds such as Y- and Z-hexaferrites, $Ba_2CoGe_2O_7$ and $LiCoPO_4$, by infrared and THz spectroscopy. Based on the measured spectra, I determined the selection rules of the spin excitations and found electromagnon as well as magnetoelectric spin excitations. For magnetoelectric spin excitations, I observed non-reciprocal light absorption that I used it to detect antiferromagnetic domains of $Ba_2CoGe_2O_7$ and $LiCoPO_4$. Finally, I demonstrated the control of the magnetic order and domain composition by static (in $Ba_2CoGe_2O_7$) as well as by oscillating electric and magnetic fields (in $LiCoPO_4$ and possibly in Y-hexaferrite $Ba_{0.2}Sr_{1.8}Co_2(Fe_{0.96}Al_{0.04})_{12}O_{22}$).

Contents

Abbreviations

AFE	antiferroelectric
AFM	antiferromagnetic
AFMR	antiferromagnetic resonance
BSCZFAO	Y-type hexaferrites $Ba_xSr_{2-x}Co_yZn_{2-y}Fe_{11+z}Al_{1-z}O_{22}$
CW	continuous-wave
DB	directional birefringence
DD	directional dichroism
DFT	Density functional theory
DM	Dzyaloshinskii-Moriya
DR	dynamic range
ELBE	Electron Linac for beams with high Brilliance and low Emittance (linear accelerator at HZDR)
EM	electromagnetic
EOS	electro-optic sampling
FEL	free-electron laser
FELBE	free-electron laser at ELBE, HZDR
FIR	far-infrared
FMR	ferromagnetic resonance
FTIR	Fourier-Transform infrared (spectroscopy)
FWHM	full-width-half-maximum
HZDR	Helmholtz-Zentrum Dresden-Rossendorf
iDM	inverse Dzyaloshinskii-Moriya
KBFI	National Institute of Chemical Physics and Biophysics (in Tallinn)
KNB	Katsura-Nagaosa-Balatsky (model)
MChD	magnetochiral dichroism
ME	magnetoelectric
OAM	orbital angular momentum
ODA	optical directional anisotropy
OME	optical magnetoelectric effect
SNR	signal-to-noise ratio
SOC	spin-orbit coupling
TD THz	time-domain terahertz (spectroscopy)
TELBE	THz beamline at ELBE, HZDR
TeraFERMI	THz beamline at the FERMI seeded FEL facility at Elettra Sincrotrone, Trieste
Y-hex	Y-type hexaferrite $Ba_{0.2}Sr_{1.8}Co_2(Fe_{0.96}Al_{0.04})_{12}O_{22}$
Z-hex	Z-type hexaferrite $(Ba_{0.2}Sr_{0.8})_3Co_2Fe_{24}O_{41}$

Motivations

Multiferroics with simultaneous ferroelectric and magnetic order attracted interest in the past two decades as they allow magnetic-field control of electric polarization, and electric-field control of magnetic states. The latter effect, if realized in an insulating magnet, provides a huge technological advantage for information storage. In a multiferroic memory device, the energy dissipated by Joule heating is expected to be 2–3 orders of magnitude smaller as compared to for example spin-transfer-torque magnetic random access memories [1, 2].

Even though room-temperature memory cells based on $BiFeO_3$/FeCo heterostructures [3, 4] and manipulation of domain walls in iron garnet films [5] have been already demonstrated more than a decade ago, there are several challenges preventing the broader technological applications of multiferroics. These are mainly the following issues: the weakness of the magnetoelectric interaction, the low operating temperatures, compatibility with current technologies or limited speed of the switching and limited miniaturization [1, 2].

The magnetoelectric coupling gives rise to intriguing phenomena at finite frequencies as well. Notably, magnetoelectric crystals can be transparent in one, but absorbing in the opposite light propagation direction [6], thus, these materials may gain applications in optical diodes [7, 8]. Moreover, the absorbing and transparent directions can be switched by a magnetic [9] and rarely even by an electric field [10, 11], which maybe utilized in optical switches, though the application of dynamic magnetoelectric effect is still in its infancy.

Despite the advantages of the electric field control of the magnetism, it has some drawbacks as it requires contacts and its speed can be limited. The optical manipulation of magnetism can help to overcome these issues. Contactless and fast all-optical access of writing and reading magnetic states of matter, attracted enormous interest in last two decades [12, 13]. Magnetoelectric materials may allow a new combination of these two fields as the coupled electric and magnetic dipole excitations provide a new handle to manipulate magnetic states.

The main goal of my PhD work was the study of the dynamic magnetoelectric effect in various multiferroic and magnetoelectric compounds. My aim was not only to observe this effect but to control it by static fields as well as by the oscillating electromagnetic fields of the light.

Chapter 1

Theoretical background of magnetoelectric multiferroics

1.1 Magnetoelectric coupling in magnetoelectrics and multiferroics

Maxwell's equations govern classical electromagnetism where electric charges are the source of electric fields, while the magnetic field is essentially dipolar. The Faraday's law of induction and the Ampère-Maxwell law, respectively connecting time-varying magnetic fields to curling electric fields and time-varying electric fields to curling magnetic fields, describe the coupling between electric and magnetic fields.

In condensed matter, usually electric fields, $\boldsymbol{E}$ can generate polarization, $\boldsymbol{P}$ or drive currents whereas magnetic fields, $\boldsymbol{H}$ induce magnetization, $\boldsymbol{M}$. More rarely, cross-coupling between these normally separate phenomena emerges, namely *static* magnetic fields induce *static* electric polarization and *static* electric fields generate *static* magnetization. These phenomena are respectively termed as direct and converse magnetoelectric (ME) effects to be distinguished from the commonly used term electromagnetic (EM), referring to classical electromagnetism. It is worth noting that ME phenomena couple static fields to static dipoles unlike Faraday's or Ampère-Maxwell's law connecting time-varying and curling fields.

In the lowest order, linear ME effect may emerge:

$$\Delta P_\beta = \frac{1}{c}\chi^{em}_{\beta\alpha} H_\alpha, \text{ and } \Delta \mathrm{M}_\alpha = \sqrt{\frac{\varepsilon_0}{\mu_0}}\chi^{\mathrm{me}}_{\alpha\beta}\mathrm{E}_\beta \tag{1.1}$$

where $\chi^{em}_{\alpha\beta}$ and $\chi^{me}_{\alpha\beta}$ are the direct and converse ME susceptibilities, defined here as dimensionless, ε_0 and μ_0 are the vacuum permittivity and permeability, respectively, and c is the speed of light in vacuum. The possible existence of the ME effect in general was predicted already by Pierre Curie in 1894 [14]. According to Neumann's principle [15], the form of the ME susceptibility tensor should reflect the ground-state symmetry of the magnetic crystal. When considering the uniform, i.e. long-wavelength response of the system, the elements of the magnetic point group constrain on the tensor elements. Since $\boldsymbol{E}$ and $\boldsymbol{P}$ are polar vectors even under time-reversal whereas $\boldsymbol{H}$ and $\boldsymbol{M}$ are time-reversal odd axial vectors, the linear ME effect is only allowed when both the inversion and the

time-reversal symmetries are broken as recognized by Landau and Lifshitz [16]. From this, it is clear that the presence of a magnetic order, breaking the time-reversal symmetry, is essential for the linear ME effect. The result of such an analysis on the static ME susceptibility can be found for all magnetic point groups in Ref. [17]; the ME tensor has nonzero elements in 58 out of 122 magnetic (Shubnikov) point groups. For the first time, Astrov detected the linear ME effect [18]. He did his pioneering experiments on Cr_2O_3, in which Dzyaloshinskii predicted this effect based on symmetry analysis [19]. In this compound, the inversion symmetry exchanges the two neighboring Cr sites thus, its up-down-up-down antiferromagnetic (AFM) order simultaneously breaks the inversion and the time-reversal symmetries.

Based on phenomenological symmetry approach, one can investigate symmetry-allowed terms of the free energy of a crystal in presence of electric and magnetic fields:

$$F = F_0 - \overbrace{P^S_\beta E_\beta}^{\text{FE}} - \overbrace{M^S_\alpha H_\alpha}^{\text{FM}} - \varepsilon_0 \chi^{ee}_{\alpha\beta} E_\alpha E_\beta - \mu_0 \chi^{mm}_{\alpha\beta} H_\alpha H_\beta - \overbrace{\frac{1}{c}\chi^{me}_{\alpha\beta} H_\alpha E_\beta}^{\text{ME}} - ... \tag{1.2}$$

Here, F_0 is the ground state free energy, P^S and M^S are the spontaneous polarization and magnetization, thus they correspond to ferroelectric (FE) and ferromagnetic (FM) materials, respectively. χ^{ee} and χ^{mm} are (dimensionless) electric and magnetic susceptibilities, respectively, c is the speed of light, while α and β stand for Cartesian coordinates.

After differentiating Eq. 1.2 with respect to fields, it turns into

$$M_\alpha = -\frac{1}{\mu_0}\frac{\partial F}{\partial H_\alpha} = M^S_\alpha + \chi^{mm}_{\alpha\beta} H_\beta + \sqrt{\frac{\varepsilon_0}{\mu_0}}\chi^{me}_{\alpha\beta} E_\beta + ... \tag{1.3}$$

$$P_\beta = -\frac{\partial F}{\partial E_\beta} = P^S_\beta + \varepsilon_0 \chi^{ee}_{\alpha\beta} E_\beta + \frac{1}{c}\chi^{me}_{\alpha\beta} H_\alpha + ... \tag{1.4}$$

One can see that indexes of the ME susceptibility tensor are exchanged for the two cases, thus using Eq. 1.1, $\chi^{me}_{\alpha\beta} = \chi^{em}_{\beta\alpha}$, i.e. the two tensors are the transposed pairs of each other.

In order to have a stable ground state, the quadratic terms in the free energy of a linear magnetoelectric material described by Eq. 1.2 must be positive definite, thus [20]

$$|\chi^{me}_{\alpha\beta}| < \sqrt{\chi^{ee}_{\alpha\alpha}\chi^{mm}_{\beta\beta}}. \tag{1.5}$$

One can see that the ME susceptibility can be large when the electric and/or magnetic susceptibilities are large. In linear nonpolar magnetoelectrics, the magnetic order is primary and the induced electric polarization is secondary, therefore the ME susceptibility scales mainly with the magnetic susceptibility. This is demonstrated for Cr_2O_3 [21–23]: While χ^{me}_{11} exhibits a power law from the Néel temperature (T_N) down to low temperatures, the other component – χ^{me}_{33} – has a maximum value close below the Néel temperature where χ^{mm}_{33} is also high [24].

Despite some progress on magnetoelectricity during 1960s, the topic has been left out of the interest afterward for more than two decades. The ME effect was considered as small and inapplicable – in fact Louis Néel claimed in 1970 in his Nobel lecture [25] that all antiferromagnets are "interesting but useless", while magnetoelectrics were a small subset of all antiferromagnets.

In 1994, Schmid came up with the term multiferroic, as he called materials with more than one spontaneous ordering [26]. Specifically for simultaneous ferroelectric and ferromagnetic orders, these compounds are termed as magnetoelectric multiferroics or multiferroics for short though other spontaneous ordering such as ferroelasticity, orbital or charge order can also be coupled [27]. Recently, the term multiferroics is used in a broader sense, describing also ferroelectrics with any magnetic ordering, including ferrimagnetism, antiferromagnetism or other more complex noncollinear magnetic orders. Magnetoelectric multiferroics have the promise to possess strongly coupled electric and magnetic dipoles, which may eventually enable electric field control/switching of magnetism. This led to the revival of the research of ME effect and related phenomena from about 2000.

However, multiferroics are rather rare as pointed out by Hill (now Spaldin) in 2000 [28]: While ferroelectricity usually occurs in compounds where the d orbitals of the transition-metals are either completely empty or filled, magnetism is driven by d (or f) electrons. Therefore, ferroelectricity and magnetism seem to be mutually exclusive, similarly to magnetism and superconductivity.

Interestingly, there are certain ways how to overcome such exclusivity. The most trivial scenario is to have different ions responsible for ferroelectricity and magnetism in a crystal. The canonical example is the well-known room-temperature multiferroic $BiFeO_3$, in which lone electron pair of Bi [29] is responsible for ferroelectricity, while Fe magnetic moments order in a a G-type AFM order with long wavelength cycloidal modulation [30]. A similar scenario can be achieved by doping – for example in mixed perovskites, where different cations can be responsible for ferroelectricity and different for magnetism [31, 32]. However, magnetically doped ferroelectrics are usually conducting, so their FE properties are difficult to measure [33].

Another possibility is to combine magnetism with charge order, often observed in transition metal compounds, especially those containing transition metal ions with different valence. If, after charge ordering, both sites and bonds turn out to be inequivalent, this can lead to ferroelectricity [32]. A further possibility is geometric ferroelectricity in $YMnO_3$, where MnO_5 block is tilted, and as a result, oxygen ions move to Y ions, creating the electric dipole [34].

In all the above cases classified as type-I multiferroics, the polar and magnetic orders emerge independently, thus coupling between them is typically weak [32]. In contrast, in type-II multiferroics the electric polarization is purely induced by the magnetic order and the different magnetic phases possess different polarization.

Altogether, there are three typical kinds of materials I deal with – canonical linear (non-multiferroic) magnetoelectrics, type I-multiferroics and type-II multiferroics. Canonical linear magnetoelectrics are typically nonpolar antiferromagnets. If a crystal has a spontaneous polarization or magnetization (FE and FM term in Eq. 1.2), its behavior in electric or magnetic field, respectively, is habitually nonlinear. Moreover easy-axis antiferromagnets serve as the best example, because the magnetic order is hardly changed by the magnetic field, thus they exhibit purely linear ME effect up to the spin-flip or spin-flop field which can be in order of several T. Type-II multiferroics are nonpolar in paramagnetic phase, similarly as canonical linear magnetoelectrics. However, they become polar upon the (meta)magnetic phase transition, or they can become polar by applying magnetic fields. Often, their magnetic structures are susceptible, because they are typically easy-plane antiferromagnets, magnets with noncollinear spin ordering (often

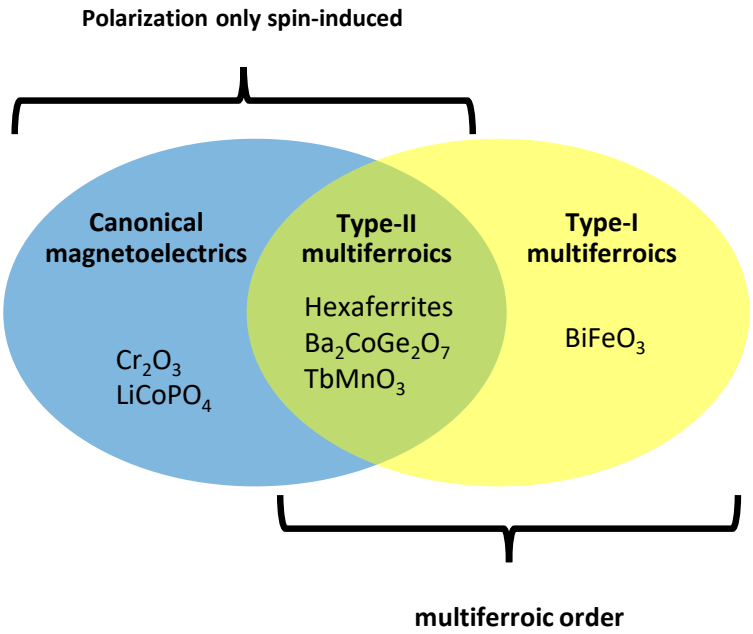

Figure 1.1: Rough biased classification of the magnetoelectric and multiferroic materials according to the author. Representative materials, with focus on those investigated in this thesis, are listed in each segment.

due to frustration), or even with spontaneous magnetic moment – i.e. ferrimagnets or ferromagnets. Habitually, the ME effects become nonlinear in type-II multiferroics. The third class are type I-multiferroics which are polar even in their paramagnetic phase. Since the spin-induced polarization is typically much smaller than the conventional one, the polarization in type-I multiferroics cannot be reversed by a magnetic field. Fig. 1.1 displays this classification which is useful for purpose of this thesis. Blue ellipse denotes materials which are nonpolar in the paramagnetic state, thus the magnetic-field-induced polarization appears only as a consequence of a magnetic order. Yellow ellipse denotes materials with multiferroic order. The green intersection then defines type-II multiferroics. In each segment, representative examples of materials are given.

From the above distinction of magnetoelectrics and multiferroics, one may get an impression that spontaneous orders are characteristic for multiferroics, while the ME coupling is characteristic for magnetoelectrics. Nevertheless, behind ME coupling, which is manifested on a macroscopic scale, there must be some long-range order of spins, combined with arrangement of ions. This typically results in spins lying at crystallographically non-equivalent positions, thus forming multi-sublattice AFM orders, crucial for the ME effects. By measuring the non-vanishing elements of $\chi^{me}_{\alpha\beta}$, different kinds of AFM orders can be identified, which is otherwise accessible only by expensive neutron scattering experiments.

The different AFM orders can be classified according to a multipolar expansion [35]. Following Refs. [35, 36], I consider magnetization density $\boldsymbol{\mu}(\boldsymbol{r})$ and inhomogeneous magnetic field $\boldsymbol{H}(\boldsymbol{r})$. The interaction Hamiltonian is then

$$H_{int} = -\int \boldsymbol{\mu}(\boldsymbol{r}) \cdot \boldsymbol{H}(\boldsymbol{r}) \mathrm{d}^3\mathrm{r}, \tag{1.6}$$

which can be expanded in powers of field derivatives calculated at some arbitrary reference point $\boldsymbol{r} = 0$:

$$H_{int} = -\int \boldsymbol{\mu}(\boldsymbol{r}) \cdot \boldsymbol{H}(0) \mathrm{d}^3\boldsymbol{r} - \int r_\alpha \mu_\beta(\boldsymbol{r}) \partial_\alpha H_\beta(0) \mathrm{d}^3\boldsymbol{r} - \dots . \tag{1.7}$$

The first term in Eq. 1.7 is the interaction with the total magnetic moment of the system, $\boldsymbol{m} = \int \boldsymbol{\mu}(\boldsymbol{r}) \mathrm{d}^3\boldsymbol{r}$, which is zero in compensated AFMs. In the second term, the tensor $\int r_\alpha \mu_\beta(\boldsymbol{r}) \mathrm{d}^3\boldsymbol{r}$ with nine components can be decomposed into three irreducible tensors:

(1) The pseudoscalar from the trace of the tensor:

$$a = \frac{1}{3} \int \boldsymbol{r} \cdot \boldsymbol{\mu}(\boldsymbol{r}) \mathrm{d}^3\boldsymbol{r}, \tag{1.8}$$

(2) the toroidal moment vector dual to the antisymmetric part of the tensor:

$$\boldsymbol{t} = \frac{1}{2} \int \boldsymbol{r} \times \boldsymbol{\mu}(\boldsymbol{r}) \mathrm{d}^3\boldsymbol{r}, \tag{1.9}$$

and

(3) the traceless symmetric tensor describing the quadrupole magnetic moment of the system:

$$q_{\alpha\beta} = \frac{1}{2} \int \left[r_\alpha \mu_\beta + r_\beta \mu_\alpha - \frac{2}{3} \delta_{\alpha\beta} \boldsymbol{r} \cdot \boldsymbol{\mu}(\boldsymbol{r}) \right] \mathrm{d}^3\boldsymbol{r}, \tag{1.10}$$

Calculation of these quantities is not straightforward as they depend on choice of origin in a bulk crystal, so one must find a high-symmetry structure in which they vanish by symmetry, similarly as for the bulk polarization [35–38].

The expansion of Eq. 1.7 can then be written in the form:

$$H_{int} = -\boldsymbol{m} \cdot \boldsymbol{H}(0) - a(\nabla \cdot \boldsymbol{H})_{r=0} - \boldsymbol{t} \cdot [\nabla \times \boldsymbol{H}]_{r=0} - q_{\alpha\beta}(\partial_\alpha H\beta + \partial_\beta H\alpha)_{r=0} - \dots . \tag{1.11}$$

One can see that the toroidal moment $\boldsymbol{t}$ couples to the curl of the magnetic field, and the quadrupole moment q_{ij} couples to the field gradient, while the pseudoscalar a is coupled to the divergence of magnetic field, and so represents a monopolar component. To distinguish it from zeroth-order monopolar term in the multipolar expansion, it can be called a ME monopole [35].

Every AFM order can be decomposed into the three irreducible components described above. All the moments change the sign under time reversal and space inversion. The lack of both symmetries is a necessary condition for the appearance of the linear ME effect. Therefore, a system with these ME multipole moments potentially shows the linear ME effect. For a localized spin system, Eqs. 1.8, 1.9 and 1.10 can be written as:

$$a = \frac{g}{3} \mu_B \sum_i \boldsymbol{r}_i \cdot \boldsymbol{S}_i, \tag{1.12}$$

$$\boldsymbol{t} = \frac{g}{2} \mu_B \sum_i \boldsymbol{r}_i \times \boldsymbol{S}_i, \tag{1.13}$$

$$q_{\alpha\beta} = \frac{g}{2} \mu_B \sum_i \left[r_{i\alpha} S_{i\beta} + r_{i\beta} S_{i\alpha} - \frac{2}{3} \delta_{\alpha\beta} \boldsymbol{r}_i \cdot \boldsymbol{S}_i \right]. \tag{1.14}$$

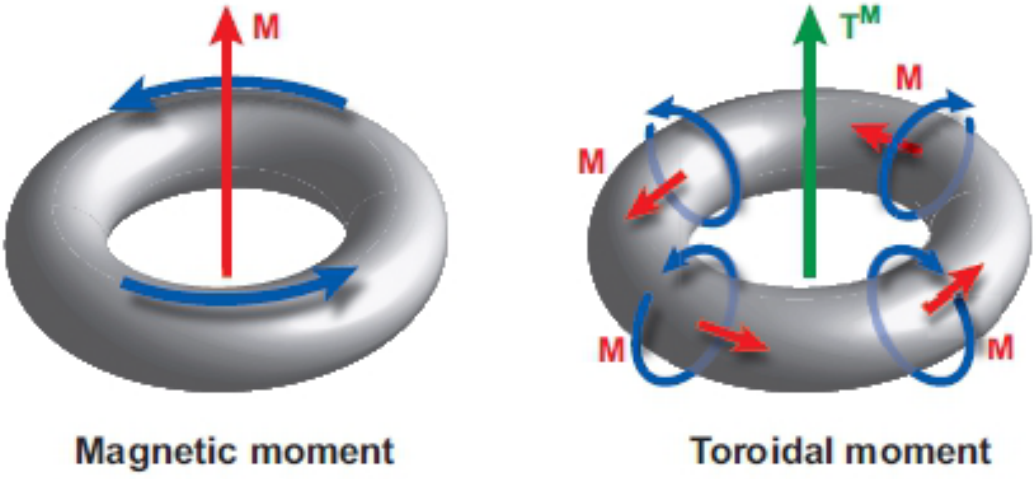

Figure 1.2: Magnetic moment and the toroidal moment, which can be understood as a moment of a magnetic moment. While magnetic moment is generated perpendicular to a current loop, the toroidal moment is generated by currents flowing in a coil bent to a shape of a torus, and it points perpendicular to the plane of the torus. On microscopic level inside magnetic materials where the magnetic field is generated by discrete magnetic moments – spins – the toroidal moment is generated in case of a whirl ordering spin configuration. (Figure reproduced from Ref. [39].)

Here, i represents a label of the individual spins S_i at the position r_i, while summation goes over a magnetic unit cell. Analogically, the ME susceptibility tensor can be decomposed into a pseudoscalar $\tilde{a}$, a vector $\tilde{t}$ and a symmetric traceless tensor $\tilde{q}_{\alpha\beta}$, while the ME free energy is

$$F_{\mathrm{ME}} = \tilde{a}(\boldsymbol{E}\cdot\boldsymbol{H}) + \tilde{\boldsymbol{t}}(\boldsymbol{E}\times\boldsymbol{H}) + \tilde{q}_{\alpha\beta}(E_{\alpha\beta}H_{\beta\alpha} + E_{\beta\alpha}H_{\alpha\beta}). \tag{1.15}$$

From comparison of Eq. 1.15 with Eq. 1.11, one can find the relationship between the ME multipole moment and the associated ME tensor. The quantities $\tilde{a}$, $\tilde{\boldsymbol{t}}$ and $\tilde{q}_{\alpha\beta}$ have the same symmetry as quantities a, $\boldsymbol{t}$ and $q_{\alpha\beta}$, respectively, but they are not the same. Therefore, the detection of the different ME tensor components may indicate the existence of ME multipolar orders, but the connection between these two quantities is not direct. For example, the ME measurements cannot define the ME multipolar orders without having additional information, and there is no direct proportionality between the ME effect and magnitude of the corresponding order.

As an example, the toroidal moment is then given by a whirling spin structure. Its symmetry is the same as symmetry of the coil with a current bent to a shape of torus, or a ring magnet magnetized along the ring perimeter (see Fig. 1.2). The toroidal moment is linked by symmetry to the antisymmetric part of the ME tensor according to Eq. 1.15 [36]:

$$\chi^{me} \sim \begin{pmatrix} 0 & -t_z & t_y \\ t_z & 0 & -t_x \\ -t_y & t_x & 0 \end{pmatrix}. \tag{1.16}$$

Analogically, the ME monopole is linked to diagonal components, and the quadrupole moment to the symmetric traceless part of the ME susceptibility tensor according to

Eq. 1.15 [35].

Importantly, these different types of AFM orders may manifest themselves by several intriguing effects, which is highly relevant not only in the field of ME multiferroics but also antiferromagnetic spintronics, for instance. Here I stick to representative examples of the three orders for ME multiferroics: 1) The ME effect in $LiCoPO_4$ has nonzero antisymmetric part [40], thus, according to Eq. 1.16, there is likely to be a ferrotoroidic order. Indeed, opposite phase of the second harmonic signal from opposite AFM domains is a signature of the ferrotoroidic order [41]. 2) The ME monopolar order is straightforwardly linked to the diagonal ME susceptibility tensor, thus suggesting $LiMnPO_4$ with its diagonal ME response [42] as an appropriate candidate for the ferromonopolar order. Indeed, symmetry analysis and density functional theory (DFT) calculations supported the ferromonopolar order in $LiMnPO_4$ [35]. 3) Magnetic-field-induced antiferroelectric behavior, implying traceless ME response, is a signature of quadrupolar order in $Ba(TiO)Cu_4(PO_4)_4$ [43].

Moreover, the above-mentioned examples are cases where the different AFM orders are uniform, i.e. described by modulation vector $\boldsymbol{Q} = 0$, so that they can be manifested macroscopically without need of any additional coupling. However, often the magnetic structures exhibit modulation, so some AFM orders can be described by modulation vector $\boldsymbol{Q} \neq 0$. For example, the orthophosphates $LiMPO_4$ (M=Co, Fe and Ni) possess local atomic-site ME monopoles according to DFT calculations, while there is no ferromonopolar, but antiferromonopolar order [35].

1.2 Microscopic mechanisms of spin-induced polarization

So far I have applied phenomenological macroscopic theory, which considers the global symmetry of the studied materials. As a step toward a microscopic model, one may consider the ME coupling allowed by local site or bond symmetries. In this approach, one searches for symmetry allowed local polarization that is induced by a certain spin configuration. The advantage of this method is having a local view, which, in combination with the knowledge of the magnetic structure, directly decides about the existence of a multiferroic state. Subsequently, one can derive even the linear ME effect for which one needs to know the magnetic field effect on spins first, which in turn gives the magnetic-field-induced polarization.

In the following, I will describe how a single spin or a pair of spins can create a polarization based on symmetry considerations and briefly mention known microscopic mechanisms which can explain the symmetry allowed terms.

1.2.1 Polarization induced by a single spin

The form of the polarization induced by a single spin can be deduced by considering the site symmetry of the ion on which the spin is localized. As the polarization is a time-reversal invariant vector, but spins are not, the polarization must couple to even-polynomial spin terms only [44]. Since the spin is invariant upon spatial inversion, any polynomial of spins is also invariant upon the space inversion. However, polarization changes the sign upon the space inversion. Therefore, the spin must not be located at an inversion center to produce a local polarization via a single-site term [45]. Also, such

terms are nontrivial only for $S \geqslant 1$, as for $S = 1/2$, higher order polynomials of the spin components are equal to a single spin component or unity.

Let me take the simplest nontrivial case – a second order (i.e. quadratic) spin term, for $S \geqslant 1$. This term has the symmetry of a magnetic quadrupole, while the polarization has the symmetry of an electric dipole. In the lack of inversion symmetry, the electric dipole and magnetic quadrupole can in principle couple via a third rank real symmetric tensor: $p_S^\alpha = K_{\beta\gamma}^\alpha S^\beta S^\gamma$. For high-symmetry cases when the site symmetry of the magnetic ion is identical to the (paramagnetic) point group symmetry, the form of this tensor for 20 nontrivial (i.e., excluding no symmetry when all terms are allowed) noncentrosymmetric point groups is listed in Ref. [45], Table I.

All mechanisms describing polarization induced by a single spin should be related to a SU(2) symmetry breaking single-ion anisotropy term coming from the spin-orbit coupling (SOC). The one first proposed and accepted in the community is the spin-dependent d–p hybridization between d-orbitals of a transition metal ion, and p-orbitals of a ligand, typically oxygen [46]. In this model, the magnetic ion is assumed to be in a crystal field, thus e_g and t_{2g} orbitals are split. When introducing the SOC into the model, occupation of d-levels, hybridized with p-levels, depends on the spin direction, thus inducing the polarization along the bond. When the magnetic ion is in an oxygen tetrahedron with broken inversion symmetry, the prescription for the single-spin-induced polarization is the following:

$$\boldsymbol{P} \sim \sum_{i=1}^{4} \left(\boldsymbol{S}\boldsymbol{e}_i\right)^2 \boldsymbol{e}_i. \tag{1.17}$$

Note that the d–p hybridization model is the second-order SOC perturbation, so one can assume this effect to be small. Another microscopic origin is the parity mixing of d and p orbitals of the magnetic ion [45] via the SOC.

1.2.2 Two-spin-induced polarization: antisymmetric case

When the polarization is induced by two interacting spins, the symmetry of the bond should be considered. Models are typically applied for two magnetic ions and a ligand in the middle of them, while the local polarization is represented by the shift of the ligand and the bonding electrons. If the ligand is at the inversion center, the inversion exchanges the roles of two spins, therefore, only antisymmetric combinations of spin components can induce a polarization. Furthermore, as formal swapping of the site indeces must result in the same polarization, the expression of the polarization has to contain the $\boldsymbol{e_{12}}$ unit vector pointing from the site of $\boldsymbol{S_1}$ to the site belonging to $\boldsymbol{S_2}$.

For the special case of the highest symmetry, Katsura, Nagaosa and Balatsky derived, similarly to the d–p hybridization model, a microscopic model for the electronic polarization [47], now known as the KNB model. (d–p hybridization model considers stronger Hund coupling.) KNB model gives polarization as

$$\boldsymbol{P_{12}} = P^{sc}\boldsymbol{e_{12}} \times \left(\boldsymbol{S_1} \times \boldsymbol{S_2}\right). \tag{1.18}$$

The KNB model results in a finite spin-induced polarization only in non-collinear magnetic structures where the polarization is perpendicular to the bond and lies in the plane spanned by the two spins. When the local polarizations arising from Eq. 1.18 are summed up for

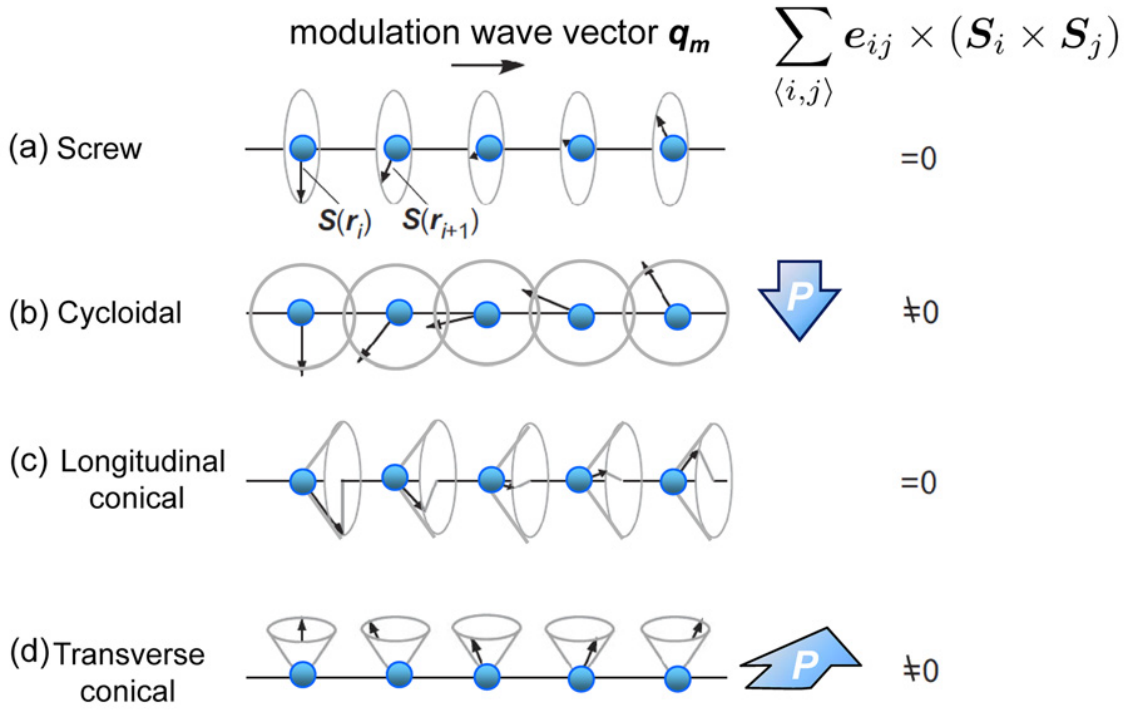

Figure 1.3: Schematic illustrations of the different types of spiral magnetic structure on a one-dimensional array of spins $\boldsymbol{S}(r)$. They include (a) proper screw, (b) cycloidal, (c) longitudinal-conical, and (d) transverse-conical magnetic structures. The directions of macroscopic polarization P calculated from the spin-current model or inverse DM model are also indicated for their respective structure. Other spiral structures (a) and (c) may potentially generate P due to the spin-dependent p–d hybridization mechanism on some specific crystal structures. (Figure reproduced from Ref. [48].)

the magnetic structure they may cancel out or give a non-zero polarization depending on the winding of the spins in case of a spin-spiral as shown in Fig. 1.3.

Strictly speaking, the ions are fixed in the KNB model, so the polarization is purely electronic. However, the motion of electrons and ionic cores are always coupled. The model for the ionic polarization, giving exactly the same formula as the KNB model, is often termed as the inverse Dzyaloshinkii-Moriya interaction [49]. To have more insight into this model, the next subsection is dedicated to the direct and inverse Dzyaloshinkii-Moriya interaction, both of them important for multiferroics.

Direct and inverse Dzyaloshinskii-Moriya interaction

In 1958, Dzyaloshinskii studied antiferromagnets from symmetry point of view. He pointed out that in case of some low-symmetry non-centrosymmetric crystal structures, spins, otherwise antiferromagnetically aligned, can tilt without breaking additional symmetries, giving rise to a weak ferromagnetism [50]. In other words, the (anti)parallel alignment of spins is not protected by symmetry. A few years later, Moriya gave the physical meaning to this discovery [51, 52]. He derived this spin canting from quantum mechanical calculations: He obtained relativistic corrections to the superexchange couplings in the Anderson model, and found that the antisymmetric part of the superexchange

interaction is responsible for the spin canting [51, 52]. The energetic reason for this effect can be expressed by the Dzyaloshinskii-Moriya (DM) Hamiltonian for the model of 2 magnetic ions with spins $\boldsymbol{S_1}$ and $\boldsymbol{S_2}$, describing the superexchange interaction through a ligand in between them:

$$H_{DM} = \boldsymbol{D_{12}} \cdot (\boldsymbol{S_1} \times \boldsymbol{S_2}), \tag{1.19}$$

where $\boldsymbol{D_{12}}$ is the Dzyaloshinskii vector, whose possible directions are determined by the local symmetry of a bond [52]. Notably, the inversion symmetry of the bond must be broken to allow finite $\boldsymbol{D_{12}}$.

In the first-order approximation, the magnitude of $\boldsymbol{D_{12}}$ is proportional to the displacement $\boldsymbol{d}$ of the ligand away from the middle point in between the spins [49]:

$$D_{12} = \zeta \boldsymbol{e_{12}} \times \boldsymbol{d}, \tag{1.20}$$

Here, e_{12} is again a vector connecting the two spins, and ζ is a microscopic parameter proportional to the strength of the SOC. The Dzyaloshinskii-Moriya Hamiltonian can be then expressed as

$$H_{DM} = \zeta (\boldsymbol{e}_{12} \times \boldsymbol{d}) (\boldsymbol{S_1} \times \boldsymbol{S_2}), \tag{1.21}$$

It is important to note that the sign of the coupling determines the sense of the spin canting and the chirality of the resulting spin spiral: For example for a one dimensional chain of otherwise ferromagnetically aligned spins, the sign of the Dzyaloshinskii vector, perpendicular to the chain and spin direction, determines whether the resulting cycloidal structure is left-handed or right-handed.

The inverse Dzyaloshinskii-Moriya (iDM) interaction is also represented by Eq. 1.21, but in a crystal where the position of the atoms are not fixed. While in the direct DM interaction, inversion symmetry breaking of the crystal lattice induces noncollinear spin structure, in the case of the iDM interaction, noncollinear spin structure induces inversion symmetry breaking by a lattice distortion, thus emergence of the polarization. Let me assume that for some reason other than the direct DM interaction (for example the magnetic frustration), the spin structure is noncollinear. In order to calculate the displacement, of the ligand, one should induce an elastic term into the Hamiltonian – as it is a small effect, it is enough to use the quadratic term. Thus, the energy to be minimized reads as

$$E_{DM} = \sum_{\alpha} \left[(\zeta \boldsymbol{e}_{12} \times \boldsymbol{d})_{\alpha} (\boldsymbol{S_1} \times \boldsymbol{S_2})_{\alpha} + \frac{K}{2} d_{\alpha}^2 \right], \tag{1.22}$$

where K is the elastic constant and summation goes over Cartesian coordinates. The minimization of this energy term with respect to the displacement $\boldsymbol{d}$ gives [49]

$$\boldsymbol{d} = \frac{\zeta}{K} (\boldsymbol{e}_{12} \times (\boldsymbol{S_1} \times \boldsymbol{S_2})). \tag{1.23}$$

The displacement, which in case of a charged ion gives the ionic polarization, is exactly the same as the KNB formula (Eq. 1.18). Altogether, the KNB and Sergienko-Dagotto (or inverse DM) models are complementary, and explain electronic and ionic polarizations, respectively. If one plugs this expression for the displacement back to the Hamiltonian in Eq. 1.19, one gets a spin-only model

$$H_{iDM} = \frac{\zeta^2}{K} \left(\boldsymbol{e}_{12} \times \left(\boldsymbol{e}_{12} \times \left(\boldsymbol{S_1} \times \boldsymbol{S_2} \right) \right) \right) \left(\boldsymbol{S_1} \times \boldsymbol{S_2} \right). \tag{1.24}$$

The energy is then fourth-order expression of spins, and can be further simplified for specific spin structures. For example for harmonic one-dimensional cycloidal structure, when spins in the chain along the z axis lie in the yz plane, the displacement is in the y direction: $d_y = \frac{\zeta}{K} |\boldsymbol{S_1} \times \boldsymbol{S_2}|$. This Hamiltonian (Eq. 1.24) can be, for the cycloidal structure, simplified to

$$H_{iDM} = -\frac{\zeta^2}{K} \left(\boldsymbol{S_1} \times \boldsymbol{S_2} \right)^2. \tag{1.25}$$

This is an interesting result: As it is a quadratic expression of an antisymmetric term, this term is symmetric, in other words both helicities have the same energy in contrast to the *direct* DM interaction. Since spirals with opposite helicity have opposite polarization induced by the ionic displacement in Eq. 1.23, when coupled to an external electric field, both helicities can be selected (sometimes combined with a magnetic field).[1] This scenario works well for several multiferroics with spiral spin structures. For example in hexaferrites, the magnetic structure forms a single domain state with defined helicity depending on the cross product of crossed electric and magnetic poling fields [53].

Altogether, the KNB model and the inverse Dzyaloshinkii-Moriya interaction, both being first-order SOC perturbations, are special cases of an antisymmetric exchange, and the presented formulas were derived neglecting further terms reducing the symmetry of the bond. For lower symmetries, the antisymmetric tensor can have more nonzero elements [54]. Nevertheless, any model for the 2-spin-induced polarization in centrosymmetric materials must be antisymmetric, and contain the vector e_{12}, connecting spins.

Note that the polarization predicted by the KNB or iDM model has the same symmetry as the polarization, predicted by Mostovoy using Landau-Lifshitz-Ginzburg theory [55] (Eq. 1.26). In multiferroics one shall ask about coupling between the spontaneous electric and magnetic orders. Due to different symmetries of electric and magnetic quantities, the lowest-order allowed polynomial coupling term to be added to the free energy is $\propto (\boldsymbol{P}^S)^2 (\boldsymbol{M}^S)^2$, i.e. 4^{th} order. For noncollinear magnetic orders, Mostovoy proposed the following 3^{rd} order term [55]

$$P = \gamma \epsilon [\boldsymbol{M}(\nabla \cdot \boldsymbol{M}) - (\boldsymbol{M} \cdot \nabla)\boldsymbol{M}]. \tag{1.26}$$

This term is the macroscopic equivalent of the KNB or iDM models.

1.2.3 Two-spin induced polarization: symmetric case

In the case when the inversion symmetry in between two magnetic ions is broken, for example if the two spins lie at non-equivalent atoms, symmetric two-spin terms can also induce polarization. The form of the symmetric tensor depending on crystal point group symmetry can be found in Ref. [45]. Importantly, the polarization induced by this effect can be invariant under global spin rotation, thus, in contrast to the above-mentioned effects, it does not need to involve the SOC [44].

[1] This is possible only in lack of *direct* DM interaction, which would select a single helicity domain.

The microscopic model behind symmetric two-spin terms is the exchange-striction (also called magnetostriction), which indeed does not involve the SOC, but only bond-length dependence of the exchange integral. The microscopic mechanism for the polarization induced by the exchange-striction mechanism was firstly proposed for multiferroics by Sergienko *et al.*, [56] but in fact, the principle is the same as the previously known spin-Peierls mechanism [57–60].

The Hamiltonian taking into account the symmetric Heisenberg exchange in between the two spins and the elastic term reads as

$$H_{es} = J(x)\,(\boldsymbol{S_1}\cdot\boldsymbol{S_2}) + \frac{K}{2}(x-x_0)^2. \tag{1.27}$$

Here I assume a linear dependence of the exchange integral $J(x) = J(x_0) + \frac{\mathrm{d}J(x)}{\mathrm{d}x}|_{x_0}(x-x_0)$, on the displacement $\delta = x - x_0$, where x and x_0 are the equilibrium distance of spins with and without perturbation H_{es}, respectively. Minimizing the Hamiltonian in Eq. 1.27 with respect to δ gives

$$\delta = -\frac{(\boldsymbol{S_1}\cdot\boldsymbol{S_2})}{K}\frac{\mathrm{d}J(x)}{\mathrm{d}x}|_{x_0}. \tag{1.28}$$

One can see that the linear dependence of the exchange integral on the distance of spins can lead to change of the distance between spins, thus the magnetic ions. This can lead to change of the polarization for example if the two magnetic ions have different charges. This is consistent with a generic symmetry condition that a symmetric term can lead to the polarization only if there is no inversion center in between the spins. Since the model is one-dimensional, the two magnetic ions can break only the mirror plane perpendicular to the bond, so the resulting polarization must lie along the bond. Moreover, the local polarizations induced by the exchange-striction can often cancel out in bulk. One of the simplest systems where the polarization does not cancel is a one-dimensional chain of two alternating ions A and B with different charges, forming ↑-↑-↓-↓ spin structure. To provide a description of the spin-induced polarization consistent with Eq. 1.18, the polarization induced by the exchange-striction is viewed as

$$\boldsymbol{P_{12}} = P^{es}\boldsymbol{e_{12}}\,(\boldsymbol{S_1}\cdot\boldsymbol{S_2})\,. \tag{1.29}$$

Altogether, the exchange-striction is expected to give the strongest spin-polarization coupling, since it is not based on the SOC as other mechanisms, but on the much stronger exchange coupling. Furthermore, this mechanism is more universal, and it is expected in large classes of materials, including those with small SOC. It also does not require a non-collinear spin structure, but special spin and/or charge arrangement so that the macroscopic polarization does not cancel out. Finally, I note that having two inequivalent magnetic ions close to each other is not essential: Inequivalent spins may refer to inequivalent clusters of magnetic ions [61].

Although the symmetry requirements for the static polarization induced by the exchange-striction are quite strong and there are not many materials exhibiting it, the selection rules for the dynamic ME effect are much looser, since several excited states are available. Therefore, the exchange-striction mechanism is often responsible for the dynamic ME effect: Ground state property is allowed if its representation contains fully symmetric representation. In contrast, excitation is allowed upon an interaction

Hamiltonian if the product of representations of (i) ground state, (ii) excited state and (iii) the interaction Hamiltonian contains fully symmetric representation.

1.2.4 "Unified" model of the spin-induced ferroelectricity and more complex approaches: Phenomenology combined with DFT calculations

The microscopic models mentioned above were derived for special high-symmetry cases, therefore, in real materials often further terms are allowed by the lower symmetry. This problem was solved by the method of Xiang *et al.*, who, besides deriving the symmetry allowed terms, developed a method to extract the symmetry-allowed coefficients from DFT calculations [62]. For example, spin-induced ferroelectricity in MnI_2 was only explained by this method.

The next problem is that some models are purely electronic (KNB) and others are purely ionic (iDM), while it is known that both electronic and ionic polarizations emerge at once, as calculated [63, 64] as well as experimentally observed [65] for prototypical spin-induced ferroelectric $TbMnO_3$. This problem was captured by a follow-up work of Xiang *et al.* [66], who separated the pure electronic and lattice contributions phenomenologically, which in turn helps to calculate the polarization by DFT method without lattice geometry relaxation. Furthermore, the spin-induced lattice strain (via piezomagnetism) can give rise to an additional polarization through the piezoelectric effect [67, 68]. Other similar trilinear or higher order couplings are also in principle allowed.

From this section, which has no ambition of comprehensiveness, it is clear that despite immerse theoretical progress in searching for microscopic models for the spin-induced polarization, a truly microscopically unified theory cannot be developed, and different materials have to be treated individually.

1.3 Dynamic magnetoelectric effect: Electromagnetism meets magnetoelectricity

The response of a driven system has some characteristic time scale, which is often relevant for applications. From the theoretical point of view, every linear response function exhibits a sum rule based on Kramers-Kronig relations, linking its dynamical and static parts. The speed of the ME effect is determined by either the resonant frequencies of characteristic ME excitations or the dynamics of ME domains. The latter contribution is zero in a single domain sample. In the general case, the frequency dependent ME susceptibility can be calculated within the linear-response theory given by the Kubo formula [69]. The task now then is to study the frequency dependence of χ^{me} and χ^{em}, introduced in Eq. 1.1, together with electric and magnetic susceptibilities χ^{ee} and χ^{mm}. The finite-temperature Kubo formula reads as

$$\chi^{ee}_{\gamma\delta}(z) = -\frac{V_c}{\varepsilon_0\hbar}\sum_{m,n}\frac{e^{-\beta\hbar\omega_n}-e^{-\beta\hbar\omega_m}}{\sum_i e^{-\beta\hbar\omega_i}}\frac{\langle n|\,\hat{P}_\gamma\,|m\rangle\langle m|\,\hat{P}_\delta\,|n\rangle}{z-\omega_m+\omega_n}, \tag{1.30}$$

$$\chi^{mm}_{\gamma\delta}(z) = -\frac{\mu_0 V_c}{\hbar}\sum_{m,n}\frac{e^{-\beta\hbar\omega_n}-e^{-\beta\hbar\omega_m}}{\sum_i e^{-\beta\hbar\omega_i}}\frac{\langle n|\,\hat{M}_\gamma\,|m\rangle\langle m|\,\hat{M}_\delta\,|n\rangle}{z-\omega_m+\omega_n}, \tag{1.31}$$

$$\chi^{me}_{\gamma\delta}(z) = -\frac{V_c}{\hbar}\sqrt{\frac{\mu_0}{\varepsilon_0}}\sum_{m,n}\frac{e^{-\beta\hbar\omega_n}-e^{-\beta\hbar\omega_m}}{\sum_i e^{-\beta\hbar\omega_i}}\frac{\langle n|\,\hat{M}_\gamma\,|m\rangle\langle m|\,\hat{P}_\delta\,|n\rangle}{z-\omega_m+\omega_n}, \tag{1.32}$$

$$\chi^{em}_{\gamma\delta}(z) = -\frac{V_c}{\hbar}\sqrt{\frac{\mu_0}{\varepsilon_0}}\sum_{m,n}\frac{e^{-\beta\hbar\omega_n}-e^{-\beta\hbar\omega_m}}{\sum_i e^{-\beta\hbar\omega_i}}\frac{\langle n|\,\hat{P}_\gamma\,|m\rangle\langle m|\,\hat{M}_\delta\,|n\rangle}{z-\omega_m+\omega_n}, \tag{1.33}$$

where $z{=}\omega{+}i\varepsilon$ and $\varepsilon{\to}0+$. $\hat{M}_\gamma$ and $\hat{P}_\delta$ are the operators of the magnetic and electric dipole density, respectively. $|m\rangle$ and $|n\rangle$ are eigenstates of the unperturbed system with energies of $\hbar\omega_m$ and $\hbar\omega_n$, while $\beta = (k_B T)^{-1}$ is the inverse temperature and V_c stands for the volume of the unit cell.

Time reversal, connects the two ME tensors according to $\{\chi^{me}_{\alpha\beta}(\boldsymbol{q},\omega,\mathcal{M})\}' = -\chi^{em}_{\beta\alpha}(-\boldsymbol{q},\omega,-\mathcal{M})$, where $\{'$ denotes operation of time reversal, $\boldsymbol{q}$ is the wavevector and $\mathcal{M}$ symbolizes all time-reversal symmetry-breaking degrees of freedom necessary to describe the actual state of the material such as magnetization, AFM vector, etc. The proof of such a symmetry relation can be derived from the Kubo formula in time-domain [69].

According to Eq. 1.32 (or Eq. 1.33), ME effect emerges from excitations, which are both electric-dipole and magnetic-dipole active. The studied excitations have typically energies comparable to the thermal energy corresponding to the magnetic ordering temperature. Since the experiments were performed at low temperatures, the zero-temperature limit of the Kubo formula is justified, in which the Boltzmann factors vanish except for the $n = 0$ zero energy ground state, i.e. $\omega_n = 0$. The ME susceptibility can be separated by two distinct ways – either to time-reversal odd (χ') and even (χ'') parts, or to real ($\Re\chi^{me}$) and imaginary ($\Im\chi^{me}$) parts. Using the former separation, the ME susceptibility can be written in zero-temperature limit as

$$\chi^{me}_{\gamma\delta}(z) = -\frac{2V_c}{\hbar}\sqrt{\frac{\mu_0}{\varepsilon_0}}\sum_m \frac{\omega_m\Re(\langle 0|\,\hat{M}_\gamma\,|m\rangle\langle m|\,\hat{P}_\delta\,|0\rangle) + i\omega\Im(\langle 0|\,\hat{M}_\gamma\,|m\rangle\langle m|\,\hat{P}_\delta\,|0\rangle)}{\omega^2-\omega_m^2-\varepsilon^2+2i\omega\varepsilon}. \tag{1.34}$$

The part related to the real (imaginary) part of the $\langle 0|\,\hat{M}_\gamma\,|m\rangle\langle m|\,\hat{P}_\delta\,|0\rangle$ transition matrix element product is equal to χ' (χ''), thus, is antisymmetric/symmetric under time reversal, respectively. This is a direct consequence of the proof of $\{\chi^{me}_{\alpha\beta}(\omega)\}' = -\chi^{em}_{\beta\alpha}(\omega)$, given above, if one realizes that the exchange of final and initial states means conjugation, which keeps the real part and changes the sign of the imaginary part. Moreover, direct and the converse ME effects can be written as $\chi^{me}_{\gamma\delta} = \chi'_{\gamma\delta} + \chi''_{\gamma\delta}$ and $\chi^{em}_{\gamma\delta} = \chi'_{\delta\gamma} - \chi''_{\delta\gamma}$.

Considering the zero-frequency limit, χ'' vanishes as $\omega \to 0$. This is in accord with symmetry considerations that the time-reversal must be broken for the static ME effect to emerge. $\chi''(\omega)$ can be nonzero even for nonmagnetic chiral crystals and it is responsible

for the natural optical activity (NOA) [6]. On the other hand, $\chi'(\omega)$ is nonvanishing only if static $\chi'(\omega = 0)$ is finite.

What kind of optical phenomena can be observed if $\chi'(\omega)$ is finite? When solving Maxwell's equations together with constitutive equations 1.3 and 1.4, in general, on can get four distinct solutions of the refractive index for a given light director, $\boldsymbol{k} = \pm k$ due to the ME susceptibility. This effect is called quadrochroism. The solutions may differ for different light polarization and, which is not common, also for its direction. The difference of the real and imaginary parts of the refractive index observed for the reversal of the light propagation directions are referred as directional birefringence (DB) and directional dichroism (DD), respectively, and the difference in the light propagation for $+\boldsymbol{k}$ and $-\boldsymbol{k}$ is termed as optical directional anisotropy (ODA). If the linear polarization of the incident beam is nearly maintained upon propagation in the material,[2] the approximate solutions can be written as (see, e.g., Refs. [7, 9, 70])

$$N^{\pm}(\omega) \approx \sqrt{\varepsilon_{\delta\delta}(\omega)\mu_{\gamma\gamma}(\omega)} \pm \frac{1}{2}\left[\chi^{me}_{\gamma\delta}(\omega) - \{\chi^{me}_{\gamma\delta}(\omega)\}'\right]. \tag{1.35}$$

Here $N^{\pm}$ stands for the refractive indices of waves propagating in opposite directions $(\pm\boldsymbol{k})$. The δ and γ coordinate axes are parallel to the direction of the electric ($\boldsymbol{E}^{\omega}$) and magnetic ($\boldsymbol{H}^{\omega}$) fields of light, respectively. Since the fields are perpendicular to each other, only off-diagonal elements of the ME tensor appear in Eq. 1.35. Nevertheless, Eq. 1.35 can be modified for any polarization state, depending on the crystal symmetry, which determines light eigenmodes of the system. In such a case, diagonal, as well as time-reversal even elements of the ME susceptibility may enter into the formula, (see e.g. Refs. [7, 71]), but only the time-reversal odd elements will contribute to the non-reciprocal ODA.

This reciprocity breaking optical process induced by the presence of the ME susceptibility can be understood in the following way: One can calculate the oscillating polarization and magnetization induced by the fields of the light propagating in the $+\boldsymbol{k}$ direction

$$P^{\omega}_{\delta} = \chi^{ee}_{\delta\delta}(\omega)E^{\omega}_{\delta} + \frac{1}{c}\chi^{em}_{\delta\gamma}(\omega)H^{\omega}_{\gamma} \text{ and } M^{\omega}_{\gamma} = \chi^{mm}_{\gamma\gamma}(\omega)H^{\omega}_{\gamma} + \sqrt{\frac{\varepsilon_0}{\mu_0}}\chi^{me}_{\gamma\delta}(\omega)E^{\omega}_{\delta}. \tag{1.36}$$

For the $-\boldsymbol{k}$ direction the relative signs of E^{ω}_{δ} and H^{ω}_{γ} are opposite, thus

$$P^{\omega}_{\delta} = \chi^{ee}_{\delta\delta}(\omega)E^{\omega}_{\delta} - \frac{1}{c}\chi^{em}_{\delta\gamma}(\omega)H^{\omega}_{\gamma} \text{ and } M^{\omega}_{\gamma} = -\chi^{mm}_{\gamma\gamma}(\omega)H^{\omega}_{\gamma} + \sqrt{\frac{\varepsilon_0}{\mu_0}}\chi^{me}_{\gamma\delta}(\omega)E^{\omega}_{\delta}. \tag{1.37}$$

The ODA is manifested as a constructive and destructive interference between the conventional and ME contribution to the materials optical response for $+\boldsymbol{k}$ and $-\boldsymbol{k}$, respectively as illustrated in Fig. 1.4.

1.3.1 Magnetoelectric sum rule

To link the static ME effect with its dynamical part, it is useful to derive the sum rule for χ^{me}. For any response function, the Kramers-Kronig relations lead, in the static limit, to

[2]The polarization rotation is sometimes inevitable effect, connected to DD. Nevertheless, the perpendicular light polarization component contributes to the intensity quadratically, thus it can be eliminated if polarization rotation is small. This approximation holds for (i) a large anisotropy in the diagonal components of the dielectric tensor ε, (ii) more rarely in the magnetic permeability tensor μ, or (iii) a thin sample.

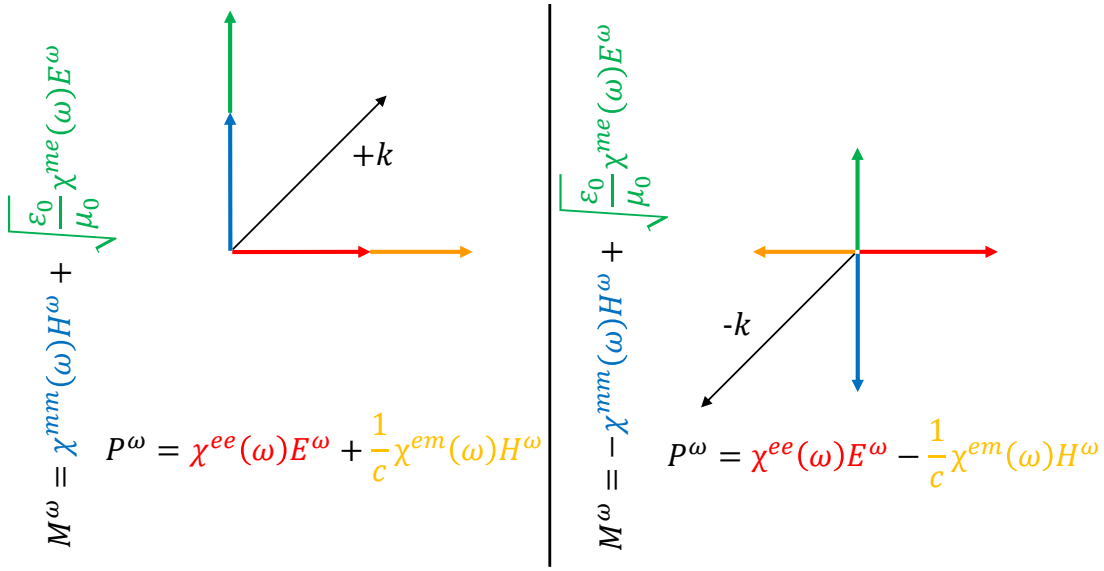

Figure 1.4: Schematic illustration of a linearly polarized EM wave propagating through a ME medium with off-diagonal elements of the ME tensor. According to Eqs. 1.36 and 1.37, for light propagating along $+\boldsymbol{k}$, the magnetization and polarization wave interfere constructively, corresponding to larger real part of the refractive index and higher absorption at the frequencies of ME excitations, compared to $-\boldsymbol{k}$

following formulas [72, 73]:

$$\Re\chi_{\gamma\delta}(\omega=0) \equiv \chi_{\gamma\delta}(0) = \frac{2}{\pi}\mathcal{P}\int_0^\infty \frac{\Im\chi_{\gamma\delta}(\omega)}{\omega}\mathrm{d}\omega, \tag{1.38}$$

$$\Im\chi_{\gamma\delta}(\omega=0) \equiv 0 = -\frac{1}{\pi}\mathcal{P}\int_{-\infty}^\infty \frac{\Re\chi_{\gamma\delta}(\omega)}{\omega}\mathrm{d}\omega. \tag{1.39}$$

When the transmittance of a sample is measured, $\Im\chi^{me}$ is manifested in the directional dichroism. According to Eq. 1.35 and the relation of the absorption coefficient to the imaginary part of the refractive index–$\alpha(\omega) = \frac{2\omega}{c}\Im(N)$–the absorption coefficient difference is

$$\Delta\alpha(\omega) = \alpha_+(\omega) - \alpha_-(\omega) = \frac{2\omega}{c}\Im(\chi^{me}_{\gamma\delta}(\omega) - \{\chi^{me}_{\gamma\delta}(\omega)\}'). \tag{1.40}$$

Since the left-hand-side of the Eq. 1.38 is time-reversal odd according to Eq. 1.34, only the time-reversal odd part of $\Im\chi(\omega)$ contributes in the integrand on the right-hand-side of Eq. 1.38. Therefore, $\Im\chi_{\gamma\delta}(\omega)$ can be replaced by $\frac{1}{2}\Im(\chi^{me}_{\gamma\delta}(\omega) - \{\chi^{me}_{\gamma\delta}(\omega)\}')$, which turns Eq. 1.38, using Eq. 1.40, into a practical ME sum rule [74]:

$$\chi^{me}_{\gamma\delta}(0) = \frac{c}{2\pi}\mathcal{P}\int_0^\infty \frac{\Delta\alpha(\omega)}{\omega^2}\mathrm{d}\omega. \tag{1.41}$$

The ME sum rule is applicable for all materials where there are finite off-diagonal elements in the static ME tensor, which can be found in Ref. [17]. It tells that the nonzero static ME susceptibility implies directional dichroism at finite frequencies. Due to the $\frac{1}{\omega^2}$ weight

in the integrand, the low-energy excitations, typically collective magnons, have a larger contribution. Note that real and imaginary parts of the ME susceptibility contribute to real (n) and imaginary (κ) part of the refractive index, as clear from Eq. 1.35, latter being called the extinction coefficient.

1.3.2 Symmetry conditions for optical directional anisotropy

Importantly, ODA given by the ME effect can be observed even for unpolarized light. This is in contrasts with the Faraday effect, for which absorption difference for counter propagating beams can be observed only if they are circularly or elliptically polarized, however, the absorption measured for $\pm\boldsymbol{k}$ is the same for linearly polarized or unpolarized light. Therefore, ODA can be observed only in materials with low symmetry. More specifically, any symmetry operation that can reverse the direction of the wavevector of light, which is a polar, time-reversal odd vector, should be broken to observe ODA. The complete classification of the magnetic point symmetry groups allowing for ODA can be found in Ref. [75].

In the first set of magnetic point groups, nonreciprocal light propagation is allowed whenever a vectorial quantity with symmetry of light wavevector (i.e. time-reversal odd polar vector), is allowed – let me call this quantity $\boldsymbol{t}$, as it has the same symmetry as the toroidal moment $\boldsymbol{t}$, defined by Eq. 1.13. ODA arises along the direction of the symmetry-allowed $\boldsymbol{t}$. In the case of crystals, $\boldsymbol{t}$ is allowed in the subgroups of $n/m'mm$ and $\overline{n}'2'm$ where $\boldsymbol{t}$ is parallel to the principal axis and $n = 4$ or 6 (here, $\overline{n}$ denotes the n-fold rotation axis combined with a perpendicular mirror plane), which is the case of 31 magnetic point groups, allowing non-dissipative supercurrent [76]. Note that in some cases ODA is allowed even though no such $\boldsymbol{t}$ vector can be defined [75].

It is instructive to further classify the cases when $\boldsymbol{t}$ is allowed. First case reveals when the material possesses a finite electric polarization and a net magnetization nonparallel to each other. Then, one can introduce the following quantity:

$$\boldsymbol{T} = g\mu_B \left(\sum_i \boldsymbol{r}_i\right) \times \left(\sum_i \boldsymbol{S}_i\right) = \boldsymbol{P} \times \boldsymbol{M}. \tag{1.42}$$

The magnetic point groups compatible with $\boldsymbol{T}$ are subgroups defined by a perpendicular polarization and magnetization, $2'mm'$, where the electric polarization is parallel to the $2'$ axis and the magnetization is perpendicular to the mirror plane m and $\boldsymbol{T}$ points perpendicular to the mirror plane m'. When ODA was observed for $\boldsymbol{k} \| \boldsymbol{T}$, it was historically called the optical magnetoelectric effect (OME). Second case, historically called magnetochiral dichroism (MChD) [77], appears when a chiral material is magnetized. In this case, the ODA appears along the magnetization direction. The third case, predicted only by Szaller *et al.* and never experimentally observed [75], appears when light propagates along the polarization, and no symmetry operation involves the time reversal. Note that the three cases do not cover all cases when $\boldsymbol{t}$ is finite [75].

Beside DB and DD observed in transmittance experiments, ODA can be manifested in various optical experiments like directional-dependent emission (luminescence) [77, 78] or Bragg scattering [79]. Next generalization comes from the fact that the symmetry conditions, allowing ODA for unpolarized light, allow directional anisotropy for propagation

Table 1.1: Classification of polarization rotation and ODA effects, caused by electric, magnetic and ME susceptibilities which are linearly proportional to magnetization (or applied magnetic field) or polarization (or applied electric field). In the first column, there are effect manifestations – polarization rotation or ODA, manifested by DD or DB. In the second column, there are names of the effects with their variations, which can be found in the literature. In case of polarization rotation, the effect can be either reciprocal (R) of nonreciprocal (N), while the ODA is by definition nonreciprocal. In the third column, there are terms contributing to the effect; i is the imaginary unit. Here $\gamma \neq \delta$ so if the subscripts are different, it explicitly means off-diagonal elements of the corresponding tensor. Fourth column states symmetry requirements; if the symmetry requirement cannot be stated easily, a reference is given.

effect manifestation	effect (R/N)	tensor elements	symmetry requirement
polarization rotation	NOA/NCD/gyrotropy (R)	$i(\chi''_{\gamma\gamma},\chi''_{\gamma\delta})$	Ch
	MCD/Faraday effect (N)	$i(\varepsilon_{\gamma\gamma}\mu_{\gamma\delta},\mu_{\gamma\gamma}\varepsilon_{\gamma\delta})$	$\boldsymbol{M}\parallel\boldsymbol{k}$
	SOA/GB (N)	$\chi'_{\gamma\gamma}$	[17]
ODA – directional dichroism (or birefringence)	OME	$\chi'_{\gamma\delta}$	$\boldsymbol{T}\parallel\boldsymbol{k}$
	MChD	$-\parallel-$	Ch+$\boldsymbol{M}\parallel\boldsymbol{k}$
	P	$-\parallel-$	no $\{\}'$+$\boldsymbol{P}\parallel\boldsymbol{k}$
	$\boldsymbol{t}$-only	$-\parallel-$	$\boldsymbol{t}\parallel\boldsymbol{k}$
	X	$-\parallel-$	[75]

NOA=natural optical activity, NCD=natural circular dichroism, MCD=magnetic circular dichroism, SOA=spin-mediated optical activity, GB=gyrotropic birefringence, OME=optical magnetoelectric effect, MChD=magnetochiral dichroism, Ch=chirality, $\boldsymbol{P}$=polar time-reversal even vector, $\boldsymbol{t}$=polar, time-reversal odd vector, $\boldsymbol{T}$=quantity defined by Eq. 1.42, no $\{\}'$ means that no time-reversal symmetry is involved in the magnetic point group.

of any waves, defined by the wavevector, including scalar ones [75]. This accounts for propagation of electrons [80–82], neutrons, spin [83–86] and acoustic [87, 88] waves or phonons [89], thus for electric or heat conduction. Moreover, the mentioned effects were related to linear transport processes. For nonlinear processes, such as dissipative current transport, much more variety of nonreciprocal processes may appear, the most known being a semiconductor diode based on a PN junction [90].

1.3.3 History of optical directional anisotropy and effects classification

Strong OME was first observed in the absorption spectrum of excitons in the polar CdS with wurtzite structure already in 1960 [91]. After decades without interest in these topics, MChD and OME were observed in chiral nonmagnetic molecules upon applying magnetic, and in a garnet placed in magnetic and electric fields, respectively [77, 92]. However, the difference for $\pm\boldsymbol{k}$ respectively detected in emission and absorption was very small. After the revival of the interest in ME phenomena in the early 2000s motivated by the discovery of ME multiferroics, ODA also started to attract attention. Small OME was found in the X-ray absorption of the core electron excitations in the polar ferrimagnet $GaFeO_3$ [93] and in the visible-ultraviolet absorption of intra-atomic *d–d* excitations [94, 95].

Since late 2000s, strong DD in order of unity was found in several compounds: It was demonstrated for intra-atomic *d–d* transitions of CuB_2O_4 in the near-infrared spectral region [96, 97], and later in THz region of collective spin excitations in several multiferroics ($Ba_2CoGe_2O_7$ [7, 9, 71], $Eu_{0.55}Y_{0.45}MnO_3$ [98], $Gd_{0.5}Tb_{0.5}MnO_3$ [99], $CuFe_0.965Ga_0.035O_2$ [100], $Sm_{0.5}La_{0.5}Fe_3(BO_3)_4$ [101], $BiFeO_3$ [8], $CaBaCo_4O_7$ [102], $MnWO_4$[103], $Ba_3NbFe_3Si_2O_{14}$ [104], among many others.

In the above-mentioned references, DD was observed in magnetically ordered phases in the presence of magnetic, and sometimes also electric fields. Nevertheless, DD was also recently observed in zero magnetic and electric fields upon ME annealing [105, 106]. Moreover, sizable magnetic-field-induced DD was observed even in the paramagnetic phase in $FeZnMo_3O_8$ on an electron spin resonance between the eigenstates of the single-ion anisotropy Hamiltonian on Fe^{2+} sites [107].

At the end of this section, it may be useful to classify the above-described effects observed in transmittance experiment done with a linearly polarized beam, one can observe a few optical effects. Table 1.1 classifies these phenomena, manifested in polarization rotation and DD (or DB) from phenomenological and symmetry point of view. Only effects caused by electric, magnetic and ME susceptibility are included, and those which are linearly proportional to the magnetization (or a time-reversal symmetry breaking order parameter) or electric field (or a spatial-inversion symmetry breaking order parameter). For the sake of comprehensiveness, several alternative names of the effects, occurring in the literature, are provided. Importantly, the third column denotes the tensor elements and their products, responsible for the effect. Here $\gamma \neq \delta$ so if the subscripts are different, it explicitly means off-diagonal elements of the corresponding tensor. ODA is manifested by the DB and DD. These effects are often accompanied by polarization rotation, which can be either reciprocal (R) or nonreciprocal (N). While NOA is caused by the time-reversal even part of the ME tensor, which is related to chiral symmetry, and the resulting polarization rotation is thus reciprocal, the Faraday effect is nonreciprocal and it is caused

by the imaginary part of the off-diagonal permittivity and permeability tensors, which appear in materials of any symmetry when the magnetic field is applied. Time-reversal odd part of the ME tensor always causes nonreciprocal effects – the diagonal elements refer to nonreciprocal polarization rotation via the gyrotropic birefringence (GB), while the off-diagonal elements refer to DD or DB, which can be further classified by symmetry, as described above.

1.3.4 Magnetoelectric excitations

The magnetic- and electric-dipole-allowed excitations contributing to different susceptibilities described by Eqs. 1.30, 1.31, 1.32 and 1.33 are listed in Table 1.2. Since I study ordered magnets in this thesis, first I review the basic properties of the collective excitations in ferro- and antiferromagnets. Due to the long wavelength of the radiation I use to excite them, I will focus on the Γ-point excitations termed as ferro- and AFM resonances, FMRs and AFMRs, respectively. FMRs correspond to precession of the overall magnetization around the effective magnetic field without changing relative angles between neighboring spins. Therefore, the exchange interactions are not violated, thus they do not influence the resonance frequency, but instead a combination of the magnetocrystalline anisotropy and the external magnetic field set its value to the GHz frequency range. FMRs are typically strongly magnetic-dipole active, their contribution to the magnetic susceptibility $\chi^{mm}(\omega)$ can easily reach or exceed unity. In contrast, upon an AFMR, sublattice magnetizations are canted with respect to each other, thus, the exchange energy is modulated, which leads to resonance frequencies in the THz frequency range. Since only a small magnetic dipole moment arises from the dynamic distortion, AFMRs contribute weakly to $\chi^{mm}(\omega)$ or some modes even remain silent.

An important question is: How many magnon modes shall one expect in an optical spectrum of a given magnetic crystal? In a classical spin-wave theory [108], number of magnon modes is equal to number of magnetic sublattices. (Typically, one mode is FMR-like, and others are AFMRs, but FMR-like mode can also be gapped.) Classical theory, however, assumes constant spin length, which is strictly valid only for elementary electron spin $S = 1/2$. Ionic spins involving more than one valence electron/hole in fact possess internal degrees of freedom, thus there may be also some internal transitions changing spin length. While classical magnons can be understood as transversal (massless) Goldstone-Nambu modes, describing direction fluctuations, internal transitions can be called longitudinal or spin-stretching (massive) Higgs modes, describing amplitude fluctuations.

In the zero temperature limit, when only a single spin state is populated at each site, the number of transitions can reach $2S$ per site. Some of modes can be degenerate or silent, so in reality, number of observed modes is typically lower. Spin-stretching modes have been studied in few magnetic systems so far [109–113]. Appearance of spin-stretching modes was found to be connected to a single-ion anisotropy, and often leads to electric-dipole activity of such modes [111, 112]. Particularly, in $Ba_2CoGe_2O_7$ and $LiCoPO_4$ which I study in chapters 3 and 6, respectively, several magnon modes beyond classical spin-wave theory have been explained by multi-boson spin-wave theory including spin-stretching modes [105, 111].

A magnetic excitation may also change the electric dipole moment via microscopic

mechanisms described above for the static ME coupling. If a magnon is both magnetic- and electric-dipole active, it contributes to both $\chi^{ee}(\omega)$ and $\chi^{mm}(\omega)$, thus to $\chi^{me}(\omega)$ and it is called a ME excitation. It is also possible that a silent (magnetic-dipole-inactive) magnon becomes electric-dipole active – then, it contributes to $\chi^{ee}(\omega)$ only, and it is termed as an electromagnon. Such a silent magnon is indistinguishable from a different electric-dipole-active excitation in optical experiments. Nevertheless, its correlation with the appearance of the magnetic state can be a hallmark of its magnetic origin.[3]

Magnetic-dipole activity of a magnon or ME excitation means that it is an excitation from Brillouin zone center. In contrast, purely electric-dipole-active electromagnons may represent spin oscillations outside Brillouin zone center [114]. Also, two-magnon magnetic-dipole-inactive excitations may become electric-dipole active [115]. Therefore, electromagnons may appear as additional modes beyond zone-center and one-magnon excitations.

Even though an electric dipole moment of magnons is induced by a weak spin-polarization coupling, the electric-dipole strength of magnons can exceed their typical magnetic-dipole strength since the Coulomb interaction is typically much stronger than the Zeeman interaction. The weak spin-polarization coupling is manifested by the fact that in theory, it hardly influences magnon modes (their eigenvectors and frequencies), determined mainly by the exchange interactions, Zeeman coupling and magnetic anisotropy. It is important to realize that the nature of eigenmodes is given by the full Hamiltonian, while their magnetic- and electric-dipole strengths are given by perturbative Hamiltonian representing the EM field. Therefore, the dipole strengths of magnon modes can be considered as accidental.

Usually, most of the spectral weight in the dielectric susceptibility can be ascribed to infrared-active phonons and electronic transitions. When spins can induce polarization, spin dynamics hybridize with polar excitations. Typically, the magnetic resonances have much lower frequencies than phonons or charge excitations, thus, the spin-induced polarization follows the spin oscillations adiabatically. In contrast, spin dynamics typically cannot follow ion motions upon phonon resonances, thus the magnetic dipole carried by phonons is usually very small. A rare case when a phonon gets a remarkable magnetic-dipole strength due to the ME effect and exhibits measurable nonreciprocal propagation, was reported recently [89]. The effect reported in Ref. [89] was observed for a low-frequency acoustic phonon hybridized with a magnon, while magnetic moment of higher-frequency optical phonons is supposed to be much smaller.

Magnetic resonances are typically weak compared to usual electric dipole excitations like phonons and electronic transitions, thus, it is difficult to measure their contribution to the refractive index away from the resonance frequency. This remains to be the case even when the spin dynamics is coupled to polarization oscillations and off-resonance detection of ODA (manifesting as DB) is challenging. However, in the vicinity of the resonance the absorption can completely vanish for one propagation direction while remaining finite for the other. This, referred as one-way transparency in the literature, can be achieved when the relative strength of the electric- and magnetic-dipole processes are equal, more precisely when $\frac{|\langle 0|M|n\rangle|}{|\langle 0|P|n\rangle|} = \frac{c}{\sqrt{\epsilon_\infty}}$ (see Ref. [7], Eq. 3). The relative strength of the transition

[3] Sometimes in literature the term electromagnon stands for both electric- and magnetic-dipole-active magnons as well, but in this thesis, I will call magnons which are both electric- and magnetic-dipole active as ME excitations, while electromagnons those which are only electric-dipole active.

Table 1.2: Selected static and corresponding dynamic quantities (response functions), linked by the sum rule (Eq. 1.38 and 1.39). Typical excitations, contributing to the response functions, are listed.

static quantity (effect)	dynamic quantity (effect)	type of excitations
dielectric susc. χ^{ee}	$\chi^{ee}(\omega)$	phonons electronic transitions dielectric relaxation electromagnons ME magnons
magnetic susc. χ^{mm}	$\chi^{mm}(\omega)$	magnons electronic transitions magnetic relaxation ME magnons
ME susc. χ^{me}	$\chi^{me}(\omega)$	ME magnons electronic transitions phonons
Hall cond. σ_H	complex Far. angle $\Theta_F(\omega)$ (Faraday effect/ MOKE/MCD)	(virtual) electronic transitions phonons [116]
— (vanishes for $\omega = 0$)	complex Far. angle $\Theta_F(\omega)$ (inverse Faraday effect)	(virtual) electronic transitions phonons [117]

dipoles may be tuned by doping or a magnetic field to reach such a case.

One-way transparency may gain application in a one-way light guide which acts as a diode for light. Before real applications there are some problems which should be addressed:

- The magnetic resonances have rather low absorption which necessitate the use of a thick crystal making miniaturization difficult.
- In most materials, the effect is typically present at low temperatures. One exception is the room temperature multiferroic $BiFeO_3$ [8], which suggest that by material design this issue could be overcome.[4]
- The effect is present only at specific frequencies which is a disadvantage for broad-band applications, and it limits compatibility with rest of a potential device.
- Miniaturization is hindered by the long wavelength at THz frequencies and the diffraction effects correspondingly appearing. This might be overcome by near-field techniques or by finding ME excitations showing DD in the higher photon energies.

So far, I was considering only the light polarization, corresponding to its spin angular momentum. In addition, as recognized relatively recently [118], the light can also carry the orbital angular momentum (OAM), which may bring an additional degree of freedom

[4]The effect reported in Ref. [8] was measured at low temperature, although $BiFeO_3$ is multiferroic above room temperature

influencing light-matter interaction. The spin-only state of light corresponds to a plane wave, while states carrying nonzero OAM are represented by so-called vortex beams, in which the phase of the wave changes by multiples of 2π upon a loop around the beam center. A recent study showed that in a ferrimagnetic crystal the optical absorption strongly depends on both the handedness of the vortex (sign of the OAM) and the direction of the beam propagation with respect to the sample magnetization [119]. This effect exceeded the conventional magnetic circular dichroism, whereby demonstrating the high potential of the vortex beams with as a new spectroscopic probe of magnetism in matter.

1.3.5 Dynamical multiferroicity: an outlook to future trends

In the beginning of this chapter, I presented the distinction between the EM induction appearing in the classical theory of electromagnetism and the magnetoelectric effect, which is a nontrivial coupling between electric and magnetic dipoles in magnetic condensed matter. As I have discussed, the latter effect is present even in the static-limit, which leads to intriguing optical phenomena.

Let me go back to Maxwell's equations, specifically, to Ampère's-Maxwell's law which states that the time-varying electric field and the electric current induce space-varying magnetic field. It is well-known fact that the current flowing in a solenoid produces homogenous magnetic field. In condensed matter, light can excite electrons to orbit on loops for example in the presence of a magnetic field, which is known as the Faraday effect (or magneto-circular dichroism). The inverse Faraday effect realizes a condensed-matter analogue of Ampère's law. At high intensities, circularly polarized light can drive such loop currents in the absence of any magnetic field, which leads to finite magnetization.

Recently, Juraschek *et al.* resurrected the idea of generating current loops, thus magnetic field, by exciting phonons [117]: Either two degenerated phonons or some phonons in low-symmetry chiral materials can carry their own orbital momentum [116]. In Ref. [117] they also developed formalism of the so-called dynamical multiferroicity, while deriving extension of the Ampère's-Maxwell's law in a condensed matter.

Although these ideas seem to be trivial, the condensed-matter effects can lead to nontrivial findings, like phonon Zeeman splitting, resonant magnon excitation by optically driven phonons, demonstrated experimentally [120], or the inverse-Faraday-like effect mediated by phonons [117] (see also Tab. 1.2), among others [121–124]. Even though some of these effects are considered to be very small, recent studies show that the condensed-matter coupling between the ionic and electronic degrees of freedom may lead to enhancement of the effects by several orders of magnitude [125–131].

For the purpose of this thesis, it makes sense to demonstrate how the formalism of the dynamic multiferroicity can be used in multiferroics. Based on the symmetry analogy between the Ampère's-Maxwell's law and the inverse Dzyaloshinskii-Moriya interaction (analogy comes by replacing $\boldsymbol{P} \leftrightarrow \boldsymbol{M}$, $r \leftrightarrow t$ [117]), the electromagnon in $TbMnO_3$ induced by the iDM interaction can be interpreted in the language of the dynamical multiferroicity: Ampère's-Maxwell's law in condensed matter can be rewritten as

$$\boldsymbol{M}(t) \propto \boldsymbol{P}(t) \times \frac{\partial \boldsymbol{P}}{\partial t}, \tag{1.43}$$

telling that a time-dependent polarization creates a magnetization. $TbMnO_3$ in its magnetic-field-induced *ab*-cycloidal phase possesses the static $\boldsymbol{P} \| a$ induced by the iDM interaction

[132], as well as the dynamic $\boldsymbol{P}(t) \| c$ upon the ME resonance induced by the iDM interaction [98, 133]. Since the two polarizations are perpendicular to each other, according to Eq. 1.43, the magnetization $\boldsymbol{M}(t) \| b$ is generated, oscillating with the same frequency as $\boldsymbol{P}(t) \| c$. This explains why the $\boldsymbol{H}^{\omega} \| b$-active magnon becomes, in presence of static $\boldsymbol{P} \| a$, also $\boldsymbol{E}^{\omega} \| c$-active [117]. Therefore, this ME excitation can be viewed as a consequence of the Ampère's circuital law, enhanced by the condensed-matter coupling. Note, however, that this is just a lucky example, as such analogy could be used only because both static and dynamic polarizations are induced by the iDM interaction.

Chapter 2

Experimental methods and techniques

Since the primary goal of my thesis was the understanding of the magnetoelectric phenomena in these materials and not methodological developments, in this chapter, I just briefly the several experimental methods and techniques I applied.

2.1 Sample preparation

I studied solely bulk samples – single crystals and polycrystals in form of ceramics. All samples were prepared by my collaborators.

By the optical floating zone method, Vilmos Kocsis grew high-quality single crystals $Ba_2CoGe_2O_7$ and $LiCoPO_4$ which I study in Chapters 3 and 6, respectively. $LiCoPO_4$ crystals were grown based on the method described in Ref. [134], and growth of $Ba_2CoGe_2O_7$ crystals is described in Ref. [135].

Hexaferrite single crystals were grown by the flux method based on Ref. [136]; Kun Zhai and Yisheng Chai grew Y-hexaferrite $BaSrCoZnFe_{11}AlO_{22}$ and Z-hexaferrite $Ba_{0.5}Sr_{2.5}Co_2Fe_{24}O_{41}$, which I study in Chapter 4 and Chang Bae Park grew Y-hexaferrite $Ba_{0.2}Sr_{1.8}Co_2(Fe_{0.96}Al_{0.04})_{12}O_{22}$ which I study in Chapter 5. Such crystals typically contain oxygen vacancies, which would make them conducting, thereby preventing static ME measurements. Therefore, the samples for static ME measurements were annealed in an oxygen atmosphere at 900 °C for 7 days, as described in Ref. [137]. Orientation of all crystals was determined by Laue camera or by powder crystal diffraction. Hexaferrite high-density ceramics with typical grain sizes 10–20 μm were prepared by the Pechini-type *in situ* polymerizable complex method by Róbert Uhrecký and Josef Buršík, as described in Ref. [138]. The elemental composition of hexaferrite crystals and ceramics was determined by energy dispersive analysis of x-rays (EDAX), since hexaferrites contain several elements and their elemental composition may continuously change.

2.2 Static magnetic and magnetoelectric characterization

Static magnetic and magnetoelectric measurements were performed on MPMS (Magnetic Properties Measurement System) and PPMS (Physical Property Measurement System) instruments (from Quantum Design company) in a temperature interval from 5 to 400 K, with a magnetic field of up to 9 T. The magnetization was measured using vibrating sample

magnetometer (VSM) and SQUID (Superconducting QUantum Interference Device) magnetometer. The permittivity was measured with Andeen-Hagerling 2500A high-precision capacitance bridge. Magnetic-field-induced polarization was determined by measuring electric current using electrometer Keithley 6517A, and its subsequent integration in time.

2.3 Spectroscopic techniques

Excitations are typically studied by spectroscopy and different methods provide complementary information. This thesis is focused mainly on far-infrared (FIR) and THz region, and I solely used optical spectroscopy techniques.

In general, light incident on a material can be reflected, absorbed, transmitted or scattered, and due to the energy conservation law, it holds

$$\frac{I_R}{I_0} + \frac{I_A}{I_0} + \frac{I_T}{I_0} + \frac{I_S}{I_0} = R + A + T + S = 1, \tag{2.1}$$

where I_0, I_R, I_A, I_T and I_S are the incoming, the reflected, the absorbed, the transmitted and the scattered intensities, whereas R, A, T and S are the reflectivity, absorbance, transmission and normalized scattering. In the evaluation of the reflectivity and transmission spectrum the scattering is usually neglected as inherent scattering on microscopic objects in a bulk material is usually small. In FIR or THz spectroscopy, the radiation of the same energy as the investigated excitations is used. Typical wavelengths are in order of tens to hundreds of μm, so the scattering is typically determined by the diffraction limit, meaning that the sample size should be in order of few millimeters. For scattering experiments such as Raman spectroscopy, the energy of the incoming radiation can be much higher, meaning shorter wavelength, so the diffraction limit allows to measure much smaller samples.

I briefly describe principles and outcomes of three spectroscopic techniques used in this thesis: Fourier-transform infrared spectroscopy, THz time-domain spectroscopy and Raman spectroscopy. The first two techniques are based on coherence by use of interferometric techniques. Their outcome is the refractive index or impedance of the materials, thus, they probe electric and magnetic dipole allowed excitations. In contrast, Raman spectroscopy probes the polarizability of materials, so its selection rules are different and it provides complementary information.

2.3.1 Fourier-Transform Infrared Spectroscopy

Fourier-Transform infrared (FTIR) spectroscopy uses a broad-band black-body source. Since the detector cannot follow the fast oscillations of the EM fields, only intensity of the radiation is detected, while the phase is not experimentally accessible. The signal is measured as a function of the position of a moving mirror (or grating or another optical element) in an interferometer, and the spectrum is obtained via the Fourier transformation. Since the intensity fluctuations of the source are typically small, and the signal is detected with very sensitive bolometer cooled to liquid He temperature, this method typically exhibits high signal-to-noise ratio (SNR) [139], detecting very small changes of the signal.

Two different setups have been used in this thesis. The first one is a Bruker IFS 113v, installed in the Institute of Physics in Prague. This spectrometer, equipped with

Oxford Instruments Optistat cryostat allowing to measure in temperature range 10–300 K, uses a Michelson interferometer and works in reflectance geometry. Its spectral range is 0.6–90 THz. A gold mirror with almost 100% reflectivity is used as a reference. Typically, strong excitations can alter the reflectivity, so this setup is used mainly for investigation of phonons.

The normal incidence reflectivity to vacuum is related to the permittivity and permeability, according to Fresnel equations, as

$$R(\omega) = \left| \frac{\sqrt{\frac{\varepsilon_{\delta\delta}(\omega)}{\mu_{\gamma\gamma}(\omega)}} - 1}{\sqrt{\frac{\varepsilon_{\delta\delta}(\omega)}{\mu_{\gamma\gamma}(\omega)}} + 1} \right|. \tag{2.2}$$

Thus, the reflectivity is a function of impedance – $Z(\omega) = \sqrt{\frac{\mu_{\gamma\gamma}(\omega)}{\varepsilon_{\delta\delta}(\omega)}}$. (Following notation from Chapter 1, the electric and magnetic fields of light are polarized along δ and γ axes, respectively.) The electric and magnetic contributions often lie in a different frequency range, so they can be separated due to their different spectral shapes in reflectivity signal; typically $\mu = 1$ in the range of phonons, which simplifies the evaluation. Nevertheless, still one needs to determine the complex spectrum (either permittivity or permeability) based on real reflectivity spectrum (Eq. 2.2), thus fitting with some model is required. Typically, 3-parameter sum Lorentz model or 4-parameter product model are used [140].

The second FTIR setup used in this thesis was TeslaFIR spectrometer at the National Institute of Chemical Physics and Biophysics (KBFI) in Tallinn. This instrument is coupled to a superconducting solenoid, which generates high magnetic field up to 17 T and allows to measure both in Voigt ($\boldsymbol{H} \perp \boldsymbol{k}$) and Faraday ($\boldsymbol{H} \parallel \boldsymbol{k}$) geometry. This spectrometer utilizing a Martin-Puplett interferometer and 0.3 K bolometers can cover the frequency range from 100 GHz to 6 THz. I performed measurements in transmission geometry, which is potentially much more sensitive to probe weak excitations. This is suitable for studying magnons, which are typically much weaker than phonons, so they give a remarkable transmittance signal for reasonably thick samples (typically hundreds of μms).

In order to avoid interference fringes induced by internal reflections, I wedged the measured sample for 2°. Instead of a free-space reference, I rather measured the relative changes in the transmission induced by magnetic fields or temperature. Such procedure then directly detects directional dichroism signal, i.e. $\Delta\alpha(\omega)$, related to ME susceptibility by Eq. 1.40. Moreover, some spectra corrections are useful for better understanding. In most of cases, I took a lower envelope of a given set of absorption spectra as a reference as described in Ref. [8] so that the displayed spectra in a given set show only positive values. Alternatively, I took a given (zero-magnetic-field) spectrum as a reference. I evaluated the spectra, which I measured using TeslaFIR spectrometer, using using RatioCalc program developed by Urmas Nagel from KBFI.

2.3.2 Time-domain THz spectroscopy

Time-domain THz (TD THz) spectroscopy developed only in 1990s together with development of ultrashort laser pulses. THz range fills the gap between optics and electronics: Black-body radiation provides high energy only above THz range, while electronics are able to produce frequencies up to hundreds of GHz.

TD THz spectroscopy is based on the fact that laser pulses (in visible or near infrared range) produce coherent reproducible THz pulses [141]. This can be done via the optical rectification in a noncentrosymmetric crystal, or via biased photoconductive antennas. The laser pulse is divided by a beamsplitter, so that the synchronized part of the beam serves for a pulse detection via the converse effect. THz electric field of the coherent pulse is detected, so the complex response function can be obtained. Since the measured signal is proportional to the electric field, which scales as square root of the intensity, TD THz spectroscopy usually exhibits very high dynamic range (DR) [139]. SNR of this method is limited by pulse-to-pulse fluctuations and temporal jitter, but current laser technology allows decent SNR values [139].

The measurements are typically performed in transmission geometry, because reflectivity would be extremely sensitive on the pulse shift, thus the advantage of getting complex spectra may be lost. The measured electric field signal $E(t)$ gives the signal in the frequency domain after Fourier transform:

$$E(\omega) = \frac{4Z}{(Z+1)^2} e^{-i\omega Nd/c} \left[1 + \left(\frac{Z+1}{Z-1} \right)^2 e^{-2i\omega Nd/c} + \cdots \right], \tag{2.3}$$

where d is the thickness of the sample. Thus, the signal is a function of both the impedance $Z(\omega)$ and the refractive index $N(\omega)$. Since the experiment provides complex function, i.e. gives two values for each frequency, both complex $Z(\omega)$ and $N(\omega)$ cannot be directly determined and some simplifications have to be done: The terms including the impedance, connected to reflections on sample surfaces, contribute mainly to the real part, which is given mostly by the permittivity. The exponentials are functions of the refractive index, which is given by the product of the permittivity and permeability, thus both response functions contribute to the signal equally, and knowledge of the refractive index cannot distinguish between them. Therefore, the reasonable approximation is to replace Z by $1/N$ in Eq. 2.3, which corresponds to the situation when $\mu = 1$, so the output of the measurement is the refractive index $N(\omega)$.

When dividing the signal in Eq. 2.3 by the free-space signal, $E_0(\omega) = e^{-i\omega d/c}$ and replacing Z by $1/N$, one gets the complex transmittance signal [142]:

$$t(\omega) = \frac{4N}{(N+1)^2} \frac{e^{-i\omega(N-1)d/c}}{1 - \left(\frac{N-1}{N+1} \right)^2 e^{-2i\omega Nd/c}}. \tag{2.4}$$

Such signal includes infinite number of reflections distributed over time, while only few of them are usually captured by the experiment. Therefore, models including only a few reflections can be chosen for numerical evaluation. From the complex transmittance function (Eq. 2.4), one can unambiguously get the complex refractive index by a straightforward numerical calculation.

Various THz setups have been used throughout my thesis. In the Institute of Physics in Prague, custom-made spectrometers have been used. THz spectroscopy with magnetic field was performed using a spectrometer comprising an Oxford Instruments Spectromag cryostat with a superconducting magnet, allowing to apply an external magnetic field of up to 7 T in both Voigt and Faraday geometry. During my PhD work, I installed well-insulated cables in to the magnetic cryostat, allowing to apply high electric fields, limited by voltage of the high-voltage source – 1500 V.

At Budapest University of Technology and Economics, Toptica Teraflash spectrometer was used [143]. The THz radiation was generated and detected by photoconductive antennas, which could be easily exchanged, thus directional dichroism could be measured directly according to its definition. A custom-made cryostat was used with inserted permanent magnets, providing magnetic field ≈ 0.1 T of both polarities in Voigt geometry, and electric field up to ≈ 1 kV/cm. During my PhD work, I assembled the THz optics and installed a box purged with nitrogen/dry air – THz experiments have to be done in a water-free environment, since several water absorption lines lie in the THz range.

I also used a custom-made TD THz spectrometer installed at FELBE facility at Helmholtz-Zentrum Dresden-Rossendorf.

I evaluated all spectra from TD THz spectroscopy using PKGraph program, developed by Petr Kužel from the Institute of Physics of Czech Academy of Sciences in Prague.

2.3.3 Raman spectroscopy

Raman spectroscopy is an extremely useful technique due to different – often complementary – selection rules than IR and THz spectroscopies. The underlying principle is an inelastic scattering of light on quasiparticles with much lower energy than energy of photons of the light. The effect is off-resonant, so it works even for transparent materials. The spectra are taken as a function of shift from the laser frequency which is usually measured with a grating spectrometer.

Raman scattering measures the polarizability is a symmetric second-rank tensor, it possesses up to six independent elements. Importantly, this information is different from the permittivity and permeability tensors. Specifically, in centrosymmetric materials, IR and Raman selection rules are exclusive: A mode active in IR spectra is forbidden in Raman spectra and vice-versa, which is known as mutual exclusion principle. As a consequence, presence of a mode active in both IR and Raman spectra is a signature of inversion symmetry breaking. A little disadvantage of Raman spectroscopy is the difficulty of quantitative evaluation, which depends on several theoretical parameters as well as experimental settings. Nevertheless, the measured quantity – polarizability at the frequency of the laser – is commonly not the target of the material research studies.

In this thesis, I use Porto notation introduced in Ref. [144] for Raman scattering in crystals, in which each spectrum is described by four symbols, denoting directions of crystallographic axes. The two symbols in parenthesis refer to laser polarization, thus they define the investigated element of the Raman tensor, while the two symbols outside of parenthesis refer to incoming and outgoing laser propagation direction. For example, $a(cb)\overline{a}$ denotes the experiment, in which incoming laser propagating along a direction was polarized along c axis, and intensity of the outgoing laser propagating along $-a$ direction (back-scattering geometry) and polarized along b axis was measured.

In this thesis, a Renishaw RM 1000 Micro-Raman spectrometer equipped with a CCD detector and Bragg filters at the Institute of Physics in Prague, was used. The experiments were performed by Dr. Fedir Borodavka, in the backscattering geometry within the 0.3–24 THz range using an Ar^+-ion laser with the wavelength of 514 nm and an Oxford Instruments Optistat optical continuous He-flow cryostat.

2.4 Sources of high-intensity THz radiation

In this thesis, I also present experiments with intense THz radiation. Such intense nonlinear driving is a hot topic in current material research, since every information writing must be connected to some nonlinear process.

A few different sources of intense THz radiation were used in this thesis. These are FELBE Free-Electron Laser and TELBE superradiant facility at Helmholtz-Zentrum Dresden-Rossendorf, and TeraFERMI THz beamline at FERMI Free-Electron laser. In order to reach high radiation intensity, all the sources operate in the pulsed mode.

2.4.1 Sources of high-intense THz radiation at HZDR

The sources FELBE and TELBE are both based on a radiation source ELBE (Electron Linac for beams with high Brilliance and low Emittance). The radiation source is based on a superconducting linear accelerator of electrons that can be operated in high average power mode. The accelerator can be driven either in continuous-wave (CW) regime, in which a train of pulses with a given repetition rate is produced, or in a so-called macro-pulse regime, in which the train of pulses is interrupted in segments of typical tens of μs. This effectively reduces repetition rate, thus overall deposited energy heating the system.

At FELBE, electron bunches from the accelerator are led to two Free-Electron Lasers (U37-FEL and U100-FEL) based on undulators, which produce coherent narrow-band radiation, tunable by electron energy and undulator magnetic field. The undulator U-100, used in this thesis, produces radiation in 1.2–16.6 THz range. For FELBE operation, the repetition rate is 13 MHz [145]. The typical parameters of the beam dramatically change with frequency of the FELBE, especially in the low-frequency edge of the FEL where I operated (see chapter 6). Therefore, typical beam parameters at two representative FELBE frequencies are given in Tab. 2.1. One can see that near the low-frequency edge 1.3 THz, the beam parameters are considerably worse (lower beam intensity, higher bandwidth) than at 2.3 THz, for which the system is better optimized.

TELBE is a THz facility at ELBE, producing coherent EM radiation with tunable repetition rate up to 200 kHz [146]. The electron bunches are lead to an undulator, producing tunable narrow-band pulses with frequencies 0.1–2.5 THz via the superradiant effect [147]. A fraction of the electron bunch hits the diffraction radiator, producing a broad band pulse, whose frequency is not tunable. The underlying principle of such coherent diffraction radiation is that the Coulomb field of the particle produces radiation when it passes a boundary between two materials with different dielectric properties [147]. For the purpose of this thesis, this radiation was used ”only” as a timing to correct the temporal jitter.

2.4.2 TeraFERMI THz beamline at Elettra Sincrotrone, Trieste

TeraFERMI is the THz beamline at the FERMI seeded free-electron laser (FEL) facility at Elettra Sincrotrone, Trieste [150]. The beamline exploits the short electron bunches of the FERMI accelerator to generate THz pulses through coherent transition radiation, which is based on a similar principle as the diffraction radiation described above, but in a transmittance mode.

Table 2.1: Comparison of parameters of EM radiation coming from FELBE free-electron laser U100-FEL at different frequencies.

	1.3 THz	2.3 THz
repetition rate	13 MHz[a]	
bandwidth	5 %	2 %
spectrum tunability	yes	
peak electric field	25 kV/cm	40 kV/cm
maximum pulse energy	0.08 μJ	0.4 μJ

[a]The FELBE repetition rate can be effectively reduced. See more information in the main text.

Table 2.2: Comparison of parameters of EM radiation coming from the used TELBE [147, 148] and TeraFERMI [149, 150] beamlines.

	TELBE	TeraFERMI
repetition rate	200 kHz[a]	50 Hz
bandwidth	20 %[b]	100 %[b]
spectrum tunability	yes	no
peak electric field	322$\pm$20 kV/cm	1.6$\pm$0.4 MV/cm
maximum pulse energy	6.6 μJ	9 μJ

[a]The TELBE repetition rate can be effectively reduced. See more information in the main text.
[b]The spectral shapes are asymmetric; they are displayed in Fig. 5.2b.

The beamline produces broadband non-tunable THz pulses ranging from 0.2–2.5 THz with peak field exceeding 1 MV/cm, which makes it one of the most powerful sources all over the world in this spectral range. On the other hand, somehow low repetition rate 50 Hz and absence of temporal jitter correction limit the sensitivity of measurements.

The comparison of parameters of TELBE and TeraFERMI beamlines is shown in Tab. 2.2. This will be useful in Chapter 5, in which I compare transmittance experiments of hexaferrites from both beamlines.

2.5 ME effect measurement by modulation technique

The ME effect is typically very small and static measurements have to be performed with high precision. Therefore, modulation techniques can be very efficient to reduce the noise. Within this thesis, I constructed a modulation technique for measuring the quasi-static ME effect at frequencies provided by a lock-in amplifier. In this technique, the electric current in a coil produces an oscillating magnetic field at the sample position, which causes an oscillating electric polarization due to the ME effect, modulated with the same frequency as the driving current, resulting in modulated voltage signal. The setup is similar as the one described in Ref. [151], while I used modulation frequency 876 Hz.

Note that the ME effect is not the only source of the voltage signal. Due to the EM induction, time-varying magnetic fields may produce currents in the sample and leads, which contribute to a parasitic voltage signal at the modulation frequency. Therefore, only the change of the ME effect is a meaningful quantity. This is not a big problem as long as one can access the paramagnetic state of the crystal, for which the ME effect vanishes, while the background signal determined by the experimental geometry remains constant. The other issue is with the quantitative evaluation of the signal, which is based on precise determination of the magnetic field at the sample position and dimensions of electrodes. Since this measurement was coupled to the experiment at FELBE, the dimensions of the sample were not optimized for the precise measurement of the ME effect. Therefore, I rather normalized the signal by the known ME effect.

Chapter 3

Isothermal Control of THz Nonreciprocal Directional Dichroism by Electric Field and Magnetic-Field Tilt in the Multiferroic $Ba_2CoGe_2O_7$

In this chapter, I introduce a relatively well-understood multiferroic, $Ba_2CoGe_2O_7$, that is often referred as a textbook example realizing the *p–d* hybridization spin-polarization coupling. Both static and dynamic magnetic and multiferroic properties of this famous compound and its sisters were investigated thoroughly in the past more than a decade [7, 9, 71, 74, 86, 111, 135, 152–176]. The simple crystal and magnetic structure of these compounds hosting several interesting phenomena including *p–d* hybridization induced electric polarization [158], magnetic field controlled chirality and DD in the THz [7, 9, 71, 74, 111, 176] and in the microwave [86] frequency range motivated enormous interest. Although the electric-field control of magnetism had been seldom studied [158, 173], $Ba_2CoGe_2O_7$ offers a rare option to control its AFM state. I exploited this opportunity to use electric fields to manipulate THz frequency DD [11]. Notably, I achieved isothermal control of the AFM domains, thus, the dynamic ME effect, in contrast to the ME annealing (poling), in which the domain selection occurs in the vicinity of the magnetic ordering temperature (see, e.g., Ref. [105]).

The experiments I have performed address one of the core question of multiferroics: Why is the electric-field control of magnetism still so challenging, despite of increasing number of known multiferroics? The answer is rather simple: The electric polarization induced either by the magnetic order or by a magnetic field is rather small, typically it is in the 1–100 μC/m^2 range. The corresponding ME energy for laboratory electric fields is usually much smaller than the interactions shaping the magnetic order including exchange, anisotropy and Zeeman energy terms. Therefore, unlike magnetic fields, electric fields can hardly change the magnetic states. Once a magnetic field is applied, it typically establishes a stable magnetic state, which can be hardly influenced by the electric field. The electric field may play a more important role only in the vicinity of some magnetic structure instability. It can be either an instability close to a paramagnetic state, which is exploited by the above-mentioned ME annealing, or some magnetic instability in the low-temperature phase, the latter being applied in this work. In order to achieve the desired

electric-field control of the magnetic state, the magnetic states should have different polarization. Moreover, to realize the electric-field control of the DD, a low-symmetry magnetic ground state allowing DD has to be established, and ME excitations in a suitable frequency window should be present. Altogether, one has four conditions for electric-field control of DD in THz range: (i) magnetic structure instability, (ii) coupling of this instability to polarization, (iii) symmetry of magnetic ground state allowing DD and (iv) ME excitations in THz range. Since all of these conditions should be fulfilled at the same time the electric-field control of DD is a challenging task, which is rather scarce and has been achieved only in case of $TlCuCl_3$ so far [10].

This Chapter loosely follows my work published in Ref. [11], while it includes details of the theory developed by my colleagues, but more experimental results.

3.1 Crystal and zero-field magnetic structure of $Ba_2CoGe_2O_7$

$Ba_2CoGe_2O_7$ belongs to the melilite crystal family together with several isostructural compounds such as $Ca_2CoSi_2O_7$ or $Ca_2MgSi_2O_7$. It crystallizes in the nonsymmmorphic, layered tetragonal $P\bar{4}2_1m$ structure, where the layers are stacked along the tetragonal $[001]$ axis. This is a peculiar crystal structure as it is noncentrosymmetric but neither polar nor chiral. In each layer, Co^{2+} cations, surrounded by oxygen tetrahedra, form a square-lattice with the nearest neighbors connected along the $[110]$ and $[1\bar{1}0]$ directions [see Fig. 3.1(a)]. In a unit cell, there are two crystallographically inequivalent Co sites with oxygen tetrahedra rotated about the tetragonal axis in the opposite directions. The CoO_4 tetrahedra are bridged by GeO_4 tetrahedra, and the layers formed by them are separated by Ba^{2+} spacer ions.

In the tetrahedral crystal field of the oxygen ligands, the outermost $3d$ orbitals of the Co^{2+} ion split into the low-lying e subset consisting of $d_{x^2-y^2}$ and d_{z^2} orbitals and the higher-energy t_2 subset of d_{xy}, d_{xz} and d_{yz}. The seven valence electrons of Co^{2+} fill the e orbitals completely and half-fill the three t_2 orbitals, resulting in $S = 3/2$ spin and a quenched orbital moment. However, since the CoO_4 tetrahedra are flattened along the tetragonal $[001]$ direction, the local symmetry felt by the Co^{2+} ion is further lowered to $\bar{4}2m$. This leads to an easy-plane magnetic anisotropy, i.e. a lower-energy level for $S^z = \pm 1/2$ than for $S^z = \pm 3/2$ states (in case of an elongated tetrahedron the situation would be the opposite) [177].[1]

At low temperatures below $T_N \approx 6.7$ K, an AFM order develops with the two Co spins of the unit cell (sublattice magnetization $\boldsymbol{M}_A$, $\boldsymbol{M}_B$) pointing into opposite directions and lying within the tetragonal (001) plane. The easy-plane magnetic anisotropy persists in the paramagnetic phase as well[152, 171] ,indicating its single-ion nature. Furthermore, a small in-plane anisotropy within the (001) plane pins the AFM ordering vector ($\boldsymbol{L} = \boldsymbol{M}_A - \boldsymbol{M}_B$) to one of the four symmetry-equivalent $\langle 100 \rangle$-directions, whereby forming four different domains, as shown in Fig. 3.1(a,b) [169, 173]. Upon the AFM phase transition, the symmetry is reduced from $P\bar{4}2_1m1'$ to $P2_1'2_12'$, corresponding to the breaking of the

[1]The actual symmetry at the Co site is even lower, S_4, which would allow further, higher order anisotropies. However, these corrections do not influence the physical observables.

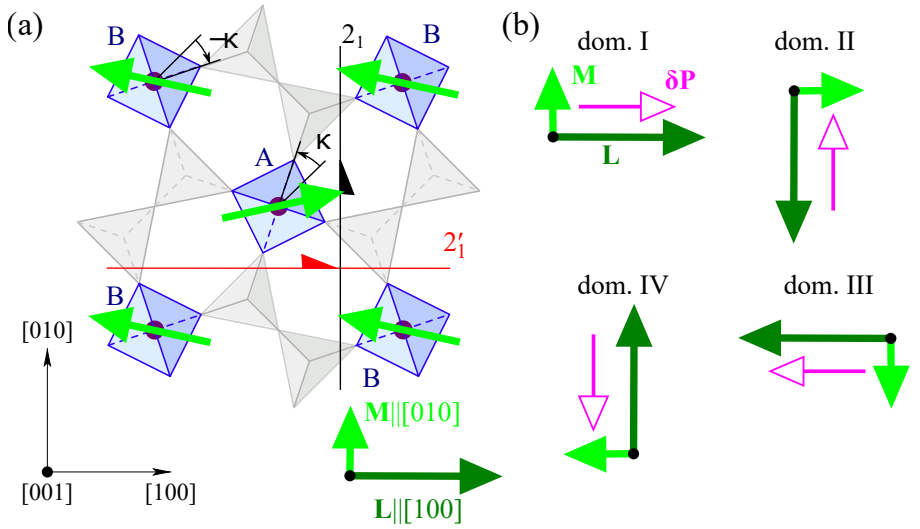

Figure 3.1: (a) The canted AFM order of $Ba_2CoGe_2O_7$ in domain I in zero fields. Purple circles denote the Co^{2+} ions with $S = 3/2$ (green arrows) in the centers of the O^{2-} tetrahedra (shown in blue). The symmetry operations are the 2_1 screw axis, (black half-arrow) and the orthogonal $2'_1$ screw axis followed by time-reversal (red half-arrow). $\boldsymbol{M}$ and $\boldsymbol{L}$ correspond to the uniform and staggered sublattice magnetizations, respectively. (b) The four AFM domains. On the account of linear magnetoelectric (ME) effect, a magnetic field applied along the [001] axis induces a polarization $\boldsymbol{P}$ (pink arrows).

rotoreflection symmetry $\bar{4}$.[2]

The weak in-plane anisotropy is explained by antiferroelectric (AFE) coupling between local (spin-induced) dipole moments of neighboring Co sites [169], thus, it disappears at T_N, in contrast to the single-ion anisotropy. In zero field, a small spin canting of $\sim 0.1^\circ$ develops [154, 170], which is either due to the AFE coupling or due to a weak Dzyaloshinskii-Moriya interaction. The canting results in a small spontaneous ferromagnetic moment $\boldsymbol{M}$ in the direction $c \times \boldsymbol{L}$, [see Fig. 3.1(a,b)].

3.2 Multiferroicity in $Ba_2CoGe_2O_7$

Both the static and the dynamic ME response of $Ba_2CoGe_2O_7$ are consistently explained by the spin-dependent *p-d* hybridization [46, 111, 158, 159, 163]. In this mechanism, the spin-quadrupole operators of the $S = 3/2$ cobalt spin directly couple to the induced polarization $\boldsymbol{P}_j$ on site j, (j =A, B)

$$\begin{aligned}
\hat{P}^a_j &\propto -\cos 2\kappa_j \left(\hat{S}^b_j\hat{S}^c_j + \hat{S}^c_j\hat{S}^b_j\right) + \sin 2\kappa_j \left(\hat{S}^a_j\hat{S}^c_j + \hat{S}^c_j\hat{S}^a_j\right), \\
\hat{P}^b_j &\propto -\cos 2\kappa_j \left(\hat{S}^a_j\hat{S}^c_j + \hat{S}^c_j\hat{S}^a_j\right) - \sin 2\kappa_j \left(\hat{S}^b_j\hat{S}^c_j + \hat{S}^c_j\hat{S}^b_j\right), \\
\hat{P}^c_j &\propto -\cos 2\kappa_j \left(\hat{S}^a_j\hat{S}^b_j + \hat{S}^b_j\hat{S}^a_j\right) + \sin 2\kappa_j \left((\hat{S}^a_j)^2 - (\hat{S}^b_j)^2\right),
\end{aligned} \tag{3.1}$$

where a, b, c are parallel to [100], [010] and [001], respectively. $\kappa_A = \kappa$ and $\kappa_B = -\kappa$ account for the different orientation of the tetrahedra [see Fig. 3.1(a)] in A and B sublattices.

[2]The number of the domains is determined by the order of the factor group $S_4 \cong P\bar{4}2_1m1'/P2'_12_12'$, which also transforms the domain states among each other.

The small anisotropy within the tetragonal plane can be easily overcome by applying a moderate magnetic field ($\lesssim 1$ T). Therefore, when a magnetic field is rotated within the tetragonal plane $\boldsymbol{M}$ ($\boldsymbol{L}$) is parallel (perpendicular) to the field [158]. Importantly, $\boldsymbol{L} \times \boldsymbol{M}$ remains parallel to the c axis, thus, the magnetic structure ground state is unique.

According to Eq. 3.1, there is no net polarization in the ground state when $\boldsymbol{L}$ is parallel to $\langle 100 \rangle$. However, the rotation of a magnetic field, thus the spin structure in the tetragonal plane, is accompanied by the appearance of a finite polarization along the c axis, P^c, oscillating with double periodicity with respect to rotation of the field: While magnetic field rotates 180°, the polarization performs a complete 360° cycle back to the original state [158]. This is well-understandable by symmetry, since 180°-rotation of the magnetic field establishes the time-reversed state, thus time-even quantities such as polarization must not change. Such scenario is responsible for observation of DD in $Ba_2CoGe_2O_7$, since switch (or, equivalently, 180°-rotation) of the magnetic field switches $\boldsymbol{M} \times \boldsymbol{P}$ parallel or antiparallel to $\boldsymbol{k}$ [7, 9, 71, 74, 111].

How to control the magnetic state by an electric field? From above, it is clear that even a small in-plane magnetic field lifts the degeneracy of the four domain states shown in Fig. 3.1(b) and establishes a single-domain magnetic state. This prevents the electric-field control, as the degeneracy of the domains are lifted by the magnetic field (condition (i) mentioned in the introduction of this chapter is missing). In zero magnetic field, there is a magnetic instability, but macroscopic polarization is zero, thus condition (ii) is not fulfilled. However, the out-of-plane magnetic field keeps degeneracy (thus magnetic instability), while inducing a polarization in the tetragonal plane, consistently with Eq. 3.1 and shown in Fig. 3.1. This polarization is always along $\boldsymbol{L}$ in the four domains, but it is rotated in the opposite direction in the plane by the broken S_4 symmetry. This was shown by Murakawa *et al.* [158], who rotated the magnetic field in the *ac*-plane and observed the polarization in *b*-direction. Abrupt switch of the polarization with remarkable hysteresis observed upon tilting the field away from the [001] axis suggests a rearrangement of the magnetic domain population. Hysteresis is also observed in the ferroelectric hysteresis loop $P^b(E^b)$ while an additional magnetic field is present along [001] [158], which suggests that the electric field can switch between the magnetic domains due to its coupling to the spin-induced ferroelectric polarization.

The last condition to achieve the electric-field control of DD is to have a magnetic ground state allowing DD by symmetry. The $P2_1'2_12'$ ground state symmetry gives rise to a finite χ_{ac}^{em} and χ_{ca}^{em}, thus allowing DD for light propagation along $\boldsymbol{k} \| c \times \boldsymbol{L}$ in a given domain, i.e. along the (unitary) 2_1 screw axis.

Altogether, the magnetic field $\boldsymbol{H} \| [001]$ produces a polarization $\boldsymbol{P}$ parallel or antiparallel to the $\boldsymbol{L}$ in each domain, as shown in Fig. 3.1(b). (This manifests finite static χ_{ac}^{em}.) If the field is perfectly aligned ($\boldsymbol{H} \| [001]$), the four domains remain equivalent and the field-induced polarizations $\boldsymbol{P}$ cancel out. However, a small perturbation such as tilting of the magnetic field or applying an in-plane electric field can break the delicate balance between the domains. In my experiments, I exploit this highly susceptible state to change the relative population of the domains by electric field $\boldsymbol{E} \| [100]$ and magnetic field tilt from [001] toward [010], and attain control over the DD along $\boldsymbol{k} \| [010]$.

3.3 Electric field control of directional dichroism in $Ba_2CoGe_2O_7$ revealed by FTIR spectroscopy

The results of the electric and magnetic-field-dependent experiments done at the KBFI in Tallinn are summarized in Fig. 3.2. Panel (a) displays the average and (b) the difference of the THz absorption spectra measured in electric fields with opposite signs ($E = \pm 3$ kV/cm) and constant magnetic fields. In agreement with former results [111], I assign the absorption peak around 0.54 THz (mode #1) to the optical magnon excitation of the easy-plane AFM ground state, whereas resonances #2, #3 and #4, showing a V-shape splitting in magnetic fields, are attributed to the spin-stretching modes involving the modulation of the spin length. In a finite magnetic field, the absorption spectra become different for the opposite signs of the electric field as evidenced by Fig. 3.2(b) for the light polarization $\boldsymbol{E}^{\omega} \parallel [001]$ and $\boldsymbol{H}^{\omega} \parallel [100]$. The electric field odd component of the signal is the manifestation of the DD and it shows that the absorption is different for light propagation along or opposite to the cross-product of the static electric and magnetic fields $\boldsymbol{E} \times \boldsymbol{H}$. This relation is further supported by the fact that the differential absorption spectra change sign under the reversal of the external magnetic field. The DD is finite only for the spin stretching modes #2 and #3 and it increases with magnetic fields up to $\sim$12 T and decreases for higher fields up to $\sim$17 T, which is the highest achievable magnetic field in Tallinn (not displayed). Note that for the orthogonal light polarization, $\boldsymbol{E}^{\omega} \parallel [100]$ and $\boldsymbol{H}^{\omega} \parallel [001]$, I did not find electric-field-induced absorption difference within the accuracy of the experiment.

The electric-field-induced change in the absorption spectra around mode #3, measured with respect to the zero field cooled state, is displayed in Fig. 3.3(a). A constant, bias magnetic field of 12 T was applied along $\boldsymbol{H} \parallel [001]$. The peak absorption, shown in Fig. 3.3(b), depends on the electric field history of the sample: the initial and the following upward and downward sweeps are all different and the absorption difference has a small but finite remanence, suggesting that the observed electric field effect is related to switching between domain states possessing different DD. The necessity of the magnetically ordered state and its domains is further supported by the fact that the electric field can change the absorption only below T_N as displayed in Fig. 3.3(c), though the intensity of the spin stretching mode remains finite even above T_N [9].

3.4 Theory and discussion

The above-analysis of the ground state symmetry implies that for light propagation $\boldsymbol{k} \parallel [010]$, the DD is caused by population imbalance of domains I and III, while domains II and IV cannot contribute to DD since the light propagates along $2_1'$ axis, transforming $\boldsymbol{k}$ into $-\boldsymbol{k}$, in these domains. When the magnetic field along $\boldsymbol{H} \parallel [001]$ is applied, which I had to do to select the domains by the electric field, 2_1 axis (along $\boldsymbol{c} \times \boldsymbol{L}$) is broken, but $2_1'$ axis (along $\boldsymbol{L}$) is preserved. Therefore, DD is still forbidden for domains II and IV when $\boldsymbol{k} \parallel [010]$, so the DD I observed must be caused by imbalance of domains I and III. In finite $\boldsymbol{H} \parallel [001]$, DD is also allowed for the $\boldsymbol{k} \parallel [001]$ due to 2_1 axis symmetry breaking, but then the analysis of results would be more complicated as the Faraday effect mixes the polarization states of the light.

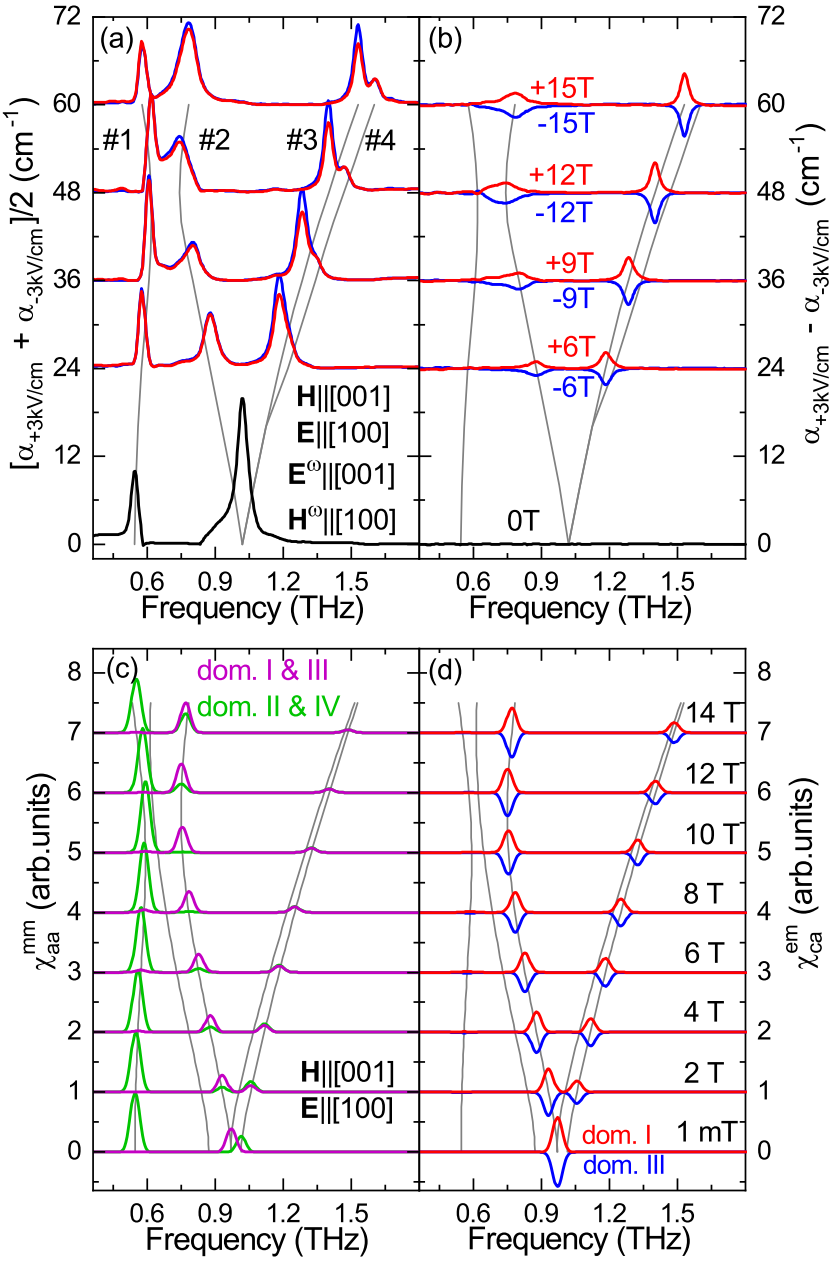

Figure 3.2: (a) Magnetic field dependence of the THz absorption spectra averaged for the measurements performed in electric fields with opposite signs, $E = \pm 3$ kV/cm at $T = 3.5$ K. The light polarization is $\boldsymbol{E}^{\omega} \parallel [001]$ and $\boldsymbol{H}^{\omega} \parallel [100]$. The spectra measured in positive(red)/negative(blue) magnetic fields $\boldsymbol{H} \parallel [001]$ are shifted in proportion with the absolute value of the field. Grey lines indicate the magnetic field dependence of the resonance frequencies. (b) Electric-field-induced change in the absorption spectra as the difference of the absorption spectra recorded in $E = \pm 3$ kV/cm. (c) The magnetic susceptibility calculated from the spin-wave theory in domain I & III (purple) and in domain II & IV (green). (d) The ME susceptibility calculated from the spin-wave theory in domain I (red) and domain III (blue).

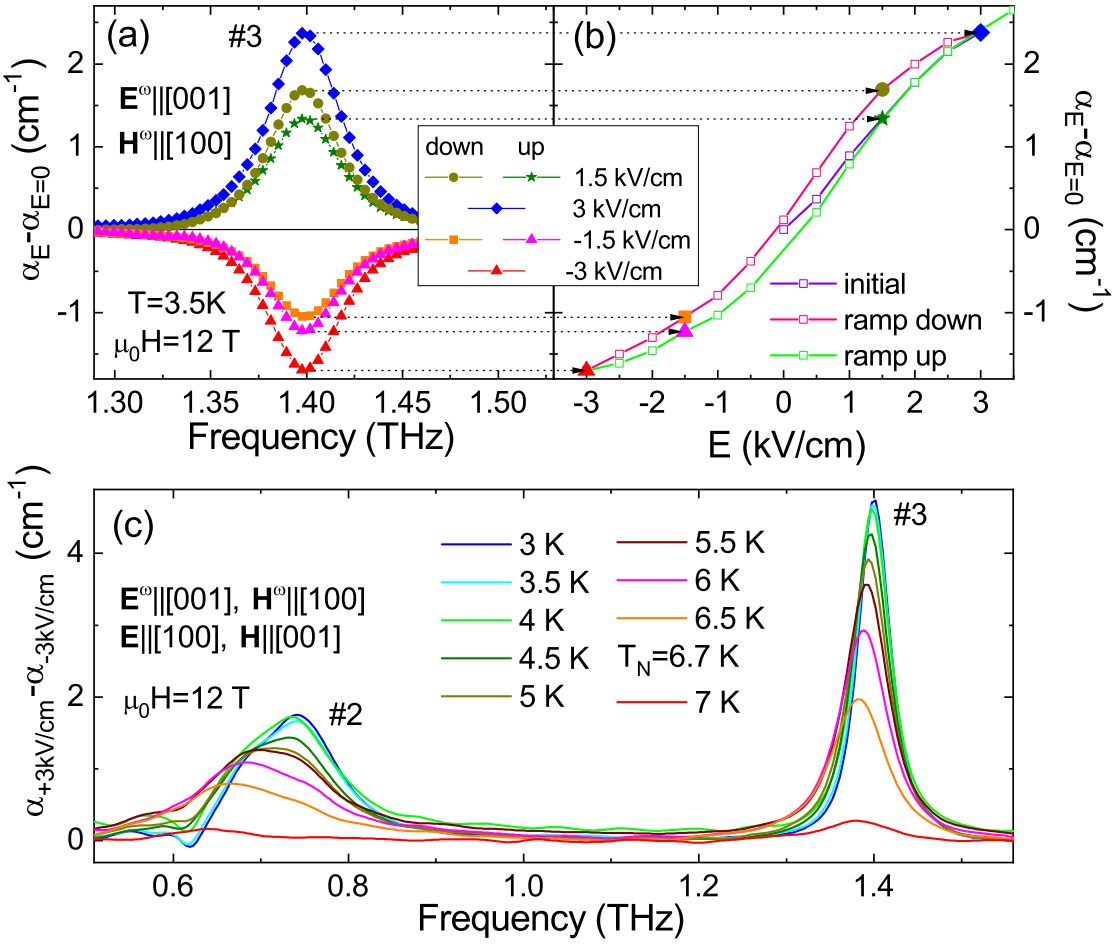

Figure 3.3: (a) The electric-field-induced change in the absorption spectra around mode #3 measured with respect to the zero field cooled state at 3.5 K and in fixed magnetic field 12 T. (b) The hysteresis of the electric-field dependence of the peak absorption. The horizontal arrows connect corresponding points of panels (a) and (b). (c) Temperature dependence of the electric-field-induced change in the absorption spectra measured in 12 T.

In order to interpret the experimental results quantitatively, my colleagues K. Penc and J. Romhányi considered the microscopic Hamiltonian of interacting $S = 3/2$ Co^{2+} spins following Refs. [111, 159]:

$$\mathcal{H} = \sum_{\langle i,j \rangle} [J(\hat{S}_i^a \hat{S}_j^a + \hat{S}_i^b \hat{S}_j^b) + J^c \hat{S}_i^c \hat{S}_j^c] + \sum_i \Lambda (\hat{S}_i^c)^2 - \sum_i [g_{cc} H_c \hat{S}_i^c + E_a \hat{P}_i^a], \tag{3.2}$$

where summation $\langle i, j \rangle$ runs over the nearest neighbors. Beside the anisotropic exchange coupling (J and J^c), single-ion anisotropy Λ, and the Zeeman term, they introduced the coupling between the external electric field, E_a, and the spin-induced polarization (see Eq. 3.1), which breaks the O(2) symmetry of the model.

Although Eq. 3.2 represents only a low-energy spin model, its microscopic parameters are known from broad knowledge of the experimental data [70, 111, 153, 166]. Without the electric field, the model has an O(2) symmetry and its ground state manifold consists of two-sublattice AFM order with $\boldsymbol{L}$ pointing to any in-plane directions. I note that this model does not explicitly contain the Dzyaloshinkii-Moriya interaction and the AFE coupling term, while the latter breaks the continuous rotation symmetry of the model and reduces the number of possible ground states to 4 corresponding to the broken S_4 symmetry. Since these energy scales are small, the discrete domain states appear in the shallow minima of the easy-plane AFM manifold. When a finite magnetic field is applied for $\boldsymbol{H} \parallel [001]$, the domain selection can be realized by an electric field (last term in Eq. 3.2). The application of a tiny $E_a > 0$ combined with $H_c > 0$ selects domain I in Fig. 3.1(b), while $E_a < 0$ selects domain III. Note that for the typical out-of-plane magnetic field I applied, the ME energy [158] is approximately an order of magnitude smaller than the in-plane anisotropy [169], thus, the rotation of the AFM vector $\boldsymbol{L}$ away from the principal axes is negligible (e.g. [173]).[3] Therefore, the model may work well if the electric field is applied along $\langle 100 \rangle$-axes, but for example rotation of the electric field within the (001)-plane would not give the exact ground state, since the (001)-plane is isotropic in the model.

My colleagues calculated the excitations above a variational site-factorized ground state using a multiboson spin-wave theory, following Ref. [111]. The magnetic dipole strengths of the excitations are estimated by the transition matrix elements of the spin operators $|\langle 0|\hat{S}^\alpha|n\rangle|^2$ between the ground state $|0\rangle$ and the excited states $|n\rangle$. The contribution of the magnetic dipole processes to the absorption is shown in Fig. 3.2(c), where $\chi_{aa}^{mm} \propto \langle 0|\hat{S}^a|n\rangle\langle n|\hat{S}^a|0\rangle$ is plotted. The electric dipole matrix elements are evaluated similarly for polarization components $\hat{P}^\beta$. The ME susceptibility, $\chi_{ca}^{em} \propto \langle 0|\hat{P}^c|n\rangle\langle n|\hat{S}^a|0\rangle$ is plotted in Fig. 3.2(d).

For light polarization $\boldsymbol{E}^\omega \parallel [001]$ and $\boldsymbol{H}^\omega \parallel [100]$, the model predicts that two spin stretching modes have finite ME susceptibility χ_{ca}^{em} and correspondingly show DD with

[3] According to inelastic neutron scattering experiments [169], there is a four-fold anisotropy within the easy-plane with characteristic energy scale of $z \cdot J_p \sim 1\,\mu$eV, where z is the coordination number and J_p is the coupling strength of the spin-nematic interaction responsible for the in-plane anisotropy.

When I consider the effect of external fields, the ME energy term should be compared to the spin-nematic interaction. I can estimate the ME susceptibility to $10\,\mu$C/(m^2·T) based on Fig. 2j in Ref. [158], corresponding to energy $\sim 0.1\,\mu$eV in the used experimental fields (12 T, 3 kV/cm) in Fig. 3.3(a,b). Correspondingly, the AFM order parameter is not rotated more than $\sim 1^\circ$ in any of the domains, thus, the model my colleagues developed with four domains is valid in this field range.

the same sign. The overall sign of the ME response is reversed upon the reversal of either the static electric or the magnetic field related to the switching from domain I to III. All of these findings are in agreement with the experiments and imply that the electric-field control of the DD is realized by influencing the AFM domains. I note that among modes #3 and #4, which show a tiny splitting in high fields ($\gtrsim 10$ T), resonance #3 is DD active in the experiment, whereas the theory predicts DD for the higher energy mode. However, my colleagues found no obvious way to reproduce the fine structure of the resonance energies within their model or by including other realistic terms such as the AFE coupling or the DM interaction [158, 159, 164]. In further analysis, I assume that mode #3 corresponds the highest-energy mode in the theory and mode #4 to the second highest one.

The absence of the DD for the orthogonal light polarization, $\boldsymbol{E}^{\omega} \| [100]$ and $\boldsymbol{H}^{\omega} \| [001]$, can be explained by the smallness of the χ_{ac}^{em}. The magnetic matrix element in χ_{ac}^{em} involves the $\hat{S}^c$, which commutes with all the terms of the Hamiltonian in Eq. 3.2 except for the small $\boldsymbol{E} \cdot \boldsymbol{P}$, which breaks O(2) symmetry of the system. Therefore the dipole oscillator strength for S^c – given by the double commutator [178] – is tiny compared to other matrix elements.

Although the theory predicts that individual domains possess a finite DD as $H_c \to 0$ [see Fig. 3.3(b)], I observed vanishing DD in this limit. This can be easily explained by the fact that for $H_c \to 0$, the spin-induced polarization $P_a \to 0$ [158], thus the electric field itself cannot induce domain imbalance, which demonstrates necessity of finite $\boldsymbol{H} \| [001]$.

Multi-domain composition at low magnetic fields can also explain non-monotonic magnetic-field dependence of the absorption contrast of modes #2 and #3, reaching maximum at 12 T: With increasing magnetic field up to 12 T, the domain selection increase is responsible for increase of absorption contrast, while above 12 T, the decrease of absorption contrast is due to decrease of overall strength of the mode [see Fig. 3.2(b)], which is also confirmed by the model [see Fig. 3.2(c,d)]. Note that for $\mu_0 H_c$ higher than the saturated field 37.1 T [179], all four domains collapse to a single ferromagnetic domain with point group symmetry $\bar{4}2'm'$, for which ODA is forbidden [75].

3.5 Electric- and tilted magnetic-field effects on the directional dichroism revealed by TD-THz spectroscopy

Note that the small difference in the averaged absorption [Fig. 3.2(a)] observed for the reversal of the magnetic field is probably caused by a small misalignment of the sample. When the magnetic field is slightly tilted toward the light propagation $\boldsymbol{k} \| [010]$, the degeneracy between domain I and III is broken. Unfortunately, this tilt cannot be compensated on the setup at the KBFI, Tallinn, which allows sample rotation only around the propagation direction. This motivated me to perform a similar experiment at the Institute of Physics, Czech Academy of Sciences, Prague, where such magnetic field tilt is possible, allowing to select AFM domains, as shown by Murakawa *et al.* [158], and thus modulate DD.[4] Furthermore, in this setup, higher voltages can be applied, which, together with the magnetic field tilt, allowed for more complete domain selection and thus more efficient control of the DD.

[4]Previously, I. Kézsmárki and my supervisor S. Bordács carried out similar THz experiments in $Ba_2CoGe_2O_7$ to control DD by tilted magnetic fields with similar results.

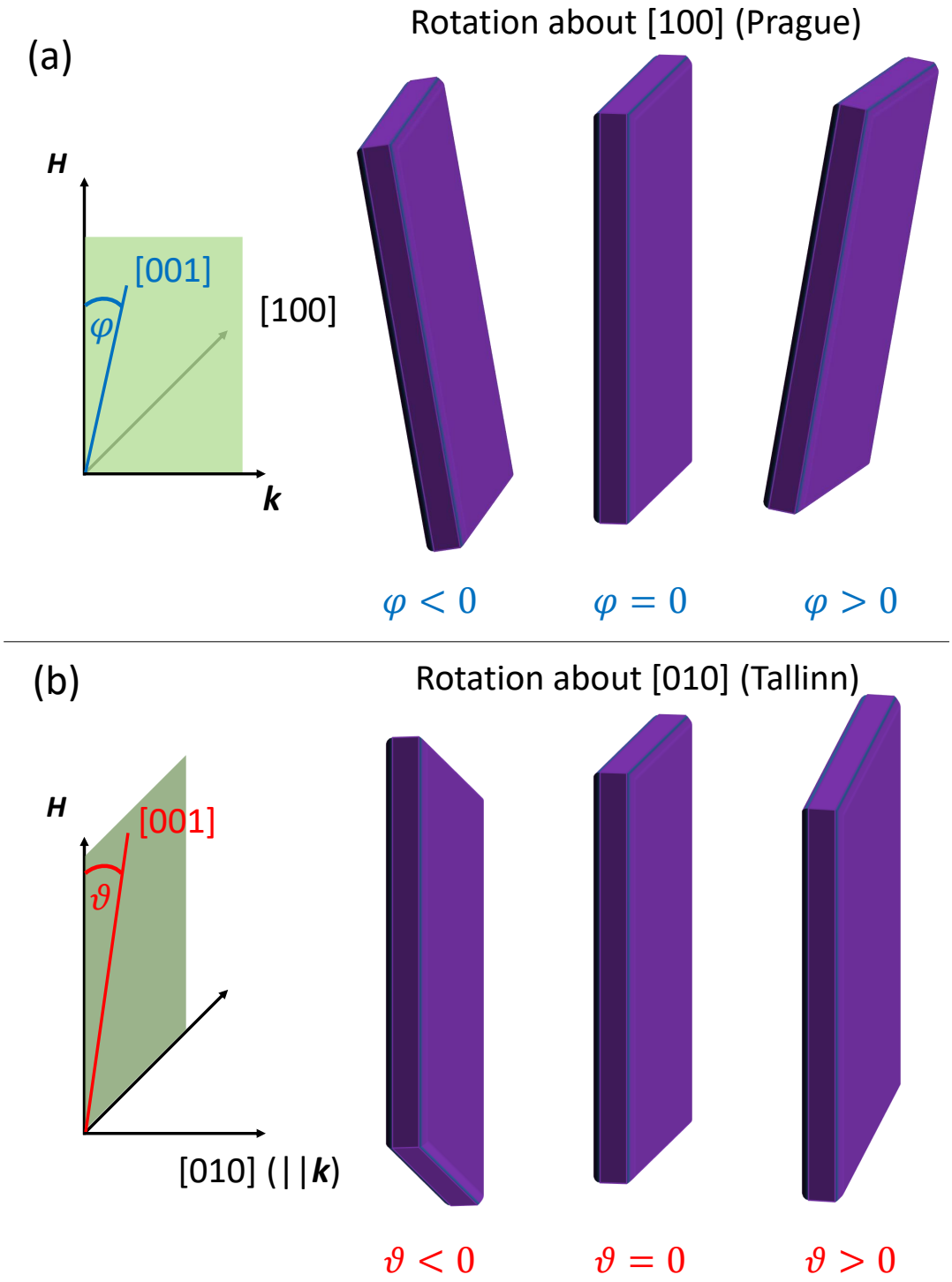

Figure 3.4: Tilting of the $Ba_2CoGe_2O_7$ crystal with respect to the vertical magnetic field. (a) At ioP in Prague, the crystal was tilted in a such a way that the magnetic field with respect to the crystal is tilted from [001] to [010] axis. The corresponding tilt angle is denoted as φ. (b) At KBFI in Tallinn, the crystal was tilted in such a way that the magnetic field with respect to the crystal is tilted from [001] to [100] axis. The corresponding tilt angle is denoted as ϑ.

The setup in Prague allows for applying a magnetic field up to 7 T, which is enough to considerably change the absorption spectrum, but quantitative comparison of the two sets of experiments is not possible as experiments in Tallinn were performed in 12 T. Anyway, quantitative comparison made difficult by several other reasons like different spectral resolution and different reference measurements. Despite the advantage of the setup in Prague that tilt toward [010] is possible it has some drawbacks as well: here it is not possible to rotate the sample along the light propagation direction, and the light path of the setup was not optimal during the measurements, which remarkably limited SNR and DR of the setup. Although these differences between the setups in Tallinn and Prague prevented direct quantitative comparison of the spectra, the complementarity of the setups provided useful additional information.

The tilt of the sample with respect to the magnetic field is displayed in Fig. 3.4(a), as realized in Prague: By tilting the sample with angle φ around the [100] axis, the magnetic field, originally aligned along the [001] direction, is tilted toward [010].

The results of the magnetic field tilting experiment are depicted in Fig. 3.5 with the focus on mode #3. Absolute spectra are displayed, showing background absorption $\approx 10\,\mathrm{cm}^{-1}$, thus only relative spectral differences should be compared to Tallinn spectra in Fig. 3.2(c). The temperature difference (3 K in Prague vs. 3.5 K in Tallinn) has only minor difference, since the effect is nearly temperature independent in this range as shown in from Fig. 3.3(c). Similarly, the difference in the applied field (7 T in Prague vs. fields shown in Fig. 3.3(c) for the experiments done in Tallinn) can also be considered by assuming smooth variation on the field, allowing reasonable comparison of the two experiments, limited rather by not optimal quality of spectra recorded in Prague.

By neglecting the background absorption, the spectra show that by $\pm 5^\circ$,tilt of the magnetic field toward [010] axis can completely turn-on and off the absorption at the resonance frequency. Difference of the peak absorption for +5° and -5° ,tilt reaches as high as $\approx 21\,\mathrm{cm}^{-1}$, which is much higher DD contrast than $\approx 4.5\,\mathrm{cm}^{-1}$, reached in Tallinn by ± 0.3 MV/m electric fields at 12 T. The average peak absorption in Prague $\approx 11\,\mathrm{cm}^{-1}$ is in a good agreement with the results obtained in Tallinn [c.f. Fig. 3.2(a)], showing reliability, though the spectra have different resolution (80 GHz in Tallinn vs. 120 GHz in Prague). In conclusion, tilt of the magnetic field toward [010] axis by a few degrees seems much more efficient for domain selection than highest available electric fields in Tallinn – ± 0.3 MV/m. This is consistent with pioneering experiment of Murakawa *et al.* [158], who observed complete switch of polarization by magnetic field tilt $\pm 4^\circ$, while hysteresis of the ferroelectric loop was observed up to highest achievable fields ± 3 MV/m (at 5 T), suggesting that even such high fields could not achieve a single-domain state.

In order to better compare the two sets of experiments, I also studied the electric-field effect on the DD in Prague. This experiment was carried out in liquid He at 1.2 K, allowing to apply higher voltages compared to experiments performed in Tallinn due to much higher breakdown electric fields of liquid He compared to low pressure ($\sim$0.3 bar) He vapors.

The four spectra in ± 7 T and ± 0.5 MV/m are displayed in Fig. 3.6.[5] The electric-field-induced difference of peak absorption is as high as $\approx 10\,\mathrm{cm}^{-1}$, which is three times higher than that of measured in Tallinn and it cannot be explained by simple extrapolation of

[5]Note that spectra for positive and negative fields are different from each other away from resonances. This is because something changed while sweeping the magnetic field - it could be either some mechanical movement, or drift of laser intensity.

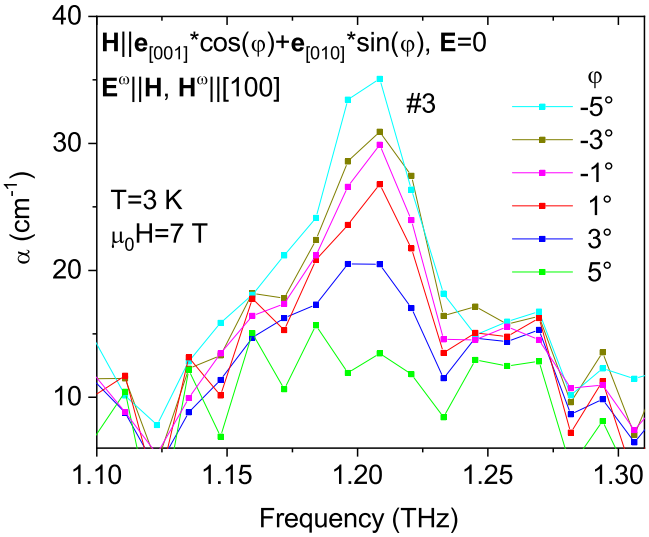

Figure 3.5: Magnetic-field tilt dependence of the absorption spectrum of $Ba_2CoGe_2O_7$. Absolute spectra of absorption coefficient α measured at $\mu_0 H = 7\,\mathrm{T}$ as a function of magnetic field tilt from [001] toward [010] ($\| \boldsymbol{k}$).

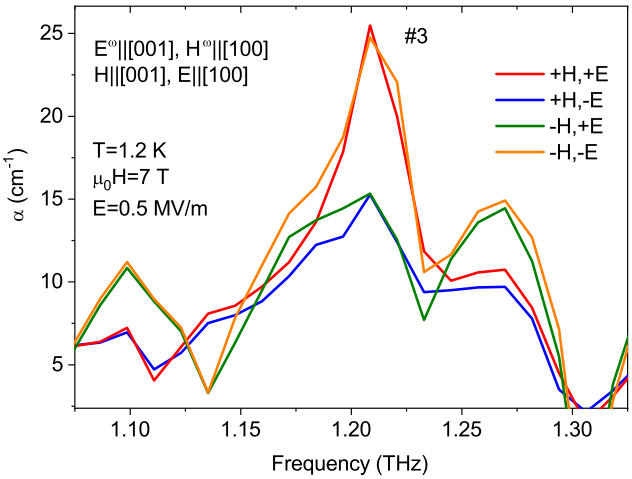

Figure 3.6: Electric field dependence of the absorption spectrum of $Ba_2CoGe_2O_7$. Absolute spectra of absorption coefficient α measured at $\mu_0 H = \pm 7\,\mathrm{T}$ and $E = \pm 0.5\,\mathrm{MV/m}$. The crystal was placed in liquid He ($T = 1.2\,\mathrm{K}$) which allowed to apply high voltage.

the hysteresis curve in Fig. 3.3(b) for higher electric fields. This ostensible discrepancy can be possibly ascribed to better alignment of the magnetic field with respect to [001] axis in Prague, meaning more susceptible state. Nevertheless, other effects may play a role as well like inhomogeneity of the electric field in the sample depending on quality of deposited electrodes. Also, the different temperature may partially explain the difference between the two experiments, thought probably not completely. These experiments prove that the electric field can control DD to high extent, although larger absorption difference can be achieved by tilting of the magnetic field (see Fig. 3.5).

3.6 Sample orientation dependence and synthesis of the results

In this section, I further elaborate the observed effects. The detailed investigation, as well as additional experiments point out that the picture of rigid domains may not be valid, especially if the magnetic field is tilted away from the [001] axis, and the details of the domain transformation should be studied further.

I ascribed the observed DD to non-equal domain population. Domains I & III possess DD with opposite signs, i.e. the absorption is lower or higher in one or in the other for a given propagation direction $\boldsymbol{k} \| [010]$, thus, I explained the measured absorption difference with the change in the volume ratio of domain I & III. Nevertheless, finite intensity of mode #1 in Fig. 3.2(a) indicates that domains II & IV coexist with domains I & III. In domains I & III, mode #1 is silent for the investigated light polarization ($\boldsymbol{E}^{\omega} \| [001]$, $\boldsymbol{H}^{\omega} \| [100]$) according to the calculation [see Fig. 3.2(c)]: It can only be excited by the $\boldsymbol{H}^{\omega} \| [010]$, which is perpendicular to $\boldsymbol{L} \| [100]$, while for domains I & III, $\boldsymbol{H}^{\omega} \| \boldsymbol{L} (\| [100])$. Furthermore, the model reveals that the polarization matrix element is also negligible for this resonance. Therefore, domains II & IV with finite magnetic-dipole strength for $\boldsymbol{H}^{\omega} \| [100]$ [see Fig. 3.2(c)] should also be present in the studied sample. Moreover, the intensity of mode #1 is unchanged with the application of the electric field, suggesting that the volume fraction of domains II & IV does not change even up to 15 T and 0.3 MV/m if the magnetic field is well aligned along [001]. If I assume that with a magnetic field precisely aligned ($\| [001]$), population of all domains is equal, one can expect that domains II & IV cover nearly 50% of the crystal volume.

These two observations – detection of finite DD, while no change of mode #1 intensity – can be explained if I assume that the electric field tunes only the volume ratio of domains I & III, while keeping domains II & IV intact. In the theoretical model defined by the Hamiltonian in Eq. 3.2, domains I & III have the highest and lowest energy, while domains II & IV have an intermediate energy upon application of $\boldsymbol{E} \| [100]$. Since a single domain state is not realized, the system cannot reach the global energy minimum within the model, therefore, there must be some other reason which prevents reaching a single-domain state in reality. Domains with higher energy may remain metastable due to the four-fold in-plane anisotropy or disorder, which are not included in the model. As a further alternative, I may assume the orthorhombic distortion coming from the AFM ordering [172]. The time-reversed pair, domains I & III possess the same orthorhombic distortion, which is 90° rotated in domains II & IV. If the crystal is clamped, domains I & III possibly cannot transform to II & IV as it costs the elastic energy. This mechanism may explain why the

volume ratio of domains II & IV does not change though the electric field drives domain wall between domains I & III. This is contrasting with electric dipole-dipole energy of ferroelectric domains, possibly responsible for almost complete equalizing of domain ratios after the electric-field removal,[6] as seen from only tiny hysteresis [Fig. 3.3(b)]. The tiny but finite hysteresis can be then explained by some kind of disorder, e.g. pinning of the domain walls on some impurities.

Related question about the energy scales is whether the ME annealing (poling) from above T_N in crossed electric and magnetic poling fields increases the domain selection with respect to isothermal field application. I performed such experiment (not displayed, see Supplementary Material in Ref. [11]) and found that the absorption difference is almost identical for ME annealing and in-situ reversal of the electric fields. These measurements confirm that at low temperature, one can control the AFM domains as much as the ME term allows.

Let me call the process described above as the *I↔III (or II↔IV) transformation scenario of rigid domains*, or shortly *scenario A*. This scenario may explain the electric-field-induced changes in the absorption and DD spectrum by changes in the domain population .

While observing DD upon tilting the magnetic field toward [010] axis [see Fig. 3.4(a) and Fig. 3.5], intensity of mode #1 is still nearly unchanged within $\varphi = \pm 5^\circ$ tilt (not displayed), thus the *scenario A* may explain the observed effect with the same logic as the electric-field effect: This scenario keeps volume fraction of domains II & IV unchanged, thus it is consistent with unchanged intensity of mode #1. On the other hand, this scenario allows I↔III domain transformation, so it can explain observed DD upon magnetic field tilt toward [010] [see Fig. 3.5].

The intensity of mode #1 gets weaker for higher tilts $\varphi \approx 15$–25° in tilting experiment in Prague at 7 T, corresponding to approaching of a single-domain state (not displayed). Altogether, the described results bring a plausible conclusion that the energy of the orthorhombic distortion sets constraints for domain transformation in low-tilt ($<15^\circ$) or electric-field regimes, keeping nearly 50% of the crystal volume in domains II & IV (I & III).

To get more insights in the possible differences between effects of the electric field and tilting of the magnetic field, I carried out detailed experiments in Tallinn with sample rotated around the propagation direction [010], i.e. tilted toward [100], which can be imagined as magnetic-field tilt toward [100]. Without any electric fields, 8 T magnetic field was applied at different angles, ϑ, measured from the [001] axis in the (010) plane perpendicular to the light propagation direction [see Fig. 3.4(b)]. Fig. 3.7 shows differential spectra of α with respect to zero magnetic field at 8 T for different ϑ. The strength of mode #1 does not change even for the largest rotation angle $\vartheta = 13^\circ$, implying that nearly 50% of the sample volume remains in domains II & IV (so I & III). This is consistent with the results of the experiments done in Prague, where the intensity of mode #1 remained the same upon magnetic field tilt toward [010] up to $\varphi = 15^\circ$ [not displayed, see definition of φ in Fig. 3.4(a)].

[6]The electric polarization generated by the magnetic field creates stray electric fields. In order to minimize the energy of the stray field, the sample breaks up to domains to cancel macroscopic polarization. In contrast to the orthorhombic distortion, dipole-dipole energy forces equalizing domains I & III (II & IV) with opposite polarizations.

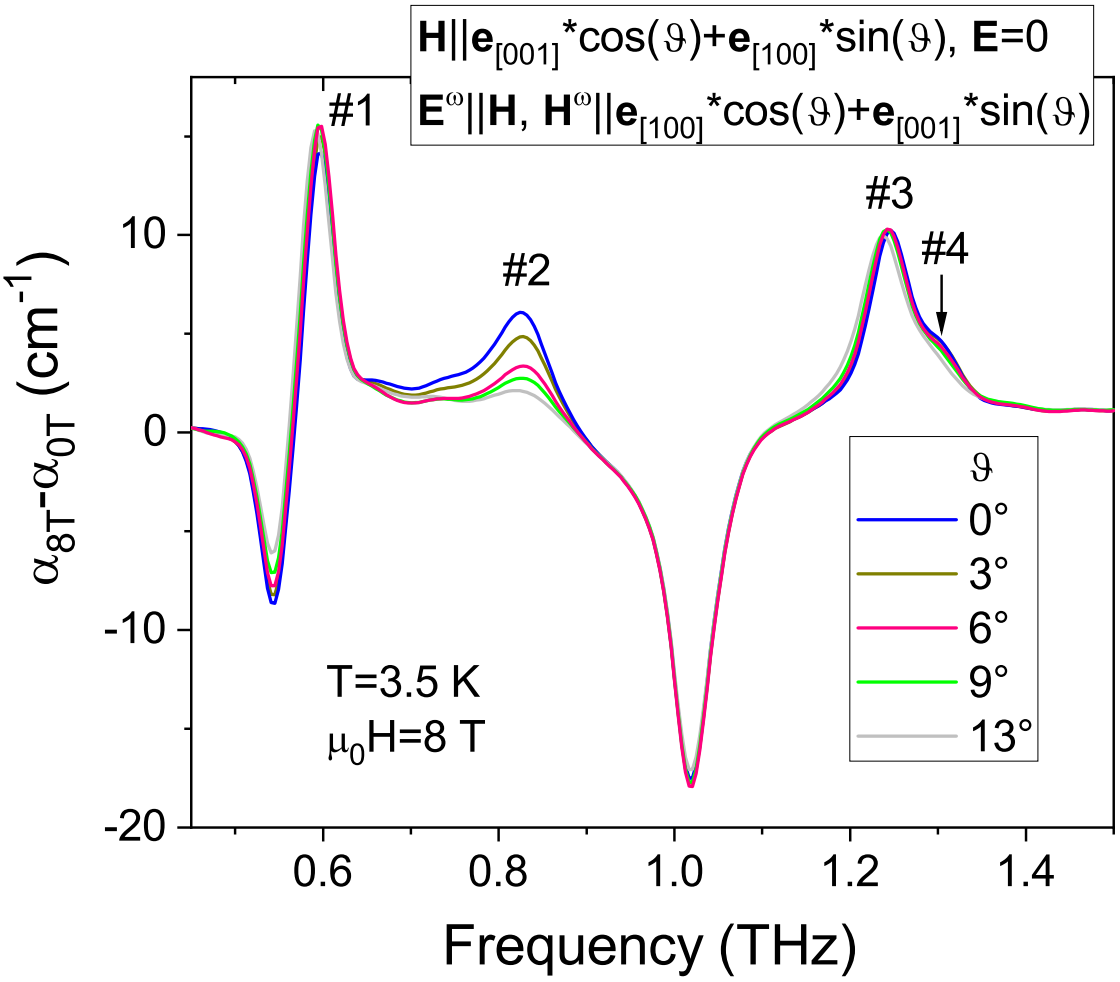

Figure 3.7: Tilt experiment in Tallinn at $\mu_0 H = 8\,\mathrm{T}$. Relative spectra of absorption coefficient α with respect to zero magnetic field as a function of magnetic field tilt toward [100] are displayed. (Note that as the crystal is rotated, there is a mismatch of light polarization and crystallographic axes, so differences are taken for the same ϑ.) Therefore, negative peaks refer to zero magnetic field field spectra, while positive peaks reflect the spectra at $\mu_0 H = 8\,\mathrm{T}$ for various tilts.

In contrast to mode #1, the intensity of mode #2 (and #4), present for sure in domains I & III due to their DD, is drastically reduced for few degree tilts, and almost vanishes for $\vartheta = 13^\circ$. This cannot be ascribed to DD of mode #2, since this tilt is supposed to induce II↔IV, but not I↔III domain transformation.[7] Therefore, in the picture of rigid domains, absence of mode #2 (and #4) implies absence of domains I & III, which would have to be transformed to domains II & IV. This, however, cannot be true as mode #1, present only in domains II & IV, does not change its intensity upon $\vartheta = 13^\circ$ tilt. Therefore, the picture of rigid domains, i.e. *scenario A*, should be revised.

It is a plausible explanation that upon magnetic field tilt toward [100] ([010]), the

[7] This is because the weak in-plane ferromagnetic component is perpendicular to the tilt-induced in-plane field in domains I & III. Note also that for opposite tilts ($\vartheta < 0$), the intensity of mode #2 (and #4) decreased symmetrically with ϑ (not displayed).

weak in-plane magnetization component is inclined toward the in-plane magnetic field component in domains I & III (II & IV). In the first approximation, such modification may be viewed as rotation of all spins, thus rotating $\boldsymbol{L}$, within the (001) plane. This change in the magnetic structure can explain the disappearance of mode #2 (and #4) (see Fig. 3.7). This scenario, which I call *domain rotation scenario*, or *scenario B*, is also consistent with the unchanged intensity of mode #1, active in domains II & IV, because the magnetic structure of these two domains is qualitatively unchanged upon magnetic field tilt toward [100], since the in-plane weak magnetization component is also along [100] in these domains. Finally, the intensity of mode #3 is unaffected because it is active in all domains, consistently with this scenario. In the following, I will simplify the language, by telling that domains I & III (or II & IV) "rotate" in *domain rotation scenario* upon the magnetic field tilt, by which I mean some magnetic structure modification, going beyond the picture of rigid domains.

Despite my elaboration of the two scenarios, neither of them can explain why modes #2 & #4 are extremely sensitive to small magnetic field tilt, while mode #1 did not disappear when magnetic field was tilted toward [010] in Prague (not displayed). If I assumed that the modes reflect orientation of dipoles, domains I & III would have to be almost 90° rotated to explain disappearance of modes #2 & #4, and such magnetic structure change should be accompanied by increasing strength of mode #1, since in rotated I & III domains, $\boldsymbol{L}$ is not anymore parallel to $\boldsymbol{H}^{\omega}$. Therefore, the explanation must go to the different nature of the excitations: While mode #1 is a classical optical magnon, all higher-energy modes involve spin stretching, and their strengths depend on the orientation of quadrupoles due to their electric-dipole activity [111]. Upon in-plane magnetic field rotation, magnetic quadrupoles change with double periodicity with respect to the magnetic dipole,[8] which determines activity of mode #1. Therefore, the *domain rotation scenario* can explain even this ostensible discrepancy, assuming that magnetic-quadrupole-related electric-dipole activity is dominating over the magnetic-dipole activity for mode #2 (and #4). This is not fully consistent with the theory, showing remarkable magnetic-dipole strength for mode #2 [see Fig. 3.2(c)], but the theory may have limited validity in this aspect.

Altogether I proposed two scenarios: (i) *I↔III (or II↔IV) transformation scenario of rigid domains* (*scenario A*), fully explaining the electric-field regime, and (ii) *domain rotation scenario* (*scenario B*), explaining some features in the small tilt regime. Importantly, *scenario A* must happen in the small tilt regime as well, because one sees both increase and decrease of mode #3 intensity with respect to zero tilt [see Fig. 3.5], while *scenario B* would explain only suppression of mode #3. Detailed investigation of the Prague tilt experiment shows that solely *scenario A* cannot explain all features: Namely, note that the decrease of mode #3 intensity upon 5° tilt is much larger than its intensity increase of upon -5° tilt with respect to zero tilt [see Fig. 3.5]. Such asymmetry, leading to complete vanishing of absorption, can be explained by *scenario B*: Besides *scenario A*, magnetic structure in domains II & IV, which also contribute to mode #3 absorption, is modified, thus almost annulling absorption. Consequently, DD contrast is much higher in

[8]This statement is not fully exact, since quadrupoles are in principle independent variables than dipoles. Nevertheless, the spin-induced polarization component $\boldsymbol{P}_c$, which is a function of magnetic quadrupoles, oscillates with double periodicity with respect to rotation of the in-plane magnetic field, i.e. with respect to rotation of magnetic dipoles. Since I measured the spectra in $\boldsymbol{E}^{\omega} \| c$ polarization, I assume that relevant magnetic quadrupoles follow double periodicity with respect to magnetic dipoles.

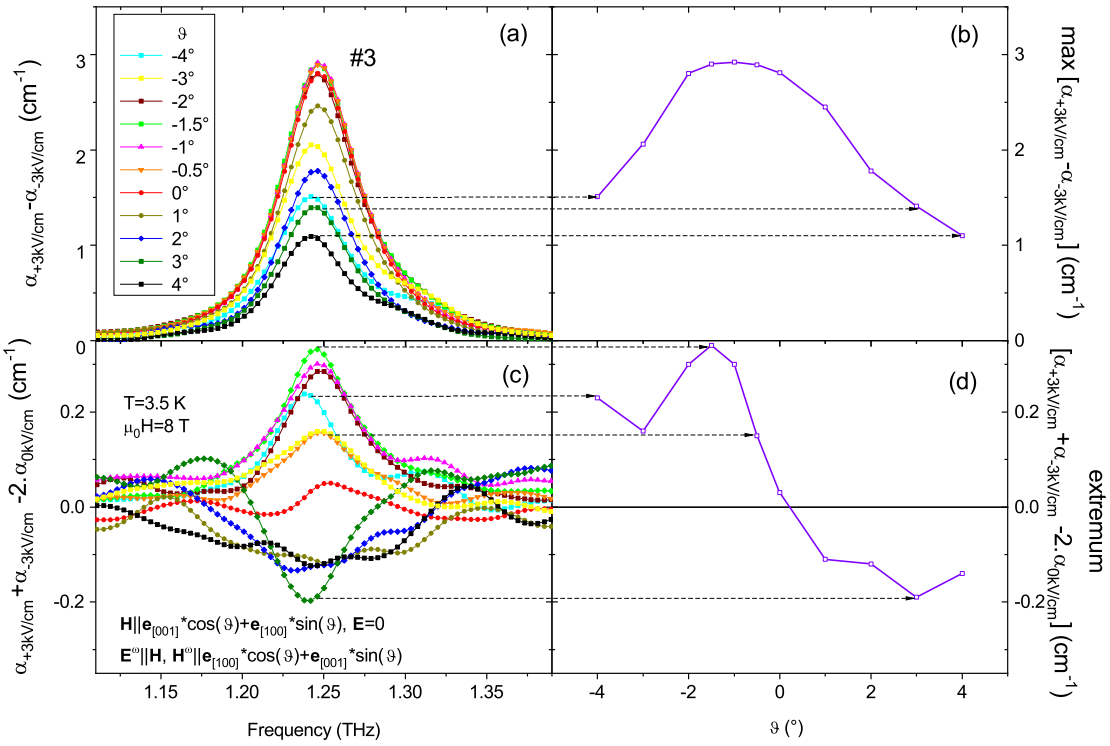

Figure 3.8: Tilt experiment in Tallinn (magnetic field was rotated toward [100]) combined with electric field $E = \pm 3$ kV/cm and zero electric field in fixed magnetic field $\mu_0 H = 8$ T at 3.5 K. (a) The electric field induced change in the absorption spectra for different tilts. (b) Maximum of peak difference absorption from panel (a) as a function of tilt. (c) Asymmetry of the influence of positive and negative electric fields with respect to zero electric field. (d) Extremum of the peak (or dip) from panel (c). The horizontal dashed arrows connect corresponding points of panels (a) and (b), and (c) and (d), respectively.

the small-tilt regime than in the electric-field regime [compare Figs. 3.5 and 3.6], since the latter does not involve modifications of domains II & IV.

Having such a detailed insight, I can now analyze the combined experiment where both the magnetic field was tilted and the electric field was applied. In Tallinn, I measured spectra at 8 T and $E = 0, \pm 3$ kV/cm for various small tilts ϑ of the magnetic field toward [100] axis. In Fig. 3.8(a), I display electric-field-induced change in the absorption spectra of mode #3 for different tilts. For small tilts of few degrees, the absorption contrast remarkably decreases, as clear from panel (b), where the absorption contrast as a function of tilt ϑ is displayed. Note that the absorption of mode #3 without electric field is unchanged up to $\vartheta = 13^\circ$ tilt, as seen from Fig. 3.7, thus the decreasing DD cannot be attributed to decrease of mode #3 strength.

Such observation could be easily explained by transformation of domains I & III into domains II & IV, in which the mode #3 is magnetic-dipole active according to the model [see Fig. 3.2(c)], but DD is forbidden by symmetry. However, the above-mentioned results and analysis suggests that such domain transformation is prevented by the orthorhombic distortion, and tilt of magnetic field toward [100] rather leads to rotations of domains I & III. Therefore, I anticipate that the I↔III domain transformation may be suppressed by the magnetic field tilted toward [100], because in rotated domains, the spin-induced

polarization is not anymore parallel to the applied electric field. Other reason for the suppressed DD may be decreasing electric-dipole strength of mode #3. Nevertheless, quantitative analysis of the observed effect is beyond the scope of this thesis.

There is one more peculiar effect that I want to analyze: In Fig. 3.3(a,b), positive electric fields generate larger absorption contrast with respect to zero electric-field spectrum than the negative fields. For the highest fields ± 3 kV/cm, the absorption contrast difference is 30%, which is much larger than the experimental error. One would expect that the average of the absorption spectra measured in positive and negative electric fields should be same as that of measured in zero electric field, $(\alpha_{+3\mathrm{kV/cm}} + \alpha_{-3\mathrm{kV/cm}})/2 = \alpha_{0\mathrm{kV/cm}}$. Therefore, the quantity $\alpha_{+3\mathrm{kV/cm}} + \alpha_{-3\mathrm{kV/cm}} - 2\alpha_{0\mathrm{kV/cm}}$ that I call as asymmetry function, measures the asymmetry of the electric field hysteresis shown in Fig. 3.3(a,b). Fig. 3.8(c,d) displays the magnetic field tilt angle dependence of this asymmetry. In contrast to the DD contrast, which is nearly an even function of ϑ [Fig. 3.8(b)], the asymmetry function is nearly an odd function of ϑ [Fig. 3.8(d)]. Up to now, I cannot explain the angular dependence.

I can only explain a vertical shift of the asymmetry function in Fig. 3.8(d) by magnetic field tilt toward [010], which could not be compensated in Tallinn: Since such tilt favors one of domains I or III, the electric field has more room to switch from the pre-selected domain to the unfavorable. As a consequence of such vertical shift, maximum of the curve in Fig. 3.8(b) lies at a different tilt than the zero-crossing point of the curve in Fig. 3.8(d).

3.7 Summary

In summary, I demonstrated the isothermal electric-field control of the non-reciprocal THz absorption in $Ba_2CoGe_2O_7$, while showing why such effect is rather scarce. Most of the former studies of non-reciprocal THz absorption is controlled by the magnetic field or the ME annealing from high temperatures using both electric and magnetic fields, with one exception – electric-field control of microwave DD of the triplet Bose-condensate in $TlCuCl_3$ [10]. Previous studies of $Ba_2CoGe_2O_7$[7, 9, 71] discussed DD generated by an in-plane magnetic field, which overcomes the small anisotropy within the (001) plane already in low fields and stabilizes a single-domain magnetic state. Once one of the AFM domains becomes favored due to the in-plane magnetic field, the electric field has a little room to control the magnetic order parameter because of the dominance of transverse magnetic susceptibility over the ME interaction. Thus, electric-field switching of the domains is not possible if the in-plane magnetic-field is higher than few hundreds of mT. Instead, here I apply magnetic field bias along the tetragonal axis, [001], the case not studied before. The magnetic field in this direction preserves the high symmetry of the tetragonal plane, and concomitantly, it induces electric polarization pointing in different directions in different domains making them susceptible to a moderate external electric field. Consequently, the electric-field-induced domain imbalance is manifested by DD.

Furthermore, I also explored the control of DD by the magnetic-field tilt and discussed the underlying low-energy physics behind such a susceptible magnetic state. Quantitative analysis of the results is difficult due to the several low-energy terms, all shaping the magnetic ground state. These are the ME energy, AFE coupling responsible for the anisotropy within the plane, Zeeman coupling to the weak in-plane magnetization component, electric

dipole-dipole energy between the magnetic-field-induced polarization of the domains, and the elastic energy of the orthorhombic distortion. Furthermore, disorder that may pin the orientation of $\boldsymbol{L}$ could possibly be the cause of small spectra hysteresis, but this can be hardly quantified. I believe that by realizing the electric-field control of the DD, my work provides an example for an electric field controllable THz property and makes an important step toward the application of multiferroics in high-frequency devices.

Chapter 4

Electromagnons in hexaferrites: spectroscopy and microscopic selection rules based on the exchange-striction mechanism

In this chapter, I will present hexaferrites, which are one of few room-temperature multiferroics. Due to their soft ferrimagnetism, they exhibit high magnetic susceptibility accompanied with high ME susceptibility – several orders of magnitude higher than for antiferromagnets, which may find some application.

Due to variety and complexity of hexaferrites as a result of doping with arbitrary ratios of ions with the same valency, hexaferrites exhibit several effects. For example, all three main microscopic mechanisms of spin-induced ferroelectricity have been observed. This demonstrates the fact that all the mechanisms are naturally present, while symmetry of the crystal and magnetic structure decides which of them are manifested macroscopically.

While all three main mechanisms can be observed in the static limit, so far, electromagnons in hexaferrites are solely explained by the exchange-striction mechanism. In this chapter, I first present the electromagnon I found in Y-hexaferrite $BaSrCoZnFe_{11}AlO_{22}$, following Ref. [180], while I found several inaccuracies in that publication, which are corrected in this chapter. Next, I also present the electromagnon in Z-hexaferrite $(Ba_xSr_{1-x})_3Co_2Fe_{24}O_{41}$ partially based on my older work [138] but containing new interpretations as well as results. Finally, I present finding of possible electromagnons in other types of hexaferrites and make a comparison studying correlation of static properties and occurrence of electromagnons among different types of hexaferrites.

4.1 Hexaferrites: Structure, static magnetic and ME properties

Ferrites are magnetic oxides with iron as the main metallic ion. Hexaferrites are ferrites with hexagonal or trigonal crystal structures. They can be classified into 6 main types according to their crystal structures, which can be described as stacking sequence of three different crystallographic blocks along the hexagonal axis: S ($Me_2Fe_4O_8$; spinel

Table 4.1: Six main types of hexaferrites and their basic properties. Last column assigns number of formula units per unit cell [181, 183].

Type	Chemical formula	Stacking sequence	c(Å)	space group	f.u./u.c.
M	(Ba,Sr)$Fe_{12}O_{19}$	RSR$^*S^*$	∼23	$P6_3/mmc$	2
W	(Ba,Sr)$Me_2Fe_{16}O_{27}$	RS$_2$R$^*S_2{}^*$	∼33	$P6_3/mmc$	2
Y	(Ba,Sr)$_2Me_2Fe_{12}O_{22}$	TST'S'T"S"	∼43	$R\bar{3}m$	3
Z	(Ba,Sr)$_3Me_2Fe_{24}O_{41}$	RSTSR$^*S^*T^*S^*$	∼52	$P6_3/mmc$	3
X	(Ba,Sr)$_2Me_2Fe_{28}O_{46}$	(RSR$^*S_2{}^*$)$_3$	∼84	$R\bar{3}m$	3
U	(Ba,Sr)$_4Me_2Fe_{36}O_{60}$	(RSR$^*S^*TS^*$)$_3$	∼113	$R\bar{3}m$	1

block), where Me denotes divalent or trivalent metal ion, R [(Ba,Sr)Fe_6O_{11}]$^{2-}$ and T block [(Ba,Sr)$_2Fe_8O_{14}$] [181, 182]. The sequence of blocks in case of 6 main types of hexaferrites, as well as their chemical formulas, unit cell size along the main axis, space groups and number of formula units per crystallographic unit cell, are in Table 4.1.

There are 3 main types of elements occurring in hexaferrites: Large nonmagnetic divalent ions Ba/Sr, transition metal ions – mainly iron, magnetic (e.g. Co, Mn) or nonmagnetic (e.g. Zn, Al) – and oxygen. Transition metal ions can be in octahedral (either centered or off-centered) or tetrahedral positions; R-block also contains trigonal bipyramidal positions. Ba/Sr ions replace some oxygen positions, whereby distorting the lattice. Importantly, all hexaferrite space groups contain inversion symmetries, so multiferroic hexaferrites are always of type-II. Detailed description of the crystal structures can be found for example in Refs. [181, 183], but here I focus only on the aspects which will be relevant not to overwhelm or confuse the reader.

From magnetism point of view, most of ferrites are ferrimagnets with Curie temperatures above the room temperature. In some cases, magnetic moments can be compensated leading to antiferromagnetism. Magnetic moments are located primarily on the Fe^{3+} ions, and on other magnetic ions, substituted to iron positions. Importantly, several competing exchange interactions lead to magnetic frustration, resulting in various noncollinear magnetic structures, some of them inducing ferroelectricity.

Due to crystal structure complexity, it is often difficult to estimate magnetic structures. Microscopically, the basic interaction is the Fe-O-Fe superexchange, which varies with the bond angle: It is strongly AFM for angles close to 180° and weakens with decreasing bond angle [184, 185]. Such a rule provides a rough guideline for magnetic structure estimation, however, the situation is complicated because exchange interactions occur via multiple paths.

In Y-type hexaferrites $(Ba_{1-x}Sr_x)_2Zn_2Fe_{12}O_{22}$ Momozawa *et al.* detected modulated magnetic structures [186]. Based on earlier work [187], they identified stronger interactions, keeping the spins collinear, and weaker ones, allowing noncollinear spin alignment. This has lead to the so-called spin-block approximation, in which spins within a block are considered collinear, thus they can be approximated as a single spin. The interactions within the (001) plane are strong, keeping the spins (anti)parallel, so such spin blocks are stacked along the hexagonal axis. These magnetic blocks, distinct from crystallographic blocks, are called L and S, possessing large and small spin moments.

The boundary between the magnetic blocks lies in the crystallographic T-block between layers 4 and 5 in Y-hexaferrite (see Fig.4.1), since Fe(4)-O(2)-Fe(5) bond is the weakest,

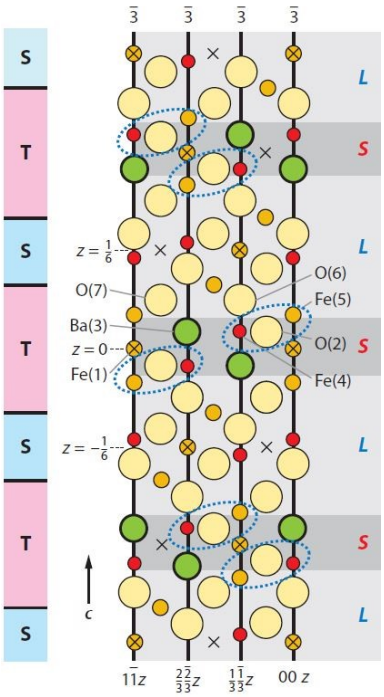

Figure 4.1: Schematic crystal structure of Y-hexaferrite with denoted crystallographic (S,T) blocks on left and magnetic (L,S) blocks on right. Ba/Sr ions are green, oxygen ions are yellow. Transition metal ions in octahedral surrounding are orange, while those in tetrahedral surrounding are red. Inversion centers are denoted by crosses. (Reproduced from Ref. [182].)

allowing non-collinear spin alignment. Because Ba (or Sr) ions are situated near these two Fe sites, the substitution of small Sr for large Ba causes the increase in the Fe(4)-O(2)-Fe(5) bond angle, whereby enhancing the magnetic frustration and in turn leading to the modulated magnetic structure [185].

Second crucial aspect (together with exchange interactions) determining magnetic structure of hexaferrites is the magnetocrystalline anisotropy, determined mostly by large Ba/Sr ions with strong SOC, and finely tunable by transition-metal ions substituting iron, partially into some preferable positions. Typical hard ferrites have the easy-axis anisotropy, while soft hexaferrites have the easy-plane anisotropy. Trigonal bipyramide, contained in the crystallographic R-block, is supposed to be responsible for the easy-axis anisotropy, dominant in most of hexaferrites [181]. The exception are Y-hexaferrites lacking the R-block, thus typically preferring the easy-plane anisotropy. The ferroelectricity in hexaferrites is induced solely in non-coplanar magnetic structures, which can be stabilized only in case of very low anisotropies.

First and most common multiferroic hexaferrites are those of Y-type, since the magnetocrystalline anisotropy can be tuned well by the chemical composition around low values due to their naturally low anisotropy owing to lack of the trigonal bipyramide. Here, I will present typical magnetic and multiferroic properties of Y-hexaferrites with general formula $Ba_xSr_{2-x}Co_yZn_{2-y}Fe_{11+z}Al_{1-z}O_{22}$ (BSCZFAO), showing that three free parameters can be tuned by doping. In this thesis, I will present results on $BaSrCoZnFe_{11}AlO_{22}$ and $Ba_{0.2}Sr_{1.8}Co_2(Fe_{0.96}Al_{0.04})_{12}O_{22}$.

Crystal structure of Y-hexaferrite is depicted in Fig. 4.2(a). Their magnetic structures depend on exact chemical composition, magnetic field, temperature and also their history. Main reported magnetic structures in BSCZFAO Y-hexaferrites are displayed in Fig. 4.2(b-g), while the above-introduced spin-block approximation is used.

Phase diagram of typical zero-field-cooled BSCZFAO crystals with subsequent applying magnetic field within the hexagonal plane, is in Fig. 4.2(j). The phase diagram varies depending on chemical composition. Magnetic structures of hexaferrites can be viewed as modifications of collinear ferrimagnetic structures, when small and large spins point in opposite directions as depicted in Fig. 4.2(b,f). BSCZFAO crystals become magnetic below ≈ 450 K, when they enter the collinear ferrimagnetic structure with spins lying in the isotropic (001) plane Fig. 4.2(b). Below ≈ 400 K, the proper-screw phase [Fig. 4.2(c)] starts to develop, while keeping the easy-plane anisotropy. Upon subsequent cooling, the anisotropy becomes more easy-axis, so spins start inclining towards the hexagonal axis, creating so called alternating longitudinal conical (ALC) structure [Fig. 4.2(d)] with compensated magnetic moments. When the magnetic field is applied along the hexagonal axis, the magnetic structure transforms to the normal longitudinal conical (NLC) via the first-order metamagnetic phase transition [Fig. 4.2(e)]. The proper-screw and the conical structures are incommensurate, and they are parametrized by (a) conical angles for small and large spins and (b) modulation vector describing helical angle dependence. Since all the structures are derived from the collinear ferrimagnetic structure with small and large spins antiparallel, small and large spins are always anti-phase in case of modulated structures.

The stabilization of conical magnetic structures manifests a delicate state of low magnetic anisotropy. Therefore, when moderate magnetic field within the (001) plane is applied ($H_{xy} \approx 0.5$ T) in the low-temperature ALC phase, the spins rotate toward the (001)

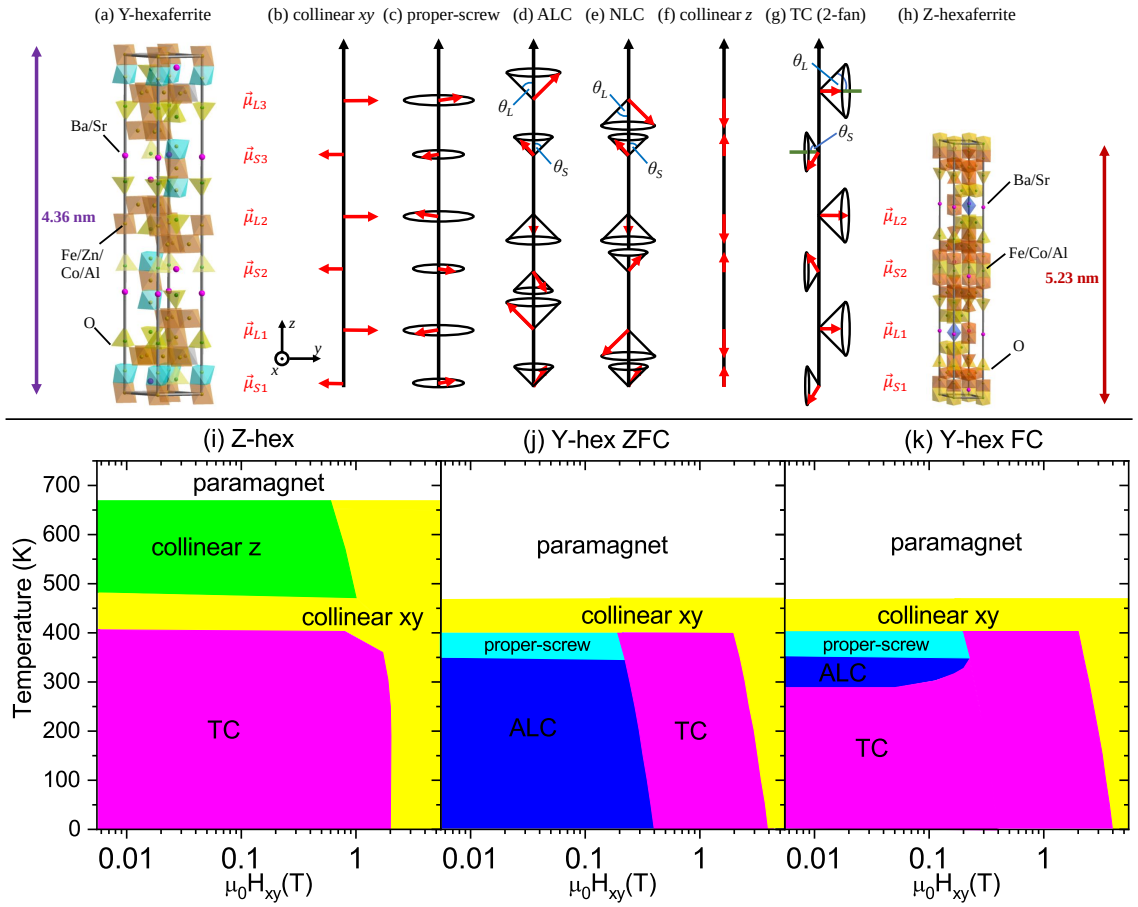

Figure 4.2: (a)–(h) Crystal and magnetic structures of the Y-hexaferrite BSCZFAO and Z-hexaferrite $(Ba_{0.2}Sr_{0.8})_3Co_2Fe_{24}O_{41}$. All depicted magnetic structures are present in Y-hexaferrite BSCZFAO, while only (b), (f), (g) panels refer to Z-hexaferrite $(Ba_{0.2}Sr_{0.8})_3Co_2Fe_{24}O_{41}$. The sizes of crystal structures match those of the magnetic structures for both Y-hexaferrite and Z-hexaferrite: The crystal unit cell of Y-hexaferrite contains 6 spin blocks, whereas the crystal unit cell of Z-hexaferrite contains only 4 spin blocks. Note that scales are therefore different for Y-hexaferrite and Z-hexaferrite, which is depicted in panels (a) and (h). The spin magnitudes also differ; for more information about the spin magnitudes, see the main text. The depicted cones and circles are only auxiliary to display 3-dimensional perspective. (i), (j), (k): Illustrative (H_{xy}, T) phase diagrams for (i) Z-hexaferrite $(Ba_{0.2}Sr_{0.8})_3Co_2Fe_{24}O_{41}$, (j) zero-field-cooled Y-hexaferrite BSCZFAO and (k) field-cooled Y-hexaferrite BSCZFAO in $H_{xy} \approx 5\,\mathrm{T}$, based on Refs. [61, 188–191]; the actual phase diagrams may somewhat differ for the samples I measured owing to their different chemical compositions. The NLC structure in the panel (e) occurs in Y-hexaferrite BSCZFAO for $H_z \gtrsim 5\,\mathrm{T}$ [61].

plane, forming the TC structure [Fig. 4.2(g)], or more specifically 2-fan or FE3 phase [192]. The cone axes in the TC structure do not coincide with high-symmetry [001] axis, thus the TC structure is commensurate with modulation vector $\boldsymbol{Q}_C$ =(0,0,3/2): While the crystalline unit cell contains six spins, the spin structure is repeated after period of four spins. [Compare Figs. 4.2(a,g)] Due to different anisotropies within the magnetic S and L blocks, the large spins lie in the (001) plane, while small spins are inclined toward the [001] axis. Further increase of H_{xy} results of continuous decrease of the cone angles θ_S, θ_L [see Fig. 4.2(g) for definition of the cone angles], finally reaching the collinear ferrimagnetic structure with spins in the (001) plane. Note that the magnetic phase diagram is simplified partially because of the spin-block approximation, and also some intermediate phases may exist in between the boundaries, coexisting with the ALC and TC structures, see for example Refs. [190, 193, 194].

Importantly, after cooling in $H_{xy} \approx$ few tenths of T, or after applying H_{xy} in low-temperature phase, once the TC structure is reached, it may persist stable even in zero magnetic field, as seen from the phase diagram in Fig. 4.2(k) [195].

The TC structure in Y-hexaferrites is responsible for the spin-induced ferroelectric polarization induced via the inverse DM interaction (and/or KNB model). The polarization points perpendicular to the hexagonal axis and to the cone axis (magnetic field). Accordingly, the rotation of the magnetic field within the (001) plane rotates the cones, thus the polarization rotates, and switch of the magnetic field is accompanied by switch of the polarization. The direction of the polarization also depends on the helicity of the TC structure, which can be selected by ME poling from high-magnetic-field collinear ferrimagnetic phase – this is possible whenever there is a direct phase boundary between the two phases [magenta and yellow areas in Fig. 4.2(j,k)]. The TC structure has two variants (domains) – left- and right-handed, depending on respective phase of subsequent small and large spins. When entering the TC structure from the collinear ferrimagnetic phase, the domain with polarization parallel to the applied electric field is selected. Therefore, the common poling procedure consists from applying electric (few kV/cm) and magnetic (few T) fields in the (001) plane, perpendicular to each other, and subsequent decrease of magnetic field to few hundreds of mT, for which the single TC domain is established. After removal of the electric field, the polarization current is measured while the magnetic field is swept or rotated [53, 193].

Multiferroic hexaferrites are necessarily soft magnets to hold the noncollinear magnetic structures. Therefore, switch of the TC domains upon switch of the magnetic field in the isotropic (001) plane happens for very small fields with only tiny hysteresis. High magnetic susceptibility of soft Y-hexaferrites upon the domain switching is accompanied by high ME susceptibility. Since the magnetic anisotropy can be continuously tuned to unlimitedly low values by chemical composition, there is in principle no upper bound for the magnetic, thus the ME susceptibility. In 2010, the record high ME susceptibility for Y-hexaferrites reached by Chun *et al.* was $\chi^{em}/c = 20\,000$ ps/m in $Ba_{0.5}Sr_{1.5}Zn_2(Fe_{0.92}Al_{0.08})_{12}O_{22}$ [196], while in 2017, Zhai *et al.* tuned chemical composition to $Ba_{0.4}Sr_{1.6}Mg_2Fe_{12}O_{22}$, reaching $\chi^{em}/c = 33\,000$ ps/m [197]. This is several orders of magnitudes higher than ME susceptibilities of canonical AFM linear magnetoelectrics, for which χ^{em}/c reaches typically tens of ps/m. Importantly, the direct ME effect is accompanied with the converse ME effect, more relevant for applications. Although the role of the electric field is limited (the electric field cannot establish a single domain state, moreover, subsequent reversal of

electric field destroys the single-domain TC state), the electric field of ± 5 MV/m was able to change magnetization by $5.5\mu_B$ per formula unit in $Ba_{1.2}Sr_{0.8}Co_2Fe_{11.1}Al_{0.9}O_{22}$ [190].

From the point of view of physics, it is instructive to mention other ME effects in Y-hexaferrites, not relevant for application. Nevertheless, they will serve as analogy to the electromagnons I studied in this thesis. It is clear that the TC structure breaks the inversion symmetry and allows the ferroelectric polarization. How about other phases? Note that the inversion symmetry breaking does not necessarily imply allowance of the polarization. Particularly, the ALC structure may lead to the polarization induced by the exchange-striction due to ↑-↑-↓-↓ c-axis spin component [61].

Similar huge ME effect as in Y-hexaferrites were also measured in other types of hexaferrites. For example Z-hexaferrites with higher T_C than Y-hexaferrites due to higher concentration of iron, exhibit ME effects up to temperatures well above the room temperature. $(Ba_{0.2}Sr_{0.8})_3Co_2Fe_{24}O_{41}$, which I also study in this thesis, transforms from the paramagnetic phase to the collinear ferrimagnet with spins along the c-axis [see Fig. 4.2(f)] at around $T_C = 670$ K [188]. Below 500 K, spins start to rotate toward (001) plane due to a change of the magnetic anisotropy, and at 410 K, the ferroelectric polarization appears due to the TC structure, similarly as in Y-hexaferrites. However, the polarization is not switched upon magnetic-field switch in Z-hexaferrites, in contrast to Y-hexaferrites; instead, a polarization with the same sign and nearly the same magnitude is established [198].

Chai *et al.* studied this difference between Y- and Z-hexaferrites more in detail, and found that upon the magnetic field rotation in the (001) plane, the polarization rotates in the (001) plane counter-clockwise with double periodicity with respect to the magnetic field rotation in Z-hexaferrites [199]. Therefore, the spin-induced polarization in Z-hexaferrites cannot be ascribed to the iDM (or KNB) mechanism, as previously believed, but to a single-ion mechanism, possibly d–p hybridization. The manifestation of this effect is explained by symmetry arguments: While both small and large spins in Y-hexaferrites, located in the middle of the crystallographic block T and S, respectively, lie at the inversion centers, the large spin in the Z-hexaferrites is located in the middle of the crystallographic R block, i.e. on (001) symmetry plane [199]. This allows manifestation of single-ion mechanisms on a macroscopic scale. The difference of the ME effects in Y- and Z-hexaferrites, otherwise very similar, points out that all the mechanisms of the spin-induced polarization are naturally present in the materials, while the symmetry of the crystal is a decisive factor about which of the effects are manifested macroscopically.

Similar ME effect can be found in other types of hexaferrites, like M-type [200], U-type [201] and W-type [202]. Nevertheless, only in Y-hexaferrites, the magnetization switch was accompanied by switch of the polarization. This is supposed to be due to symmetry reasons as described in the previous paragraph [199] and/or due the finding that TC structure must be stable in zero magnetic field in order to allow polarization switch [203].

Importantly, the magnetically isotropic (001) plane in hexaferrites allows to observe ME effects even in hexaferrite polycrystals [198], which may be relevant for applications, since production of polycrystals is much less costly than growth of single crystals. This comes from the fact that only relative directions of the electric and magnetic poling fields are relevant for establishing multiferroic domains [53]. Thus, irrespectively of the orientation of a polycrystalline grain with respect to fields, given crossed electric and

magnetic fields always favor the same domain. Other feature preventing room temperature application is conductivity due to defects, mainly oxygen vacancies, rapidly increasing with temperature increase. For this reason, hexaferrites are usually annealed in oxygen atmosphere for several days, whereby drastically decreasing the conductivity [137].

Altogether, multiferroic hexaferrites are superior in record high ME susceptibility among single-phase multiferroics. They attract application interest, as the effect works at low magnetic fields at elevated temperature including room temperature.

4.2 Dynamic ME effect in hexaferrites

What is the characteristic process and speed of the gigantic ME effect in hexaferrites? It corresponds to reorientation of magnetic domain walls, which occurs typically in MHz regime. In fact, the lower limit of domain-wall reorientation frequency was determined to 10 kHz due to limitation of speed of electronics [53].

This thesis is focused on spin excitations in THz regime, which are not necessarily connected to the static ME effects described above. In $\boldsymbol{E}^{\omega} \parallel c$ spectra of several Y-type hexaferrites, strong purely electric-dipole-active electromagnons were detected [204–207], and their activation in $\boldsymbol{E}^{\omega} \parallel c$ spectra was explained by the exchange-striction mechanism. This is supported by symmetry arguments and by the fact that the dielectric strength of electromagnons is high to be explainable by the mechanisms involving SOC.

The exchange-striction mechanism leads to the static polarization $\boldsymbol{P}$ induced by spin structures with collinear ordering of some spin components, $\boldsymbol{P} \propto \sum_{i,j} \boldsymbol{S}_i \cdot \boldsymbol{S}_j$ [c.f. Eq. 1.29]. For noncollinear spin alignment of spin components, terms in the sum cancel out after summing up, giving zero polarization.

Electromagnons induced by the exchange striction correspond to the polarization oscillating along the c axis, P_c, while the first-order terms into the fluctuating polarization are of type $\boldsymbol{S}_i \cdot \boldsymbol{\delta S}_j$, where $\boldsymbol{\delta S}_j$ represents fluctuations of the neighboring spin j. Since $\boldsymbol{\delta S}_j$ is perpendicular to $\boldsymbol{S}_j$, these term are zero for collinear spin alignment, in contrast to the static exchange-striction.

The exchange-striction mechanism can well describe the purely electric-dipole-active electromagnons in Y-hexaferrites: In order to explain the impossibility of exciting the magnon by the magnetic field, the electromagnons must correspond to antiphase oscillation of spins, conserving total magnetization. If there was a nonzero uniform electric dipole upon the magnon oscillation, the magnon is activated in optical spectra. The presence of electromagnons in Y-hexaferrites well correlates with the static magnetic structures, while noncollinear spin alignment is essential [204–207].

A purely electric-dipole-active electromagnon was also detected in $\boldsymbol{E}^{\omega} \parallel c$ spectra of Z-hexaferrite $Ba_{0.5}Sr_{2.5}Co_2Fe_{24}O_{41}$ in its TC structure, and it is explained by the exchange-striction, analogically to Y-hexaferrites [208]. Since the polarization oscillates along the c-axis, the symmetry arguments for the electromagnons in Y- and Z-hexaferrites are the same – it is because both inversion center and (001) symmetry plane, on which the spins are located, act the same way on the polar vector along the c-axis.

In this chapter, I present observation of electromagnons in Y-hexaferrite $BaSrCoZnFe_{11}AlO_{22}$, Z-hexaferrite $(Ba_xSr_{1-x})_3Co_2Fe_{24}O_{41}$ and possible electromagnons and other excitations in other types of hexaferrites. Even though the electromagnons in

Y-hexaferrites have been already known, I carried out a comprehensive experimental study of single-crystalline $BaSrCoZnFe_{11}AlO_{22}$, including magnetic, magnetodielectric measurements with THz and Raman spectroscopies, by which I linked static and dynamic properties. Especially the combination of THz and Raman spectra provide a useful tool into both ground state symmetry of the material, and symmetry of the excitations. Further, I developed explicit formulas for the activation of electromagnons by the exchange striction in Y-hexaferrites within the spin-block approximation for various spin structures. These allow quantitative predictions of electromagnons' strength and limit number of possible modes, and they are valid for other types of hexaferrites than Y-type as well.

Comparative study of the electromagnons in various types of hexaferrites is provided at the end of this chapter, which first follows the work published in Ref. [180] about the electromagnon in Y-hexaferrite $BaSrCoZnFe_{11}AlO_{22}$, including also few results included in Ref. [209]. Next, there are results about the electromagnon in Z-hexaferrites $(Ba_xSr_{1-x})_3Co_2Fe_{24}O_{41}$, published in Refs. [138, 209], and then about possible electromagnons in other types of hexaferrites.

4.3 Results on Y-hexaferrite $BaSrCoZnFe_{11}AlO_{22}$

4.3.1 Magnetization measurements

The goal of this work is to relate the electromagnon to the static magnetic structure, which is extremely sensitive on chemical composition. Therefore, static magnetic structure of each specimen has to be checked. Ultimately, the magnetic structure is determined by neutron diffraction. Nevertheless, several neutron diffraction studies of $Ba_xSr_{2-x}Co_yZn_{2-y}Fe_{11+z}Al_{1-z}O_{22}$ Y-type hexaferrites determined their magnetic structures and correlated them with magnetization data [61, 192, 210]. Therefore, it is possible to determine the magnetic structures of the sample I measured just from measurements of magnetic-field-dependent magnetization and permittivity.

To verify the presence of conical structures, I measured the temperature-dependent magnetization for $\boldsymbol{H} \parallel c$ and $\boldsymbol{H} \perp c$. [See Fig. 4.3(d)] The phase transition from the collinear to the proper-screw structure was revealed at $T_{con} = 383\,\mathrm{K}$ which is in agreement with previous results, as the temperature of this phase transition is sensitive to chemical composition [211]. After $\boldsymbol{H}_{\mathrm{DC}} \perp c$ poling at $T = 10\,\mathrm{K}$, the magnetization in the (001) plane remains high up to 230 K, meaning stability of the TC structure even at $\boldsymbol{H} = 0$ which is consistent with the previous work of Shen *et al.* [195].

Two longitudinal-conical (LC) magnetic structures, the NLC and ALC one, were reported to exist after ZFC in $Ba_xSr_{2-x}Co_yZn_{2-y}Fe_{11+z}Al_{1-z}O_{22}$ Y-hexaferrites [61, 206]. To identify the one present in my samples at low temperatures, I measured magnetization curve along the c-axis at 10 K [Fig. 4.3(a)]. I observed a curve with a remarkable hysteresis up to $\approx 4\,\mathrm{T}$ similar to that observed by Shen *et al.* [195], indicating that the ALC structure is the ground state after ZFC. If the NLC structure were the ground state, the hysteresis would not extend to such a high magnetic field, since the NLC structure continuously transforms into the high-field collinear phase. A hysteresis coming from domain switching would be expected only at low fields, as it is the case of magnetization in the (001) plane (Fig. 4.3(e,f)). From the comparison of my magnetization curve and of the magnetic-field dependent permittivity [Fig. 4.3(a),(c)] with the work of Shen *et al.* [61], I can claim that

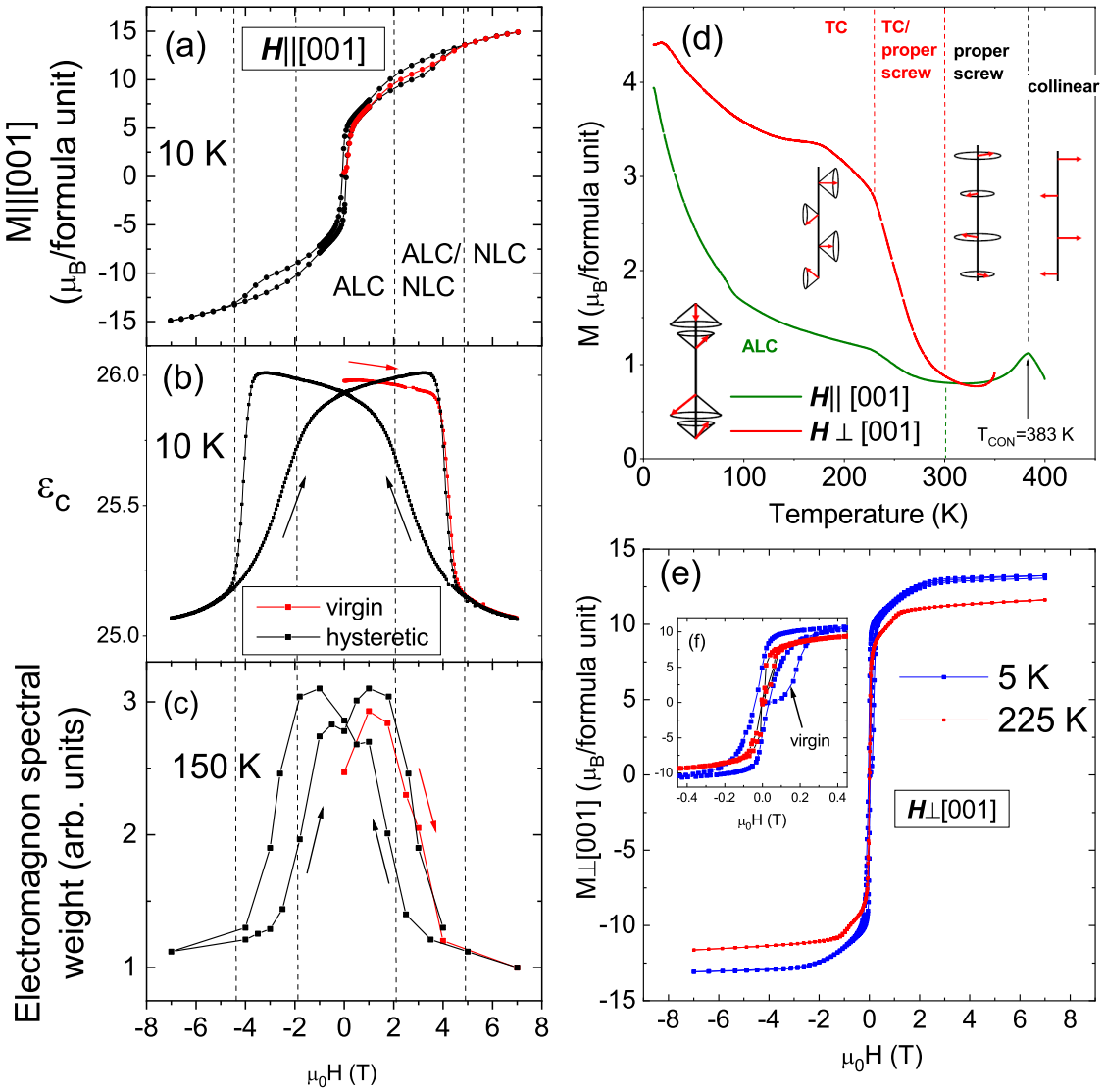

Figure 4.3: (a) Magnetization per formula unit, (b) permittivity at 1 kHz and (c) spectral weight of the electromagnon as a function of $\mu_0 \boldsymbol{H} \parallel c$ calculated from THz $k(\omega)$ spectra for Y-hexaferrite $BaSrCoZnFe_{11}AlO_{22}$. Red curves correspond to virgin magnetization curves after ZFC. Note that at $T = 10\,\mathrm{K}$ and $T = 150\,\mathrm{K}$ the phase diagram is qualitatively the same, therefore, I can compare both measurements. (d) Temperature dependence of magnetization measured on heating at $\mu_0 \boldsymbol{H} = 0.02\,\mathrm{T}$ after poling at 7 T at the lowest temperature. The magnetic field was applied $\parallel c$ and $\perp c$ directions. (e) Magnetization curve for $\boldsymbol{H} \parallel [100]$. The inset (f) shows the detailed $M(H)$ dependence at low fields revealing the magnetization after leaving the virgin state reached by ZFC.

the ALC structure persists up to ≈ 4 T if coming from low-field region, and it recovers only when the field is decreased to ≈ 2 T. A similar behavior was observed at temperatures up to 200 K (not displayed - see Supplement of Ref. [180]), so I expect the ALC structure to exist in this temperature region at zero field after ZFC. At higher fields, the NLC structure appears, and it continuously transforms into the collinear ferrimagnetic structure with spins along the c-axis.

After applying $\boldsymbol{H}$ in the (001) plane, the TC structure is known to establish in $BaSrCoZnFe_{11}AlO_{22}$ [53]. I confirmed it by comparing the magnetization curve after application of the in-plane $\boldsymbol{H}$ with the virgin one – while the virgin in-plane magnetization curve grows slowly in the low-field region, indicating the ALC structure after ZFC, the hysteretic curve after $H_{\perp c} = 7$ T field treatment grows rapidly, indicating stabilization of the TC structure [Fig. 4.3(f)]. These results are consistent with those reported in Ref. [195], and their interpretation is intuitive: If the ALC structure is established in zero magnetic field and in-plane magnetic field is applied, the spin cone axes rotate to the (001) plane, by which they have to overcome anisotropy barrier, which explains slow increase of the virgin curve. Once the TC structure is established, spin cones can freely rotate in the magnetically isotropic (001) plane, which is manifested by high susceptibility of the hysteretic curve. At 0.3 T, the virgin curve coincides with the hysteretic one, which is then the field sufficient to establish the TC structure at 5 K.

4.3.2 Electromagnon in zero field cooling

I measured polarized THz transmittance of $BaSrCoZnFe_{11}AlO_{22}$ (001)- and (100)-oriented crystal plates, providing a complete set of spectra at temperatures from room temperature down to 8 K. In the spectral window given by the THz spectrometer, I observed an excitation present exclusively in the $\boldsymbol{E}^{\omega} \parallel c$ polarization (Fig. 4.4(a,b)), implying it is purely electric-dipole active. If it were magnetically active, it would be present also in the $\boldsymbol{E}^{\omega} \perp c$, $\boldsymbol{H}^{\omega} \perp c$ polarized spectra; however, THz spectra in other polarizations show no remarkable features (not displayed). This polar excitation is relatively weak and overdamped at room temperature, whereas on cooling, its damping decreases and its frequency and intensity rise. As I show below, this excitation strongly depends on magnetic field, therefore, it has a magnetic origin. Consequently, this is an electromagnon, similar to that observed in $Ba_2Mg_2Fe_{12}O_{22}$ [204–206, 212], $BaSrCo_2Fe_{11}AlO_{22}$ and $Ba_{0.5}Sr_{1.5}Cu_2Fe_{11}AlO_{22}$ [207]. In contrast to $Ba_2Mg_2Fe_{12}O_{22}$, where the electromagnon was revealed below ≈ 100 K [204, 205], I observed the corresponding absorption up to 300 K. Upon heating, the ALC structure gradually transforms to the proper-screw one, while its strength gradually decreases. With further temperature increase, the angles in between spins within the helical phase become gradually smaller, and at 383 K, the magnetic structure changes from the proper-screw to the collinear one, where the electromagnon is forbidden by symmetry. Therefore, decrease of the electromagnon strength towards this temperature is expected, as well as frequency decrease.

Investigating the THz spectra in more detail, one can see a clear double-peak structure in the extinction coefficient $\kappa(\omega)$ [Fig. 4.4(b)] at 200 K. At higher temperatures, the peaks are also asymmetric. Below 200 K, the transmission signal around the peak in $\kappa(\omega)$ is low

which prevents from reliably determining the peak shape. [1] The double-peak structure at higher temperatures does not imply the same feature at lower temperatures—it may mean a mixture of magnetic phases, while at low temperatures, only pure ALC (or NLC) phases were reported in a part of $Ba_xSr_{2-x}Zn_yCo_{2-y}Fe_{11+z}Al_{1-z}O_{22}$ hexaferrites [61, 189]. From Raman spectra [see Fig. 4.4(c)], I deduce that the double peak structure persists down to low temperatures, and one can then see two electromagnon modes with similar frequencies in the pure ALC phase.

To get a complete knowledge about activity of the electromagnon in various spectra, I measured temperature-dependent polarized Raman spectra [Fig. 4.4(c–f)]. In the $a(cc)\overline{a}$-polarized spectra [Fig. 4.4(c–d)], one can clearly see the same electromagnon as in the THz spectra [Fig. 4.4(a–b)]. The presence of the electromagnon in both THz and Raman spectra is a signature of broken inversion symmetry due to the mutual exclusion principle, mentioned in Subsec. 2.3.3. Since the parent paramagnetic structure is centrosymmetric, the inversion symmetry must be broken by the magnetic structure. The collinear ferrimagnetic structure preserves the inversion symmetry, but any helical ordering breaks it; therefore, mutual presence of the electromagnon in both THz and Raman spectra below T_{con}=383 K is expected.

To get more deeper insight into the selection rules of the $\boldsymbol{E}^{\omega} \| c$-active electromagnon in various Raman spectra, my supervisor Stanislav Kamba performed the factor-group analysis. In the parent paramagnetic centrosymmetric space group $D^5_{3d} - R\overline{3}m$, the factor-group analysis of Brillouin-zone-center vibrations reads [213]

$$\begin{aligned}\Gamma_{D^5_{3d}} &= 14A_{1g}(a^2+b^2,c^2) + 4A_{1u}(-) + 4A_{2g}(-) + \\ &+16A_{2u}(c) + 18E_g(a^2-b^2,ab,ac,bc) + 20E_u(a,b)\,,\end{aligned} \tag{4.1}$$

representing the mutual exclusion principle of IR-active and Raman-active modes. Now the question is what symmetry lowering I should take into account when analyzing selection rules of the electromagnon. Heliconical noncoplanar magnetic structures may lower the symmetry drastically, thus making the analysis too trivial. Therefore, here I assume only some symmetry lowering. Specifically, the low-temperature ALC structure with the ↑-↑-↓-↓ spin configuration along the c axis induces electric polarization $\boldsymbol{P} \| c$ in a low-field region, including $\boldsymbol{H} = 0$ where this structure exists [61]. Therefore, I assume only the symmetry breaking induced by $\boldsymbol{P} \| c$, resulting in C_{3v} point group, and the factor-group analysis of phonons reads

$$\Gamma_{C_{3v}} = 30A_1(c, a^2+b^2, c^2) + 8A_2(-) + 38E(a,b,a^2-b^2,ab,ac,bc)\,. \tag{4.2}$$

In this phase, polar phonons and electromagnons have the same A_1 symmetry and they are active in both $\boldsymbol{E}^{\omega} \| c$-polarized IR or THz spectra and c^2 and a^2 (or b^2) Raman spectra, consistently with my experiments [see Figs. 4.4(d,e,f)].

Note that mutual observation of electromagnons in IR and Raman spectra was also shown for multiferroic $BiFeO_3$ [214]. Nevertheless, in Raman spectra of $BiFeO_3$, electromagnons are much weaker than phonons [215], while in Y-type hexaferrite the electromagnon is stronger than any phonon [Fig.4.4(f)]. It can be explained by the different

[1] In principle, I could have made the sample thinner and resolve the spectra with high absorption. However, I possess just one exemplar of the crystal and plan other measurements with it, so I decided to keep the crystal as a whole.

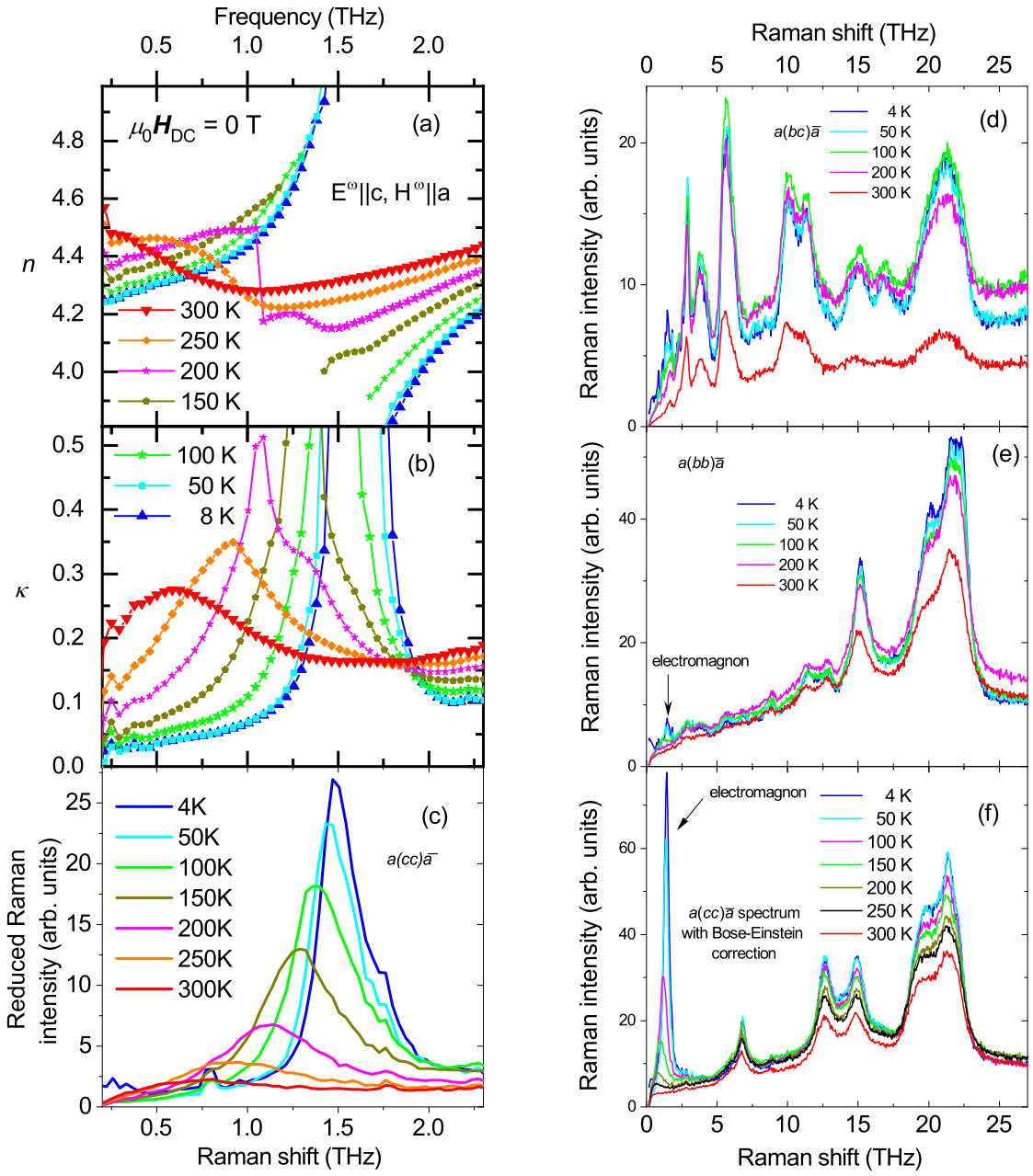

Figure 4.4: Temperature dependent THz spectra of (a) real and (b) imaginary part of the refractive index in $\boldsymbol{E}^{\omega} \| c$, $\boldsymbol{H}^{\omega} \| a$ polarization. Below 200 K, the parts of the spectra exhibiting high absorption due to the electromagnon are missing. (c) Temperature dependence of $a(cc)\bar{a}$ Raman spectra with focus on the electromagnon. Temperature dependence of (d) $a(bc)\bar{a}$ (e) $a(bb)\bar{a}$ and $a(cc)\bar{a}$ Raman spectra.

mechanism of their activation: Electromagnons in $BiFeO_3$ are induced by the iDM interaction, which originates in the SOC which is a weak effect [216, 217]. In contrast, the electromagnon in my sample is activated by exchange-striction and this spin-lattice coupling can give a stronger polarization.

Analyzing the intensity of the modes in Raman spectra is a difficult task. It reflects polarizability of the lattice at the laser frequency, changing upon the mode vibration.

Definitely, the high intensity of the electromagnon mode in $a(cc)\overline{a}$-polarized Raman spectra must come from the ionic motion and resulting lattice distortion, since magnetic-dipole-active modes are usually very weak in Raman spectra [218]. I speculate that it comes from the extremely high susceptibility of the frustrated magnetic structures, allowing large polarizability modulation upon the electromagnon excitation. The off-diagonal polarizability elements are supposed to be much smaller than diagonal ones, which explains lower intensity of the electromagnon in $a(bb)\overline{a}$-polarized Raman spectra [see Fig. 4.4(e)].

4.3.3 Evolution of the electromagnon upon $\boldsymbol{H} \perp c$

Below 270 K, I measured polarized THz spectra in external static magnetic field $\boldsymbol{H} \perp c$, which stabilizes the TC structure below $\approx$ 230 K. The magnetic-field dependence is qualitatively the same within the whole temperature range; below I discuss the spectra measured in Voigt geometry in order to avoid the Faraday effect, carried out at 150 K where the transmission at the peak position is still above the noise level [Fig. 4.5(a,)]. The strength of the electromagnon gradually decreases with increasing $\boldsymbol{H}$, becoming small above 2 T and negligible above 4 T. This corresponds to the continuous phase transition into the collinear ferrimagnetic structure and it is consistent with the assumption that the electromagnon is induced by the exchange striction in the ALC and TC magnetic structures. In the high-field collinear phase, the fluctuations $\delta\boldsymbol{S}_i$ are perpendicular to all $\boldsymbol{S}_j$, and their scalar products are then practically zero; thus the electromagnon vanishes.

Further, one can see a low-frequency resonance which appears at 4 T at $\approx$ 0.2 THz and whose frequency increases linearly with the magnetic field with a slope of ca. 0.05 THz/T. Such ferromagnetic-like resonance is expected, since $\boldsymbol{H} \perp c$ breaks the SU(2) symmetry of the magnetically isotropic (001) plane, thus the corresponding Goldstone mode becomes gapped. Nevertheless, its slope is much higher than the gyromagnetic ratio for a free electron, $\gamma_0 = 0.028$ THz/T, and its value is not a multiple of γ_0, so the resonance is not likely to be due to a multiple-magnon state. Note that in my Voigt-geometry experiment [Fig. 4.5(a,b)], I have $\boldsymbol{H}^\omega \parallel \boldsymbol{H}$, while ferromagnetic resonances should be absent when the oscillating magnetic field $\boldsymbol{H}^\omega$ is parallel to the spin direction. This can be a signature that spins are not collinear with the magnetic field direction, which is the case of low fields. Nevertheless, strength of the excitation does not decrease with increasing field and it is present even at 7 T, for which spins are supposed to be almost collinear with the magnetic field. This can mean that the assumption of spins collinearly aligned with the magnetic field is not valid, or, alternatively that decrease of magnetic-dipole strength of this ferromagnetic-like resonance is compensated by its electric-dipole strength increase. Note that for the Faraday geometry with $\boldsymbol{H} \perp c$, in which $\boldsymbol{H}^\omega \perp \boldsymbol{H}$, this resonance was approximately two-times stronger as expected for the ferromagnetic resonance, confirming the dominance of the magnetic-dipole strength (not displayed).

In the other light polarization, $\boldsymbol{E}^\omega \parallel a$, $\boldsymbol{H}^\omega \parallel c$, I observed a resonance with frequency linearly increasing with $\boldsymbol{H} \perp c$ (in the Voigt setup) with a slope 0.031 THz/T, which is close to γ_0 (not displayed). This resonance is similarly strong as the resonance in Faraday setup, while in both of these experiments $\boldsymbol{H}^\omega \perp \boldsymbol{H}$. Altogether, one can see two distinct ferromagnetic-like resonances for different light polarizations, which may be due to different crystallographic positions of iron ions, possessing different gyromagnetic

ratios.

4.3.4 Evolution of the electromagnon upon $\boldsymbol{H} \| c$

I also measured THz spectra when applying $\boldsymbol{H} \| c$. Similarly to applying $\boldsymbol{H} \perp c$, I observed a suppression of the electromagnon intensity; this occurs at magnetic field values of ca. 2 T [see Fig. 4.5(c,d)]. Furthermore, I also notice a hysteresis of the electromagnon intensity, closely related to that of the magnetization, as also seen in Fig. 4.5(c,d). To better represent the hysteresis, Fig. 4.3(c) shows the magnetic-field dependence of the electromagnon strength [here defined as the integral of $\kappa(\omega)$ over the frequency range of the peak] for $\boldsymbol{H} \| c$ at 150 K. The strength decreases the most at the transition from the ALC to the NLC magnetic structure, and the electromagnon is absent in the saturated state, where the spins are assumed to align collinearly along c-direction.

As electromagnons are electric-dipole active, they contribute to the static dielectric susceptibility according to a general sum rule (Eq. 1.38), thus to the permittivity. When the electromagnon is suppressed by the magnetic field, the static permittivity should decrease correspondingly. To verify this, I measured magnetic-field-dependent low-frequency (1 kHz) dielectric permittivity in the c-direction, ε_{cc}, since the electromagnon is active for $\boldsymbol{E}^{\omega} \| c$. In Fig. 4.3(b), one can see the expected decrease in the permittivity at the phase transition from the ALC to the NLC structure upon $\boldsymbol{H} \| c$ when the electromagnon is suppressed. To evaluate this sum rule quantitatively, I fitted the THz spectra by the Lorentz oscillator model. At zero field, the contribution of the electromagnon to the permittivity is 1.4. Assuming its contribution at 7 T to be zero (verified by the fit), one should expect the same step in the static permittivity; I observed a step of ≈ 1 [Fig. 4.3(b)] which is in a rough agreement. The mismatch may come from the conductivity contribution to the permittivity and/or from errors in the size and distance of electrodes of the measured capacitor.

Unfortunately, in Fig. 4.3(b,c), I could not compare the magnetic-field dependent permittivity with the electromagnon spectral weight at the same temperature, because the sample was leaky at 150 K and the electromagnon absorption was too high at 10 K (note that I was not able to determine the peak maximum in the κ spectrum, because the sample becomes opaque in this frequency range—see Fig. 4.4(b). For that reason, the field dependencies of the permittivity and of the spectral weight are only qualitatively the same.

When applying $\boldsymbol{H} \parallel c$ of 7 T, one can see a peak in spectra of κ at ≈ 0.25 THz, not present at low magnetic fields [see Fig. 4.5(d)]. This is again a ferromagnetic-like resonance, similarly as the one appearing upon $\boldsymbol{H} \perp c$, which is consistent with $\boldsymbol{H}^{\omega} \perp \boldsymbol{H}$. The field $\boldsymbol{H} \| c$ leaves the (001) plane isotropic, thus not gapping the Goldstone mode, which should then stay at low frequencies. Nevertheless, the anisotropy is not strictly easy-plane and the observed resonance may represent rather a local resonance of a single spin. I cannot evaluate the field dependence of its frequency, but when assuming frequency close to zero at zero magnetic field, its gyromagnetic ratio is very similar to that of a free electron.

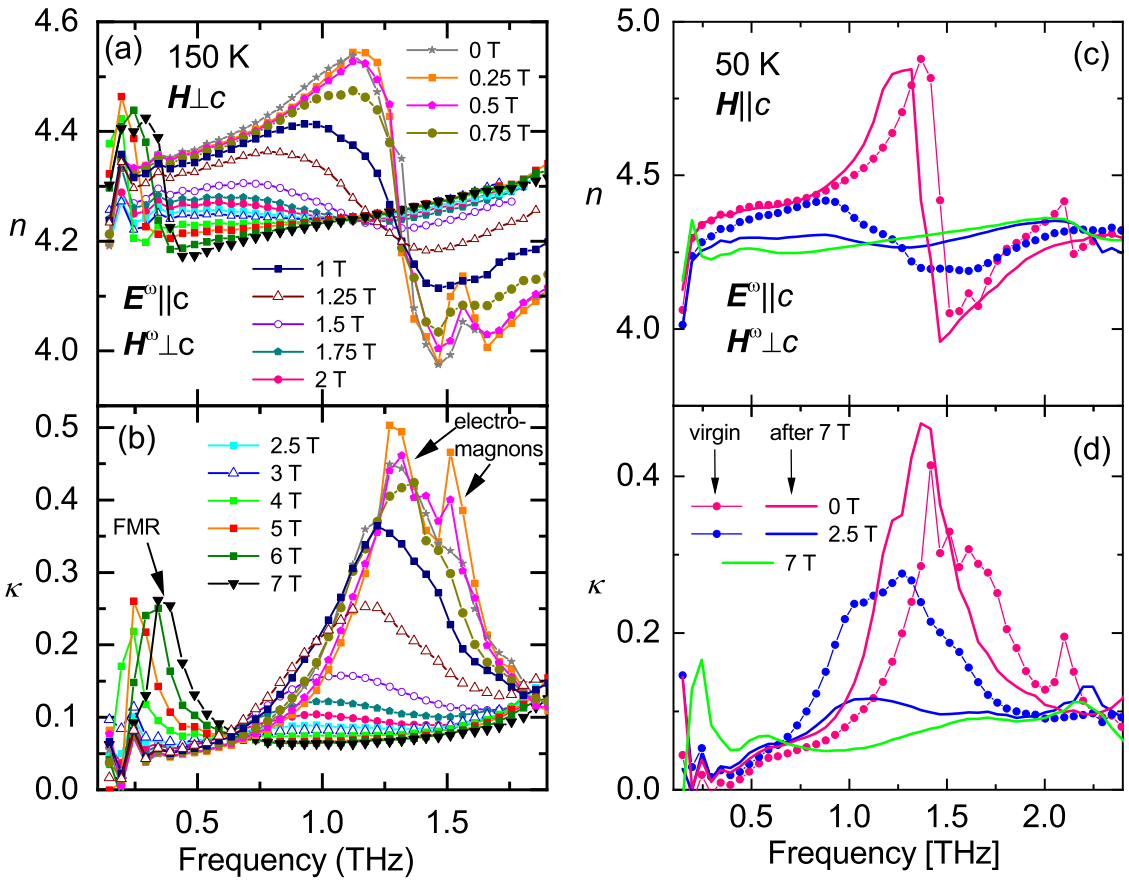

Figure 4.5: THz spectra of (a) real and (b) imaginary part of refractive index as a function of external magnetic field $\boldsymbol{H} \parallel a$ at 150 K in $\boldsymbol{E}^{\omega} \parallel c$, $\boldsymbol{H}^{\omega} \parallel a$-polarized THz spectra. All spectra were taken after applying high magnetic field, therefore, the TC magnetic structure is assumed at low $\boldsymbol{H}$. (c,d) $\boldsymbol{E}^{\omega} \parallel c$, $\boldsymbol{H}^{\omega} \parallel a$-polarized THz spectra of (a) real and (b) imaginary parts of refractive index measured at $\mu_0 H = 0$ and 2.5 T, before and after applying a magnetic field of 7 T along [001]. The spectra were measured at 50 K and their shapes strongly depends on the magnetic-field history. The spectrum at 7 T is also shown, exhibiting low-frequency ferromagnetic-like resonance at ≈ 0.25 THz

4.3.5 Microscopic origin of the electromagnon

I experimentally investigated the electromagnon activity in all principal directions of the DC magnetic field with respect to the crystallographic axes. I observed the electromagnon in the TC, ALC and possible proper-screw magnetic structures, but not in the NLC and collinear ones (with spins in the (001) plane or along the c-axis). Such a comprehensive information enables me to apply, to my observations, the exchange-striction theory describing electromagnons in related Y-type hexaferrites [192, 204–206, 219].

Since the (001) plane is magnetically isotropic, for describing magnetic states, I can employ an orthogonal basis instead of the hexagonal one; I assume axes x, y, z in the new orthogonal basis coinciding with directions [100], [120], [001] in the hexagonal system. My task now is to employ the exchange-striction mechanism possibly inducing the electromagnon to all existing magnetic structures, and to compare the analytically calculated selection rules with the experiment.

The polarization induced by spins according to the exchange-striction model (Eq. 1.29) reads as

$$\boldsymbol{P} = \sum_{i,j} \boldsymbol{P}^{es}_{i,j}(\boldsymbol{S}_i \cdot \boldsymbol{S}_j), \tag{4.3}$$

where the summation involves the nearest neighbors and goes over a magnetic unit cell. Since only noncollinearly aligned spins contribute to the oscillating polarization via the exchange-striction mechanism, the spin-block approximation is justified: Even though exchange interactions within the collinearly aligned spins in individual blocks may be violated upon electromagnon's excitation, the collinearly aligned spins cannot contribute to the polarization induced by the exchange striction. In this sense, violation of weak superexchange interaction on boundaries of the blocks plays the most important role for the strength of electromagnons. The spin-block approximation verifies the nearest neighbor approach as well, as the next nearest neighbors are far apart from each other, and large spins can be also treated classically.

The prefactor $\boldsymbol{P}^{es}_{i,j}$ must respect the crystal symmetry [44, 56]. Taking the Y-hexaferrite crystal structure and the magnetic structure in the spin-block approximation, the polarization along the z axis has the following form [61, 192, 206]:

$$P_z \propto \sum_{i=1,2} (\boldsymbol{S}^L_i \cdot \boldsymbol{S}^S_i - \boldsymbol{S}^S_i \cdot \boldsymbol{S}^L_{i+1}). \tag{4.4}$$

The alternating signs are because of inversion centers at spins [61].[2] For the dynamic ME effect, I assume all spins in Eq. 4.4 as time-dependent, resulting in a time-dependent polarization $P_z(t)$, while the formula can be used for static ME effect as well [61]. More specifically, I formally separate the static equilibrium spins known from the magnetic structure, and the dynamical spin deviations, $\delta\boldsymbol{S}_i$. I assume the spin deviations to be small and perpendicular to the equilibrium spin direction, as the spin lengths must be conserved. As I am interested only in the dynamic ME effect, I omit the scalar products of static spins and take into account only the first-order dynamic terms of type $\boldsymbol{S}_1 \cdot \delta\boldsymbol{S}_2$, since

[2] The same formula holds for Z-hexaferrite crystal structure, as pointed out later: Even though large spins are not at the inversion centers but at (001) symmetry planes, action of both operations on polar vector $\boldsymbol{P}^{es}_{i,j}$ along the z axis is the same.

the second-order terms of type $\delta\boldsymbol{S}_1 \cdot \delta\boldsymbol{S}_2$ are assumed to be small. Next, I separate the contributions to P_z coming from x, y and z components of spins' deviations, which will allow me to determine which spin oscillations may be responsible for the activation of magnons in $\boldsymbol{E}^{\omega} \| c$ spectra. Although using Cartesian coordinates may not be the best for some magnetic structures, using same coordinates for all magnetic structures allows to compare selection rules among various magnetic structures.

I now look for possible spin deviations which can sum up constructively to the oscillating $P_z(t)$ in various spin structures. Among the TC structures, I take the one called 2-fan, described as [192, 220]

$$\boldsymbol{S}_1^S = \begin{pmatrix} 0 \\ -S^S \cos(\theta^S) \\ S^S \sin(\theta^S) \end{pmatrix}, \quad \mathrm{S}_1^{\mathrm{L}} = \begin{pmatrix} S^L \sin(\theta^L) \\ S^L \cos(\theta^L) \\ 0 \end{pmatrix},$$

$$\boldsymbol{S}_2^S = \begin{pmatrix} 0 \\ -S^S \cos(\theta^S) \\ -S^S \sin(\theta^S) \end{pmatrix}, \quad \mathrm{S}_2^{\mathrm{L}} = \begin{pmatrix} -S^L \sin(\theta^L) \\ S^L \cos(\theta^L) \\ 0 \end{pmatrix}$$

where θ^L and θ^S denote the conical angles in the large and small blocks, respectively, taken from the y-axis [i.e. the cone axis, see Fig. 4.2(g)].

For the LC structures, the situation is more complex, since there is also an incommensurate component, so the magnetic unit cell can be in principle infinitely large. Nevertheless, it is always possible to choose some commensurate component to work with finite-size magnetic unit cell. The length of the incommensurate modulation vector $\boldsymbol{Q}_{\mathrm{IC}}$ depends on temperature and it reaches a value of ca. $0.7\,c^*$ (c^* being inverse of the c-axis lattice constant) below 150 K [221]. For simplicity, I use the approximate value of $0.75\,c^*$ which is commensurate; then, the magnetic unit cell is only doubled compared to the TC structure, and contains 8 spins.

For a general ALC structure with ↑-↑-↓-↓ z-spin-component configuration, the spin structure is the following [192]:

$$\boldsymbol{S}_1^S = \begin{pmatrix} S^S \sin(\theta^S)\cos(\phi) \\ S^S \sin(\theta^S)\sin(\phi) \\ S^S \cos(\theta^S) \end{pmatrix}, \quad \mathrm{S}_1^{\mathrm{L}} = \begin{pmatrix} 0 \\ -S^L \sin(\theta^L) \\ S^L \cos(\theta^L) \end{pmatrix},$$

$$\boldsymbol{S}_2^S = \begin{pmatrix} -S^S \sin(\theta^S)\cos(\phi) \\ S^S \sin(\theta^S)\sin(\phi) \\ -S^S \cos(\theta^S) \end{pmatrix}, \quad \mathrm{S}_2^{\mathrm{L}} = \begin{pmatrix} S^L \sin(\theta^L) \\ 0 \\ -S^L \cos(\theta^L) \end{pmatrix},$$

$$\boldsymbol{S}_3^S = \begin{pmatrix} -S^S \sin(\theta^S)\cos(\phi) \\ -S^S \sin(\theta^S)\sin(\phi) \\ S^S \cos(\theta^S) \end{pmatrix}, \quad \mathrm{S}_3^{\mathrm{L}} = \begin{pmatrix} 0 \\ S^L \sin(\theta^L) \\ S^L \cos(\theta^L) \end{pmatrix},$$

$$\boldsymbol{S}_4^S = \begin{pmatrix} S^S \sin(\theta^S)\cos(\phi) \\ -S^S \sin(\theta^S)\sin(\phi) \\ -S^S \cos(\theta^S) \end{pmatrix}, \quad \mathrm{S}_4^{\mathrm{L}} = \begin{pmatrix} -S^L \sin(\theta^L) \\ 0 \\ -S^L \cos(\theta^L) \end{pmatrix},$$

and for the NLC structure:

$$\boldsymbol{S}_1^S = \begin{pmatrix} S^S \sin(\theta^S)\cos(\phi) \\ S^S \sin(\theta^S)\sin(\phi) \\ S^S \cos(\theta^S) \end{pmatrix}, \quad \mathrm{S}_1^{\mathrm{L}} = \begin{pmatrix} 0 \\ -S^L \sin(\theta^L) \\ -S^L \cos(\theta^L) \end{pmatrix},$$

$$\boldsymbol{S}_2^S = \begin{pmatrix} -S^S \sin(\theta^S)\cos(\phi) \\ S^S \sin(\theta^S)\sin(\phi) \\ S^S \cos(\theta^S) \end{pmatrix}, \quad \mathrm{S}_2^{\mathrm{L}} = \begin{pmatrix} S^L \sin(\theta^L) \\ 0 \\ -S^L \cos(\theta^L) \end{pmatrix},$$

$$\boldsymbol{S}_3^S = \begin{pmatrix} -S^S \sin(\theta^S)\cos(\phi) \\ -S^S \sin(\theta^S)\sin(\phi) \\ S^S \cos(\theta^S) \end{pmatrix}, \quad \mathrm{S}_3^{\mathrm{L}} = \begin{pmatrix} 0 \\ S^L \sin(\theta^L) \\ -S^L \cos(\theta^L) \end{pmatrix},$$

$$\boldsymbol{S}_4^S = \begin{pmatrix} S^S \sin(\theta^S)\cos(\phi) \\ -S^S \sin(\theta^S)\sin(\phi) \\ S^S \cos(\theta^S) \end{pmatrix}, \quad \mathrm{S}_4^{\mathrm{L}} = \begin{pmatrix} -S^L \sin(\theta^L) \\ 0 \\ -S^L \cos(\theta^L) \end{pmatrix}.$$

In both cases, the helical angle $\phi = 45^\circ$ for $\boldsymbol{Q}_{\mathrm{IC}} = (0, 0, 0.75)$, and the relative phase of small and large spin modulations is 180°.

In the ALC structure, small spins were once reported to be lying in the (001) plane [192], thus exhibiting ↑-0-↓-0 z-spin-component configuration, which can be derived by setting $\theta^S = 90^\circ$ for the ALC structure – both possible ALC structures are taken into account. The proper-screw structure can be derived by setting $\theta^S = 90^\circ$ and $\theta^L = 90^\circ$, in either the ALC or NLC structure. However, the proper-screw structure appears at high temperatures for which $\boldsymbol{Q}_{\mathrm{IC}}$ is much larger than (0,0,0.75) as the spin structure is approaching the collinear one. Therefore, the electromagnon is supposed to weaken with temperature increase, as confirmed by the experiment [see Fig. 4.4(a,b)].

Since the electromagnon is not magnetic-dipole active, I took only the modes in which $\delta\boldsymbol{S}_1^S$ is opposite to $\delta\boldsymbol{S}_2^S$, and $\delta\boldsymbol{S}_1^L$ is opposite to $\delta\boldsymbol{S}_2^L$, as in Ref. [192]. Upon such spin deviations, the exchange interaction are violated, thus these mode are AFMRs which are expected to appear at frequencies ∼1–2 THz. Therefore the model does not capture low-frequency ferromagnetic-like resonances, which are supposed to be magnetic-dipole active. It is important to stress that real spin deviations are unknown – they must be derived by determining normal modes from the spin Hamiltonian, which is difficult to determine. Here, I only derive which component of spin deviations contribute to $P_z(t)$ according to the exchange-striction model. Using the model, correlation of experimentally determined electromagnon strength and static magnetic structure may give a hint about the nature of the modes.

Calculated selection rules for the exchange-striction-induced electromagnon are in Tab. 4.2. For various magnetic structures, the first-order contribution to $P_z(t)$ is given in the second column, while contributions of spin deviations in x, y and z directions are separated in different rows for clarity. Note that this division does not at all correspond to the normal modes of the system: (i) the real modes may represent oscillations of spins in different than Cartesian directions, (ii) the modes are typically elliptical, and (iii) small and large spins generally deviate in different directions. Nevertheless, the ellipticity of the modes is typically high [208], and magnetic symmetry gives restrictions that the ellipticity axes must be along to magnetic anisotropy axes. Therefore, some features of the modes can be roughly guessed. In the third column of Tab. 4.2, I list possible distinct modes based on cited literature. The remaining terms, not presented in literature, may be contributing via additional modes. In fourth column, there are constraints for the cases when spin deviations, which must be perpendicular to spins, cannot be parallel

with the respective Cartesian coordinates. This is useful for quantitative analysis of electromagnons' strengths.

The criterion for finite $P_z(t)$ induced by the exchange striction is the appearance of oscillating ↑-↑-↓-↓ spin pattern of any of Cartesian spin components. Taking for example the 2-fan structure and spin components in the z-direction, the static magnetic structure is ↑-0-↓-0, leading to zero static P_z. However, if I add small spin deviations with ↑-↑-↓-↓ amplitudes, I can get oscillating P_z—this is exactly the so-called out-of-phase mode, proposed by Nakajima *et al.* for Y-hexaferrite $Ba_2Mg_2Fe_{12}AlO_{22}$ [206]. As the spins oscillate in the z-direction, I then call it z-mode [see Tab. 4.2]. In fact, only oscillations of large spins along z-direction contribute to the $P_z(t)$ in the first approximation, while small spins already have nonzero z-component in static limit. In other words, the first-order contribution is the static pattern of small spins ↑-0-↓-0, overlapping with the dynamic pattern of large spins 0-↓-0-↑.

Alternatively, ↑-↑-↓-↓ spin pattern in x-direction may appear upon deviations of small spins into x-direction, $(\delta S_i^S)_x$. If there is a normal mode, involving such deviations, this may give rise to an electromagnon appearing in $\boldsymbol{E}^\omega \| c$ spectra. Whether such a mode is an additional one beyond the z-mode is a question which cannot be answered without a microscopic spin model. Chun *et al.* developed a spin model for the 2-fan structure in Z-hexaferrite $Ba_{0.5}Sr_{2.5}Co_2Fe_{24}O_{41}$, and found that there is a highly elliptical mode, involving both $(\delta S_i^S)_x$ and $(\delta S_i^L)_z$ [208], which could be called xz-mode. This is just an illustration about possible modes, while I cannot guess anything for my case, since the spin model for Z-hexaferrite cannot be used for my Y-hexaferrite due to different exchange interaction paths. Nevertheless, I can conclude that for the 2-fan structure, one may expect up to two modes at maximum, involving $(\delta S_i^S)_x$ and $(\delta S_i^L)_z$ in the spin-block approximation. On the other hand, all oscillations in the y-direction (the cone axis) add up destructively, yielding no contribution to $P_z(t)$ [see Tab. 4.2].

The LC structures differ just in z-spin components in my model, while they may differ in the helical spin component as well. The ALC structure has either a ↑-↑-↓-↓ z-component spin structure yielding even static P_z (static P_z generally allows oscillating $P_z(t)$ by symmetry arguments) or a ↑-0-↓-0 structure with $P_z = 0$. Nevertheless, in both cases, adding ↑-↑-↓-↓ spin deviations in the z-direction can lead to oscillating $P_z(t)$ as in the case of the 2-fan structure via the z-mode. For the ↑-↑-↓-↓ ALC structure, both $(\delta S_i^S)_z$ and $(\delta S_i^L)_z$ are involved, thus up to two modes may contribute to $P_z(t)$, while for ↑-0-↓-0 ALC structure, only $(\delta S_i^S)_z$ is involved, thus only one mode in maximum contributes to $P_z(t)$. In contrast, in the NLC and proper-screw structures, z-spin components add up always destructively yielding no oscillating P_z, as demonstrated in Tab. 4.2.

For all LC and proper screw structures, the oscillations in x and y directions are equivalent due to magnetically isotropic (001) plane. (Magnetic isotropy of the (001) plane is justified by the incommensurate structures with helical ordering.) An electromagnon mode, involving oscillations of all spin in (001) plane only, was proposed by Nakajima *et al.* [192]; it corresponds to clockwise deviations of small spins and counter-clockwise deviations of large spins in x and y directions, and I call it here the xy-mode (see Tab. 4.2). This mode is allowed in all LC structures, but as the temperature rises, the incommensurate helical ordering approaches the collinear structure, thus this mode is supposed to weaken upon heating.

Altogether, there are up to three distinct modes contributing to the $P_z(t)$ in the ↑-↑-↓-↓

Table 4.2: Analytically calculated activity of electromagnons in $\boldsymbol{E}^{\omega} \| c$ spectra induced by the exchange-striction in the Y-type hexaferrite with various magnetic structures. S^L and S^S are the magnitudes of large and small spins, respectively; θ^L and θ^S are the conical angles taken from the conical axes (z in the case of the NLC and ALC structures and y in the TC structure, see Fig.4.2(d),(e),(g)); $(\delta S_1^S)_i$ and $(\delta S_1^L)_i$ denote spin deviations along $i = x, y, z$ for small and large spin blocks, respectively.

Magnetic structure	Oscillating polarization according to Eq. 4.4: $P_z(t) \propto$	Distinct modes	Constraints
TC (2-fan)	$4S^L \sin(\theta^L) \cdot (\delta S_1^S)_x$ $+0 \cdot (\delta S_1^S)_y$ $+4S^S \sin(\theta^S) \cdot (\delta S_1^L)_z$	mode containing $(\delta S_1^S)_x$ — z-mode [206]	
ALC ↑-↑-↓-↓	$2\sqrt{2}\left[S^L \sin(\theta^L) \cdot (\delta S_1^S)_x + S^S \sin(\theta^S) \cdot (\delta S_1^L)_x\right]$ $+2\sqrt{2}\left[S^L \sin(\theta^L) \cdot (\delta S_1^S)_y + S^S \sin(\theta^S) \cdot (\delta S_1^L)_y\right]$ $+4S^L \cos(\theta^L) \cdot (\delta S_1^S)_z + 4S^S \cos(\theta^S) \cdot (\delta S_1^L)_z$	xy-mode [192] mode(s) containing $(\delta S_1^S)_z$, $(\delta S_1^L)_z$	$(\delta S_1^S)_z \propto \cdot \sin(\theta^S)$, $(\delta S_1^L)_z \propto \cdot \sin(\theta^L)$
ALC ↑-0-↓-0	$2\sqrt{2}\left[S^L \sin(\theta^L) \cdot (\delta S_1^S)_x + S^S \cdot (\delta S_1^L)_x\right]$ $+2\sqrt{2}\left[S^L \sin(\theta^L) \cdot (\delta S_1^S)_y + S^S \cdot (\delta S_1^L)_y\right]$ $+4S^L \cos(\theta^L) \cdot (\delta S_1^S)_z$	xy-mode [192] mode containing $(\delta S_1^S)_z$	$(\delta S_1^S)_z \propto \sin(\theta^L)$
NLC	$2\sqrt{2}\left[S^L \sin(\theta^L) \cdot (\delta S_1^S)_x + S^S \sin(\theta^S) \cdot (\delta S_1^L)_x\right]$ $+2\sqrt{2}\left[S^L \sin(\theta^L) \cdot (\delta S_1^S)_y + S^S \sin(\theta^S) \cdot (\delta S_1^L)_y\right]$ $+0 \cdot (\delta S_1^S)_z + 0 \cdot (\delta S_1^L)_z$	xy-mode [192] —	
proper-screw	$2\sqrt{2}\left[S^L \cdot (\delta S_1^S)_x + S^S \cdot (\delta S_1^L)_x\right]$ $+2\sqrt{2}\left[S^L \cdot (\delta S_1^S)_y + S^S \cdot (\delta S_1^L)_y\right]$ $+0 \cdot (\delta S_1^S)_z + 0 \cdot (\delta S_1^L)_z$	xy-mode [192] —	
collinear	0	—	

ALC structure, up to two modes in 2-fan structure and ↑-0-↓-0 ALC structure, up to one mode in the NLC and proper-screw structures, and no mode in the collinear structures according to my analytical calculations, as summarized in Tab. 4.2.

How is this qualitative finding consistent with my experimental results? Upon cooling in zero magnetic field, the crystal is supposed to be in the ALC structure below $\sim$300 K, while I observed a doublet [see Fig. 4.4(b,c)], which is consistent with prediction of up to two or three modes in the ALC structure. One can see a more clear doublet upon $\boldsymbol{H} \perp c$ i.e. in the 2-fan structure [see Fig. 4.5(a,b)], again consistent with prediction of up to two modes. When $\boldsymbol{H} \| c$, one can see a drastic disappearance of the electromagnon intensity upon ALC-to-NLC phase transition [see Fig. 4.3(c)]. This suggests that spin deviations along z-direction, leading to an electromagnon in the ALC but not in the NLC structure, may be relevant for the electromagnon excitation. Nevertheless, it is also possible that upon the ALC-to-NLC phase transition, helical angle changes drastically, which may be responsible for switching-off the electric-dipole activity of the mode involving spin deviations in the x and y directions. Thus, the strong absorption in the ALC structure could be due to the xy-mode, which was proposed by Nakajima *et al.* [206] for the related Y-hexaferrite $BaSrCo_2Fe_{11}AlO_{22}$, and confirmed by inelastic neutron scattering.

The discussion above was qualitative with aim of determining number of electromagnon modes. Let me now dive deeply into quantitative discussion of electromagnons' strength. As the spin deviations are perpendicular to the original spin directions, there are additional constraints (last column in Tab. 4.2), providing an insight into the dependence of the oscillating polarization on conical angles entering into the formulas for the polarization (second column in Tab. 4.2). Due to high-symmetry or cancellation of polarization, these apply only for the case of z-mode in the ALC structure, for which additional constraints yield nontrivial dependencies of the oscillating polarization on the conical angle: $P_z(t) \propto \cos(\theta^L) \sin(\theta^S) + \cos(\theta^S) \sin(\theta^L)$, which, for $\theta^L = \theta^S = \theta$, becomes $P_z \propto \sin(2\theta)$, providing the maximum value of electromagnon absorption at an angle of $\theta = 45^\circ$. Such

a nontrivial dependence can be the reason why the electromagnon strength first increases with magnetic field and starts decreasing only at ≈ 1 T [Fig. 4.3(c)].

For the 2-fan structure, the predicted dependence of the electromagnon strength on the conical angle is monotonic, $P_z \propto \sin(\theta^L)$ for $(\delta S_i^S)_x$ deviations and $P_z \propto \sin(\theta^S)$ for $(\delta S_i^L)_z$ deviations. In the experiment, one can see some discrepancy from this behavior: First, the intensity of the electromagnon increases with increasing $\boldsymbol{H}$ ($\perp c$), reaching a maximum at 0.25 T; only then it starts decreasing [Fig. 4.5(a,b)]. Notice that when reaching $\mu_0 H \approx 0.25$ T, a single-domain 2-fan structure is established. It is worth noting that in $BaSrCo_2Fe_{11}AlO_{22}$, at similar fields, Nakajima *et al.* observed a maximum in the neutron diffraction intensity[192] which was not completely explained either. My observation can have three explanations: First, zero-field magnetic structure was not single-phase TC. Second, the single domain state provides a constructive interference of polarization in the material and that of the EM wave. Third, going beyond the block approximation and assuming spin directions varying within the blocks, the exchange striction term may depend differently on the spin configuration. This would cause the highest absorption to occur at an angle between 0° and 90°, as proposed by Kida *et al.* for the TC structure in Y-hexaferrite $Ba_2Mg_2Fe_{12}O_{22}$ [205].

Let me yet comment on the high-frequency part of the doublet in the 2-fan structure, i.e. the narrow peak at ~1.5 THz in Fig. 4.5(b), seen in the range from 0 T to 0.75 T and observed the most clearly at 0.25 T. This feature is not seen in the ZFC spectra plotted in Fig. 4.4(a,b), and it is weak at zero field at 150 K, where the ALC structure can be present beyond the 2-fan structure. Since it abruptly appears when 0.25 T is applied, whereby stabilizing the 2-fan state, it should be connected with the 2-fan state, but not with the ALC one. Note that it disappears below 1 T, i.e. at much lower fields than the main, broad peak. This may be connected to different conical angle dependence for small and large spins: One mode possibly involves deviations $(\delta S_i^S)_x$, thus its strength is proportional to $\sin(\theta^L)$, while the other mode involving $(\delta S_i^L)_z$ is proportional to $\sin(\theta^S)$. Nevertheless, these are just speculations, while these features may be related to the physics beyond the model.

In summary, I listed spin deviations, which may contribute to the $\boldsymbol{E}^\omega \parallel c$ spectra via the exchange-striction mechanism for various magnetic structures (Tab. 4.2). These give qualitative hint on number of $\boldsymbol{E}^\omega \parallel c$-active electromagnon modes, and quantitatively predict strength of the mode depending on the magnetic structure. Nevertheless, there are several limitations of my approach: First, I do not know how the actual magnon modes are, due to the lack of the spin Hamiltonian. Next, I used the spin-block approximation using effective large spins, while internal spin structure may play a role as well. The model assumes only purely electric-dipole-active modes to explain $\boldsymbol{E}^\omega \parallel c$-active excitations, thus ferromagnetic-like resonances appearing at low frequencies are not captured by the model.

4.3.6 Conclusions for Y-hexaferrite $BaSrCoZnFe_{11}AlO_{22}$

In conclusion, I investigated experimentally static and dynamic magnetoelectric properties of the Y-type hexaferrite $BaSrCoZnFe_{11}AlO_{22}$. Its magnetic structures were determined by static magnetization measurements, and a purely electric-dipole-active electromagnon was observed by THz and Raman spectroscopies. The Raman intensity of the electromagnon was unusually high. I suggest that this is due to an anomalously high susceptibility

of frustrated magnetic structure, but this hypothesis would require deeper theoretical clarification.

I also studied in detail the properties of the electromagnon in various magnetic phases determined by the magnetic-field direction and history. Using the exchange-striction model, it was possible to identify the origin of the electromagnon to explain its magnetic-field dependence and to correlate the electromagnon strength with the static magneto-dielectric properties.

Using the model, I described the dominant features in the field dependence of the spectra, but some minor ones remain unexplained. In order to gain an even deeper insight into the observed behavior, microscopic theory using a spin model is required.

4.4 Results on Z-hexaferrites $(Ba_xSr_{1-x})_3Co_2Fe_{24}O_{41}$

Growing of single crystals is much more difficult task than producing hexaferrite ceramics. Single crystals of hexaferrites are typically small, and they naturally grow as plates parallel to (001) plane. Therefore, I disposed only a (001)-plane-oriented single crystal of $(Ba_{0.5}Sr_{0.5})_3Co_2Fe_{24}O_{41}$ and dense $(Ba_{0.2}Sr_{0.8})_3Co_2Fe_{24}O_{41}$ ceramics. I studied mostly the ceramics, while I used (001)-oriented single crystal to specify selection rules.

4.4.1 Static magnetic and magnetoelectric properties

Similarly as for Y-hexaferrite $BaSrCoZnFe_{11}AlO_{22}$ in the previous section, I first verified the phase diagram, displayed in Fig. 4.2(i), for my ceramics, since the magnetic structure may be very sensitive to chemical composition. I correlated my magnetization and ME measurements with those published in Ref. [188] (see Fig. 4.6).

My temperature-dependent magnetization measurements [see Fig. 4.6(d)] confirm behavior measured by Chun *et al.* in Ref. [188] [see Fig. 4.6(a)]: The crystal becomes ferrimagnetically ordered at around 700 K. Maximum of $\boldsymbol{M}$ seen for 0.05 T at around 500 K in panel (d) corresponds to anisotropy change observed on a single crystal at a similar temperature. Also the minimum observed between 200–300 K is consistent with measurements on a single crystal. Therefore, I assume that my sample is in the TC structure at low temperatures. Since the TC structure exhibits magnetic-field-induced polarization, I verified its presence by ME measurements. I poled the sample by crossed electric and magnetic fields, and I turned off the electric field at 1 T, where a single-domain TC structure is established. Indeed, I observed qualitatively same $\Delta P(H)$ behavior at 10 K as observed in a single crystal. (Compare panels (c) and (f) in Fig. 4.6.) The magnitude of the ME effect in ceramics was two orders magnitude lower than in a single crystal, which cannot be explained just by polycrystalline nature, and I cannot explain it. My magnetization curves show anomalies at same fields as the $\Delta P(H)$ curve at low temperatures. Small hysteresis at low fields corresponds to domain reorientation.

4.4.2 THz spectra

The spectroscopic results are displayed in Fig. 4.7. In panels (a) and (b), there are temperature dependent THz spectra of real and imaginary part of the refractive index

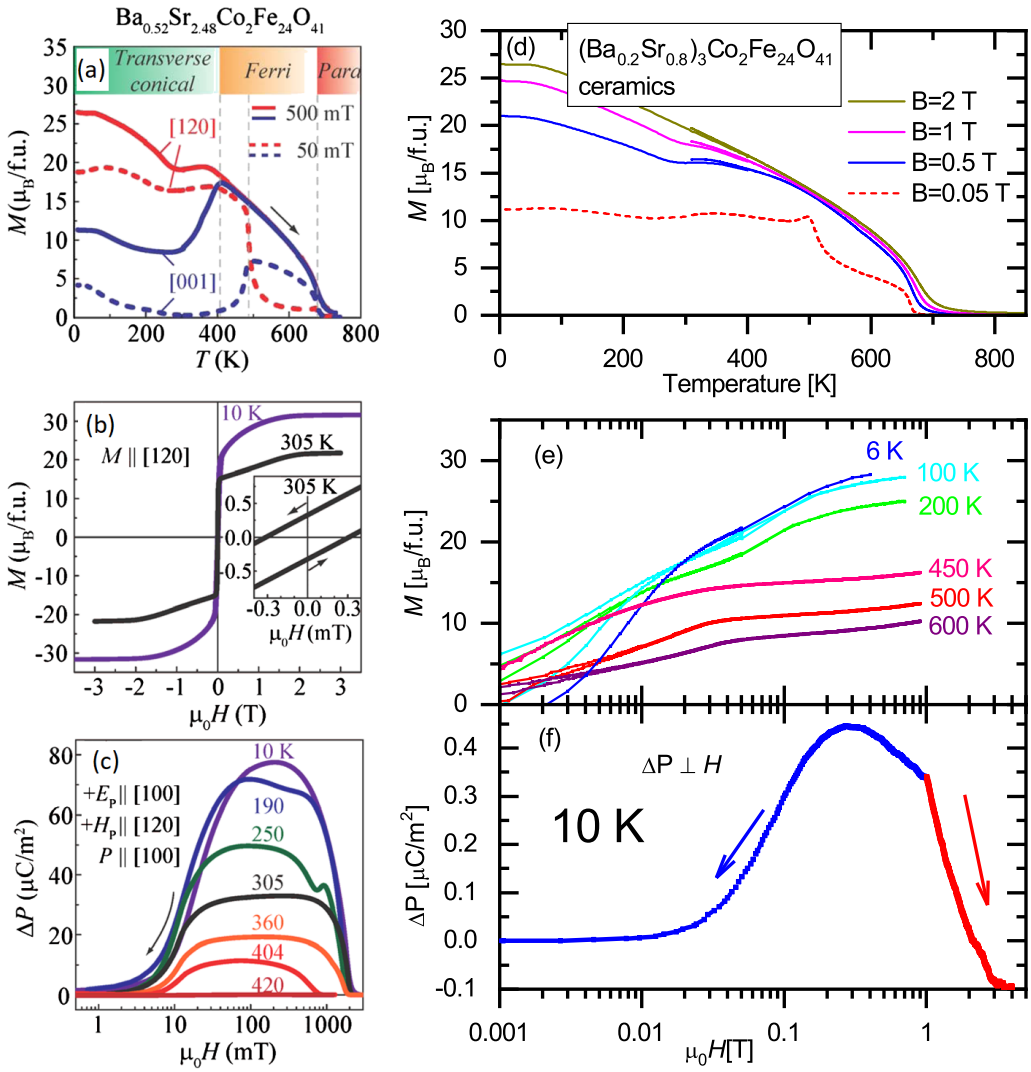

Figure 4.6: Magnetic and ME characterization of $(Ba_{0.2}Sr_{0.8})_3Co_2Fe_{24}O_{41}$ (a)–(c) single crystal (Reproduced from Ref. [188]) and (d)–(f) ceramics. (a) Temperature dependence of $\boldsymbol{M} \parallel [120]$ and $\boldsymbol{M} \parallel [001]$ measured at $\mu_0 H = 50\,\mathrm{mT}$ (dashed) and 500 mT (solid) after the field cooling. (b) $\boldsymbol{M}(\boldsymbol{H})$ curves at 10 and 305 K. The inset shows the magnified curve at 305 K. (c) $\Delta\boldsymbol{P}(\boldsymbol{H})$ $(= \boldsymbol{P}(\boldsymbol{H}) - \boldsymbol{P}(H_p))$ curves after ME poling with $+\mu_0 H_p = 2\,\mathrm{T}$ ($\parallel [120]$) and $+E_p = 230\,\mathrm{kV/m}$ ($\parallel [100]$). (d) Temperature dependence of $\boldsymbol{M}$ measured at several fields after the field cooling. (e) $\boldsymbol{M}(\boldsymbol{H})$ in ceramics at several temperatures. (f) $\Delta\boldsymbol{P}(\boldsymbol{H})$ $(= \boldsymbol{P}(\boldsymbol{H}) - \boldsymbol{P}(H_p))$ curves after ME poling in ceramics with $+\mu_0 H_p = 1\,\mathrm{T}$ and $+E_p = 220\,\mathrm{kV/m}$, while $\boldsymbol{P} \perp \boldsymbol{H}$.

for 100 μm-thick ceramics and 488 μm-thick (001)-plate-oriented single crystal. Such comparison allows to assign all modes absent in the single crystal but present in ceramics as $\boldsymbol{E}^{\omega} \parallel c$-active. Spectra of the single crystal exhibit only tiny changes with temperature, while magnetic structure changes drastically in this temperature range, thus all the modes present in the single crystal are supposed to be nonmagnetic, i.e. $\boldsymbol{E}^{\omega} \perp c$-active. For example, the sharp mode observed at 1.3 THz in the crystal is seen at 1.35 THz in ceramics, their slightly different frequency can be ascribed to their different chemical compositions.

This $\boldsymbol{E}^{\omega} \perp c$-active polar excitation is probably a phonon, since it remains in the spectra up to highest measured temperature 800 K [138].

Besides overall absorption increase, caused by a tail of an $\boldsymbol{E}^{\omega} \parallel c$-active phonons at higher frequencies, two additional excitations appear in ceramics below 300 K. Both of them remarkably sharpen and harden on cooling, reaching frequencies 1.11 and 1.83 THz at 7 K, respectively. The dramatic changes of these excitations concomitant with magnetic structure changes suggest their magnetic origin. Both of the modes are absent in single crystal spectra, but the higher-frequency mode is possibly missing only due to the low transmission signal – note that the single crystal was much thicker than the ceramics. Therefore, I can assign the mode at 1.11 THz as $\boldsymbol{E}^{\omega} \parallel c$-active excitation of magnetic origin, i.e. a purely electric-dipole-active electromagnon, similarly as $\boldsymbol{E}^{\omega} \parallel c$-active electromagnons in Y-hexaferrites [180, 204–207, 212]. The higher-energy magnetic excitation is either an $\boldsymbol{E}^{\omega} \parallel c$-active electromagnon as well, or it is a $\boldsymbol{H}^{\omega} \perp c$-active magnon. Note that both excitations have similar temperature dependence and disappear at 300 K close to the phase transition into the collinear magnetic structure, so they seem to be linked to the low-temperature TC structure.

In order to link the magnetic excitations to the static magnetic structure, I measured THz spectra of ceramics in external magnetic field (in Faraday configuration). Unfortunately, I measured a different – thicker ceramics than the one for temperature dependence, thus, I could not resolve the high-frequency magnetic mode. The magnetic-field-dependent THz spectra of such 477 μm-thick ceramics at 50 K are in panels (c) (real part) and (d) (imaginary part) of Fig. 4.7. The electromagnon is drastically suppressed by magnetic field 1 T and disappears above 2 T, i.e. at the same magnetic fields for which the TC structure transforms to the collinear one, which is exactly the same selection rule as for the electromagnons in Y-hexaferrite. Note that qualitatively same behavior is observed up to 250 K. Since the selection rules for Z-hexaferrite are the same as for Y-hexaferrite in the spin-block approximation [see Tab. 4.2], the electromagnon in Z-hexaferrite can be highly probably ascribed to the exchange-striction mechanism.

Expectedly, there is yet a FMR, whose frequency linearly increases with magnetic field with proportionality constant $\gamma = 0.032$ THz/T, which is comparable to the gyromagnetic ratio for a free electron, $\gamma = 0.028$ THz/T. Note that my experiment was performed in Faraday geometry, $\boldsymbol{H}^{\omega} \perp \boldsymbol{H}$, i.e. the geometry supporting activity of the FMR. The offset extrapolated frequency for zero magnetic field is close to zero and gyromagnetic ratio is temperature-independent, as plotted in panel (e) of Fig. 4.7.

4.4.3 Raman spectra and factor-group analysis

In order to determine relevant symmetry breaking for the electromagnon activation, Dr. Fedir Borodavka measured Raman spectra of both single crystal and ceramics. Besides almost temperature-independent phonons in 7–25 THz frequency range, in $a(cc)\overline{a}$ spectra, there is an excitation with similar temperature dependence of frequency and damping as the electromagnon observed in THz spectra of ceramics. The difference of frequencies and their temperature dependencies [compare blue and red curves in Fig. 4.7(g)] can be ascribed to a different chemical composition, thus, I expect that it is the same electromagnon mode.

In some grains of ceramics, an excitation with similar temperature dependence but

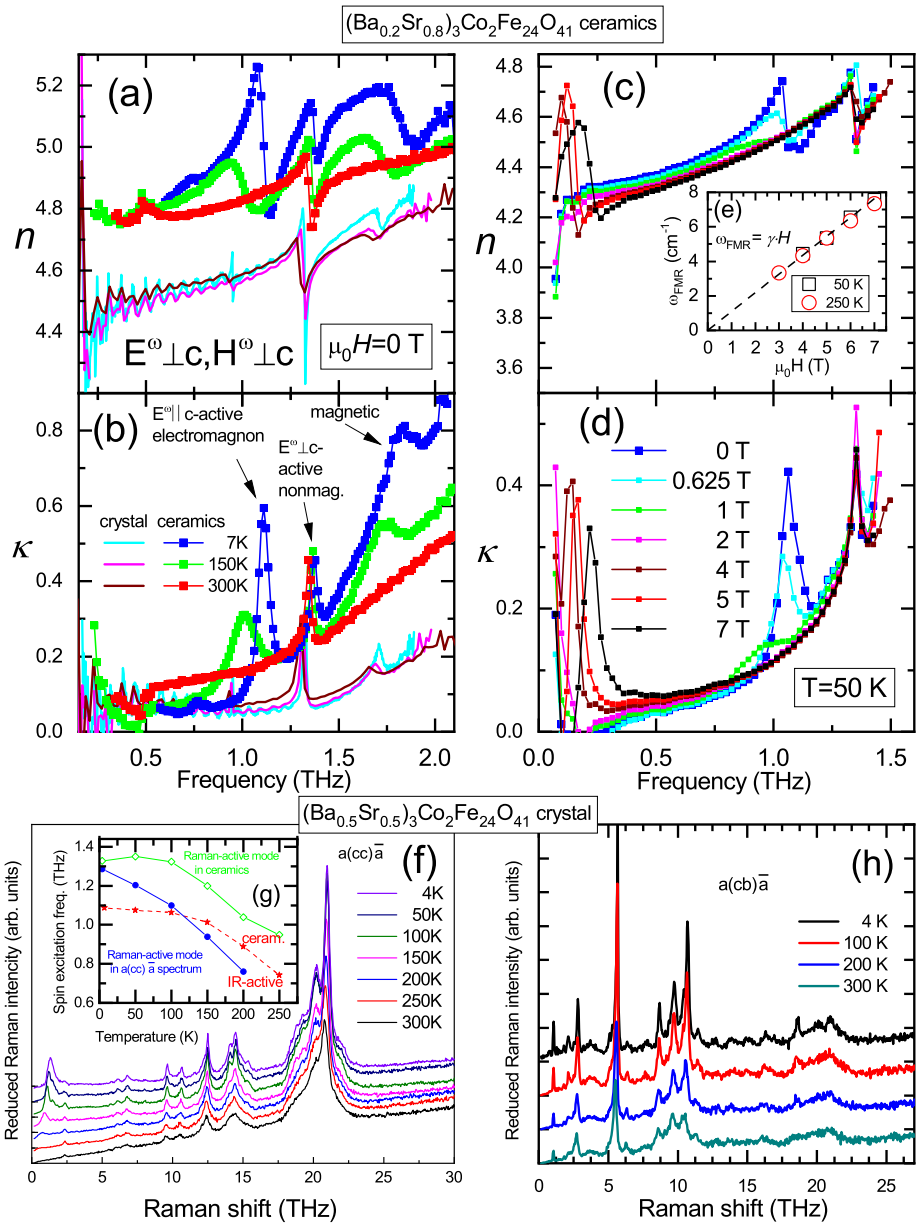

Figure 4.7: Spectroscopic results on $(Ba_{0.2}Sr_{0.8})_3Co_2Fe_{24}O_{41}$ ceramics and $(Ba_{0.5}Sr_{0.5})_3Co_2Fe_{24}O_{41}$ single crystal. (a),(b) Temperature-dependent THz spectra of both ceramics and (001)-oriented single crystal in zero magnetic field. (c),(d) Magnetic-field-dependent THz spectra of ceramics at $T = 50$ K. (e) Frequency dependence of FMR resonance frequency is shown. (f) $a(bb)\bar{a}$ and (h) $a(cb)\bar{a}$ Raman spectra of the single crystal. (g) Temperature dependence of spin excitation frequencies observed in various experiments and in various samples.

systematically higher frequency than that of the electromagnon in ceramics, was observed [compare green and red curves in Fig. 4.7(g)]. This difference can be possibly a consequence of an angular dependence of the mode frequency (oblique mode) relevant to the ceramic grains. Also, a different ceramic specimen was measured in THz and Raman spectra, and individual grains may have different chemical composition. Thus, I assume that in all cases, I observe the same electromagnon mode.

The electromagnon mode is absent in $a(cb)\overline{a}$ Raman spectra [see Fig. 4.7(h)], such information allows for the analysis of relevant symmetry breaking responsible for the electromagnon activation. To this aim, my supervisor Stanislav Kamba performed the factor-group analysis of lattice vibrations [209]. Similarly as for Y-type hexaferrite, the TC structure in Z-type hexaferrite reduces the symmetry drastically, while making the analysis too trivial, so he took into account only particular symmetry breaking. Since the TC structure produces polarization within the hexagonal plane, he made product of the non-polar parent phase D_{6h}^4 with polarization within the (001) plane. If the polarization is along the high-symmetry [100] axis, the resulting point group is orthorhombic C_{2v}, and the factor-group analysis yields

$$\Gamma_{C_{2v}} = 107A_1(c, a^2, b^2, c^2) + 102A_2(ab) + 108B_1(a, ac) + 103B_2(b, bc)\,. \quad (4.5)$$

In case of general polarization direction within (001) plane, the point group is monoclinic C_s, and the factor-group analysis yields

$$\Gamma_{C_s} = 215A'(a, b, a^2, b^2, c^2, ab) + 205A''(c, ac, bc)\,. \quad (4.6)$$

In the former case, $\boldsymbol{E}^{\omega} \| c$-active mode is active in $a(cc)\overline{a}$ Raman spectra, while it is not possible in the latter case. Nevertheless, it is known that the (001) plane is magnetically isotropic and thus the activity of the mode should not depend on magnetic field orientation within the (001) plane. Therefore, the symmetry lowering induced by the magnetic-field-induced polarization is irrelevant for the electromagnon activity, and factor-group analyzes in Eqs. 4.5 and 4.6 should not be used for analyzing the electromagnon selection rules.

How to then explain the simultaneous presence of the electromagnon in $\boldsymbol{E}^{\omega} \| c$ THz and $a(cc)\overline{a}$ Raman spectra but absence in $a(cb)\overline{a}$ Raman spectra? Further symmetry lowering would lead to a trivial solution in which all excitations have the same symmetry, thus no exclusivity rule is valid. This is in contradiction with the fact that the electromagnon is present in only in some IR and Raman spectra but absent in the others, and it demonstrates failure of the factor-group analysis using only nonmagnetic symmetries. Note that no other phonon modes appear in the magnetic phase, and their selection rules are unchanged, thus phonon spectra can be fully understood using high-temperature centrosymmetric phase. Even though the electromagnon can be viewed as a vibrational mode, magnetic symmetries are critical for explaining its selection rules. Group analysis for Raman scattering in 58 nontrivial magnetic point groups was published decades ago [222], and explicit representations of vectors and bidirectors for 122 magnetic point groups which refer to IR activity of both electric- and magnetic-dipole-active modes, was derived recently [223]. However, for applications of these selection rules, one needs to know the exact magnetic point group of the TC structure in Z-hexaferrite, which I do not know. Moreover, it is possible that such approach would fail for similar reasons as in the case of nonmagnetic factor-group analysis – i.e. the resulting symmetry would be too low, thus only relevant symmetry breakings should be considered.

4.4.4 Microscopic model of the electromagnon in Z-hexaferrite

After I and my coworkers published observation of the electromagnon in Z-hexaferrite ceramics [138], Chun *et al.* published observation of the same electromagnon in a single crystal, which allowed more precise experimental investigation [208]. They also proposed a microscopic model which explained some features of the electromagnon. Therefore, in this subsection, I review the work of Chun *et al.* [208] and propose more detailed microscopic view. Moreover, I propose a hands-on improvement of the model, which can be easily implemented in future calculations.

Chun *et al.* investigated a single crystal of Z-hexaferrite $Ba_{0.5}Sr_{2.5}Co_2Fe_{24}O_{41}$ and they indeed confirmed by polarized THz spectroscopy that it is present solely in $\boldsymbol{E}^{\omega} \parallel c$ spectra [208]. They explained some features of static magnetic properties as well as the electromagnon using a spin model in the spin-block approximation, based on Ref. [224]:

$$H = J_{LS} \sum_{i,j=1,2} \left(\boldsymbol{S}_i^S \cdot \boldsymbol{S}_j^L\right) + 2J_{LL} \left(\boldsymbol{S}_1^L \cdot \boldsymbol{S}_2^L\right) + 2J_{SS} \left(\boldsymbol{S}_1^S \cdot \boldsymbol{S}_2^S\right) + A_L \sum_{i,j=1,2} \left(S_{iz}^L\right)^2 + \\ + A_S \sum_{i,j=1,2} \left(S_{iz}^S\right)^2 - H_y \sum_{i,j=1,2} \left(S_{iy}^L + S_{iy}^S\right) + \sum_{i,j=1,2} \boldsymbol{D}_{ij} \cdot \left(\boldsymbol{S}_i^S \times \boldsymbol{S}_j^L\right). \quad (4.7)$$

J_{LS}, J_{LL} and J_{SS} are the superexchange constants of the LS, LL, and SS blocks; A_L and A_S are the magnetic anisotropy constants of L and S blocks along the z axis, while x, y and z axes are along [100], [120] and [001] axes; H_y is the sum of internal (H_y^{int}) and external (H_y^{ext}) magnetic fields along the y axis; $\boldsymbol{D}_{ij}$ is the Dzyaloshinskii vector between $\boldsymbol{S}_i^S$ and $\boldsymbol{S}_j^L$.[3]

Note some major simplifications of this model: First, the superexchange interactions in between the blocks only approximate much more numerous superexchange paths in between neighboring irons. Next, large internal magnetic field $\mu_0 H_y^{int} = 6\,\mathrm{T}$ is needed to reproduce ground state TC structure, thus it serves as a replacement of some neglected exchange interactions. Thus, the meaningfulness of the model can be checked only by comparison with the experiment.

Due to the single-crystalline nature, Chun *et al.* were able to observe behavior of the electromagnon with magnetic field of different orientations. For small magnetic field 0.2 T, they observed a red-shift with $\boldsymbol{H} \parallel [001]$ but blue-shift for $\boldsymbol{H} \parallel [120]$. They explained it by modification of the DM interaction upon magnetic structure change, i.e. by the iDM interaction in terms of this thesis. By comparing Eqs. 1.24 and 1.19, the Dzyaloshinskii vector can be written as

$$\boldsymbol{D}_{12} = \frac{\zeta^2}{K} \left(e_{12} \times \left(e_{12} \times \left(\boldsymbol{S_1} \times \boldsymbol{S_2}\right)\right)\right), \quad (4.8)$$

i.e., it diminishes with increasing parallelity of spins. By modifying magnitude of $\boldsymbol{D}_{ij}$, Chun *et al.* were able to explain both red-shift and blue-shift of the electromagnon, as well as pronounced nonlinearity of $M_y(H_y^{ext})$ curve, while fixed parameters in Eq. 4.7 lead to nonrealistic linear $M_y(H_y^{ext})$ curve. Although the modification of $\boldsymbol{D}_{ij}$, elaborated by Chun *et al.*, followed the trend given by Eq. 4.8, they tuned $\boldsymbol{D}_{ij}$ at will to fit the experimental $M_y(H_y^{ext})$ curve. Instead, I propose to treat the inverse Dzyaloshinskii-Moriya interaction self-consistently by modifying $\boldsymbol{D}_{ij}$ according to Eq. 4.8, or in other

[3] Notation is changed with respect to Ref. [208] to keep consistency with notation used in this thesis.

words, I propose replacement of the last term in Eq. 4.7 by the term in Eq. 1.24. Elaborating such calculations is beyond the scope of this thesis; moreover, it is a question whether the model requires more detailed revision due to its major simplifications.

4.5 Possible electromagnons in U-hexaferrites and absence of electromagnons in W-hexaferrites

Up to now, electromagnons only in Y-type and Z-type hexaferrites have been reported as far as I know. Nevertheless, static ME effect coming from noncoplanar magnetic structures was reported in some other types of hexaferrites, making them potential candidates for hosting electromagnons induced by the exchange striction, similarly to Y-type and Z-type hexaferrites.

Static ME effect was reported in U-type hexaferrite $Sr_4Co_2Fe_{36}O_{60}$ up to $\sim$350 K [201]. Although the static $P(H)$ was much smaller than in Y- and Z-type hexaferrites (0.5 μC/m vs. tens to hundreds of μC/m, see e.g. Refs. [188, 198]), the modulation vector $\boldsymbol{Q}$=3/2 seen in neutron diffraction measurements suggests presence of the TC structure, crucial for presence of the electromagnon induced by the exchange striction.

Indeed, I measured temperature-dependent THz spectra of U-type hexaferrite $Sr_4Co_2Fe_{36}O_{60}$ ceramics [see Fig.4.8(a,b)]. Several features are observed in 0.5–2 THz frequency range: A sharp excitation slightly below 1 THz exhibits only tiny changes with temperature, thus it has nonmagnetic origin. On the other hand, a doublet at $\sim$0.7 THz dramatically sharpens on cooling from 293 K to 7 K, thus it has probably magnetic origin. Since it is sharp and its frequency does not have dramatical temperature dependence, it is probably rather a local excitation, independent on the magnetic structure modulation, which changes dramatically in this temperature range. On the other hand, the excitation present at 1.3 THz at 7 K is broad and it remarkably hardens on cooling, similarly as the electromagnons in Y-type and Z-type hexaferrites. Moreover, it is quite strong, which is uncommon for magnetic-dipole-active excitations, thus it is likely to be an electromagnon induced by the exchange-striction. There is yet another broad temperature-dependent feature, discerned mainly from enhanced n above 1.5 THz, but sensitivity of measurement is low due to low transmittance signal, thus yet a thinner sample has to be measured to investigate its temperature dependence.

Even though I observed a hint of an electromagnon in U-hexaferrite $Sr_4Co_2Fe_{36}O_{60}$, polarized spectra of a single crystal and/or spectra in magnetic field have to be measured to determine selection rules of the excitations. Nevertheless, besides magnetic field, the magnetic structure can be tuned by the chemical composition. Therefore, investigating which excitations change upon the chemical composition change may provide a useful information about character of the excitations. Indeed, I also measured THz spectra of U-hexaferrite $Sr_4CoZnFe_{36}O_{60}$, see Fig. 4.8(c,d). While the excitations below 1 THz exhibit similar features as for relative $Sr_4Co_2Fe_{36}O_{60}$, the spectra of κ above 1 THz exhibit almost no change with temperature. Detailed investigation reveals a small doublet appearing at 7 K at 1.5–1.6 THz (marked by arrows). More importantly, spectra of n show remarkable temperature dependence, referring to some broad excitation at higher frequencies. Whether it is a phonon softening or some magnetic feature is a subject of further investigation.

Altogether, comparison between the two U-hexaferrites supports the hypothesis that

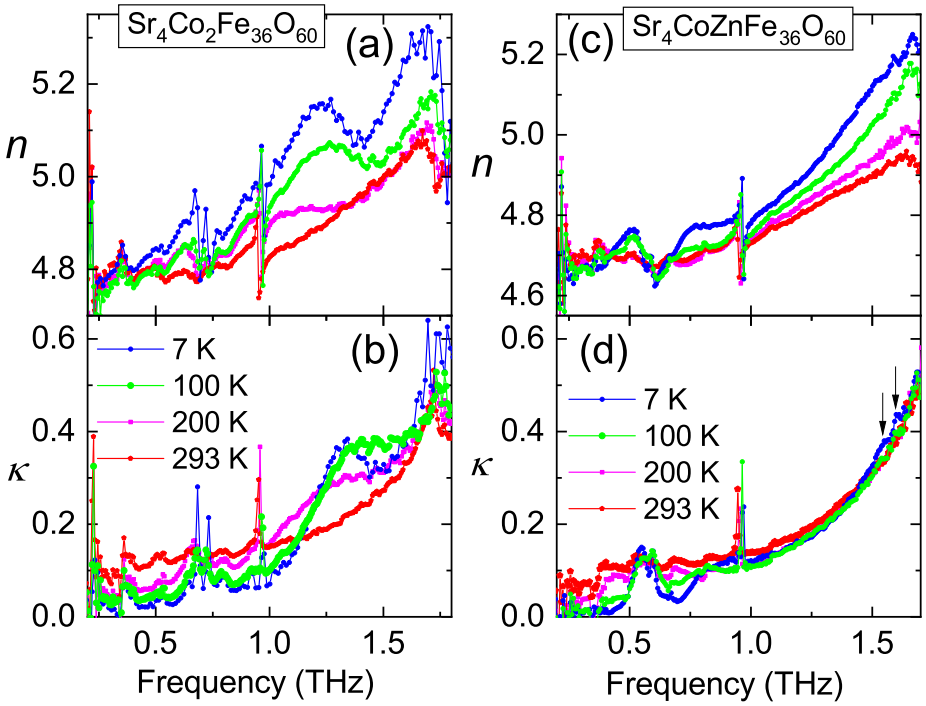

Figure 4.8: Temperature-dependent spectra of U-hexaferrites (a),(b) $Sr_4Co_2Fe_{36}O_{60}$ and (c),(d) $Sr_4CoZnFe_{36}O_{60}$. Panels (a,c) and (b,d) refer to real and imaginary part of the refractive index, respectively.

the broad excitation observed at around 1.3 THz is an electromagnon, since it is sensitive to chemical composition, which suggests sensitivity to modulated magnetic structure. Nevertheless, more detailed dependence on chemical composition, and particularly investigating Co-free U-hexaferrite in order to assign possible local Co excitations, is desired.

Static ME effect was also measured in W-type hexaferrite $SrZn_{1.15}Co_{0.85}Fe_{16}O_{27}$ below 275 K [202]. Ferroelectric polarization at low-temperature TC structure reached 600 μC/m, which is remarkably higher than in other types of hexaferrites. Therefore, I measured series of W-type hexaferrites $SrZn_xCo_{1-x}Fe_{16}O_{27}$ ceramics (x=0, 0.9, 1.05, 1.15, 2) from room temperature down to 7 K, however, I did not find any excitation remarkably dependent on temperature, which would assign a magnetic excitation (not displayed). Since I did not characterize static ME effect on my samples, I cannot make any conclusion from this measurement.

In summary, I believe that exchange-striction-induced electromagnons in hexaferrites are generic and related to modulated magnetic structure. Whether it is worth further investigation is an open question.

Chapter 5

Search for nonlinear THz absorption by electromagnons in multiferroic hexaferrites

This chapter closely follows my publication with the same title [225]. Several detailed calculations, related to this chapter, can be found in Chapter 7, which closely follows the supplemental material related to Ref. [225].

5.1 Idea of manipulating magnetic structures by intense THz pulses

One of the crucial requirements for the applicability of magnetic memories is their speed, related to a fast response of the spin system associated with some non-adiabatic process. In particular, accessing the spin system via spin resonances provides a high speed with low energy required. Magnets possessing more sublattices exhibit AFMRs, which promise high operational speed. The states of such complex magnets can be then potentially switched on a picosecond timescale [226, 227].[1] The influence of the light on the spin subsystem is often indirect (via incoherent, instantaneous absorption [231], scattering [232] or other coupling processes [227, 233]), and some of the appropriate pathways can be accessed by light sources with various frequencies. In contrast, for a direct (i.e., coherent) driving, the radiation frequency is tuned to match the spin resonance, and the spin response critically depends also on the radiation phase [234–236].

So far, switching the spin system from one (meta)stable structure to another by light was possible in magnets with a very low magnetic anisotropy, in which the energy barrier between the two different magnetic structures (or domains) is low [226, 227, 229, 233]. Nevertheless, due to the weakness of interactions between the light and spins, use of most powerful available sources is essential to achieve this goal, especially if one needs to drive the system by low-energy photons [226, 233]. Hexaferrites with their (i) tunable

[1] Note that the time in which the spin system is switched into a new equilibrium does not necessarily correspond to the time of the driving pulse. For an off-resonant drive, the driving pulse can be much shorter than the actual switching time (so-called inertial switching), which is crucial for the speed of a future memories [228–230].

low anisotropy, (ii) electromagnons providing fast and strong spin response to the EM radiation and (iii) various (meta)stable magnetic structures with similar energies, serve, according to my idea, as a promising systems for picosecond spin switching by intense THz pulses.

Observation of ultrafast switch is a challenging task which requires some pump-probe technique. Nevertheless, every such switch must be connected to some nonlinear process. Therefore, as the first step, I investigated in this chapter possible electromagnons' absorption changes depending on THz radiation intensity—i.e. nonlinear absorption—in hexaferrites. The electric THz field $\boldsymbol{E}^{\omega}$, in resonance with the electromagnons, induces spin inclinations, which are—in a linear regime—proportional to $\boldsymbol{E}^{\omega}$, thus transmission does not depend on strength of $\boldsymbol{E}^{\omega}$. I suspected that for large $\boldsymbol{E}^{\omega}$, spin inclinations cannot be anymore proportional to $\boldsymbol{E}^{\omega}$ due to constant spin lengths, which should be manifested in nonlinear (intensity-dependent) transmission spectra. Since the electromagnons are sensitive to magnetic structures, THz transmission experiment should serve as a sensitive probe of the magnetic structure. Note that in the nonlinear transmission experiment, THz radiation serves both as pump and probe, thus such an experiment can be understood as THz pump-THz probe at a zero delay.

I selected the multiferroic Z-type hexaferrite $(Ba_{0.2}Sr_{0.8})_3Co_2Fe_{24}O_{41}$ (in the following abbreviated as Z-hex) and the Y-type hexaferrite $Ba_{0.2}Sr_{1.8}Co_2(Fe_{0.96}Al_{0.04})_{12}O_{22}$ (abbreviated Y-hex) as model materials for observing nonlinear absorption by electromagnons. I expected that exciting these electromagnons with high dielectric strength by an intense THz radiation should lead to large amplitudes of spin tilts, which should produce nonlinear spin motions. It was my aim to detect such effects by observing a nonlinear THz absorption with respect to the amplitude $\boldsymbol{E}^{\omega}$ of the exciting THz electric field. I expected the electromagnons to change their parameters, owing to high deviations of the spins from their equilibrium positions, when strong $\boldsymbol{E}^{\omega}$ is applied at the electromagnons' frequencies.

To the best of my knowledge, nonlinear absorption due to electromagnons has not been reported yet. Recently, in antiferromagnetic NiO, nonlinear spin dynamics of a magnon, driven by a THz magnetic field of up to 0.4 T via the Zeeman torque, and generation of its second harmonic were observed [237]. However, the magnon nonlinearity was rather due to unusual properties of the magnon mode, whereas spin tilts from the equilibrium positions were much smaller than the spin magnitudes. In multiferroic $TbMnO_3$, an intense electric THz field of 300 kV/cm, interacting with a strong electromagnon, induced spin tilts of 4.2° [236]. I assumed that in the present case of Y-hex and Z-hex, the spin tilts could be even larger, thus leading to an observable nonlinear absorption.[2]

The presence of a nonlinear process is not, however, the only requirement which must be fulfilled for rewriting stored information. For resonant switching of information, one additionally needs (a) the presence of at least two distinguishable (meta)stable spin states, which are (b) separated by a low energy barrier, and (c) an infrared-active resonance capable of switching the spins between these two states. This scenario was predicted in a

[2]The spin deflections increase with increasing dielectric strength of the electromagnons and with intensity of THz radiation. The intensity of THz radiation I used was comparable or higher with those compared to work studying $TbMnO_3$ [236]. The electromagnon in Z-type hexaferrite $(Ba_{0.2}Sr_{0.8})_3Co_2Fe_{24}O_{41}$ is remarkably weaker than that in $TbMnO_3$ (Compare Refs. [138, 238], but the one in Y-hexaferrite $BaSrCo_2Fe_{11}AlO_{22}$ is comparable to that in $TbMnO_3$ (Compare Refs. [207, 238]). Nevertheless, it depends on the spectrum of THz radiation as well as its phase, and the character of the electromagnons' eigenmodes. These details are evaluated later in the text.

form of driving the electromagnon in $TbMnO_3$ by a single few-cycle pulse with a peak field of $\approx 10\,\mathrm{MV/cm}$ [239]; in this frequency range (1–2 THz), pulses with such intensity cannot be currently produced in the far field. This process would be fully coherent, which would be manifested by a sensitivity with respect to the THz pulse shape. Schlauderer *et al.* observed experimentally, on the ps timescale, fingerprints of spin switching induced by a single THz pulse in $TmFeO_3$ [226]. In their case, however, the effect proved active in a very narrow range of temperatures only, because the spin system is susceptible enough just in the vicinity of the spin-reorientation phase transition in $TmFeO_3$. Moreover, the switched spin configuration did not persist permanently, since the effect was based on an incoherent excitation of electric dipole transitions between crystal-field-split states of the electronic ground state of the Tm^{3+} ions, and these states are only short-lived [226].

In the case of Z-hex, besides the ground TC state, there is no other known low-temperature metastable magnetic structure at zero magnetic field.[3] In contrast, the ground state of a $Ba_{0.2}Sr_{1.8}Co_2(Fe_{0.96}Al_{0.04})_{12}O_{22}$ Y-hexaferrite pristine sample has an ALC structure, and a metastable TC structure after application of $\boldsymbol{H} \perp c$. [189] The only missing requirement for coherent switching is the last one listed above—(c)—i.e., after the high-amplitude oscillations of spins during the electromagnon excitation, the spin system should end up in the TC structure. However, a simple model of the electromagnon in Y-hexaferrites, based on the exchange-striction mechanism, does not support this scenario, since spin oscillations upon the electromagnon excitation do not transform the ALC structure to the TC structure [180, 192]. Therefore, I attempted just to observe a nonlinear THz absorption by the electromagnons in hexaferrites, without trying to detect the coherent picosecond spin switching.

In Z-hex, I did not observe any nonlinearity besides one due to sample heating, inducing a red shift of the electromagnon frequency. My results are interpreted based on an existing classical model of the electromagnon, which I extended to a nonlinear case.

In Y-hex, there is some hint of nonlinearity which is, however, difficult to resolve due to a low transmission signal. I hypothesize that it is because of the intense THz magnetic field driving the system from the ALC to the TC phase, similarly as the static field does. However, the spectra were found to be temperature-history dependent, so a dedicated experiment with a careful history protocol is necessary in order to investigate the possible nonlinearity in more detail. My results also show the possibilities and limits of the adopted method of the nonlinear THz transmission experiment.

I investigated polycrystals of the Z-type hexaferrite $(Ba_{0.2}Sr_{0.8})_3Co_2Fe_{24}O_{41}$ and single crystal (100) cut of the Y-type hexaferrite $Ba_{0.2}Sr_{1.8}Co_2(Fe_{0.96}Al_{0.04})_{12}O_{22}$. I measured their THz transmission spectra as a function of radiation intensity using highly-intense THz radiation coming from the TELBE [147, 148] and the TeraFERMI beamlines [149, 150]. The free-space reference and transmission signals of the samples were detected via the electro-optic sampling providing complex transmission spectra. At the TELBE beamline, I measured with both continuous-wave (CW) and macropulse regimes. In the macropulse regime, the train of pulses is sequentially on for 10 ms and off for 40 ms, thereby mimicking

[3] There are actually multiple domain states, which can be selected by crossed electric and magnetic poling fields. However, the electromagnon absorption what I measured is assumed to be insensitive to domain population. Nevertheless, strong THz fields can in principle serve similarly as the poling fields, and change the domain population. Subsequently, the domain population can be detected similarly as in Ref. [188]. This can be another experiment I propose.

a five times lower repetition rate in terms of the overall deposited power. Linear THz spectra at weak THz fields ($E^{\omega} \approx 15$ V/cm) were measured as described in Ref. [138].

5.2 Effect of intense THz radiation on Z-type hexaferrite $(Ba_{0.2}Sr_{0.8})_3Co_2Fe_{24}O_{41}$

In Fig. 5.1, I present the transmission amplitude spectra of a 244 μm-thick Z-hex irradiated at the TELBE beamline, tuned to 1.1 THz, for different intensities of the incoming THz radiation. Panels (b) and (c) show spectra obtained in the CW and macropulse regimes, respectively, at $T = 16$ K; the amplitude spectrum of the source is also shown. For comparison, in Fig. 5.1(a), I also display the amplitude transmission spectra at different temperatures from my linear spectroscopy experiment.

In the CW regime (Fig. 5.1b), I observed see huge effect of the THz pump pulses on the electromagnon. At low powers, the spectra resemble those obtained by linear spectroscopy at low temperatures, but with increasing power, the electromagnon absorption becomes weaker, and at the highest power (132 mW, $E^{\omega} = 322$ kV/cm), it is completely suppressed. However, at the same time, I observed also a red shift of the resonance and an increase in its damping (see the violet curve in Fig. 5.1(b) for 73 mW, 239 kV/cm), which very much resembled the spectra at higher temperatures shown in Fig. 5.1(a). This leads me to the hypothesis that the spectral changes observed with increasing power were caused just by sample heating by the intense THz radiation from TELBE. If, upon increasing the intensity of the incident THz radiation, the magnetic structure gradually changed from the TC structure to the collinear one, the electromagnon would gradually weaken as it was reported in a static magnetic field [138], but it would not exhibit a frequency shift so large as the one I observed.

The heating hypothesis can be very well verified by measuring in the macropulse regime which mimics a lower repetition rate. In fact, if the effect were caused by a true nonlinearity, it would scale with the magnitude of $\boldsymbol{E}^{\omega}$ in a single pulse. In the heating scenario, though, the spectra for similar radiation power should be similar. Looking at the results from the macropulse regime [Fig. 5.1(c)], one can see that the electromagnon changes with E^{ω} are very small compared to the CW regime. Whereas at the field intensity of 322 kV/cm, the electromagnon was completely suppressed in the CW regime, it was still present at 381 kV/cm in the macropulse regime. It is then obvious that the effect does not scale with the electric field of a single pulse, and that the heating effect dominates over a possible nonlinearity even in the macropulse regime.

However, it is still possible that besides the dominant heating effect, a small nonlinearity is present. Nevertheless, a quantitative evaluation of the spectra confirms that the electromagnon parameters scale in the same way with power for both CW and macropulse regimes within the accuracy of the experiment (see Chapter 7). Therefore, I can conclude that a possible intrinsic nonlinearity would be fully hidden by the dominant thermal effect. This is further supported by the fact that when the TELBE source was tuned to the frequency of 1.37 THz (resonance frequency of a phonon for which the sample absorbs almost all radiated power [138]), the electromagnon exhibited the same behavior with an increase of the radiation power (not displayed; more information is in Chapter 7).

Based on the problems with sample heating encountered at TELBE, it is clear that a

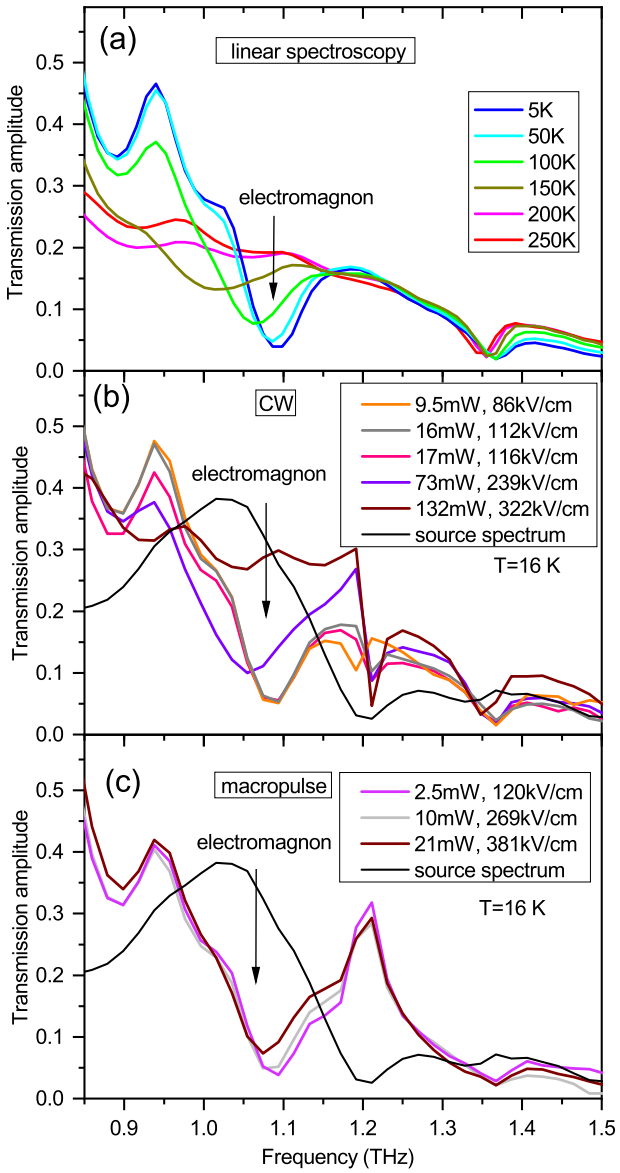

Figure 5.1: (a) Temperature-dependent amplitude linear THz transmission spectra of the 244 μm-thick Z-type hexaferrite $(Ba_{0.2}Sr_{0.8})_3Co_2Fe_{24}O_{41}$ polycrystal for low radiation power using a table-top broadband source [138]. (b), (c) Amplitude transmission spectra as a function of THz radiation intensity from the narrow-band TELBE source (b) in the CW regime, in which continuous train of pulses with 100 kHz repetition rate was applied and (c) in the macropulse regime, in which a train of pulses was sequentially on for 10 ms and off for 40 ms. The spectra are assigned according to the overall power and peak electric field values. The amplitude spectrum of the source (in arbitrary units) is shown in panels (b) and (c).

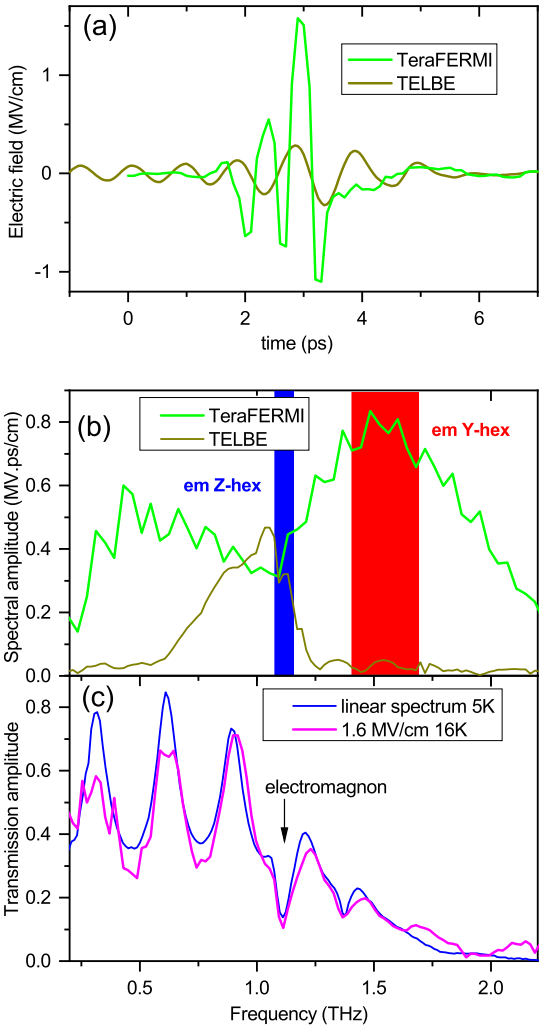

Figure 5.2: (a) Comparison of THz electric field time-domain signals in absolute units for TELBE and TeraFERMI sources. For TELBE, the pulse is multi-cycle, while for TeraFERMI, the pulse has only a few cycles. (b) Spectral amplitudes of the TELBE and TeraFERMI sources in absolute units, calculated as Fourier transforms of the time-domain traces from panel (a). The overall spectral amplitude (thus the pulse energy) is remarkably higher for TeraFERMI, but there is a minimum near the frequency of the electromagnon in Z-hex. Therefore, at the electromagnon frequency, the spectral amplitude of TELBE, whose frequency can be tuned, is a little higher. The frequency ranges of the electromagnons in Z-hex and Y-hex are shaded in blue and red, respectively. (c) Transmission amplitude spectra of the 101 μm-thick Z-type hexaferrite $(Ba_{0.2}Sr_{0.8})_3Co_2Fe_{24}O_{41}$ polycrystal at the highest available power from the TeraFERMI source providing a peak field of $E^{\omega} = 1.6$ MV/m as displayed in panel (a). The linear transmission spectrum at 5 K from Fig. 5.1(a) is displayed for comparison.

possible solution consists in using a radiation source with a significantly lower repetition rate. In this sense, one suitable source is the TeraFERMI beamline operating at 50 Hz, which I used for another investigation of possible nonlinear interaction of Z-hex with THz radiation. In these measurements, a thinner sample than at TELBE—101 μm-thick—was used, which brought two advantages. First, a higher signal at the detector improves both the SNR and DR. Second, a lower beam attenuation means that a higher proportion of the sample should be subjected to the nonlinear regime.

Figs. 5.2(a) and (b) show comparisons of reference (free space) time traces and the corresponding amplitude spectra from TELBE and TeraFERMI, respectively. From Fig. 5.2 (a), it is clear that TeraFERMI provides a higher peak field, but the Fourier transform [Fig. 5.2(b)] shows that the vast majority of the spectral intensity is located away from the electromagnon frequency, near which the spectrum from the TeraFERMI source (which cannot be tuned) exhibits a dip. Therefore, the spectral amplitude near the electromagnon frequency, which is the key quantity for transferring energy to the spin system via the electromagnon, is a little higher at TELBE. In conclusion, the pulses from TELBE and TeraFERMI sources are expected to induce similarly large spin tilts when exciting the electromagnon resonance but TeraFERMI should heat the sample less due to a much lower repetition rate.

Fig. 5.2(c) shows the transmission amplitude spectrum of Z-hex using the highest available power of TeraFERMI at 16 K, in comparison with the linear spectrum at 5 K. As the electromagnon properties are almost constant in this temperature range—see Fig. 5.1(a), I can neglect the difference in temperature. I did not observe any systematic difference between the two spectra in Fig. 5.2(c), within the accuracy of the measurement. The spectrum taken at a lower radiation intensity from TeraFERMI is not displayed, because it was noisy due to a poor SNR and DR of the beamline, especially at the frequency where its spectrum displays the dip (0.9–1.1 THz). The poor SNR at TeraFERMI originates in the source fluctuations, whereas the poor DR comes from its low repetition rate.

In conclusion, within the accuracy of the experiment, I did not detect any inherent nonlinearity of the electromagnon absorption. However, as a consequence of the used measurement approaches, the accuracy of my experiment was rather poor, so it is possible that there is still a non-negligible nonlinearity. I can then formulate a different question: How large a nonlinearity there may be so that I overlooked it in my experiment? To answer this question, two main problems have to be solved. First, I should quantitatively evaluate the accuracy of my experiment. Since the experiment performed at TELBE was influenced by sample heating, I will focus on the spectra taken at TeraFERMI in the further analysis. Second, I have to develop some spin model predicting a nonlinear electromagnon behavior. These two issues are the subjects of the next four subsections.

5.3 Simple estimation of magnitudes of spin tilts in Z-hexaferrite $(Ba_{0.2}Sr_{0.8})_3Co_2Fe_{24}O_{41}$

Before calculating the magnitude of nonlinearity of transmission in the experiment, let me first estimate how much the spin structure changes when it is exposed to the THz radiation. To this aim, I calculate the number of absorbed photon quanta in the case of a resonant one-photon absorption, meaning that one absorbed photon excites one magnon.

For the electromagnon in ferrimagnetic Z-hex, spins oscillate anti-phase, so the staggered magnetization is the relevant parameter. Therefore, I estimate that the overall change of the staggered magnetization is roughly $\Delta S = 1$ upon one excited quantum [108]. This is of course just a simplification, since the magnon modes are not circular but elliptical, so the sublattice magnetizations are not in fact conserved upon the electromagnon excitation, and the spins at different sublattices precess with different magnitudes and ellipticity values.

My calculations yield that for the most intense pulses at TeraFERMI, at the front sample side in the beam focus, the number of photons absorbed per pulse and per unit cell volume of Z-hex is 0.03. (See details in Chapter 7] Such a small number, determined purely based on the THz absorption spectrum, provides a first idea of why I did not observe any nonlinearity. Nevertheless, more detailed calculations aiming at a quantitative prediction of the nonlinearity are the subject of next three subsections.

5.4 Linear spin model for Z-hexaferrite $(Ba_{0.2}Sr_{0.8})_3Co_2Fe_{24}O_{41}$

For predicting the nonlinearity, I use a simple classical spin model, represented by Hamiltonian in Eq. 4.7, which was elaborated by Chun *et al.* [208]. This model describes, consistently with the experiments, the TC structure as a zero-temperature magnetic ground state [see Fig. 4.2(g)] as well as the purely electric-dipole-active electromagnon and its behavior in the external magnetic field [208].

The magnetic unit cell consists, within the spin-block approximation, of four effective spins associated with magnetic moments $\boldsymbol{\mu}_{S1}$, $\boldsymbol{\mu}_{L1}$, $\boldsymbol{\mu}_{S2}$, $\boldsymbol{\mu}_{L2}$, as shown in Fig. 4.2(g). I assume the magnitudes of the large and small magnetic moments $\mu_L = 35\mu_B$ and $\mu_S = 5\mu_B$, respectively, as in Ref. [208], where μ_B is the Bohr magneton. The TC structure can be parametrized by conical angles θ_S and θ_L [see Fig. 4.2(g)]. For a zero magnetic field, the model yields $\theta_S = 66.42^\circ$ and $\theta_L = 49.46^\circ$ [240].

The electromagnon is induced by the exchange-striction mechanism, and it corresponds to a precession of the magnetic moments. The moments $\boldsymbol{\mu}_S$ and $\boldsymbol{\mu}_L$ precess in the opposite directions, while being markedly elongated along the y and z axes, respectively. The modulations $\delta\boldsymbol{\mu}_{S1}$ and $\delta\boldsymbol{\mu}_{S2}$, as well as $\delta\boldsymbol{\mu}_{L1}$ and $\delta\boldsymbol{\mu}_{L2}$, are opposite to each other, which is consistent with the fact that the resonance is not magnetic-dipole active. The phase relation, crucial for the induced electric dipole moment, is the following: When $\delta\boldsymbol{\mu}_{S1}$ points in the $-y$ direction, $\delta\boldsymbol{\mu}_{L1}$ points in the $+z$ direction. The above information can be found in Fig. 4 of Ref. [208]. Moreover, since I aim to quantitatively estimate the magnitude of the modulating magnetic moments to introduce a nonlinearity, I need to know the respective magnitudes of the modulating moments. I know [240] that when one sets infinitesimally small modulations $\delta\boldsymbol{\mu}_S \parallel -y$, $\delta\boldsymbol{\mu}_L \parallel +z$ (linear regime), then $\delta\mu_S/\mu_S$ is $\approx$ 12-times larger than $\delta\mu_L/\mu_L$. Here and in the following, $\delta\mu_S$ ($\delta\mu_L$) denotes the magnitude of $\delta\boldsymbol{\mu}_S$ ($\delta\boldsymbol{\mu}_L$) in $-y$ ($+z$) directions. The above information can be used as an input for my nonlinear model.

Before introducing the nonlinear model, I look at the linear model of the electromagnon. As mentioned before, the electromagnon is induced via the exchange-striction. The associated spin-induced electric polarization within the magnetic unit cell along the

hexagonal axis, P_c, stands as [199, 208]

$$P_c = P_{\mathrm{ES}}(\boldsymbol{\mu}_{S1} \cdot \boldsymbol{\mu}_{L1} - \boldsymbol{\mu}_{L1} \cdot \boldsymbol{\mu}_{S2} + \boldsymbol{\mu}_{S2} \cdot \boldsymbol{\mu}_{L2} - \boldsymbol{\mu}_{L2} \cdot \boldsymbol{\mu}_{S1}). \tag{5.1}$$

This equation describes both the static polarization [199] and the dynamic one [208] associated with the electromagnon. Here, P_{ES} is the exchange-striction coefficient determining the inter-block polarization between the blocks S and L. The signs are alternating due to symmetry reasons [199, 208].

In the static TC structure, P_c is zero according to Eq. (5.1). The finite oscillating P_c comes from spin modulations upon the electromagnon excitation. Because of large ellipticities of the spin trajectories, I take into account the modulations $\delta\boldsymbol{\mu}_S \parallel -y$ and $\delta\boldsymbol{\mu}_L \parallel +z$ only. For infinitesimally small spin modulations, Eq. (5.1) can be linearized, and the electromagnon-related polarization can be written as

$$P_c = P_{\mathrm{ES}}(-4\mu_S \cdot \sin\theta_S \cdot \delta\mu_L + 4\mu_L \cdot \sin\theta_L \cdot \delta\mu_S). \tag{5.2}$$

One can see that this value is nonzero except for the accidental case if the two terms in the parenthesis are equal. This is, however, not the case if one uses the parameters listed above. Note that the ME coefficient P_{ES} can be estimated from the strength of the electromagnon in the linear THz spectra (see the discussion below), and that the ratio $\delta\mu_S/\delta\mu_L$ is known from the model. Therefore, the magnitudes of spin tilts can be well estimated by calculating the number of photons absorbed per unit volume.

5.5 Nonlinear spin model for Z-hexaferrite $(Ba_{0.2}Sr_{0.8})_3Co_2Fe_{24}O_{41}$

Eq. (5.2) is valid only for small spin tilts $\delta\mu \ll \mu$ ($\delta\boldsymbol{\mu} \perp \boldsymbol{\mu}$), and the polarization P_c increases linearly with $\delta\mu$ in this approximation. However, this linear relation cannot be satisfied when the condition $\delta\mu \ll \mu$ is not fulfilled, since the spin magnitudes are constant in my approximation. Below I estimate the nonlinearity coming just from this geometrical constraint. There may be other contributions to the nonlinearity, such as an anharmonicity of the Hamiltonian, but I omit these, because I am not able to evaluate their magnitudes.

In a general (not linearized) case, if one sums $\boldsymbol{\mu}$ and $\delta\boldsymbol{\mu}$, the resulting vectors need to be normalized in such a way that their magnitudes are conserved. I decided to normalize them such that after summing up, I divided all Cartesian coordinates of the magnetic moments by their actual magnitudes, whereby I determined the trajectories of the magnetic moments beyond the linear approximation: $\boldsymbol{\mu}_S$ ($\boldsymbol{\mu}_L$) oscillate along an arc connecting their equilibrium positions [Fig. 4.2(g)] and the y-axis (z-axis). The oscillations of $\boldsymbol{\mu}_{S1}$ are illustrated in Fig. 5.3(b). Note that the generalized case is described by Eq. (5.1) which has to be solved numerically.

Since $\delta\mu_S$ and $\delta\mu_L$ are linked together, the parenthesis in Eq. 5.2, and thus also P_c, can be considered as a function of one parameter only, for example $\delta\mu_S$. In the nonlinear case, I generalize $\delta\mu_S$ into *the length of the trajectory of* $\boldsymbol{\mu}_S$ *passed from the equilibrium spin configuration* and in the following, I denote it by q. This coordinate expressed in units of $\mu_S = 5\mu_B$ is equivalent to the tilt angle of $\boldsymbol{\mu}_S$ in radians, see Fig. 5.3(b). I then deal with the function $P_c(q)$ whose deviations from linear behavior correspond to the nonlinear

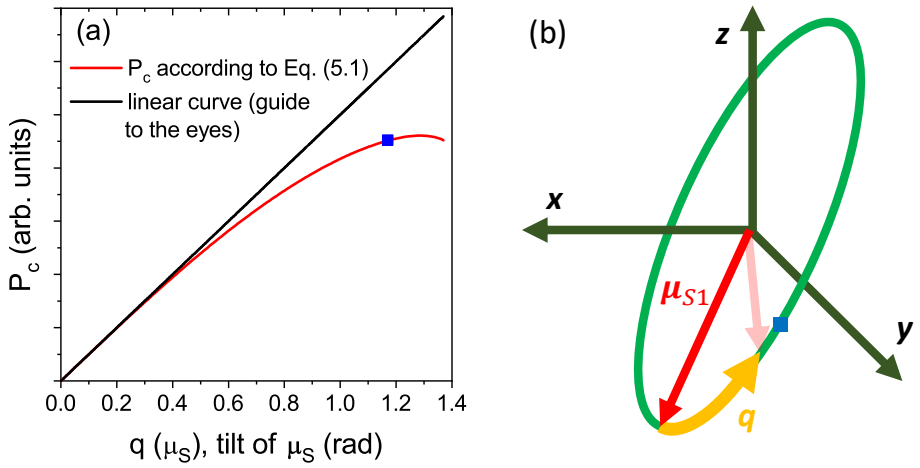

Figure 5.3: (a) Electric polarization in Z-hex as a function of the *small magnetic moments' trajectory length*, $P_c(q)$, calculated numerically using Eq. 5.1 for the TC structure (red). In black, a straight line with the same slope at origin is displayed to visualize the deviation of $P_c(q)$ from the linear behavior. The blue point on the red curve marks the maximum $P_c(q)$ reached upon using the most intense pulse from TeraFERMI and assuming $\tilde{P}_{ES} = 26\,\mu\mathrm{C}/(\mathrm{m}^2 \cdot \mu_\mathrm{B})$. (b) Scheme of the movement of a magnetic moment $\boldsymbol{\mu}_{S1}$ upon the electromagnon resonance according to the presented nonlinear model. The equilibrium position of the magnetic moment $\boldsymbol{\mu}_{S1}$ is marked in red and it lies in the xz-plane cf. [Fig. 4.2(g)]. The green circle passing through the equilibrium position of $\boldsymbol{\mu}_{S1}$ and the y-axis indicates a trajectory of the magnetic moment $\boldsymbol{\mu}_{S1}$ which oscillates on the circle close to its equilibrium position, as indicated by the partially transparent arrow. The orange arc indicates the coordinate q at the given instant. The blue point denotes the maximum deviation with the given ME coefficient and pulse, and it corresponds to the same mark in panel (a).

absorption by the electromagnon. The substitution by q proves useful later when I assume an approximation in which the Hamiltonian is a quadratic function of q.

In Fig. 5.3(a), I show by the red curve the function $P_c(q)$ calculated using Eq. (5.1). Note that P_c is expressed in arbitrary units, because the ME coefficient P_ES is considered as a free (unknown) parameter. One can see that for quite large spin tilts of several tenths of a radian, the dependence is almost linear. A remarkable nonlinearity in $P_c(q)$ appears only for trajectories of $\boldsymbol{\mu}_S$ comparable with its magnitude ($q \approx 1$), and for $q > 1.3$, the polarization starts decreasing. I note that for such large spin tilts, the model is probably no more valid, because the spin trajectory can be different from the one resulting from my normalization. Nevertheless, different spin trajectories would probably yield very similar dependences of $P_c(q)$, and only this function is in fact relevant for the calculations of nonlinearity.

The fact that the function $P_c(q)$ deviates from a linear dependence only very slowly can provide a qualitative indication of why I do not observe any nonlinearity of the THz transmission, even with quite an intense THz radiation. In fact, observing a remarkable nonlinearity in the THz transmission would require extremely large deviations of $\boldsymbol{\mu}_S$ from their equilibrium positions. The use of such an extremely intense source of THz radiation was beyond possibilities of the used THz sources.

Although I could conclude here this qualitative picture, I will attempt to quantitatively estimate how large the nonlinearity in Z-hex might be, or, the other way, how large the spin tilts would need to be for the nonlinearity to be observable within the accuracy of my experiment. For this, I need to model the temporal evolution of the polarization linked to the spin system. Since I am dealing with a coherent excitation, the knowledge of the radiation phase (pulse shape) is important. As for the relation between the model and experiment, I dispose of a time-domain measurement setup providing directly the THz radiation phase.

The dependence $P_c(q)$ displayed in Fig. 5.3 can be further rewritten as

$$P_c = \tilde{P}_{\mathrm{ES}} \cdot G(q), \tag{5.3}$$

where G is a geometrical function in units of q normalized in such a way that $\frac{dG}{dq}|_{q=0} = 1$, and that $\tilde{P}_{\mathrm{ES}}$ is the corresponding renormalized ME coefficient (which can be defined as $\tilde{P}_{\mathrm{ES}} = \frac{dP_c}{dq}|_{q=0}$). This is useful because from the model, I know exactly the function $G(q)$, whereas $\tilde{P}_{\mathrm{ES}}$ is a free parameter of the model. Note that changing the value of $\tilde{P}_{\mathrm{ES}}$ has an impact on the scaling of the vertical axis in Fig. 5.3 (which is anyway in arbitrary units), but it does not change the scaling of the horizontal axis, so the function reaches its maximum value for $q \approx 1.3$, independently of $\tilde{P}_{\mathrm{ES}}$.

Next, I introduce a normalized spin trajectory $Q = \tilde{P}_{\mathrm{ES}} \cdot q$. Since $\frac{dG}{dq}|_{q=0} = 1$, one may write $P_c = Q$ for the linear case of small spin tilts. In my terminology, Q has the meaning of P_c in the linear limit. In short, I will deal with the function $P_c(Q)$, for which $\frac{dP_c}{dQ}|_{Q=0} = 1$.

5.5.1 Modeling the nonlinear influence of light on spins in Z-hexaferrite $(Ba_{0.2}Sr_{0.8})_3Co_2Fe_{24}O_{41}$

The electromagnon I am dealing with has quite a symmetric shape of the spectral density which can be approximated by a Lorentzian. Therefore, I use the model of a classical damped harmonic oscillator driven by the electric component of THz radiation. I start with a one-dimensional model of a charged particle of mass m and charge e which can be displaced by a distance x. The equation of motion reads

$$\ddot{x} + \gamma\dot{x} + \omega_0^2 x = \frac{1}{m}\left(-\frac{\partial U(x,t)}{\partial x}\right) = \frac{eE(t)}{m}, \tag{5.4}$$

where ω_0 and γ are the angular frequency and damping of the oscillator, respectively, and they will be later related to the electromagnon. The space derivative of the electrostatic potential energy,

$$U = -exE(t), \tag{5.5}$$

determines the conservative force driving the oscillator.

It is important to mention that not all parameters in Eq. (5.4) have to be known, and they are not all experimentally accessible. Therefore, Eq. (5.4) has to be rewritten by using parameters I can acquire from my experiment. First, the displacement x has to be substituted by the electric polarization which I can measure by THz spectroscopy:

$$P_c = Nex, \tag{5.6}$$

where N is the number of dipoles per unit volume. Next, I can eliminate the quantities N, e, and m by expressing the contribution of the oscillator to the dielectric permittivity:

$$\Delta\varepsilon = \frac{Ne^2}{m\omega_0^2\epsilon_0}, \tag{5.7}$$

where ϵ_0 is the vacuum permittivity. Using Eqs. (5.6) and (5.7), Eq. (5.4) can be rewritten as

$$\ddot{P}_c + \gamma\dot{P}_c + \omega_0^2 P_c = \omega_0^2\epsilon_0\Delta\varepsilon E(t). \tag{5.8}$$

The values of parameters ω_0, γ and $\Delta\varepsilon$ were determined from a fit of the linear THz spectrum at 5 K cf. [Fig. 5.1(a)].

The model expressed by Eq. (5.8) is linear in the sense that its solution is proportional to the driving field. Before converting the model into a nonlinear one, it is important to understand the nature of the electromagnon. Commonly in models, including the model for the electromagnon in Z-hex from Ref. [208], the resonance frequency of electromagnons is given solely by the spin system similarly as for magnons, and the ME coupling, thus the electric-dipole activity, is only secondary, i.e., completely independent, and it does not influence the dynamics by any feedback. Next, the electric dipole P_c is assumed to instantaneously follow the spin system evolution (but not vice versa) according to Eq. (5.1), since it is given by the ionic contributions (polar phonons) with frequencies above the electromagnon frequency. Therefore, the dynamics are determined by the spin system only, so I should deal with a differential equation for the normalized spin trajectory Q rather than P_c. This is a mathematical way of expressing my previous expectation that the Hamiltonian (not including the ME coupling) should be a function quadratic in Q. The modification of the linear model—Eq. (5.8)—appears on the right-hand side only, which I do not express in terms of the physical force $-\frac{\partial U(x,t)}{\partial x}$ but in terms of a generalized force $-\frac{\partial U(Q,t)}{\partial Q}$. In analogy with the linear regime for which $P_c = Q$ and Eq. 5.6, the substitution is taken as $\frac{\partial U(Q,t)}{\partial Q} = \frac{1}{Ne}\frac{\partial U(x,t)}{\partial x}$. The generalized force is evaluated using Eqs. (5.5) and (5.6), as $-\frac{\partial U(Q,t)}{\partial Q} = -\frac{\partial U(Q,t)}{\partial P_c}\frac{\partial P_c}{\partial Q} = \frac{E(t)}{N}\frac{\partial P_c}{\partial Q}$. The resulting nonlinear differential equation then stands as

$$\ddot{Q} + \gamma\dot{Q} + \omega_0^2 Q = \omega_0^2\epsilon_0\Delta\varepsilon\left(\frac{\partial P_c}{\partial Q}\right)E(t). \tag{5.9}$$

I see that the driving electric field must be multiplied by the factor $\frac{\partial P_c}{\partial Q}$, i.e., the derivative of the function displayed in Fig. 5.3(a), at every instant.

For solving Eq. (5.9), I need to choose a scaling of the function $P_c(Q)$, i.e., I have to set the ME coefficient $\tilde{P}_{\mathrm{ES}}$ (or P_{ES}). In following, I will show that if I specially choose $\tilde{P}_{ES} = 26\,\mu\mathrm{C}/(\mathrm{m}^2\cdot\mu_{\mathrm{B}})$, nonlinearity which is on the limit of sensitivity of my detection system is reached. Later, I will show that based on the dielectric strength of the electromagnon and the amplitude of the THz radiation, the spin tilts must be much smaller than those obtained by using $\tilde{P}_{ES} = 26\,\mu\mathrm{C}/(\mathrm{m}^2\cdot\mu_{\mathrm{B}})$. Therefore, $\tilde{P}_{\mathrm{ES}}$ must be much higher.

The chosen value of $\tilde{P}_{\mathrm{ES}}$ implies that the $1\mu_B$-long spin trajectory of $\boldsymbol{\mu}_S$ creates a

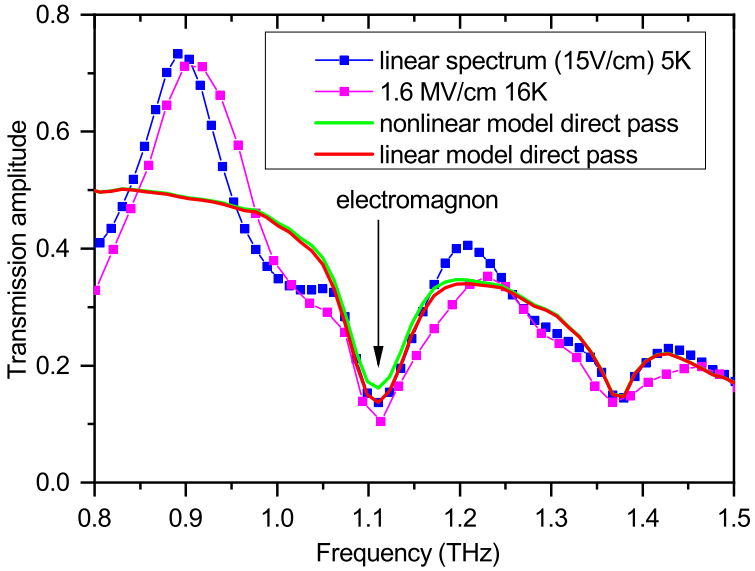

Figure 5.4: Comparison of modeled transmission amplitude spectra of Z-hex with the experimental ones from Fig. 5.2(c). The modeled spectra assume only a direct pass, neglecting the Fabry-Perot reflections. The peaks in the experimental spectra seen near 0.9 and 1.2 THz are interference maxima.

polarization $\approx 26\,\mu\mathrm{C/m^2}$.[4] This $\tilde{P}_{\mathrm{ES}}$ is chosen in such a way that for the most intense pulse from TeraFERMI—see Fig. 5.2(a), taking the linear $P_c(q)$ dependence [black line in Fig. 5.3(a)], one would reach the highest spin inclinations of $q \approx 1.6\mu_S$, i.e., very high spin tilts beyond the validity of both a linear and a nonlinear model. Taking the nonlinear model, the highest spin inclinations reach $q \approx 1.17\mu_S$ [blue point in Fig. 5.3(a)], corresponding to a highly nonlinear regime, but this would be still within the possible validity range of the model. More detailed calculations can be found in Chapter 7.

My further goal is to model the response of the 101 μm-thick sample using Eq. (5.9), and to compare it with the experimental transmission amplitude spectra obtained at TeraFERMI [see the magenta curve in Fig. 5.2(c)]. Besides the complex refractive index measured by the linear THz spectroscopy, the following input parameters were used in the model: $\frac{\omega_0}{2\pi} = 1.1$ THz, $\frac{\gamma}{2\pi} = 62$ GHz, $\Delta\varepsilon$=0.27. Details of calculations can be found in Chapter 7 For simplicity, I modeled only the direct pass propagation, disregarding the internal Fabry-Perot reflections (interferences). This is a reasonable simplification because (i) the reflected beams have low intensities, thus they interact with matter linearly, and (ii) the transmission signal at the electromagnon frequency, the main subject of my interest, is almost unaffected by the interferences, because the vast majority of photons at this frequency are absorbed during the direct pass.

The transmission amplitude spectrum calculated according to the nonlinear model is displayed by the green curve in Fig. 5.4, and it can be compared with the experimental transmission amplitudes from Fig. 5.2(c). The direct pass spectrum calculated using the

[4]Note that $1\mu_B$-long spin trajectory of $\boldsymbol{\mu}_S$ means its tilt of 0.2 rad from its equilibrium position. Also, it corresponds to $0.6\mu_B$-long spin trajectory of $\boldsymbol{\mu}_L$, meaning its tilt of 0.017 rad. The difference of P_c created by such spin tilts from $26\frac{\mu C}{m^2}$ is given by a small nonlinearity—compare the values of black and red curves in Fig. 5.3(a) for $q = 0.2$.

linear model is displayed in red, showing that at the electromagnon frequency, where the transmission is low, the linear model is almost the same as the linear spectrum (blue), otherwise exhibiting interference fringes. This allows for comparing the value of transmission at the electromagnon resonance (at its local minimum) as a measure of nonlinearity. (This is verified by the calculations: The nonlinearity has a major effect on the electromagnon strength $\Delta\varepsilon$, and it exerts only minor effects on the shift of its frequency ω_0 and change in its damping γ, see Chapter 7) I conclude from Fig. 5.4 that the linear transmission amplitude (blue and red) reaches a value of 0.137 ± 0.001 at ω_0. The much less precise spectrum from TeraFERMI (magenta curve) reaches a value of 0.104 ± 0.05, which is, within the experimental error, the same as the linear spectrum. (For an estimation of experimental errors, see Chapter 7.) The nonlinear modeled spectrum (green) reaches a value of 0.161, which is just beyond the limit of the sensitivity needed to distinguish the nonlinearity based on the spectrum taken at TeraFERMI (magenta). I conclude, as mentioned previously, that if the ME coefficient were lower than the used $\tilde{P}_{ES} = 26\,\mu\mathrm{C}/(\mathrm{m}^2 \cdot \mu_\mathrm{B})$, the spin tilts and the nonlinearity would have to be higher than I calculated, which would have been resolved in the experiment as an increased transmission, within the accuracy I disposed of.

As mentioned previously, I can well estimate the value of $\tilde{P}_\mathrm{ES}$ from the linear THz spectroscopy experiment. Taking into account the calculated spin change per unit cell volume, amounting to 0.03, I determined the maximum tilt of the small spin as $q = 0.075\,\mathrm{rad}$ (4.3°) (see Chapter 7), which is much less than $q = 1.17\,\mathrm{rad}$ which I obtained by assuming $\tilde{P}_{ES} = 26\,\mu\mathrm{C}/(\mathrm{m}^2 \cdot \mu_\mathrm{B})$ using the nonlinear model, and even much less than $q = 1.6\,\mathrm{rad}$ obtained using the linear model. This means that the actual $\tilde{P}_\mathrm{ES}$ must be correspondingly higher—I can estimate it as $\tilde{P}_\mathrm{ES} \approx 26 \cdot \frac{1.6\,\mathrm{rad}}{0.075\,\mathrm{rad}}\,\mu\mathrm{C}/(\mathrm{m}^2 \cdot \mu_\mathrm{B}) \approx 555\,\mu\mathrm{C}/(\mathrm{m}^2 \cdot \mu_\mathrm{B})$. Similarly, I can say for how large fields I would observe a nonlinearity with the TeraFERMI setup and given spectral shape: $E^{\omega}_{\mathrm{max}} = 1.6\,\mathrm{MV/cm} \cdot \frac{1.17\,\mathrm{rad}}{0.075\,\mathrm{rad}} \approx 25\,\mathrm{MV/cm}$. Apparently, some nonlinearity can be observed for much lower fields if SNR and the spectral intensity at the electromagnon frequency are higher.

It is then very clear that the experimental conditions were very far from those which would allow for observing nonlinearity. This was mainly due to a very poor SNR of the experiment coming from high pulse-to-pulse fluctuations and from a temporal jitter. With the current settings, the nonlinearity would have been observed only if the assumptions of the model were not valid. For example I assumed the Hamiltonian to be quadratic in q, which is a very sufficient approximation for the Hamiltonian used in Ref. [208]. However, a very strong nonlinearity of the Hamiltonian within the range of spin tilts of 4.3° could contribute to an additional nonlinearity in the electromagnon absorption. My experimental results thus exclude a strong nonlinearity of the Hamiltonian within a tilt of 4.3° of $\boldsymbol{\mu}_S$. Moreover, I used the model of rigid spins within magnetic blocks. It is, however, possible that spins within the block change their orientations with respect to each other, which could possibly lead to nonlinearity at smaller THz intensity than predicted by my model.

Note that the estimated spin tilts (4.3°) are higher than those estimated by Baierl *et al.* in NiO [231] who observed a nonlinearity, and comparable to those measured by Kubacka *et al.* in $TbMnO_3$ [236]. Nevertheless, I did not employ a sensitive pump-probe setup, so even for such high spin tilts, a possible nonlinearity was hidden in the noise.

Finally, I note that the one-dimensional differential equation I used, Eq. (5.9), assumes an electric field oriented along the polarization, which can be achieved in a single crystal;

in contrast, I measured using a polycrystalline specimen. However, this does not change my conclusion that I was very far from observing a possible nonlinearity.

5.6 Effect of intense THz radiation on Y-type hexaferrite $Ba_{0.2}Sr_{1.8}Co_2Zn(Fe_{0.96}Al_{0.04})_{12}O_{22}$

The Y-hex single crystal was measured at the TeraFERMI beamline only, because the intensity available at the TELBE beamline would be too low in the frequency range of its electromagnon [$\approx$ 1.5 THz, see Fig. 5.2(b)]. The TeraFERMI beamline is also much more suitable for the Y-hex than for the Z-hex as the intensity, thus also the SNR and DR, are much higher in the relevant frequency range. Furthermore, the electromagnon in Y-hex is stronger than the one in Z-hex. These two facts lead to a much higher transfer of energy (and of angular momentum) to the spin system, as one can see from the comparison of the blue vs. red areas under the green curve in Fig. 5.2(b).

In Fig. 5.5, I show THz transmission amplitude spectra of Y-hex measured at different intensities of the THz radiation. The highly intense radiation provided by the TeraFERMI beamline exhibited high fluctuations, therefore I display statistical error bars for the spectra related to TeraFERMI. The linear spectrum measured at the table-top setup shows very low statistical errors, so the error bars are omitted. I have to stress that the statistical error bars do not express the total errors, since they omit the systematic ones. This is obvious from the low-frequency part of the spectra clearly exhibiting measurement errors. The difference among them exceeds their statistical errors, but they must be obviously independent of the radiation intensity.

With the increase in incident beam intensity, I observed a shift of the electromagnon towards higher frequencies, which was somewhat larger than the statistical errors. At high incident intensities, the transmission was clearly higher at around 1.4 THz than the linear one, whereas at around 1.6 THz, the situation was the opposite. Moreover, the frequency shift between the two spectra taken at TeraFERMI (see the spectra shown by green and blue lines in Fig. 5.5), although not larger than statistical errors, does not seem to be caused just by an error, since the spectral shapes of both these spectra are similar. Therefore, the observed frequency shift is very likely related to the physics of the material. Also, the peak absorption of the electromagnon is higher for the spectra measured at TeraFERMI than that observed in the linear spectrum, which is expressed by a much deeper dip in the transmission amplitude.

In summary, I observed a clear blue-shift of the electromagnon frequency with radiation intensity increase, and a possible increase in its strength, without a significant spectral narrowing or broadening. Note that the model presented in the previous sections predicts mainly a decrease in the electromagnon strength with the increasing radiation intensity. Therefore, the model does not appear to be valid for these experiments; I rather describe the results only qualitatively, and discuss the possible effects not captured by the model.

Let me first assume that the sample consists of a single phase, and that no phase transition occurs due to the intense THz radiation, so the sample exhibits a single potential determining the electromagnon frequency. In a harmonic potential, the energy levels would be equidistant. Commonly, the potential is shallower at higher energies, whereby the energy levels are closer to each other. Therefore, for higher intensities of the driving

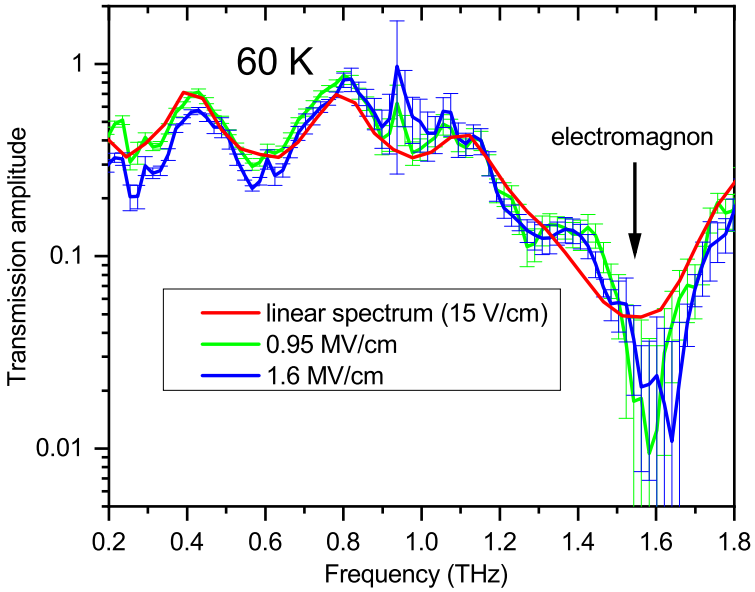

Figure 5.5: Transmission amplitude THz spectra of a 87 μm-thick Y-type hexaferrite $Ba_{0.2}Sr_{1.8}Co_2(Fe_{0.96}Al_{0.04})_{12}O_{22}$ single crystal with $\boldsymbol{E}^{\omega} \parallel c$, $\boldsymbol{H}^{\omega} \perp c$ at 60 K, as a function of the THz radiation intensity. The linear spectrum for a very low intensity (red line) was measured using a table-top source, whereas the spectra upon strong irradiation were measured at the TeraFERMI beamline, and they are labeled by the peak electric field. The error bars reflect statistical errors related to the subsequent acquisitions.

field, one would expect a red shift. Further, a broadening of the occupation distribution should result in a broadening of the peak in the spectral range—especially for the case of a non-equidistant energy spectrum. In the described scheme, the observed blue shift would imply a hardening of the potential for high energies which is not probable. Moreover, such hardening would be, in such a picture, accompanied by a spectral broadening, which was not observed.

A possible explanation of the blue shift as well as of the increase in the absorption strength can be found in the work of Shishikura *et al.* [207], who observed a tiny blue shift and an increase in strength of the electromagnon in Y-type hexaferrite $BaSrCo_2Fe_{11}AlO_{22}$ when a static in-plane magnetic field drove the system from the ALC to the TC phase. In my case, I cooled down the sample in a zero magnetic field, and the pristine sample was assumed to be in the ALC phase. Nevertheless, the THz radiation was $\boldsymbol{E}^{\omega} \parallel c$, $\boldsymbol{H}^{\omega} \perp c$-polarized, so the magnetic component of the THz radiation was directed along the hexagonal plane. At the highest intensity, the peak free-space THz electric field of 1.6 MV/cm corresponds to a peak THz magnetic field of 0.9 T inside the material (see Chapter 7). Such an intensity, albeit only transient, is comparable with the static field necessary to drive the system from the ALC to the TC phase (see Chapter 7). Therefore, I hypothesize that the THz magnetic field drove the system to the TC phase, and this is why I observed the frequency increase. I conclude that the picture of a transition from the ALC to the TC phase is consistent with the blue shift, the strength increase and with the insignificant change in the electromagnon damping, according to Ref. [207].

Even though I hypothesized that the THz magnetic field is crucial for the observed changes, it does not necessarily mean that the electric field does not play any role. My

calculations show that for the highest intensity at the beam focus, there are on average 0.4 of photon quanta per unit cell volume absorbed, which is more than an order of magnitude per sum of spin sizes higher than in Z-hex (See Chapter 7). I cannot directly calculate the magnitudes of spin tilts from this number, because I do not know the magnetic structure exactly, and I do not dispose of a quantitative model of the electromagnon, in contrast to Z-hex. Nevertheless, I estimate the spin tilts to be about 10°, which is not negligible. (See Chapter 7) Therefore, it is possible that a unique interplay between the THz electric and magnetic fields causes the hypothesized ALC-to-TC phase transition. Such an interplay would be sensitive to the pulse shape—different orientations of magnetization in the TC structure would be expected for different pulse shapes. Unfortunately, in the experiments, it was not possible to change the pulse shape. Moreover, also the used detection technique is not sensitive to the orientation of magnetization in the TC structure.

At this point, it is necessary to mention that the history of the sample may have a crucial importance. The relevant question is: Is the supposed THz-field-driven phase transition from the ALC to the TC phase only short-lived, or is it a permanent one? To answer this, it would be the best to measure a linear spectrum just before and after the application of an intense THz field. Unfortunately, the low-intense spectra were very noisy in the experiment at TeraFERMI. However, the spectrum with a peak field of 0.95 MV/cm was measured after the one with peak field 1.6 MV/cm. Therefore, if I assume that the frequency shift of the electromagnon between these two spectra does occur and that it is related to this transition, it is more likely that the phase transition between the two phases is only temporary. If the transition were permanent, the electromagnon frequency shift observed in the 0.95 MV/cm spectrum would be the same as in the 1.6 MV/cm spectrum.

What is then the physical picture behind such transient phase transition? One can imagine that the front side of the sample exposed to the most intense THz radiation is switched to the TC structure, which is surrounded by the ALC structure. Once the radiation fades, the domain walls move back, so the stable ALC phase pushes the metastable TC phase away.

A related question is how the TC phase is formed as a consequence of a short THz pulse. I believe that the spin dynamics representing the ALC-to-TC phase transition is slower than the THz pulse, so the TC phase could be formed by an inertial manner after the pulse is gone. If I assumed that I detected this phase transition by THz spectroscopy, it would mean that the TC phase persisted until the next pulse, i.e. 20 ms. Resolving such dynamics can be a topic of a future pump-probe experiment.

I have to admit also that the linear spectra measured at the table-top setup before and after application of the intense THz field were slightly distinct, which can be possibly caused by a small fraction of unwanted TC domains in the crystal measured before the TeraFERMI experiment or other effects (See more information in the Chapter 7). This stresses again the importance of recording the spectra while paying attention to the temperature and magnetic-field history (including stray fields in cases when small fields can cause the phase transition), as shown in previous works [180, 207]. Moreover, the history of intense THz radiation may play a role as well.

In summary, my results are promising but not quite conclusive. Nevertheless, my experience can help in the future investigation. Therefore, I list here the critical points and possible directions of the future experimental research related to a possible effect of the intense THz radiation on the electromagnon in Y-hexaferrites:

1. Although I used the highest possible intensity of the EM field available in this spectral range, I did not see a convincing difference in the spectra with respect to the linear one. Therefore, any future experiment will have to deal with comparably intense THz field to observe any significant changes. The field could be even locally enhanced by employing a metamaterial, in which case the probe should be much more localized than in my far field THz experiment, limited by diffraction limit to hundreds of μm.

2. Any future experiment must provide a much higher accuracy—SNR and DR, the latter being important for measuring at several intensities, including low ones, in a single experiment. A high DR can be achieved when pump and probe pulses are decoupled, which was not the case in my experiments. A higher accuracy is typically reached in table-top setups. For example, the 2D THz spectroscopy was successfully used to study nonlinearities in a magnetic system [241]. Nevertheless, table-top setups do not always provide a sufficient radiation intensity, compared to accelerator-based sources.

3. The sample history, in terms of the applied temperature and magnetic field, is important for Y-type hexaferrites, and the history of intense THz fields can play a role as well. Therefore, it is favorable to use a sufficiently high temperature (in case of Y-hex up to 410 K) in order to erase in-situ any prior history, before applying the magnetic field (in case of Y-hexaferrites typically 0.1–1 T) to reach the TC phase at will.

4. The experimental geometry and settings may be crucial. I measured the 87 μm-thick sample in the transmission geometry. The thickness was not optimized with respect to the penetration depth at the electromagnon frequency (<20 μm), because there was a risk of damaging the crystal when making it thinner. Another strategy may consist in using the reflection geometry combined with some surface-sensitive probe technique.

The first two and the last point strongly suggest that employing a pump-probe scheme is highly desired. Note that in my experiment, the intense THz pulses served both for pumping (exciting the electromagnon, thus distorting the magnetic structure or changing the magnetic structure by the THz magnetic field) and probing (detecting the magnetic structure via the electromagnon strength). Therefore, such experiments can be also viewed as THz pump-THz probe experiments with a zero delay time, for which the pump and probe pulses are identical. Such experiment is easy to realize, but, as a drawback, the SNR and DR are limited.

I actually tried to employ a THz pump—THz probe setup (2D THz spectroscopy), but the conditions were not optimized as it can be done in the table-top setups. How about other probing techniques? Conventionally, the free induction decay of THz-pumped magnons can be well observed by the Faraday rotation [235]. However, I deal with electric-dipole-active resonances, so, in the first approximation, I do not expect any Faraday signal to occur. Nevertheless, the possible ALC-to-TC phase transition may be detectable via the Faraday signal if the magnetization is not compensated over various TC domains. There may be of course other optical effects besides the Faraday rotation, and possible probe

techniques do not need to be necessarily optical. Here I list possible probe techniques to follow intense THz pump:

- Second harmonic generation (SHG): Upon the electromagnon excitation, I can expect modulation of the SHG signal. However, the sample is already noncentrosymmetric so one would expect a small modulation on top of a large signal. Therefore, I do not expect this method to be sensitive enough.
- Birefringence: Similarly, the crystal is already birefringent, and the polarization oscillates parallel to the hexagonal axis upon the electromagnon excitation, so I would again expect a small modulation on top of a large signal.
- Resonant inelastic x-ray scattering (RIXS): This method can directly access the magnetic structure changes. However, its sensitivity is again limited, especially in the pump-probe scheme [236]. Similarly to previous cases, I would probably expect a small modulation on top of a large signal. Moreover, this method is rather expensive and it is a question whether the current topic is worth studying.

Note that different probe techniques detect different aspects than the THz spectroscopy I used. My view was narrowly focused on the effect of the intense THz radiation on the electromagnons, which are detectable by THz spectroscopy. Different complementary techniques can bring more insight into microscopic nature of the electromagnons, which are still not completely understood. Finding a suitable probe technique following the THz pump, which would be sensitive to the magnetic structures in hexaferrites, remains a challenge for future research.

5.7 Summary and Outlook

I studied the effect of an intense THz radiation on the electromagnons' absorption in Z-type hexaferrite $(Ba_{0.2}Sr_{0.8})_3Co_2Fe_{24}O_{41}$ and Y-type hexaferrite $Ba_{0.2}Sr_{1.8}Co_2(Fe_{0.96}Al_{0.04})_{12}O_{22}$. In their low-temperature phases, I measured the transmission at different intensities of incident THz radiation provided by two accelerator-based sources with different complementary properties.

At TELBE, I observed a disappearance of the electromagnon in Z-hex upon applying a highly intense THz radiation, which I ascribed to sample heating, based on an analysis of my results at different effective repetition rates. Therefore, I concentrated on the results from the TeraFERMI source which exhibits a much lower repetition rate, so the heating can be excluded. Although the integral THz electric field at TeraFERMI was much higher than that at TELBE, the intensity of the TeraFERMI source was reduced at the frequency of the electromagnon in Z-hex; therefore the spectra exhibited a poor SNR and DR near the electromagnon frequency. Within the experimental error, I did not detect any difference of the spectrum taken at TeraFERMI from the linear one.

I then tried to explain the observed results theoretically. First, I calculated the number of photons absorbed in a pulse per unit volume, which equals number of generated electromagnon quanta. Second, I generalized the existing model of the electromagnon in Z-hex, showing the electromagnon eigenvector, to a nonlinear one, assuming a form of Hamiltonian quadratic in the length of the spin trajectory. I considered only a geometrical

nonlinearity coming from the fact that the spin lengths are constant. The calculations showed that the maximum spin tilt upon exciting the electromagnon resonance was about 4.3°, implying that the Hamiltonian can be roughly considered quadratic in terms of the length of the spin trajectory in this range. A large anharmonicity of the Hamiltonian would lead to an observable frequency shift of the electromagnon, whereas a markedly lower absorption can be expected only for higher spin tilts.

In other words, I experimentally mapped the spin Hamiltonian in the vicinity of its global minimum to check for possible nonlinearities, which could be hallmarks of the potential getting shallower, and possibly indicate the presence of some metastable state. I did not find any sign of a nonlinearity, probably because I mapped only a minor part of spin configuration space. Note that no metastable state is known in Z-hex, in contrast to Y-hex, but several metastable states can exist, taking into account that the Hamiltonian used in [208] is very simplified, and it cannot describe the whole spin configuration space.

It was much more suitable to use the TeraFERMI source for investigating the electromagnon in Y-hex than the one in Z-hex, owing to a much higher number of absorbed photons per pulse and unit volume, and also due to a significantly higher SNR and DR. With the intensity radiation increase, I observed a small increase in the electromagnon frequency and in its strength, which can be possibly ascribed to a transient phase transition from the ALC to the TC phase. This transition would be caused primarily by the THz magnetic field reaching 0.9 T, whereas the THz electric field exciting the electromagnon may also play a role.

I cannot provide any conclusive statement about the observed effect, which was on the edge of the statistical error, also due to a lack of data. I found that the history of the sample including history of the THz radiation may be crucial. Although the experiment at TeraFERMI was on the verge of the current possibilities and suitably designed for studying Y-hex, I suggested further improvements for studying the effect of an intense THz radiation on Y-type hexaferrites in detail. In particular, I pointed out the necessity of using a pump-probe setup in future experiments.

If future experiments confirm that the short THz pulses can switch between the two different magnetic structures (ALC and TC), it would be a great achievement. Comparing to the ballistic switching in $TmFeO_3$ [226], it would provide significant advantages: First, these two (meta)stable structures exist over a broad temperature range, so the hypothetical switching might be feasible in the same range, including even at room temperature [190, 194]. Second, the metastable TC structure can be stable for a long time (at least days but probably much more), allowing for conceiving long-term nonvolatile memories. The remaining question would then be how to switch back from the TC to the ALC state without heating which brings a high energy amount.

Chapter 6

Selection of magnetoelectric domains by static and oscillating electromagnetic fields in $LiCoPO_4$

In this chapter, I will show that the dynamic magnetoelectric coupling can not only affect light, but it may enable EM fields to influence the magnetic order responsible for this cross-coupling. The model material I studied is $LiCoPO_4$, and the key factor is its off-diagonal ME response, which couples the orthogonal electric and magnetic fields of the radiation. First, with my colleagues I demonstrated that THz frequency DD can be used to detect the AFM domains of this compound [105]. In this work, I applied ME poling and established a single domain in the sample by orthogonal, static electric and magnetic fields. More intriguingly, in a following series of experiments, I demonstrated that the orthogonal electric and magnetic fields of light can also select ME domains. This novel effect described in the second part of this chapter may open new possibilities to apply ME materials in all-optical memory elements, in which information is both read out and written by light. Such memory is nonvolatile and, more importantly nondestructive, in contrast to the most known all-optical memory – the CD-ROM.

6.1 Structure and properties of $LiCoPO_4$

$LiCoPO_4$ crystallizes in the orthorhombic *Pnma* non-symmorphic crystal structure [242, 243]. The structural unit cell consist of 4 formula units, containing CoO_6 octahedra and PO_4 tetrahedra. Due to the strong distortion of CoO_6 octahedra, the local point-symmetry of the Co^{2+} ions is reduced to m_y, thus allowing a local electric polarization in the xz plane. Since *Pnma* structure has inversion symmetry, the local polarizations at Co^{2+} sites form an anti-polar order, as shown in Fig. 6.1(b), where the x-component of the local polarization is displayed.

Magnetic properties of $LiCoPO_4$ are governed by the Co^{2+} ions with octahedral ligand coordination, which potentially have two different ground states: $t_{2g}^5 e_g^2\ ^4T_1$ high-spin state with $S = 3/2$, $L = 1$ and $t_{2g}^6 e_g^1\ ^2E$ low-spin state with $S = 1/2$, $L = 0$. Magnetization measurements suggest that the former state is realized in $LiCoPO_4$, but the orbital momentum is quenched due to the distortion of the O_6 cage [242, 244].

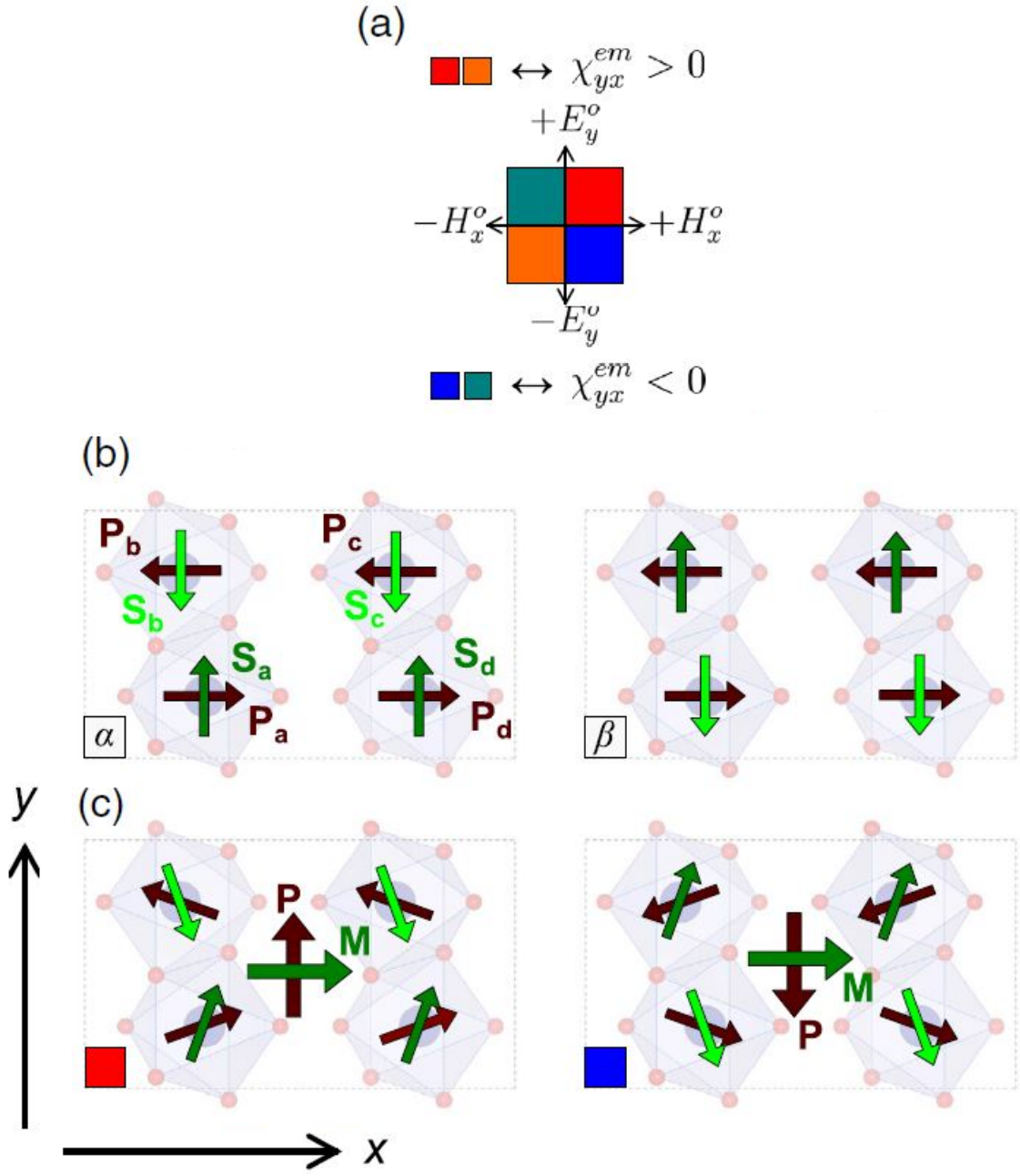

Figure 6.1: (a) Four combinations (+,+), (+,-), (-,+), (-,-) of poling fields (H_x,E_y) represented by four colors. (b) Spin and polarization pattern in α and β AFM domains: The spin sublattices (green and olive arrows) in α and β domains are interchanged, while the antipolar polarization pattern (brown arrows) is the same for the two domains. (c) Domains α and β are selected by the poling fields (+,+) (red) and (+,-) (blue) via the ME effect.

Early neutron scattering measurements revealed that below $T_N \approx 21.7$ K, a Néel-type AFM structure is formed with $S = 3/2$ spins mostly parallel the y axis [242] [see Fig. 6.1(b)], which was later ascribed to strong single-ion anisotropy [243, 244]. Consequently, the paramagnetic *Pnma* symmetry is reduced to the orthorhombic *Pnma′* space group.[1] The magnetic order breaks both time-reversal and the space inversion symmetries. Since $|Pnma|/|Pnma'| = 2$, two AFM domains are present, denoted as α and β, as displayed in Fig. 6.1(b). As the structural and the magnetic unit cells are identical, the antiferropolar and AFM orders are commensurate.

The low-temperature magnetic point group $m_x m_y m_z'$ allows two independent nonzero elements of the ME tensor, χ^{em}_{yx} and χ^{em}_{xy}. Since space-inversion and time-reversal symmetries are broken upon the magnetic ordering, they transform one domain to the other, thus their ME tensors have opposite signs, $\chi^{em}(\alpha) = -\chi^{em}(\beta)$. For this reason, the free energy of the domains are different when the $LiCoPO_4$ crystal is exposed to crossed electric and magnetic fields: equation

$$F_{ME} = \frac{1}{c}\chi^{em}_{yx} H_x E_y + \frac{1}{c}\chi^{em}_{xy} H_y E_x, \tag{6.1}$$

which allows domain selection by ME poling as depicted in Fig. 6.1(c). Values $\chi^{em}_{yx} \approx 30$ ps/m and $\chi^{em}_{xy} \approx 18$ ps/m were reported in literature [151, 245], which are one of the highest values among canonical linear magnetoelectrics. Due to the orthorhombic symmetry, the ME susceptibility is anisotropic: χ^{em}_{yx} is larger than χ^{em}_{xy} as the corresponding magnetic fields, H_x and H_y are perpendicular and longitudinal with respect to the AFM order, respectively. Actions of magnetic and electric fields upon probing χ^{em}_{yx} are depicted in Fig. 6.1(c).

Besides the magnitudes of ME tensor elements, their relative signs have to be known to have a complete knowledge of the ME tensor. A recent careful study showed that the two ME tensor components have the same sign [40], thus, the symmetric (traceless) part of the ME tensor related to a quadrupolar order is dominant over the antisymmetric part related to a ferrotoroidal order. As a result, when the poling electric and magnetic fields are simultaneously 90° rotated in the xy plane, they select the opposite domain, as observed in Ref. [40]. In fact, the ferrotoroidal order in $LiCoPO_4$ was predicted first on symmetry arguments [151], and later observed indirectly via the phase-sensitive SHG measurements [41, 246].

In the magnetically ordered phase, the volume fraction of the domains can be tuned by external fields just below T_N due to the strong magnetic anisotropy. At 17 K, i.e. 5 K below T_N, the "ME coercive field" was determined as $\mu_0 H_x E_y \approx 10$ T·kV/cm at 17 K, and rapidly increasing with decreasing temperature [246]. Similar trend was confirmed when modifying $LiCoPO_4$ domain structure with electric field pulses (0.5 ms–5 s) and magnetic field bias, while coercive field was even higher [247]. Dramatic increase of the coercive field upon shortening pulses from 5 s down to 0.5 ms suggests that domain wall dynamics gets very slow when temperature decreases. Therefore, short pulses can change the domain population only in the vicinity of T_N.

[1] More recent neutron diffraction measurements revealed that the spins are in fact uniformly rotated by ~4.6° around the x axis, reducing the magnetic space group to the monoclinic $P2_11'11$ [243]. Since this weak distortion is not relevant for my results, I will describe the present results assuming *Pnma′* magnetic space group.

6.2 Identification of Magnetoelectric Domains Via the Optical Magnetoelectric Effect

V. Kocsis who grow the $LiCoPO_4$ crystals characterized their ME properties as well. From the magnitude and saturation of the ME effect, he found that fields as small as $E_y \approx 0.1\,\mathrm{kV/cm}$ and $\mu_0 H_x \approx 0.1\,\mathrm{T}$ applied upon cooling through T_N establish a single-domain state. His measurements of static ME effect, $P_y = \chi^{em}_{yx} H_x$, and its temperature dependence are displayed in Fig. 6.2(a,b). He measured the magnetic-field-induced polarization after ME poling with all four combinations of the signs of the electric and magnetic fields, denoted with four colors as shown in Fig. 6.1(a).

According to the ME sum rule (Eq. 1.41), the static ME effect must be accompanied by ME excitations. Moreover, the off-diagonal ME response in $LiCoPO_4$ implies modes exhibiting DD and DB. Due to the four inequivalent Co ions in the unit cell, four magnon modes are expected in $LiCoPO_4$ based on classical spin-wave theory, and even much more modes are expected when $\Delta S > 1$ spin excitations are allowed.

I determined the real and imaginary parts of the refractive index spectra of $LiCoPO_4$ using TD THz spectroscopy with linearly polarized light H^{ω}_x, E^{ω}_y in order to investigate $\chi^{em}_{yx}(\omega)$. Spectra plotted in Fig. 6.2(c,d) with four different colors were obtained after poling the sample from $T > T_N$ to $T = 5\,\mathrm{K}$ using four combinations of the poling fields ($\pm H_x$, $\pm E_y$), as described for the static ME measurements. To observe the remanent changes, the fields were switched off during the measurements. Below T_N, two strong resonances appear at 1.13 THz and 1.36 THz for this light polarization, thus they must be of magnetic origin. The strength of the resonance at 1.36 THz (which I denote as mode #3, consistently with Refs. [40, 105]) strongly depends on the poling conditions, namely it is weak for the same signs and strong for the opposite signs of poling fields. Moreover, the two spectra obtained for the same sign of poling fields are identical within the precision of the experiment as well as the two spectra measured with poling fields of opposite signs. This indicates the strong ME character of the mode at 1.36 THz, and it also demonstrates the realization of either of the two ME domain states after the poling process. In contrast, the mode at 1.13 THz (denoted as mode #1) shows only a weak optical ME effect, with the opposite sign compared to mode #3.

The absorption difference detected for the time-reversed pair of ME domains implies that for the reversal of the light propagation the absorption contrast should be reversed. The direct observation of this DD, which has opposite sign for the two domains, requires changing source and detector, which is impossible in most of setups. In contrast, the setup I used, which I aligned by myself, allowed exchanging source and detector photoconductive antennae, while keeping the sample and the rest of the light path untouched. The results of this experiment are shown in Fig. 6.2(e,f). I verified that the absorption changes upon the reversal of light propagation for a given domain state. Spectra measured for light propagation along the $+z$ direction with the same sign of poling fields coincide with spectra measured for light propagation along the z direction with opposite signs of the poling fields. This observation implies that the DD indeed changes sign for the two domains. For the combination of propagation direction and domain state having lower absorption, the sample is nearly transparent even at the resonance frequency 1.36 THz. The large difference in κ corresponds to a factor of ≈ 300 in the light intensity transmitted by the two domains for sample of 1 mm thickness.

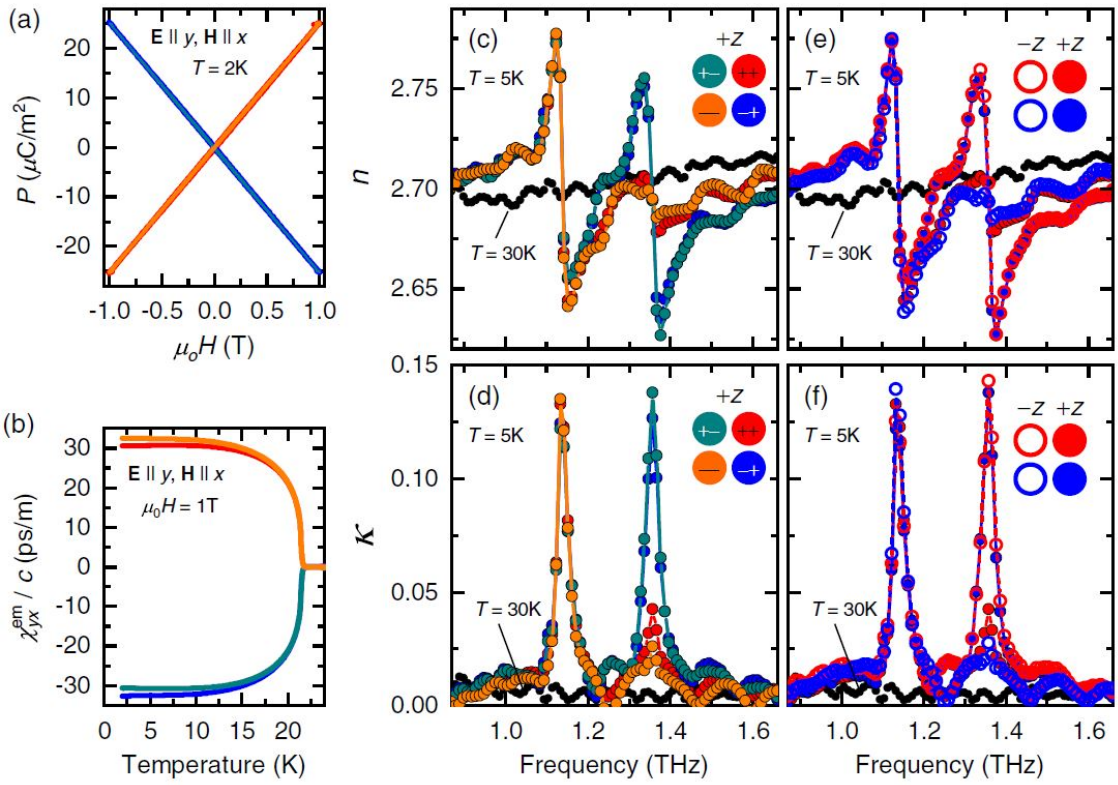

Figure 6.2: (a) Magnetic field dependence of the static ME effect at $T = 2$ K measured after poling the sample in the four combinations (+,+), (+,-), (-,+), (-,-) of poling fields ($H_x = 0.1$ T,$E_y = 1$ kV/cm). The poling fields were switched off during the measurement; hence, the linear slope of the polarization (P) versus magnetic field curve shows the linear ME effect. (b) Temperature dependence of the linear ME effect, χ^{em}_{yx}, measured in warming up after poling in the four configurations of (H_x,E_y). Spectra of the (c) real and (d) imaginary part of the refractive index at $T = 5$ K measured after poling. Spectra of the (e) real and (f) imaginary part of the refractive index measured at $T = 5$ K after poling in two selected configurations, (+,+) and (+,+) and for light propagation along the $+z(= x \times y)$ direction (full symbols) and the $-z$ direction (open symbols). The spectra in (c)–(f) were measured using linearly polarized light with (H^{ω}_x,E^{ω}_y). Spectra measured in the paramagnetic state are plotted in black. The color of each curve corresponds to the applied poling process following the convention introduced in Fig. 6.1(a).

My analysis showed that for a given light propagation directions, when the cross-product of the poling fields and the light propagation point to the same direction, i.e. $H_x^\omega \times E_y^\omega \uparrow\uparrow H_x^0 \times E_y^0$, mode #3 has the high-absorption state, thus it has a positive contribution to the static ME effect according to Eq. 1.41. Mode #1 showing DD with opposite sign has negligible contribution to the static ME effect. Quantitative evaluation of the sum rule was elaborated in a later work of my colleagues [40].

In summary, I demonstrated the detection of AFM domains in $LiCoPO_4$ by the measurement of THz DD. My experiments showed that DD can be finite even in zero external fields, in contrast to experiments performed so far [7–9, 71, 77, 91–104]. In these previous works, DD is commonly identified by measuring the absorption spectra under magnetic (or electric) fields with opposite signs, however, here I directly detected the change in the absorption upon the reversal of the light propagation. Although the AFM domains can also be identified via phase sensitive SHG, those experiments require high precision in the alignment of the optical setup and intense laser beams. In contrast, linear THz spectroscopy that I applied is an easy and sensitive technique nowadays. Moreover, the huge absorption contrast at 1.36 THz allows the detection of small changes in domain population. Due to the long wavelength of the THz radiation the spatial resolution of this techniques is rather poor. However, DD may be present even at higher frequencies for local Co excitations, while allowing microscopic identification of AFM domain structure, similar to SHG microscopy measurements.

6.3 Idea of selecting magnetoelectric domains by electromagnetic radiation

The fact that the *static* ME effect can control (write) and identify (read) the ME domains in $LiCoPO_4$ was known long time ago [242]. In the previous section, I demonstrated that the *dynamic* ME effect can also identify the ME domains. A logical question arises: To complete the puzzle, is it also possible to control the ME domains by the dynamic ME effect? By symmetry, this effect is allowed: It is enough to realize that the ME susceptibility components in Eq. 6.1 are nonzero at finite frequencies, which is obvious from the ME sum rule and observation of DD, mentioned in previous section. Thus, the energy of the two domains is supposed to be different when oscillating electric and magnetic fields act inside the material. Since the oscillating electric and magnetic fields of the EM radiation are perpendicular to each other just like the static fields used to select the domains, linearly polarized EM radiation propagating in the $LiCoPO_4$ may result in a finite free energy difference between the domains (Eq. 6.1). Even though the electric and magnetic fields of light oscillate quickly, sign of their product is unchanged for a given light propagation (and linear polarization), thus the time average of this energy is non-zero. Moreover, when illuminating the sample from the other side, the product of the fields changes the sign, and the other domain should be selected based on a symmetry ground.

Such an idea suggested by my supervisor, S. Bordács and I. Kézsmárki, is based on an analogy between the static and dynamic cases, and it is a non-trivial question if this phenomena is realized and if so what the (microscopic) processes behind are. If one wanted to apply a continuous wave at THz frequencies with similarly high fields sufficient for static poling ($E_y^\Omega H_x^\Omega = 0.01\,\mathrm{T{\cdot}kV/cm}$, Ω denotes the frequency of the poling EM

radiation), extremely intense EM radiation would be needed (10^3 W/mm^2) which would burn the crystal even if illuminating in its nearly transparent area. For this reason and for unavailability of high-intense CW sources of THz radiation, I decided to use pulsed source of THz radiation, which makes the analogy with static poling even more distant.

I selected FELBE free-electron laser (FEL) at Helmholtz-Zentrum Dresden-Rossendorf, Germany, as the optimal source to attempt for selection of ME domains in $LiCoPO_4$. The key parameter is its narrow bandwidth (see Tab. 2.1), which allows to study the effect at precisely defined frequencies along the ME resonances. Its high repetition rate is an also important parameter, by which the poling resembles more the static poling with well-defined static fields.

6.4 Selecting magnetoelectric domains by electromagnetic radiation - results

6.4.1 Basic poling experiment with THz probe

I aimed to select one of the ME domains by cooling the sample through T_N in the presence of intense THz radiation of the FEL. First, I set the FEL polarization to be $\boldsymbol{E}^{\Omega} \parallel y$ & $\boldsymbol{H}^{\Omega} \parallel x$, since the poling is the most effective for $\boldsymbol{E}^0 \parallel y$ $\boldsymbol{H}^0 \parallel x$ in case of static fields, and the strongest ME resonance at 1.36 THz (mode #3) is also present for this polarization. While irradiating the sample by the FEL with $\Omega = 1.35$ THz tuned to the vicinity of the ME resonance, I cooled the sample through T_N to the lowest achievable temperature ($\sim$5 K). I used a slow well-defined cooling rate (5 K per minute) so that the temperature change in between the pulses is negligible even in the vicinity of T_N where the poling occurs. After reaching the base temperature, I blocked the FEL beam and probed the induced imbalance of domain population by THz transmission spectroscopy.

After poling by the FEL with highest available beam power 1.1 W, at $\Omega = 1.35$ THz, I probed the distribution of the domain population by linear THz spectroscopy. The results are depicted in Fig. 6.3(e). I irradiated the crystal from one side, as depicted in Fig. 6.3(a), and measured THz spectra while illuminating the sample from both sides [Fig. 6.3(c,d)], to directly probe DD. Here, the setup did not allow exchanging the source and detector, so I rotated the cryostat while keeping the crystal at low temperature. Indeed, I observed absorption contrast at #3 ME resonance almost as high as reached by the static poling: Red and blue solid lines in Fig. 6.3(e) refer to the FEL poling experiment, while red and blue lines with dots refer to the static poling experiment, reproduced from Fig. 6.2(f). Black curve, measured without FEL poling lies in the middle as expected for a sample with equally distributed domains, which confirms that an external stimulus is essential to create a domain imbalance. Assuming that the poling by static fields establishes a single domain, the FEL beam with power 1.1 W results in 80%:20% volume ratio. For lower powers, absorption contrast was smaller, while scaling roughly linearly with power up to 1.1 W (not displayed), signing that also high FEL powers are essential for considerable domain selection.

Unfortunately, when I irradiated the crystal from the other side, as depicted in Fig. 6.3(b), I did not observe any FEL-induced change in the THz spectrum. I confirmed that this is due to the heating of the FEL: When I was simultaneously irradiating

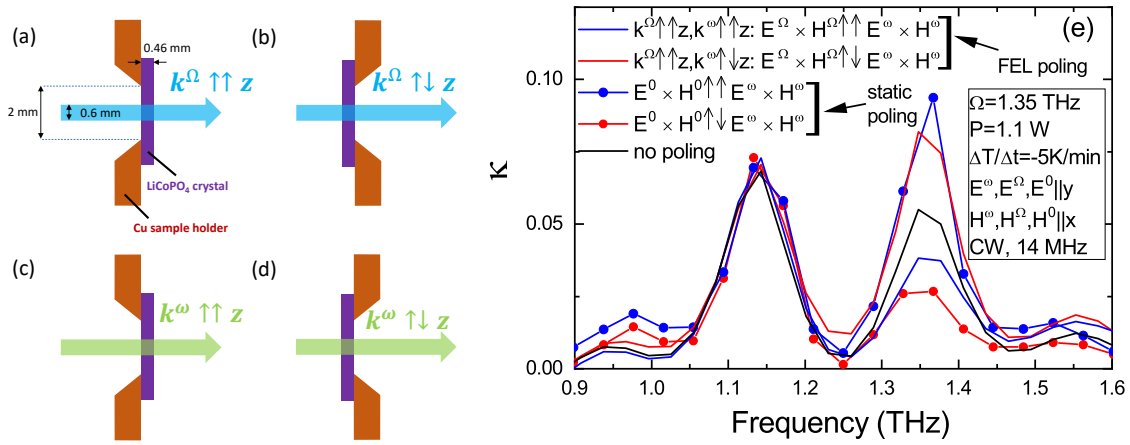

Figure 6.3: (a)-(d) Sketch of the experiment at FELBE showing directions of (a,b) FEL poling beams and (c,d) THz probing beams. $LiCoPO_4$ crystal was possible to pole by FEL only when the FEL illuminated the sample from the side closer to the sample holder, panel (a). When the crystal was illuminated from the other side [panel (b)], FEL with even small energy heated the sample above T_N, thus preventing poling. After the sample was poled by the FEL, the FEL beam was blocked and domain imbalance was probed by THz spectroscopy. First, I illuminated the sample from the same side as the FEL, panel (c). Then, I rotated the cryostat while keeping the crystal at the base temperature, and probed the domain imbalance from the other side, panel (d). In panel (a), dimensions of relevant parameters are marked: sample aperture ≈ 2 mm, beam waist ≈ 0.6 mm and sample thickness ≈ 0.46 mm (e) THz spectroscopy results after FEL poling, compared with results of static poling from Fig. 6.2(f). Both FEL and probing light beams had the same polarization, $\boldsymbol{E}^{\Omega} \| y$ & $\boldsymbol{H}^{\Omega} \| x$ and $\boldsymbol{E}^{\omega} \| y$ & $\boldsymbol{H}^{\omega} \| x$.

the sample by the FEL and measuring THz spectrum at $T = 5\,\mathrm{K}$ nominal temperature of the cryostat, the magnon modes disappeared for much lower FEL power compared to the case depicted in Fig. 6.3(a). In the experimental geometry shown in Fig. 6.3(b), the irradiated face of the sample, which is glued on the cold finger of the cryostat, was further away from the heat bath, thus, the low heat conductivity of the electrically insulating $LiCoPO_4$ crystal results in higher temperatures limiting the highest applicable FEL power.

Interestingly, the FEL selects the opposite domain than the static fields: Using static fields ($\boldsymbol{E}^0 \| y$, $\boldsymbol{H}^0 \| x$), the domain with higher absorption at the #3 resonance is selected when the propagation of the probe beam is chosen to point along the cross product of the static fields – $\boldsymbol{E}^0 \times \boldsymbol{H}^0 \uparrow\uparrow \boldsymbol{E}^\omega \times \boldsymbol{H}^\omega (\uparrow\uparrow \boldsymbol{k})$. In contrast, the low-absorption domain is stabilized by the FEL $\boldsymbol{E}^\Omega \times \boldsymbol{H}^\Omega \uparrow\uparrow \boldsymbol{H}^\omega \times \boldsymbol{E}^\omega (\uparrow\uparrow \boldsymbol{k})$, here again ($\boldsymbol{E}^\Omega \| y$, $\boldsymbol{H}^\Omega \| x$). As the mechanism of domain selection is different for static and high-frequency fields, the study of the frequency dependence is highly desirable.

6.4.2 Frequency dependence of poling efficiency

I studied effect of FEL in the frequency range of 1.25–2 THz. The low-frequency edge is determined by working range of FELBE. I always followed the same protocol: I cooled the crystal with a well-defined cooling rate of 5 K/min upon FEL irradiation. After, I blocked the FEL beam, at $T = 5\,\mathrm{K}$ I measured THz spectra with the same propagation direction as the FEL. By comparing THz spectra to a single-domain spectra reached by static poling from Fig. 6.2(f), I determined volume ratio of the domains. Since this volume ratio increases linearly with the FEL power, I can define the poling efficiency for each FEL frequency as the domain ratio which would be achieved by using FEL power of 1 W. Such poling efficiency can be taken as a function of FEL frequency to determine for which FEL frequencies, the FEL poling is the most efficient.

The spectrum of poling efficiency is displayed in Fig. 6.4 together with a representative THz absorption spectra measured at 5 K for comparison. The green curve shows the poling efficiency for $\boldsymbol{E}^\Omega \| y$ & $\boldsymbol{H}^\Omega \| x$ FEL polarization. Clearly, the poling efficiency is enhanced in the vicinity of the ME resonance, which suggests that the DD is responsible for the FEL induced changes. The peak in the spectrum of poling efficiency is broader and little shifted with respect to the THz spectrum. This can be ascribed to the broadening and red-shift of the ME resonance close to T_N where the poling occurs [40]. More intriguingly, the poling efficiency is nonzero even far away from the ME resonance at 2 THz. In fact, at this frequency, there is a very weak ME resonance for $\boldsymbol{E}^\omega \| y$ & $\boldsymbol{H}^\omega \| x$ polarization which shows DD with opposite sign compared to #3 mode. However, this resonance should not influence the poling, since it appears at temperatures only well below T_N, while poling occurs around T_N [40]. The finite poling efficiency at 2 THz may either sign that this is because of some ME resonance, which gets much broader close to T_N, or the effect may work off-resonantly as well.

At 2 THz, I also rotated FEL polarization to $\boldsymbol{E}^\Omega \| x$ & $\boldsymbol{H}^\Omega \| y$ and evaluated the corresponding poling efficiency. In this range, there is no ME resonance for this light polarization [40]. I found that even for this case (magenta point in Fig. 6.4), the poling efficiency is finite, albeit little smaller than for the off-resonant case in the $\boldsymbol{E}^\Omega \| y$ & $\boldsymbol{H}^\Omega \| x$ polarization. More importantly, the same ME domain is selected for the rotated FEL polarization, i.e. for $\boldsymbol{E}^\Omega \times \boldsymbol{H}^\Omega \uparrow\uparrow \boldsymbol{E}^\omega \times \boldsymbol{H}^\omega (\uparrow\uparrow \boldsymbol{k})$, the crystal ends up in the low-absorption

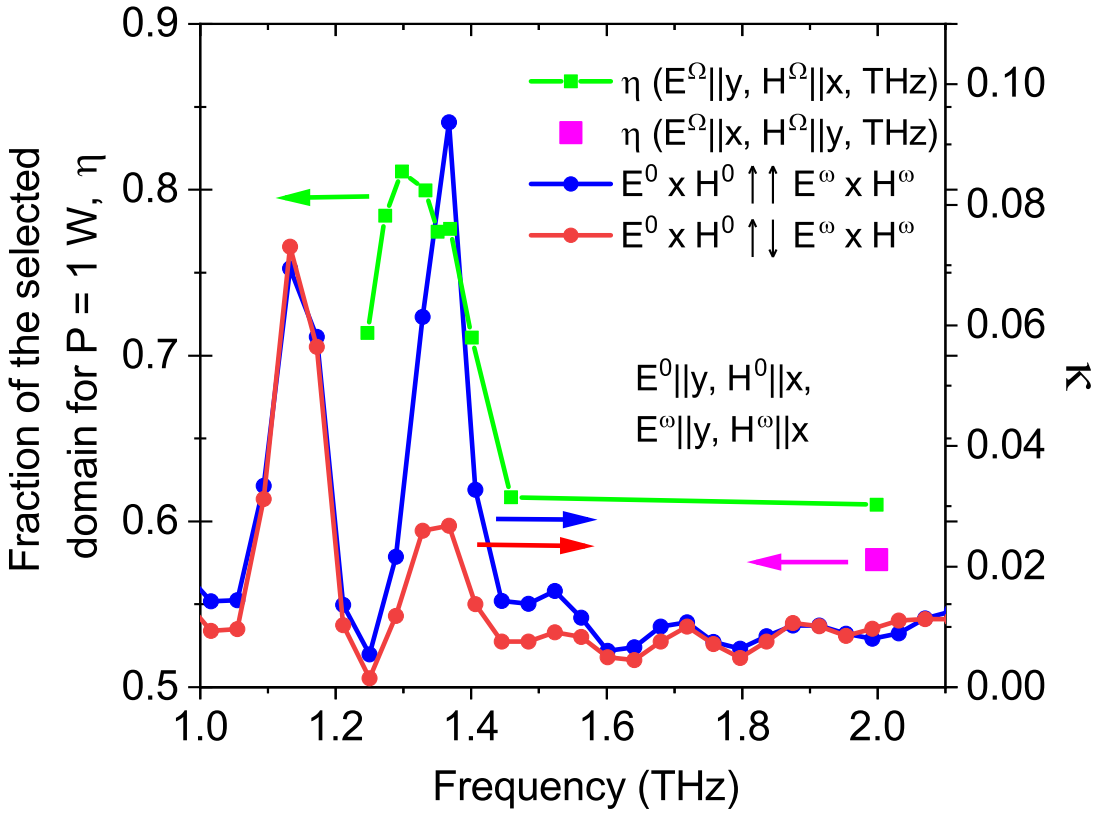

Figure 6.4: Frequency dependence of poling efficiency, η, defined as the domain ratio which would be achieved by using FEL power of 1 W, for both FEL polarizations (left axis). The domain ratio was determined strength of mode #3 in linear THz spectra. Note that $\eta = 0.5$ means non-poled crystal, while $\eta = 1$ means fully-poled crystal. For both FEL polarizations, FEL irradiation caused decrease of absorption at the #3 resonance when $\boldsymbol{E}^{\Omega} \times \boldsymbol{H}^{\Omega} \uparrow\uparrow \boldsymbol{H}^{\omega} \times \boldsymbol{E}^{\omega}$. Representative single-domain spectra for high- and low-absorption states reached by static poling [same as in Fig. 6.2(f) and Fig. 6.3(e)] are shown to see relation between the ME resonance and poling efficiency (right axis).

state in $\boldsymbol{E}^{\Omega} \parallel y$, $\boldsymbol{H}^{\Omega} \parallel x$ FEL polarization. Note that this is contrasting with the static ME effect, in which rotated fields select the opposite domains [40], which again implies that the direct analogy with the static ME effect is inappropriate. Again, nonzero poling efficiency for this light polarization may be an off-resonant feature, or it may come from some higher-energy excitations, broadening and softening close to T_N [40].

6.4.3 Summary of the first part, improvement of the experiment

In the previous two subsections, I demonstrated that light fields can not only be applied to detect the ME domains of $LiCoPO_4$, but also to select one of the domains. I found that the selection of ME domains is more efficient at ME resonances. However, due to sample heating, I could not study this effect when illuminating the sample from the side not touching the cold finger of the cryostat.

I encountered another issue: the sensitivity and resolution of THz spectroscopy makes quantitative evaluation of the volume ratio of the domains difficult. Moreover, in contrast to optical pump-probe setups where the probe area is usually much smaller than the pump area, here, the two areas are comparable, because I focused the FEL and the probe beam with the same parabolic mirror and it is difficult to control the spot size at such long wavelength where the diffraction-limited spot size is supposed to be similar. Nevertheless, since I used an aperture bigger than the spot size [2 mm vs. $\sim$0.6 mm, see Fig. 6.3(a)], it is possible that the absorption contrast I observed was systematically lower due to mismatch of FEL and THz probe beams. Moreover, when investigating poling efficiency over a broad frequency range, the spot size may vary a lot.

Besides THz spectroscopy, two other probes of AFM domains have been exploited so far: the measurement of the static ME effect, and SHG. The latter one allows microscopic visualization of ME domains, but the method is difficult to develop and its sensitivity is limited. On the other hand, measurement of the static ME effect is highly sensitive and quantitative, therefore, I applied this technique, while differences between the old and new setup related to thermal contact are shown in Fig. 6.5 . A small modulation coil provided an oscillating magnetic field ($\approx$ 1 mT) along the x axis, which generates an oscillating polarization along the y axis via the linear ME effect. Side-contacts painted by silver paste allowed the detection of this polarization component, or more precisely, the magnetocurrent induced by the time-varying polarization. I detected this signal proportional to the ME susceptibility by a lock-in amplifier as described in Sec. 2.5. A disadvantage of this method is that it measures the ME effect of the whole sample and not only the illuminated area. I improved the thermal contact between the sample and the cold finger by making the aperture smaller (1 mm vs. 2 mm) and the electrodes also carried some heat away. The reduced crystal lateral dimensions have several advantages: First, the detection area is not much larger than the aperture and the spot size, thus less signal from possibly ambiguously-oriented domains is detected. Next, the reduced dimension in x direction (not displayed) allowed to place the coil producing modulation current closer to the sample. Finally, the electrodes placed to the sample allowed effective heat transport to the copper plate. To have the best heat transport, the sample was placed directly onto a copper plate, and insulation polypropylene (PP) foil was placed only aside. In order to prevent from shortcut of the silver paste with the copper plate, diluted BF2 glue was put along the sample edge area (not displayed) and dried over a night before adding the silver

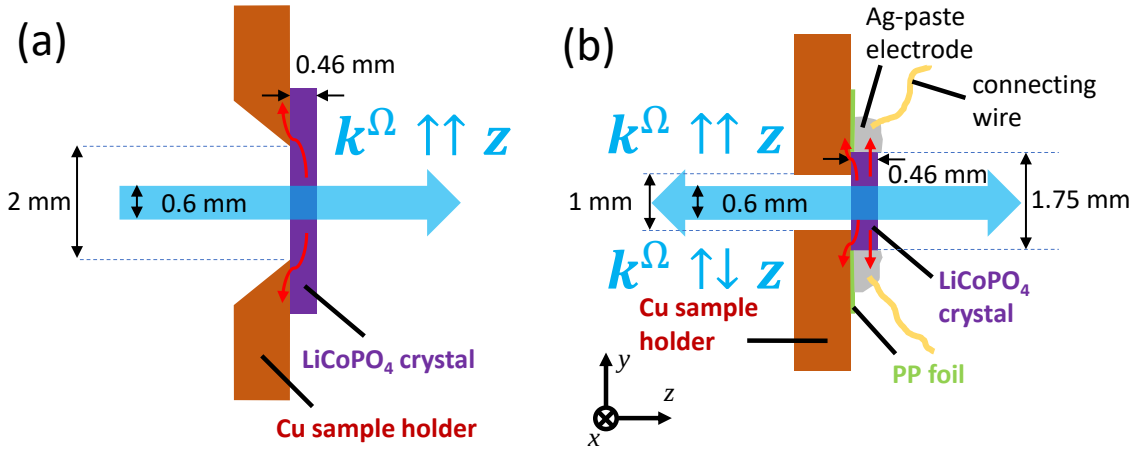

Figure 6.5: (a) Old and (b) new sketch of the experiment at FELBE. Several differences can be seen between panels (a) and (b), as described in the main text.

paste.

The installed leads allowed to apply static electric field to employ the static ME poling. In this case static magnetic fields were provided by strong NdFeB magnets placed outside the cryostat, producing field 0.2 T at the sample position. Possibility of static poling allowed me to calibrate the ME signal, which would be otherwise difficult to quantify due to several geometrical constraints. Moreover, it allowed me to study combined effect of static and FEL poling.

6.4.4 Extended poling efficiency measurements by the detection of ME susceptibility

By probing the ME susceptibility, I investigated effect of the FEL on domains at several frequencies for both FEL polarizations. I followed the same protocol as previous time: I cooled the crystal with cooling rate 5 K/min through T_N and at low temperature, I probed the domain imbalance by measuring the quasi-static ME effect. Here, I estimated magnitude of the effect simply by the measured ME signal. Since there was a parasitic signal coming from leads, I took the difference of the ME signal with respect to the paramagnetic phase, in which the ME effect should disappear by symmetry. To normalize the signal and determine sign of the effect, I used static poling fields. I again verified linear dependence of the ME effect on the FEL intensity for low FEL intensities below saturation.

Compared to previous experiments using THz probe, much lower nominal FEL powers were needed to reach comparable domain selection in the current experiment. This can be possibly ascribed to different power measurement: In the previous setup, I had to measure the power of the beam long distance before the cryostat, so the actual power at the sample position was probably systematically lower due to some losses, even though THz radiation is transparent in the frequency range of the #3 resonance. Other source of the systematically lower poling efficiency while using THz probe can be ascribed to mismatch of FEL and probing THz beam. Later, I show that the thermal gradient is crucial for the effect, thus different thermal contact can be the other reason, among others. Therefore,

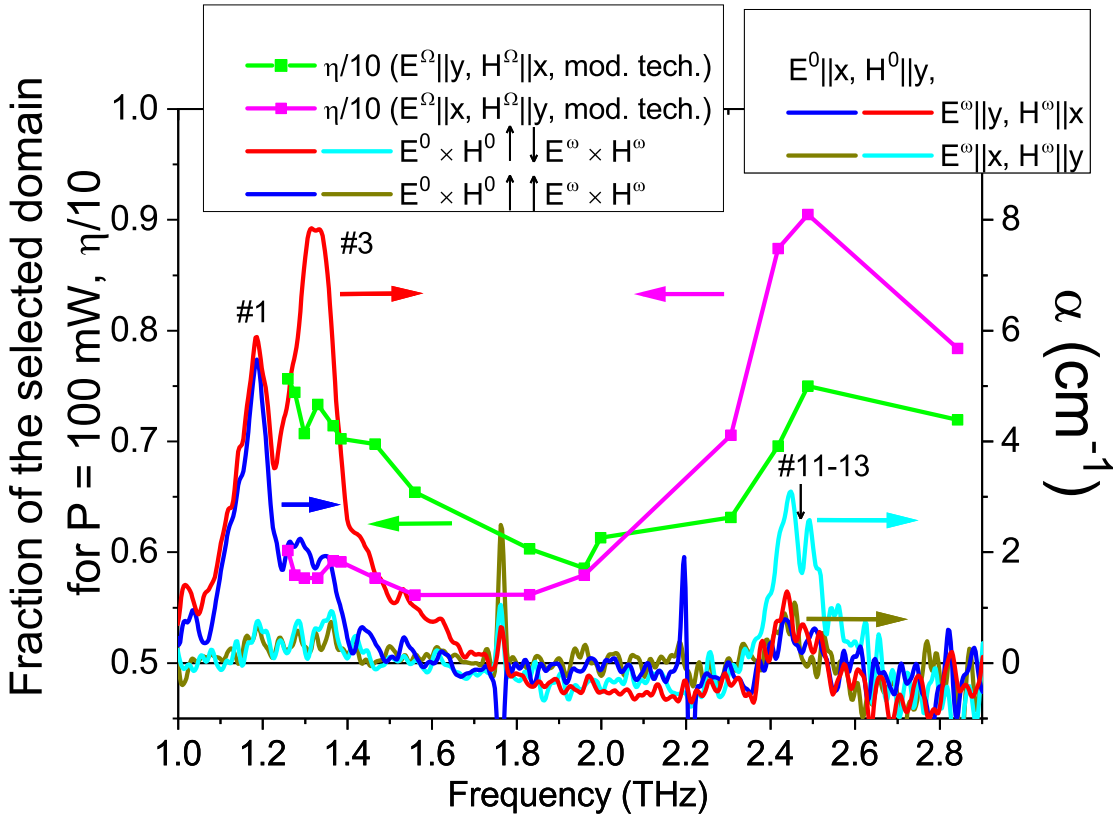

Figure 6.6: Frequency dependence of 10-times reduced poling efficiency $\eta/10$, defined as the domain ratio which would be achieved by using FEL power of 100 mW, for both FEL polarizations – $\boldsymbol{E}^{\Omega} \| y$, $\boldsymbol{H}^{\Omega} \| x$ and $\boldsymbol{E}^{\Omega} \| x$, $\boldsymbol{H}^{\Omega} \| y$ (left axis). The ME effect was measured by modulation technique. Note that η =0.5 means a non-poled crystal, while η =0.5 means a fully-poled crystal. In both cases, FEL irradiation caused decrease of absorption at the #3 resonance when $\boldsymbol{E}^{\Omega} \times \boldsymbol{H}^{\Omega} \uparrow\uparrow \boldsymbol{H}^{\omega} \times \boldsymbol{E}^{\omega}$. (Confirmed by later THz detection.) Representative single-domain spectra of absorption coefficient α at 21 K for high- and low- absorption states reached by static poling, for $\boldsymbol{E}^{\omega} \| y$, $\boldsymbol{H}^{\omega} \| x$ and $\boldsymbol{E}^{\omega} \| x$, $\boldsymbol{H}^{\omega} \| y$ light polarizations. These data are taken from Ref. [40], and they were measured after static poling in the $\boldsymbol{E}^{0} \| x$, $\boldsymbol{H}^{0} \| y$ fields, i.e. 90°-rotated fields compared to rest of cases in this chapter. Note that such rotated fields select the opposite domain. The modes assignment also follows Ref. [40].

here I display fraction of the selected domains for $P = 100\,\mathrm{mW}$, i.e. poling efficiency divided by the factor of 10; saturation was reached much below $P = 1\,\mathrm{W}$.

The evaluated poling efficiency for both polarizations in range 1.25–2.85 THz is displayed in Fig. 6.6. I compare these curves with absorption spectra measured in single domain sample for both light polarizations, reproduced from Ref. [40]. These low-noise spectra, measured with TeslaFIR setup in Tallinn by my colleagues, were taken at 21 K, i.e. just below T_N, at which the poling occurs. Therefore, they are more appropriate to compare to poling efficiency than the low-temperature spectra.

First, I briefly summarize the dynamic ME effect of the spin excitations appear in the frequency range studied at the FEL. Besides #3 ME resonance, there are two other resonances in $\boldsymbol{E}^{\omega} \parallel y$, $\boldsymbol{H}^{\omega} \parallel x$ light polarization: First, a very weak #6 resonance at 2 THz, which can be discerned only at temperatures below 10 K with opposite sign of DD compared to #3 resonance. Second, a #11-13 triplet at 2.4–2.6 THz, exhibiting a small DD with the same sign as #3 resonance – although the DD cannot be distinguished in Fig. 6.6, the absorption peak is still visible at 21 K. This triplet is stronger and exhibits stronger DD in the other light polarization – $\boldsymbol{E}^{\omega} \parallel x$, $\boldsymbol{H}^{\omega} \parallel y$ – as clear from Fig. 6.6. Importantly, both the resonance #3 in $\boldsymbol{E}^{\omega} \parallel y$, $\boldsymbol{H}^{\omega} \parallel x$ light polarization and resonance #11-13 in both polarizations are in the high-absorption state for the domain selected by static fields $\boldsymbol{E}^{0} \parallel y$, $\boldsymbol{H}^{0} \parallel x$ when $\boldsymbol{E}^{0} \times \boldsymbol{H}^{0} \uparrow\uparrow \boldsymbol{H}^{\omega} \times \boldsymbol{E}^{\omega}$. The only ME resonance which is in the low-absorption state under these conditions is a weak #6 resonance. (Features at 1.76 THz and 2.2 THz in Fig. 6.6 are related to experimental errors.)

After analyzing the linear spectra, it is easier to interpret spectra of poling efficiency in Fig. 6.6. For $\boldsymbol{E}^{\Omega} \parallel y$, $\boldsymbol{H}^{\Omega} \parallel x$ poling (green curve), the poling efficiency is enhanced near #3 resonance, consistently with previously evaluated poling efficiency from THz domain identification in Fig. 6.4. Moreover, it is enhanced to similarly high values in the range of resonance #11-13, which is rather surprising, since this resonance and its DD are much weaker than of #3 resonance. Moreover, for $\boldsymbol{E}^{\Omega} \parallel x$, $\boldsymbol{H}^{\Omega} \parallel y$ poling (magenta curve), the poling efficiency in range of #11-13 resonance increases to higher values than for $\boldsymbol{E}^{\Omega} \parallel y$, $\boldsymbol{H}^{\Omega} \parallel x$ poling. This is consistent with stronger DD of #11-13 resonance in $\boldsymbol{E}^{\omega} \parallel x$, $\boldsymbol{H}^{\omega} \parallel y$ polarization, and signs that resonance #11-13 is much more efficient for FEL poling.

As a general result, I found that the same domain is selected independent of the frequency or polarization of the FEL. This may be explained by the fact that the DD spectrum is dominated by ME resonances, which have contributions with the same sign - they have lower absorption if $\boldsymbol{E}^{\Omega} \times \boldsymbol{H}^{\Omega} \uparrow\uparrow \boldsymbol{H}^{\omega} \times \boldsymbol{E}^{\omega}$. In other words, the more transparent domain is always selected. The fact that the poling efficiency is finite away from resonances might be explained by their huge broadening close to T_N.

The biggest puzzle is much higher poling efficiency for the #11-13 resonance compared to #3 resonance. Note that in Fig. 6.6, absorption coefficient α is displayed instead of ME susceptibility, thus, since $\alpha \propto \chi^{em} \cdot \omega$, the contrast between strength and DD is even larger in κ which I display in Fig. 6.4. Thus, the contrast in between effects of #11-13 and #3 resonance may be viewed even larger depending of how I define the quantities.

There are several questions to be answered: Does the poling efficiency naturally grow with frequency? Or is the poling efficiency specific to each mode? Is the ME character of the mode and its DD contrast relevant for the effect at all, or one can observe the same enhancement for any absorption peak? All these questions could be answered only when measuring FEL effect at frequencies of other resonances – I could not measure the effect

at the frequency of weakly ME magnon at 1.1 THz due to low-frequency limit of U-100 undulator of FELBE, but other magnetic modes may appear at higher frequencies where FELBE operates well. I believe that such huge contrast between the resonances cannot be ascribed to frequency, and it must be specific for each mode. Also, I believe that the ME character of modes should be important, and I expect the poling efficiency to be minute when illuminating at frequencies far from the ME modes. However, these hypotheses should be verified by future experiments.

Last but not least, I note that for the high poling efficiency configurations, the effect was so huge that for high FEL powers, also domains not directly illuminated were affected: If I assume that the illuminated area was fully-poled to a single-domain state, it means that 70% of the rest crystal volume was poled as well for $P = 100\,\mathrm{mW}$ for $\boldsymbol{E}^{\Omega} \parallel x$, $\boldsymbol{H}^{\Omega} \parallel y$ at $\Omega = 2.48\,\mathrm{THz}$. Therefore, the effect could not be simply ascribed to direct impact of FEL on domains, but some correlation effects play a role.

6.4.5 Full symmetry analysis and discussion of possible microscopic mechanisms

I found that the poling efficiency is the highest for $\boldsymbol{E}^{\Omega} \parallel x$, $\boldsymbol{H}^{\Omega} \parallel y$ polarization at $\Omega = 2.49\,\mathrm{THz}$, while the average absorption remains moderate. Therefore, I illuminated the crystal from the other side, as displayed in Fig. 6.3(b). This experiment was previously challenging due to overheating, however, I hoped that the high poling efficiency will allow me to detect finite domain imbalance even at smaller FEL powers.

I expected that the FEL stabilizes the domain with opposite linear ME susceptibility compared to the case depicted in Fig. 6.3(a) or equivalently, the one with smaller absorption at mode #3 measured with a co-propagating probe beam. However, after poling with the FEL illuminating the sample as shown in Fig. 6.3(b), the sign of the ME susceptibility remained the same. Since this effect is surprising, I verified it by THz detection: When the crystal was illuminated from the side glued to the sample holder [Fig. 6.3(a)], the more transparent domain was selected for co-propagating FEL and detection THz pulses. In contrast, when the crystal was illuminated from the side not touching the sample holder [Fig. 6.3(b)], the more absorbing domain was selected for co-propagating FEL and detection THz pulses. This means that not only the intrinsic crystal symmetry, but also some extrinsic effects play a role.[2] The extrinsic effects may be related to some defects in the crystal or to the laboratory settings. I excluded the former case by carrying out the FEL poling experiment while gluing the crystal the other way: Indeed, I confirmed that the sign of the effect depends on relative crystal orientation with respect to the sample holder, but not the absolute orientation of the z axis of the crystal. Therefore, I conclude that the FEL-induced domain imbalance must be related to the m_z symmetry breaking by the laboratory settings.

This peculiar effect can be analyzed from a symmetry point of view. In a free-energy expansion, the external stimulus distinguishing between the domains should couple to first or at least odd powers of the order parameter. Since the magnetic order breaks time-reversal and inversion symmetries, the stimulus should also break both. It is clear

[2]Note that in the paramagnetic state, $LiCoPO_4$ has m_z symmetry plane, perpendicular to light propagation. Therefore, it should matter only on relative direction of FEL and probing beam, but not on absolute orientation of the crystal and the FEL beam.

that the laboratory settings breaks the inversion symmetry, as there is a sample holder on one side of the sample, but not on the other. Nevertheless, it must be responsible for some time-reversal symmetry breaking quantity in order to explain the observed effect. There are limited number of effects which I can imagine, most of them are obvious. Already from previous experiments, it is clear that there is a temperature gradient, which I consider as the most probable source of the effect. Although the temperature gradient breaks space inversion, it respects time-reversal symmetry. Nevertheless, temperature gradient is always accompanied by a heat flow, which breaks time reversal symmetry. Other space-inversion breaking quantity may be a strain gradient, thus a stress gradient due to the fact that the crystal is attached to a copper sample holder with different thermal expansion coefficient. In principle, the stress gradient can be also coupled to a heat flow, but this effect is supposed to be negligible, since stress effects play a role mostly in thin layers, but I measure a bulk crystal. Therefore, from a symmetry point of view, I ascribe the effect to a FEL-induced temperature gradient and subsequent heat flow. Importantly, a direction of the temperature gradient must be the same irrespective of FEL propagation direction; I naturally expect the colder side to be closer to the sample holder.

What is then the microscopic mechanism behind the FEL poling? I assume the limit of low absorption (which is justified as the poling occurs just below T_N): Since the inverse of the absorption coefficient is much larger than the thickness of the sample, d, $\alpha << 1/d \approx 10\,\mathrm{cm}^{-1}$, the power (per unit area) deposited by the FEL is approximately uniform along the propagation direction. Thus, only the position of the crystal with respect to the sample holder matters for both FEL propagation directions: Upon cooling, the cold side of the crystal closer to the copper sample holder is cooled down through T_N sooner than the other side. Since the strength of the ME excitations increases with decreasing temperature, the light creates more ME excitations in the colder part. Due to diffusion, they propagate to the hotter part, which breaks the time-reversal symmetry. It is possible that such propagation can be non-reciprocal, i.e. different for opposite domains, which may favor one or the other domains. Note that nonreciprocal propagation of quasiparticles was reported several times, as also mentioned in Chapter 1. For ME quasi-particles, such nonreciprocity is more natural, even though any quasi-particle can exhibit nonreciprocal propagation when ODA is allowed by symmetry [75]. Specific microscopic mechanism of such nonreciprocal propagation, and especially the dynamics of this process, are far beyond the scope of this thesis and they would require a careful microscopic and mesoscopic theoretical investigation.

Note that the ME excitations are assumed to propagate opposite to heat propagation, i.e. opposite to acoustic phonons, carrying the heat. With the same symmetry argument, propagation of thermally-activated acoustic phonons may be causing the observed effect. A remarkable enhancement of the poling efficiency spectra at frequencies of ME resonances stresses their vital role, but the FEL poling worked for all observed frequencies, thus acoustic phonons may be responsible for the effect away from resonances. Moreover, there may also be some thermally activated magnons: Despite high magnetic anisotropy, a magnon reaching frequency as low as 0.29 THz was found by the inelastic neutron scattering [244], and these magnons should be thermally activated near T_N. Moreover, one should realize some consequences of a pulsed regime: Since the pulses are present in ≈ 30 ps within 71.5 ns (i.e. 0.04% of time) and the lifetime of the ME resonances is in the order of few ps close to T_N, the process of nonreciprocal propagation of FEL-excited ME

resonances occurs only for a short fraction of time. In contrast, nonreciprocal propagation of thermally-activated quasi-particles can happen without interruption. Therefore, even thermally activated high-energy ME resonances may contribute to off-resonant (frequency-independent) part of the effect: Although their number is much smaller than number of thermally activated phonons, their nonreciprocal propagation, responsible for the effect, it is potentially much higher than for phonons, as shown from the increase of poling efficiency at their frequencies.

Importantly, when the FEL illuminated the side of the sample further from the copper plate (the hotter one), the effect was little larger than if FEL illuminated the colder side. This can be easily understood on a qualitative level by the fact that illuminating the hotter side further increases temperature gradient, thus the heat flow. In fact, I suspect that in the case of high absorption near T_N, caused for example by a strong magnon or a phonon tail, the heat gradient could change the sign, so the other domain could be in principle selected. Nevertheless, the magnitude of the effect is comparable for opposite FEL directions, thus the effects contributing to such difference must be negligible compared to a major mechanism of the FEL poling. Even though I cannot determine microscopic mechanisms behind the observed effect, the symmetry of the effect excludes processes contradicting the symmetry. These are processes which depend on FEL propagation direction. In the following, I list the processes which should be negligible due to the symmetry reasons:

1. The original idea that one or the other domain is preferred upon FEL fields in analogy to the static ME effect: Since the relative phase of fields are opposite to each other for opposite FEL propagation, the oppositely propagating lights should select the opposite domains. (This scenario was already not supported by observation that rotated FEL fields select the same domain, in contrast to the static ME effect, however, the symmetry of the effect forbids this scenario more strictly.)

2. Selective heating scenario: The domain with stronger absorption is heated by the FEL above T_N and thus the other domain is favored. This scenario would always favor the domain which is more transparent when co-propagating FEL and THz beams, which is not the case.

3. Similarly as the previous scenarios, selection of the domain within the scenario of ME quasi-particles propagation should not depend on the direction of the incoming FEL beam: Imagine the situation when the crystal is illuminated by FEL from one and the opposite side, as depicted in Fig. 6.7. In both cases, the colder side is the one attached to the sample holder. I assume the situation when part of the sample is below T_N and the other part above T_N. The green line divides these two parts. First, one should realize that the domain selection should not directly depend on propagation direction (point 1), so let me assume a thin layer below T_N to have equally distributed domains, which is in Fig. 6.7 visualized by two equally-sized domains – α and β. The relative absorption of the two domains is different for opposite FEL propagation directions, but this effect should not matter (point 2). Nevertheless, I can still assume that in one domain, there are more ME quasi-particles than in the other domain. However, if I assumed that let say the less-absorbing domain with fewer ME quasi-particles expands to the more absorbing domains (or vice versa), it would again break the symmetry I observed: For both

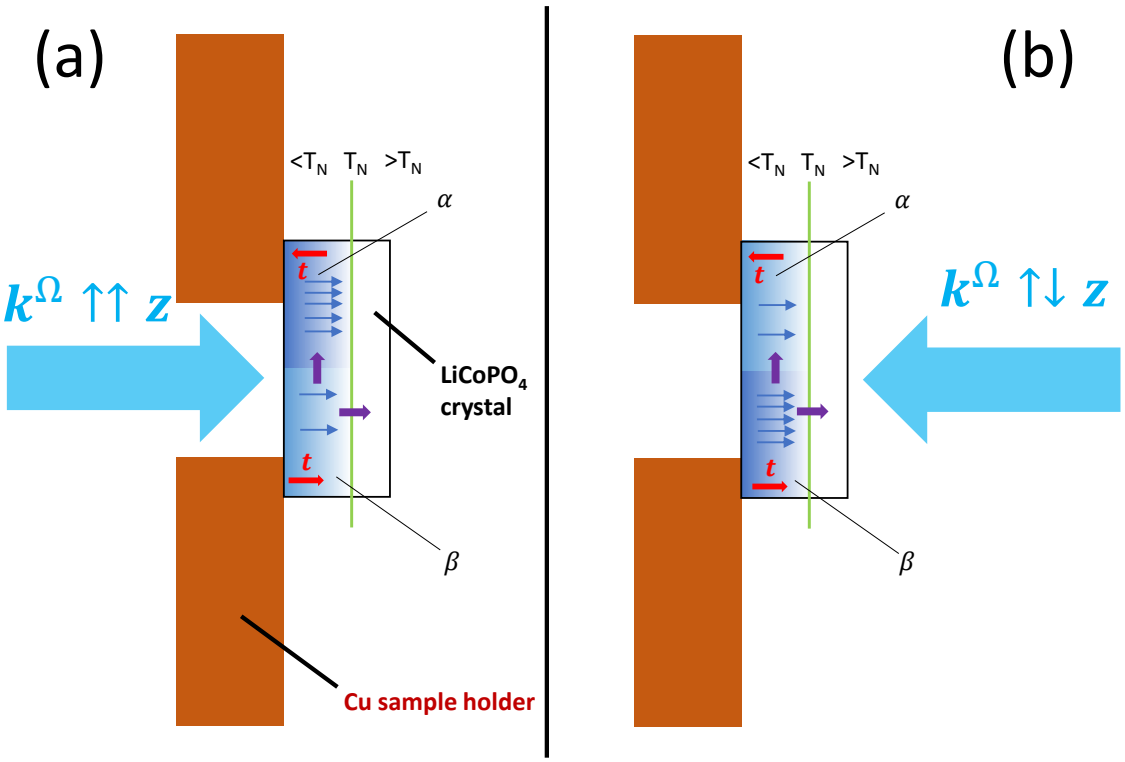

Figure 6.7: Demonstration that selection of the domain within the scenario of ME quasi-particles propagation should not depend on the direction of the incoming FEL beam. Panels (a) and (b) show cases of FEL beam propagating from opposite directions, while in both cases, β domain should be preferred irrespective of the fact that in the two cases, the two domains exchange roles: In case of panel (a), α domain is more absorbing and possesses more ME quasi-particles, while in panel (b), situation is the opposite. Propagating quasi-particles are assigned by blue arrows, the expansion of β domain is illustrated by purple arrows - it can be either in lateral (x and y) directions while shrinking α domain, or in the z direction into the area above T_N. Expansion of the β domain can be explained on symmetry basis: In this domain, static toroidal moment is parallel to the quasi-particle propagation, while in the α domain, it is antiparallel.

cases, the more transparent domain for the FEL beam would become more probable. Instead, both cases should favor β domain (i.e. the domain in which co-propagating beams from the colder side select the more transparent domain), while propagating quasi-particles being the underlying mechanism.

On what symmetry aspect can be β domain selected in the scenario of quasiparticle propagation? To this aim, I can label the domains by arrows pointing along $\pm z$ directions, which denote a space- and time-reversal odd vectors, representing some static order parameter. Since these vectors have the same symmetry as the toroidal moment, they are labeled as t in Fig. 6.7. Importantly, the wavevector of the quasiparticle propagation has the same symmetry, therefore, relative directions of t and quasi-particle propagation direction matter: The propagation of quasiparticle parallel and antiparallel to t can be nonequivalent. Such ME anisotropy was demonstrated for diffusive transport of electrons as a general effect [82], thus I may anticipate that it can be enhanced for ME materials.

Another question is the dynamics of the poling process. β domain can grow either in the direction perpendicular to the quasi-particle propagation direction, pushing α domain away, as displayed by the vertical purple arrows in Fig. 6.7. Alternatively, β domain can grow in the direction parallel to the quasi-particle propagation direction, which is displayed by the horizontal purple arrows in Fig. 6.7: In this case, it can grow to the area which is being cooled down below T_N, thus it does not necessarily need to push α domain. Nevertheless, these processes are indistinguishable by my experiment, and theoretical simulations would be required. Note that quasiparticle flow nonparallel with z direction may also be relevant, since the crystal is supposed to be hotter in the beam center.

In this aspect, it may be relevant that I reached poling even in part of the crystal not directly illuminated by the FEL, in which ME quasi-particles were not excited. This can be ascribed either to the fact that only heat gradient is enough for poling to occur, although the effect is stronger for the case of FEL in resonance with ME excitations. The other explanation is that the domain selected by the FEL expands to parts not illuminated by the FEL. However, these parts are colder, thus pre-selected domains are supposed to be more stabilized and robust against pushing away. These considerations demonstrate possible complexity of the observed effect and limitations of the current experimental investigations, lacking microscopic view.

Besides these limitations, there is still possible to investigate experimentally role of the ME resonances on the domain selection, and confirm or exclude the possibility of ME poling in case of solely heat gradient. This can be investigated by illuminating the crystal in regions far from ME resonances, or heat the crystal by a heat resistor upon cooling through T_N. Varying the light frequency among transparent and absorbing regions of the crystal can also switch the heat gradient and possibly lead to selection of the opposite domain. These are further experiments I propose.

6.4.6 Cooling rate, intensity, pulse-sequence dependences and combination of FEL and static poling

In the previous subsection, I analyzed the possible physics behind the observed effect in detail. The symmetry of the effect gives a deep insight, which rules out several mechanism. Even though I narrowed possible mechanisms, microscopic view behind the observed

effect is still unclear, since theoretical analysis would be required. Nevertheless, the poling by FEL can be studied as a function of several parameters, which can potentially give a lot of new information, giving a hint for theorists – it is supposed that the ab-initio theory can hardly explain such effects including mesoscopic physics, and rather theory inspired by experiment could potentially help to explain my observations. Therefore, I can now present other experiments I performed, which will be easier to interpret after the analysis I carried out in the previous subsection.

So far, I presented the FEL poling as a function of the following parameters: (i) FEL polarization and (ii) frequency. Here, I will yet present dependence of the effect on (iii) cooling rate, (iv) FEL intensity, (v) sequence of pulses (repetition rate). Furthermore, I will present results of FEL poling combined with poling using static fields.

The most intriguing from these is the cooling rate dependence. In Fig. 6.8, I display THz spectra after FEL poling $\boldsymbol{E}^{\Omega} \parallel y$, $\boldsymbol{H}^{\Omega} \parallel x$, $\Omega = 1.35\,\mathrm{THz}$, $P = 1.1\,\mathrm{W}$, for different cooling rates. One can see a huge dependence of the FEL-induced domain imbalance on cooling rate in a very broad range of time-scales. The effect is remarkable even for fastest achievable cooling rate 10 K/s, but it further increases when decreasing cooling rate even down to 1 K/min. Note that these timescales are much longer than typical timescales of microscopic objects, thus, such a dependence requires some analysis.

First reason for such longer timescales comes from the assumption that the poling occurs, or is at least efficient, in a very narrow temperature range below T_N. If the cooling rate is too fast, the temperature when the poling is effective can be possibly crossed without any pulse to act. Note that when shortening the switching electric-field pulses, the coercive field dramatically increases [247], so for the extremely short pulses I used, the temperature range of poling may be very narrow.

However, the process behind the observed effect is different from that reported in Ref. [247], so I shall go deeper into the microscopic mechanisms. As the FEL poling process is supposed to be caused by presence of ME excitations, the considerable number of excitations is required. Since near T_N, the magnetic excitations are very weak, the concentration of ME excitations is low even for a strong pulse. Next, I assume zonal cooling with heat gradient, as depicted in Fig. 6.7, suggesting that the poling happens in a thin layer close to T_N. If the cooling is fast, this layer moves fast and there are possibly no ME quasi-particles generated in the layer before it moves to another place. The results reported in Ref. [247] also imply slow motion of AFM domain wall, which means that movement of the thin layer close to T_N should not be faster than the domain wall motion. When temperature is decreased, the domain wall motion gets slower, thus poling is not possible. In other words, the cooling rate determines thickness of the layer in which the poling is efficient: For fast cooling, the isothermal border moves fast, so poling is efficient only in a thin layer where temperature is sufficiently close to T_N for which domain walls can move faster. For these reasons, the described scenario is consistent with the fact that even very slow cooling rates may enhance the poling process.

Next, I analyze poling in the macropulse regime and its comparison to the CW regime. In the macropulse regime, pulses were on for 10 ms and off for 40 ms. FEL power dependence of the ME effect in the CW and macropulse regimes is displayed in Fig. 6.9(a); FEL was in a resonance with excitation #3 ($\Omega = 1.35\,\mathrm{THz}$). The same power for CW and macropulse regime means 5-times higher intensity of pulses in the macropulse regime. One can see that in both cases, there is nearly a linear dependence for low FEL powers,

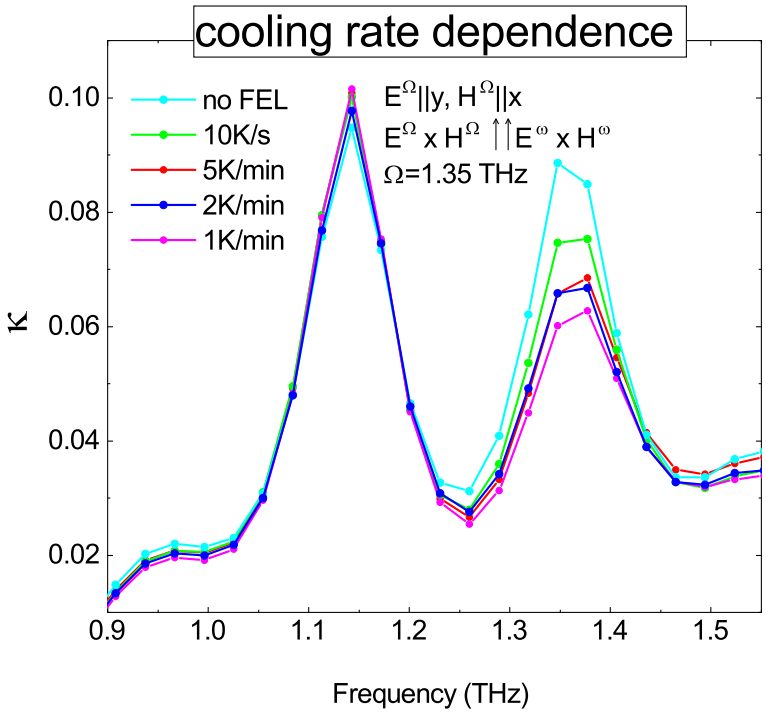

Figure 6.8: Cooling-rate dependence of the FEL-induced effect. THz spectra of κ in $\boldsymbol{E}^{\omega} \parallel y$, $\boldsymbol{H}^{\omega} \parallel x$, polarization after FEL poling in $\boldsymbol{E}^{\Omega} \parallel y$, $\boldsymbol{H}^{\Omega} \parallel x$, $\Omega = 1.35\,\mathrm{THz}$, $P = 1.1\,\mathrm{W}$, for different cooling rates.

which starts to saturate for higher powers. For low powers ($> 50\,\mathrm{mW}$), there is a clear statistical variance, as clear from remarkable differences of the ME effect measured for same conditions. For higher powers ($> 75\,\mathrm{mW}$), the statistical variance gets smaller.[3]

Important information is whether the FEL-induced domain imbalance scales with overall deposited power or with pulse energy. One can see that the poling in the macropulse regime is approximately 1.5-times larger than in the CW regime for the same powers. Therefore, it does not scale with either overall power or with pulse energy, but the reality is in between these two limits. It is important to note that the macropulse regime does not need to be necessarily equivalent to the case of just reduced repetition rate with equidistant pulses in time. One can imagine that in the macropulse regime, the poling efficiency is enhanced (dehanced) because the subsequent switching of the train of pulses on and off causes temperature fluctuations, thus the crystal may spend more (or less) time in the narrow temperature region where the poling occurs. This may lead to systematic enhancement (or dehancement) of the effect. Systematic enhancement is more probable, since presence of pulses decelerates the cooling, while their absence makes it faster.[4] Thus,

[3]Note that absolute power in power dependence measurements should not be compared between different setups. Previously, it was mentioned that the saturation occurred at around 1.1 W FEL power, while results obtained on an upgraded setup suggest saturation for much lower power. This can be caused by a different geometry of the crystal, difference in focal point size, and difference in power measurement: For THz and quasi-static probes, power was measured at a different distances from cryostat due to different technical constraints on light path.

[4]Note that temperature controller cannot compensate for such fast changes, moreover, it measures temperature away from the sample where such temperature fluctuations are smeared due to heat conduction.

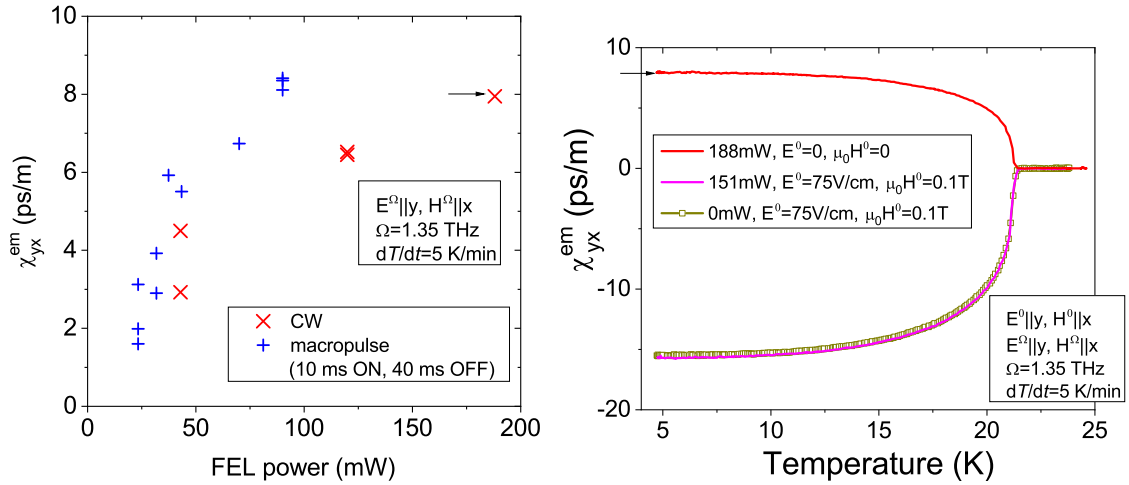

Figure 6.9: (a) FEL power dependence of the ME effect in the CW (red) and macropulse (blue) regimes. The poling conditions are indicated. (b) ME effect measured in warming run after different poling conditions including static poling fields. Red curve shows FEL poling without static poling, while dark yellow curve shows static poling only. Magenta curve shows combined static and FEL poling and it is overlapping with the dark yellow curve, demonstrating that in the presence of static poling, the FEL does not play any role on the domain imbalance. The small black arrow in the panel (a) corresponds to the magnitude of the ME effect measured for 188 mW at low temperature, which is the value denoted by the same arrow in panel (b).

it is possible that for different repetition rates, the effect would scale with the same slope as a function of overall FEL power. Therefore, I cannot conclude that the pulse energy itself is a relevant quantity.

The last experiment to analyze is combination of poling with static fields and poling by the FEL. In Fig. 6.9(b), I display ME susceptibility measured in heating run after poling with different conditions. I employed the experiment at one of the highest achievable FEL powers at that time (188 mW, red), while static poling was performed for low fields, which are not able to select a single domain state (75 V/cm, 0.1 T). To see competition of both effects, the static fields were chosen to select the other domain than the FEL. The ME susceptibility measured after the static poling is larger in absolute values than for FEL poling (15 ps/m vs. 8 ps/m), however, I note that the FEL poled only a part of the sample, so domain imbalance in the irradiated part of the sample may be comparable. When combining the static poling and poling by the FEL (magenta), the ME susceptibility is the same as in the case of static poling without FEL. Thus, in presence of static poling fields, FEL poling does not play any role, even if static fields are not able to select a single-domain state.

This dominance of static over FEL poling is possibly connected to the fact that static fields are present all the time, while FEL pulses are present only a tiny fraction of time. This further supports the idea that the FEL poling occurs just at the time of pulse due to presence of resonantly-excited ME quasi-particles, while thermal quasi-particles, present all the time, do not play any role. However, it is possible that the static field, directly influencing energy of the ME domains, makes the FEL poling, which is more subtle,

impossible. In this aspect, dominance of static poling has rather expected and it has multiple explanations, while competition of both polings would be more challenging to explain.

6.5 Summary and outlook

In this chapter, I presented $LiCoPO_4$, which is a canonical linear easy-axis magnetoelectrics with nonzero off-diagonal elements of the ME tensor. The magnetic order breaks simultaneously both time-reversal and space-inversion symmetries, resulting in two ME-AFM domains with opposite sign of the ME susceptibilities, thus the domains can be selected by cooling down through $T_N \approx 21$ K in crossed electric and magnetic fields. Due to the strong easy-axis magnetic anisotropy, the domain walls can be hardly moved when the temperature is remarkably below T_N ($\lesssim 15$ K), thus domain fraction remains stable at low temperature.

The nonzero off-diagonal elements of the ME tensor are manifested by DD of ME excitations at THz frequencies. Since the opposite domains have opposite sign of the ME tensor, DD changes sign for opposite domains, thus it can serve as their identification, similarly to measurement of static ME effect or SHG, reported previously. This allows optical reading at THz frequencies, which follows ME writing by static fields.

It was an alluring idea of my supervisor S. Bordács and I. Kézsmárki to complete the puzzle and demonstrate that THz pulses can be exploited to select the ME domains as well, thus employing THz writing – THz reading, i.e. all-optical scheme. Indeed, I selected ME domains by strong THz pulses, while the effect was enhanced for pulses tuned to frequencies of ME excitations, demonstrating their vital role. Nevertheless, in contrast to poling with static fields ($\boldsymbol{E}^0$, $\boldsymbol{H}^0$), the exchange of respective phases of electric and and magnetic THz fields ($\boldsymbol{E}^\Omega$, $\boldsymbol{H}^\Omega$), i.e. exchange of direction of THz poling pulse, did not lead to selection of the opposite domain, as in case of static fields, but to selection of the same domain. Such different symmetry of the THz poling effect with respect to static poling must be related to the inversion and time-reversal symmetry breaking originated from the experimental setup, in which the crystal was attached to a sample holder by only one side. In the symmetry point of view, I found only one reasonable time-reversal odd quantity which can lead to the observed effect – heat flow along the anticipated temperature gradient, directed collinearly with propagation direction of the poling THz pulse. Microscopically, I ascribed the effect to nonreciprocal flow of ME quasi-particles, while I ruled out several mechanisms which cannot contribute to the observed effect for symmetry reasons. Furthermore, I proposed further experiments which can confirm or exclude essential role of the ME resonances.

I observed the THz poling effect as a function of several parameters: Intensity, frequency and polarization of the poling pulses, their different sequences, and different cooling rates. Further, I employed combination of poling by THz pulses with static poling, showing absolute dominance of the latter. These experiments helped to reveal possible underlying physics. I used two different complementary techniques to probe domain imbalance – THz spectroscopy revealing DD, and the quasi-static ME effect.

I tried the same THz poling for relative magnetoelectrics $LiFePO_4$ with pretty unclear result, but suggesting that THz poling of ME domains may work for other ME compounds

as well; it needs further investigation though. I believe that such a novel effect is in fact universal for ME crystals and does not sensitively depend on material parameters. Nevertheless, its practical usage is unlikely since high-intense radiation is necessary to select the domains. Moreover, the effect of writing is slow, it needs temperature change between writing and reading, and it appears at low temperature. Rather, the experiments I performed can be used as an indirect probe of underlying physics of non-reciprocal quasi-particle propagation.

Summary

The major achievements of my Ph.D. research are summarized in the following points:

1. I demonstrated isothermal control of the directional dichroism, i.e. absorption difference for counter-propagating light beams, in a multiferroic $Ba_2CoGe_2O_7$ single crystal by an electric field and tiny rotation of the crystal with respect to a magnetic field. By studying the electric-field ($\boldsymbol{E} \| [100]$) and temperature dependence of the absorption contrast using Fourier-Transform Infrared and time-domain THz spectroscopy, I revealed that the domains of the easy-plane antiferromagnetic structure play an essential role in the electric-field effect, while the magnetic-field ($\boldsymbol{H} \| [001]$) dependence allowed me to assign the experimentally observed resonances to those deduced from a microscopic spin model developed by Dr. Judit Romhányi and Dr. Karlo Penc. By studying spectra upon magnetic field rotation around [100] and [010] axes, I proposed specific scenarios of domain transformations. [P1]

2. In multiferroic Y-hexaferrite $BaSrCoZnFe_{11}AlO_{22}$ and Z-hexaferrite $Ba_{0.5}Sr_{2.5}Co_2Fe_{24}O_{41}$, I found purely electric-dipole-active magnons, so-called electromagnons, by measuring and comparing their THz and Raman spectra, the latter measured and evaluated by Dr. Fedir Borodavka. I studied their temperature and magnetic field dependence in THz spectra, and correlated their features with the changes in the static magnetic structures. I developed microscopic selection rules based on the exchange-striction mechanism of electromagnon activations, which allowed me to explain the temperature and magnetic-field dependences of their spectral strength. [P2, P3, P4]

3. I investigated the influence of intense THz radiation on electromagnons in Z-hexaferrite $(Ba_{0.2}Sr_{0.8})_3Co_2Fe_{24}O_{41}$ ceramics and Y-hexaferrite $Ba_{0.2}Sr_{1.8}Co_2(Fe_{0.96}Al_{0.04})_{12}O_{22}$ single crystal. I did not observe any change in the absorption spectrum upon THz irradiation in case of $(Ba_{0.2}Sr_{0.8})_3Co_2Fe_{24}O_{41}$ besides sample heating. This motivated me to extend an existing model of the electromagnon in the Z-hexaferrite into a nonlinear one. Using the model, I determined changes of spin structure upon THz irradiation, and explained the absence of any spectral changes. In case of Y-hexaferrite $Ba_{0.2}Sr_{1.8}Co_2(Fe_{0.96}Al_{0.04})_{12}O_{22}$, I observed some spectral changes, which I interpreted without invoking any specific spin model. [P6]

4. In a magnetoelectric $LiCoPO_4$ single crystal, I measured directional dichroism as it is defined, i.e. by the reversal of the light propagation direction. Applying this method, I identified antiferromagnetic domains following magnetoelectric annealing

in electric ($\boldsymbol{E} \| [010]$) and magnetic ($\boldsymbol{H} \| [100]$) fields selecting either of the domains. For that purpose, I developed a setup for time-domain THz spectroscopy at Budapest University of Technology and Economics, allowing to exchange the source and the detector antennae. By these experiments, I demonstrated that the absorption spectroscopy can be used to detect relative population of antiferromagnetic domains in magnetoelectric compounds. The $LiCoPO_4$ single crystal was previously grown and characterized by Dr. Vilmos Kocsis. [P5]

5. I selected a magnetoelectric domain in $LiCoPO_4$ single crystal by intense THz radiation tuned to frequencies of magnetoelectric excitations. As an intense THz source, I used narrow-band pulses from FELBE free electron laser at Helmholtz-Zentrum Dresden-Rossendorf. I detected the relative population of the domains by THz spectroscopy and by a modulation technique, which I developed: A coil produced a small oscillating magnetic field, while the measured current corresponded to the induced polarization oscillating at the same frequency. I found that counter-propagating light pulses selected the same domain, which implies that the asymmetry introduced by the sample holder is important. Therefore, I ascribed the observed effect to temperature gradient and subsequent propagation of magnetoelectric quasiparticles, which must be nonreciprocal in the magnetoelectric domains.

List of publications

Publications related to thesis points

[P1] J. Vít, J. Viirok, L. Peedu, T. Rõõm, U. Nagel, V. Kocsis, Y. Tokunaga, Y. Taguchi, Y. Tokura, I. Kézsmárki, P. Balla, K. Penc, J. Romhányi and S. Bordács,
In Situ Electric-Field Control of THz Nonreciprocal Directional Dichroism in the Multiferroic $Ba_2CoGe_2O_7$
Phys. Rev. Lett. **127**, 157201 (2021).

[P2] F. Kadlec, C. Kadlec, J. Vít, F. Borodavka, M. Kempa, J. Prokleška, J. Buršík, R. Uhrecký, S. Rols, Y. S. Chai, K. Zhai, Y. Sun, J. Drahokoupil, V. Goian and S. Kamba,
Electromagnon in the Z-type hexaferrite $(Ba_xSr_{1-x})_3Co_2Fe_{24}O_{41}$
Phys. Rev. B **94**, 024419 (2016).

[P3] J. Vít, F. Kadlec, C. Kadlec, F. Borodavka, Y. S. Chai, K. Zhai, Y. Sun and S. Kamba,
Electromagnon in the Y-type hexaferrite $BaSrCoZnFe_{11}AlO_{22}$
Phys. Rev. B **97**, 134406 (2018).

[P4] S. Kamba, F. Borodavka, F. Kadlec, C. Kadlec, Y. S. Chai, K. Zhai, J. Buršík and J. Vít,
Vibrational spectra of multiferroics with Y- and Z-type hexaferrite structures
Ferroelectrics **532 (1)**, 208 (2018).

[P5] V. Kocsis, K. Penc, T. Rõõm, U. Nagel, J. Vít, J. Romhányi, Y. Tokunaga, Y. Taguchi, Y. Tokura, I. Kézsmárki and S. Bordács,
Identification of Antiferromagnetic Domains via the Optical Magnetoelectric Effect
Phys. Rev. Lett. **121**, 057601 (2018).

[P6] J. Vít, D. Repček, C. Kadlec, F. Kadlec, N. Adhlakha, P. Di Pietro, F. Piccirilli, S. Kovalev, J.-C. Deinert, I. Ilyakov, N. Awari, M. Chen, J. Buršík, C. B. Park, K. H. Kim, M. Gensch, A. Perucchi and S. Kamba,
Search for Nonlinear THz Absorption by Electromagnons in Multiferroic Hexaferrites
J. Phys. Soc. Jpn. **91**, 104703 (2022).

Other publication

[P7] S. Kamba, V. Goian, F. Kadlec, D. Nuzhnyy, C. Kadlec, J. Vít, F. Borodavka, I. S. Glazkova and A. A. Belik,
Changes in spin and lattice dynamics induced by magnetic and structural phase transitions in multiferroic $SrMn_7O_{12}$
Phys. Rev. B **99**, 184108 (2019).

Chapter 7

Appendix – additional data for Chapter 5

7.1 Determination of the THz field strength

I determined the THz electric field strength via measurement of the beam intensity and its spatial profile, and subsequent relating it to the temporal profile measured by the electro-optic sampling (EOS).

First, the pulse energy was determined using knowledge of the repetition rate and measuring the overall beam power by a pyroelectric power detector (pyrodetector). To reach lower powers, I used rotating wire-grid polarizers and calculated the actual power by the Malus law. I determined maximum pulse energies $I = 6.6\,\mu$J for TELBE and $I = 9\,\mu$J for TeraFERMI as noted in Tab. 2.2.

Next, the spatial beam profile was measured using a pyrocamera. The beam had approximately the Gaussian profile, and I determined the beam profile radius $w_{FWHM} = 325\,\mu$m at full-width-half-maximum (FWHM) at both TELBE and TeraFERMI.

In Gaussian optics, it is common operate with the coordinate z along the beam, and the radial coordinate r. To relate the electric field at the focus—$E(r = 0, z = 0, t)$—and the intensity profile, I make use of the standard Gaussian beam relation [248]

$$E(r = 0, z = 0, t)^2 = \frac{\eta 4P(t)}{\pi w_0^2} = \frac{\eta \cdot 2\ln(2)P(t)}{\pi w_{FWHM}^2}, \tag{7.1}$$

where $\eta = 377\ \Omega$ is the free space impedance, $w_0 = 2 \cdot w_{FWHM}[2\ln(2)]^{-0.5}$ is the $1/e^2$ beam waist, and $P(t)$ is the power of the beam, i.e. the beam intensity integrated over the radial coordinate.

When averaging Eq. 7.1 over the time τ covering all the pulse Here I chose τ over the full length of the EOS scan to cover as much power as possible, since pyrodetectors measure all the power. I took $\tau = 70\,$ps for TELBE and $\tau = 60\,$ps for TeraFERMI. Even though these values cover a vast majority of the pulses, there may be other (e.g. thermal) contributions to the pyrodetectors, which overestimate the THz power. This may bring a systematic error leading to overestimation of the THz electric field., one gets

$$\langle E(r = 0, z = 0, t)^2 \rangle_\tau = \frac{\eta \cdot 2\ln(2)I}{\pi w_{FWHM}^2 \tau}, \tag{7.2}$$

where $I = \langle P(t) \rangle_\tau \cdot \tau$ is the known pulse energy. I then identified the electric field measured by the EOS to the $E(r = 0, z = 0, t)$ and normalized it in the way that the Eq. 7.2 is fulfilled.

At TeraFERMI, I got maximum absolute-value data point $E(r = 0, z = 0, t)_{max} = 1.67\,\mathrm{MV/cm}$. Note that this is the highest possible field available for $r = 0$, $z = 0$, while my experimental output—THz transmission—which I also calculated using the nonlinear model, reflects properties of all the beam. This is why I considered the maximum absolute-value data point as $1.6\,\mathrm{MV/cm}$. This corresponds to $E(r \approx 80\,\mu\mathrm{m}, \mathrm{z} = 0, \mathrm{t})_{\mathrm{max}}$ in the Gaussian-profile approximation, so such field is, in calculations, still a little overestimated, considering that $w_{FWHM} = 325\,\mu\mathrm{m}$ was much smaller than a 2-mm sample aperture.

At TELBE, conditions of the beam including the alignment changed remarkably between measuring reference and the sample—mainly the power fluctuated and the quality of the EOS signal was improved. Nevertheless, I assume the reference pulse shape at the sample position to be almost unchanged. Therefore, for the electric field calculation, I considered the highest power available in the CW regime ($P = 132\,\mathrm{mW}$, corresponding to the pulse energy $I = 6.6\,\mu\mathrm{J}$, c.f. Tab. 2.2), but I used the reference EOS signal measured at a lower power. The above-described procedure gives $E(r = 0, z = 0, t)_{max} = 322\,\mathrm{kV/cm}$, which is the case of the wine curve in Fig. 5.1(b). The peak electric field for the other curves in the CW regime was assigned simply by assuming $[E(r = 0, z = 0, t)_{max}]^2 \propto P$.

For the macropulse regime, the situation was somehow more complicated, because it contained some portion of weak pulses which were excluded. As the EOS technique measures the electric field of a single pulse, the electric field for the most intense pulse in the macropulse regime was calculated by normalizing it to the electric field of the most intense pulse of the CW regime. Nevertheless, the assigned power, relevant for the heating effect, was still determined by using the pyrodetector and the Malus law, so the proportionality $[E(r = 0, z = 0, t)_{max}]^2 \propto P$ is not valid for the macropulse regime.

Due to such pulse discrimination, the determination of the electric field in the macropulse regime is indirect and possibly not accurate. Nevertheless, I remind that I interpreted the effect at TELBE as heating and I did not use the electric field values for any calculations. On the other hand, the THz electric field at TeraFERMI was used for the calculation of nonlinearity, so its accurate determination is relevant for calculations of the magnitudes of spin tilts.

7.2 Evaluation of the heating effect in Z-hex at TELBE

7.2.1 Scaling with THz electric field vs. scaling with power

I plot the transmission amplitude at the electromagnon frequency for continuous wave (CW) and macropulse regimes as a function of the THz peak electric field (Fig. 7.1a) and as a function of the total average power (Fig. 7.1b). In case of pure nonthermal nonlinearity, the curves for CW and macropulse regimes would match in Fig. 7.1a. In case of the heating effect only, the curves for CW and macropulse regimes would match in Fig. 7.1b.

The clear shift of the two curves in Fig. 7.1a points out the dominant heating effect. On the other hand, there is no clear shift of the two curves in Fig. 7.1b. Although the highest blue point, laying above the red curve, may sign an additional nonlinearity beyond the

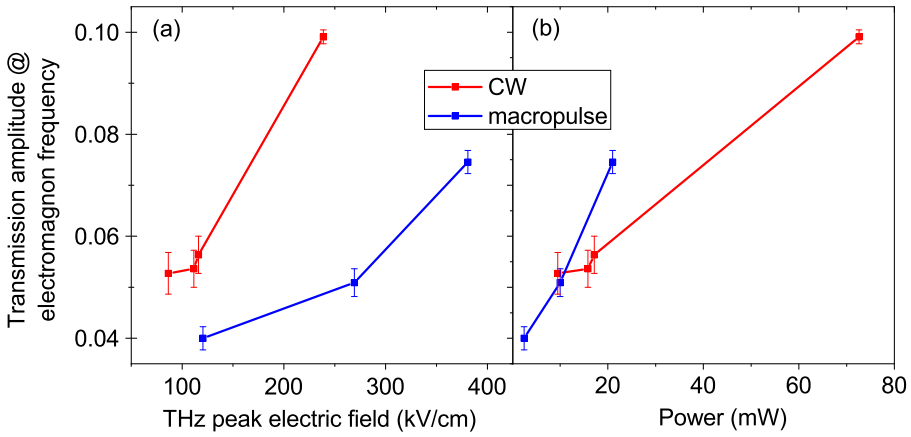

Figure 7.1: Transmission amplitude at the electromagnon frequency as a function of (a) THz peak electric field and (b) power for CW (red) and macropulse (blue) regimes. The errorbars of the transmission amplitude refer to the statistical errors, cf. Sec. 7.6. The errorbars of the THz electric field and power may be remarkable, but they are not displayed, because they are difficult to determine.

heating effect, I cannot confirm it due to lack of data. Nevertheless, a possible nonthermal nonlinearity would have to be small for the used THz electric fields, which is confirmed by the experiment at TeraFERMI.

7.2.2 Correlation of phonon and electromagnon frequencies

A shift of the phonon frequency at 1.37 THz [see Fig. 5.1(b)] at the highest power is another independent proof of sample heating: I cannot imagine any other reason for the shift when pumping at the electromagnon frequency. Qualitatively similar shift of the electromagnon frequency with temperature was observed in linear spectra [Fig. 5.1(a)]. Unfortunately, the signal at the phonon frequency was low when pumping at the electromagnon frequency [see Fig. 5.2(b)], so for low powers, there is no clear power dependence of the phonon frequency. On the other hand, pumping at the phonon frequency allowed to observe both phonon and electromagnon changes due to a long low-frequency tail of the spectrum from TELBE. Evaluation showed behavior fully consistent with the heating hypothesis: Two sets of temperatures calculated [using temperature dependence from the linear spectroscopy experiment, see Fig. 5.1(a)] from the electromagnon and the phonon frequencies for different powers show correlation as high as 0.97, proving also high evaluation accuracy. Having only this result, it would be hypothetically possible that both the electromagnon and the phonon exhibited the same nonlinearity as the temperature effect, although highly improbable. However, comparison CW and macropulse regimes proves that it is indeed the heating effect.

7.3 Calculation of number of absorbed photon quanta per unit cell volume

For both Z-hex and Y-hex, I determined number of absorbed photon quanta per unit cell volume analogically as described in Ref. [226], Methods section. Moreover, I did not take the real part of the refractive index (n) and the absorption coefficient (α) as constants, because especially in the latter case, such approximation would not be sufficient due to resonant feature of these quantities. Thus, I assumed frequency dependence of n and α based on my linear THz spectroscopy experiment.

I calculated the unit cell volume of Z-hex based on lattice parameters from Ref. [188], and the one of Y-hex from Ref. [189]. In calculations, I used the electric field time trace from the most intense THz pulse at TeraFERMI, Fig. 5.2(a) (green).

7.4 Calculation of magnitudes of spin tilts

Once I have calculated the number of absorbed photon quanta per unit cell volume, I can calculate magnitudes of spin tilts. As mentioned in Chapter 5, I take the staggered magnetization as the relevant quantity. I do this in the way that I simplify the investigated systems (both Z-hex and Y-hex) into two-sublattice magnets, because I need to group all small and large spins, respectively, which oscillate anti-phase. Then, I numerically calculated magnitudes of spin tilts, for which the staggered magnetization changes by the previously calculated number of absorbed photon quanta. Such spin tilts are the maximum spin tilts upon the resonance.

For Z-hex, I assume a specific magnetic structure and I can use the model of the electromagnon [208], so such a calculation is straightforward. For Y-hex, I need yet to assume some magnetic structure and some model of the electromagnon, which is the topic of the next subsection. Note, however, that all these calculations are done to have just a rough estimate about spin tilt magnitudes, which justifies several simplifications.

7.4.1 Calculation of magnitudes of spin tilts in Y-hex

Magnitudes of effective magnetic moments in Y-hex

Magnetic structure of Y-hex is known in the block approximation [189, 249]. However, from neutron diffraction studies, only the modulation vector can be typically estimated, but neither angles or even magnitudes of effective magnetic moments can be determined precisely.

In order to determine magnitudes of effective magnetic moments within the block approximation, I need to dive deep in the internal magnetic structure of individual magnetic ions. Unfortunately, this work has not been done for the sample with exactly the same composition as the one I measured. Therefore, I deduced the magnetic structure of Y-hex from an early work of Momozawa on $Ba_{1-x}Sr_xZn_2Fe_{12}O_{22}$ [250]. I assumed the basic high-temperature ferrimagnetic structure with magnetic moments in the hexagonal plane, from which conical structures are derived.

Now, the crucial question is into which crystallographic positions are Co and Al substituted in Y-hex. While in Zn-doped Y-hexaferrites, Zn goes to tetrahedral sites [250],

Co goes to octahedral sites in Co-doped Y-hexaferrites [189]. In order to determine to which octahedral sites, I use magnetization data measured by Chang Bae Park: Specifically, I compare the magnetization at the in-plane field $B_{\perp c} = 6\,\mathrm{T}$, in which the samples are supposed to be in the collinear ferrimagnetic phase, which I call saturated. The saturated magnetization is high for Al-free $Ba_{0.2}Sr_{1.8}Co_2Fe_{12}O_{22}$ ($\approx 14\,\mu_B$ per formula unit (f.u.)), indicating that Co with lower magnetic moment compared to Fe must substitute Fe at spin-down positions. Therefore, one can assume Co to be substituted to the off-centered octahedral positions. This gives the saturated magnetization $12.4\,\mu_B$ per f.u., which is much closer to the observed value than for hypothetical cases of Co substitution into random ($8.56\,\mu_B$ per f.u.) or even centered ($7.6\,\mu_B$ per f.u.) octahedral positions. (The observed magnetization at 6 T is higher than the theoretical value probably because the magnetic structure is not fully saturated, i.e. not collinear—small spins may not be completely antiparallel with the field.)

As regards to Al substitution, it is known to preferably occupy octahedral positions in $Ba_{0.5}Sr_{1.5}Zn_2(Fe_{1-y}Al_y)_{12}O_{22}$ [196, 251]. Note that all remaining octahedral positions are spin-up after Co substitution, which is consistent with huge magnetization drop upon Al substitution (not displayed), but they can contribute to different spin blocks. Since I do not have any other information, I assume random Al distribution over remaining (centered) octahedral positions.

Altogether, Co fully occupies the off-centered octahedral positions, and Al is randomly distributed over other (centered) octahedral positions. This gives the following magnitudes of magnetic moments: $\mu_S = 5.3\,\mu_B$ and $\mu_L = 15.3\,\mu_B$ for Y-hex when assuming magnetic moments of Fe, Co and Al to be $5\,\mu_B$, $3.8\,\mu_B$ and 0, respectively.

Simplified calculation of spin tilts in Y-hex

Since there is no model of the electromagnon in Y-hex based on some model Hamiltonian up to my knowledge, I simply assume that both sublattices tilt by the same angle. This is mathematically equivalent to assuming only one sublattice. Therefore, it is analogical to calculating a tilt of a pendulum with constant length from knowing its projection length onto its equilibrium state.

7.5 Modeling effects of TeraFERMI radiation on the electromagnon in Z-hex

My aim was to relate the nonlinear model elaborated in Chapter 5 to the experimental output, represented by a transmission amplitude spectrum of a dielectric slab. Therefore, I need to calculate propagation of the radiation through the slab, while it is attenuated. Since I deal with nonlinearity, I cannot simply apply the exponential absorption law. Instead, I have to calculate electric field propagation inside the slab with a small step.

7.5.1 Extracting parameters from the linear spectroscopy experiment

The dielectric slab is described by a complex frequency-dependent response function—dielectric permittivity (later denoted as $\varepsilon^{tot}(\omega)$), relating the applied time-dependent

electric field and the time-dependent polarization. The dielectric permittivity is given by several contributions, mainly phonons, and the electromagnon. I assume that the electromagnon-related part of the permittivity (later denoted as $\Delta\varepsilon^{em}(\omega)$) is a subject of nonlinearity, while the rest (mainly the phononic part) is not. That is why I have to separate these two contributions first, and then apply the nonlinear model on $\Delta\varepsilon^{em}(\omega)$ only.

The separation can be well done by fitting the spectra. Here, I benefited from the fact that the linear THz spectra are complex. In fact, the experimental output is the complex refractive index (later denoted as $N^{tot}(\omega)$) given by the product of the complex dielectric permittivity ($\varepsilon^{tot}(\omega)$) and the complex magnetic permeability ($\mu(\omega)$). Since (i) the electromagnon is purely electric-dipole-active, (ii) there are no magnetic-dipole active magnons in the THz spectra at zero magnetic field and (iii) no magnetic contributions are expected at higher frequencies, I can assume that the observed refractive index ($N^{tot}(\omega)$) is given purely by dielectric contributions, so I approximated the complex magnetic permeability as $\mu = 1$.

Since my linear THz spectra cover only a small part of phonons, I rather used FIR reflectance spectra measured by FTIR spectroscopy technique to get better precision in determination of the complex permittivity [138]. I fitted the spectrum at $T = 5\,\mathrm{K}$ using the Lorentz oscillator model. The only relevant part for the model are the parameters of the oscillator related to the electromagnon. I got the following parameters, as mentioned in Chapter 5: $\frac{\omega_0}{2\pi} = 1.1\,\mathrm{THz}$, $\frac{\gamma}{2\pi} = 62\,\mathrm{GHz}$, $\Delta\varepsilon = 0.27$. Using these parameters, I constructed the part of the complex permittivity related to the electromagnon—$\Delta\varepsilon^{em}(\omega)$. I subtracted it from the experimentally measured permittivity spectrum (at $T = 5\,\mathrm{K}$)—$\varepsilon^{tot}(\omega)$, by which I got the part of the permittivity not related to the electromagnon—$\varepsilon^{bcg}(\omega)$.

Altogether, I introduced the following complex response functions which will be used in the calculations:

- $\varepsilon^{tot}(\omega)$: The experimentally observed complex dielectric permittivity at $T = 5\,\mathrm{K}$. (Index *tot*, meaning total, refers to the fact that it includes both phonons and the electromagnon.)
- $\Delta\varepsilon^{em}(\omega)$: The electromagnon-related part of the permittivity, which is a subject of nonlinearity.
- $\varepsilon^{bcg}(\omega) = \varepsilon^{tot}(\omega) - \Delta\varepsilon^{em}(\omega)$: The permittivity without the electromagnon, which is not a subject of nonlinearity.
- $N^{tot}(\omega)$: The experimentally observed complex refractive index, which is in this case of no magnetic-dipole-active contributions directly related to the complex permittivity: $(N^{tot}(\omega))^2 = \varepsilon^{tot}(\omega)$. The reason for having it is that in Fresnel formulas, I will work rather with the complex refractive index than the dielectric permittivity.

7.5.2 Calculation of the THz radiation propagation through Z-hex

I want to model propagation of the linearly polarized THz pulse (assuming the electric field only, since I approximated $\mu = 1$) from TeraFERMI, displayed in Fig. 5.2(a) (green),

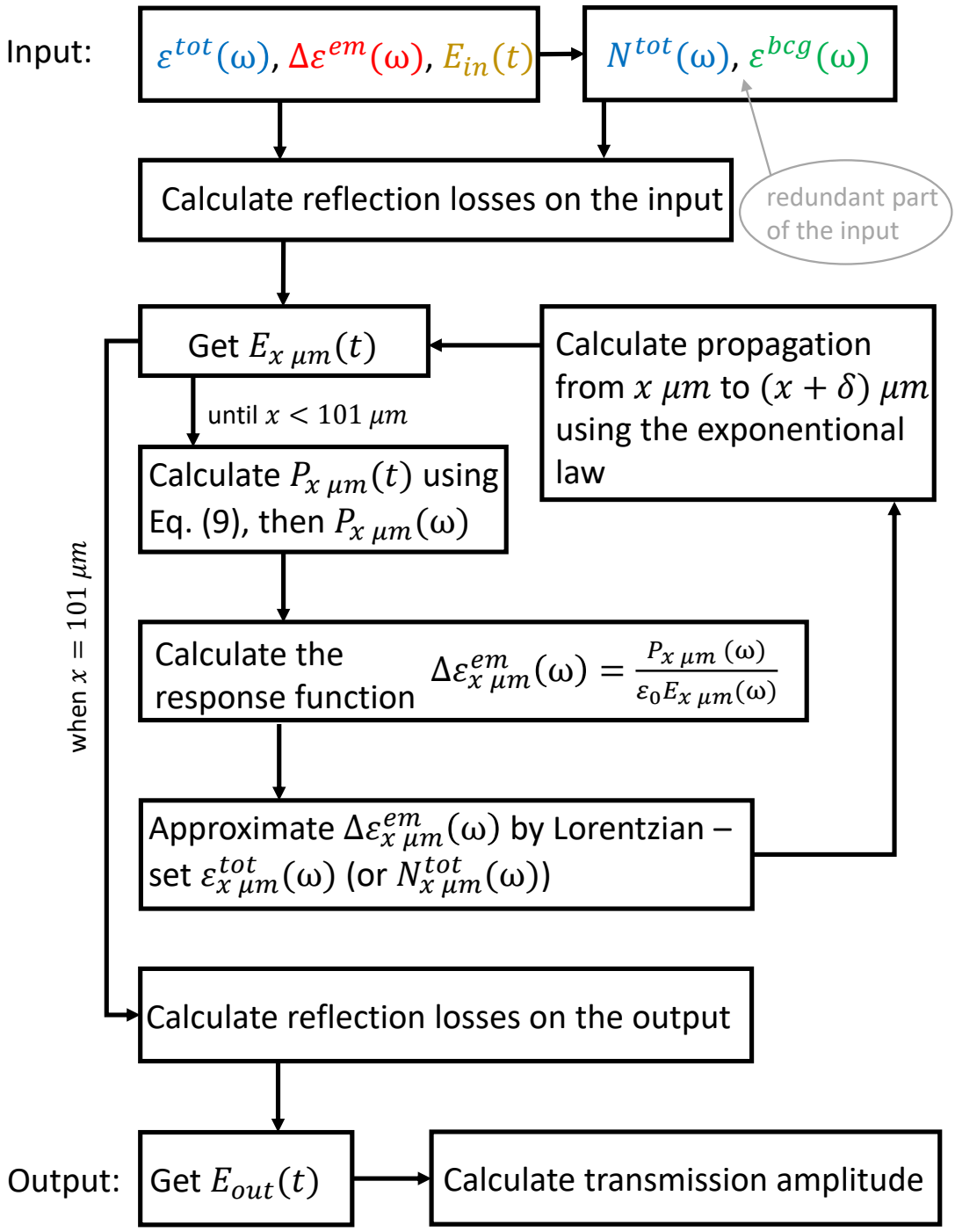

Figure 7.2: Block diagram depicting the sequence of calculations of the THz radiation propagation through Z-hex described in Sec. 7.5.

through a 101 μm-thick slab of Z-hex. (Note that for the linear case, this problem can be solved numerically with standard procedures.) Simply spoken, I have a pulse just before the slab $E_{in}(t)$ and I want to get a pulse just after the slab $E_{out}(t)$, which I can directly compare to the experimental time traces. (Fine effects like Gouy shift are neglected, because their effect is minor compared to the precision of the experiment.) To compare the results in the Fourier (frequency) space, I yet calculate the complex transmission amplitude and compare it to the experimental one, calculated the same way. For simplicity, the field is expected to be homogenous in lateral direction (plane wave), and it changes only in the direction of light propagation.

The sequence of the calculation, described in the following, is depicted in Fig. 7.2

Calculation of reflection losses

Since I want to calculate a time-domain pulse but I know the spectrum in the frequency domain, I will need to perform the Fourier Transform after each step. First, I need to calculate reflection losses to get a pulse shape just after entering the slab of Z-hex. The reflection losses are mainly given by the real part of the permittivity determined mostly by phonons, so I can neglect any nonlinearity and use the refractive index $N^{tot}(\omega)$ determined by the linear THz spectroscopy. I first perform Fourier-Transform to transform $E_{in}(t)$ into $E_{in}(\omega)$, and then calculate reflection losses according to the Fresnel formula: $E_{0\mu\mathrm{m}}(\omega) = E_{in}(\omega) \cdot \frac{2}{1+N^{tot}(\omega)}$, where $E_{0\mu\mathrm{m}}(\omega)$ is the electric field just after entering the sample (in 0 μm depth). By performing the inverse Fourier-Transform of it, I get a time-domain pulse inside the sample in 0 μm depth—$E_{0\mu\mathrm{m}}(t)$.

Calculation of the electromagnon-related polarization from the electric field using the nonlinear model, Eq. 5.9

Having the internal electric field $E_{0\mu\mathrm{m}}(t)$, I can directly calculate the polarization in the sample in 0 μm depth using (i) Eq. 5.9 and (ii) the function $P_c(Q)$. The only variable parameter of the model is the function $P_c(Q)$ (red curve of Fig. 5.3) and its derivative $\frac{\partial P_c}{\partial Q}$. First, I need to set the ME coefficient $\tilde{P}_{ES}$ which was set as $26\frac{\mu C}{m^2\mu_B}$ as mentioned in Chapter 5. Next, for solving the differential equation (Eq. 5.9), I need to know $\frac{\partial P_c}{\partial Q}$ at any Q, meaning that I need its analytical expression. For this, I first fitted the function $P_c(Q)$ with 7^{th}-order polynomial and then used the analytical derivative of it as an approximation of the function $\frac{\partial P_c}{\partial Q}(Q)$. (In later notations, I will omit lower index c for simplicity, as I always mean polarization in the c-direction.)

Having this, I calculated the nonlinear differential Eq. 5.9 using the Euler method with time step as small as 1 fs to ensure convergence of the method. As a result, I got the electromagnon-related polarization $P_{0\mu\mathrm{m}}(t)$, i.e. the polarization induced in 0 μm depth.

Calculation of electric field propagation inside Z-hex

Nonlinearity in the model can be viewed as that the response function (permittivity, refractive index) is not constant in space but it changes upon propagation of THz radiation. Now I am going to calculate the response function at the surface of the sample (0 μm depth).

Table 7.1: Parameters of the electromagnon-related response function $\Delta\varepsilon^{em}_{0\mu\mathrm{m}}(\omega)$ with respect to the linear electromagnon-related contribution $\Delta\varepsilon^{em}(\omega)$ upon electric field propagation through a 101 μm-thick slab of Z-hex.

depth (μm)	relative strength of the electromagnon
0	0.8
0-20	0.82
20	0.84
20-50	0.855
50	0.865
50-101	0.87

I first Fourier-Transform $P_{0\mu\mathrm{m}}(t)$ into $P_{0\mu\mathrm{m}}(\omega)$ and then calculate $\Delta\varepsilon^{em}_{0\mu\mathrm{m}}(\omega) = \frac{P_{0\mu\mathrm{m}}(\omega)}{\varepsilon_0 \cdot E_{0\mu\mathrm{m}}(\omega)}$, which should, for a linear regime, exactly equal $\Delta\varepsilon^{em}(\omega)$ which is a complex Lorentzian.

In further calculations, I cannot work directly with the function $\Delta\varepsilon^{em}_{0\mu\mathrm{m}}(\omega)$, because for the input of the differential equation, I need parameters of the Lorentzian function which approximates it. By comparing these two functions—$\Delta\varepsilon^{em}_{0\mu\mathrm{m}}(\omega)$ and $\Delta\varepsilon^{em}(\omega)$ (not displayed)—I concluded that the main difference is in the magnitude of the peak, while its frequency and damping are unchanged. Therefore, I fitted the function $\Delta\varepsilon^{em}_{0\mu\mathrm{m}}(\omega)$ by the Lorentzian while keeping the frequency and damping of the Lorentzian $\Delta\varepsilon^{em}(\omega)$, and compared these two functions, while they differ by some factor only. Specifically for 0 μm depth, I found that $\Delta\varepsilon^{em}_{0\mu\mathrm{m}}(\omega)$ can be approximated as $0.8 \cdot \Delta\varepsilon^{em}(\omega)$. This means that the corresponding response function for the 0 μm depth can be calculated as $\varepsilon^{tot}_{0\mu\mathrm{m}}(\omega) = \varepsilon^{bcg}(\omega) + 0.8 \cdot \Delta\varepsilon^{em}(\omega)$, and corresponding refractive index $N^{tot}_{0\mu\mathrm{m}}(\omega)$ can be calculated. The response function can be parametrized by one number only—relative dielectric strength with respect to the electromagnon in the linear regime, i.e. 0.8.

Now I want to calculate propagation through the sample using the exponential law, with the response function as a parameter changing upon propagation. Nevertheless, the exponential law is valid only in a narrow range of depth, so I have to calculate propagation to a small depth only using the parameters obtained for the 0 μm depth, and then calculate a new response function by the same procedure as described for 0 μm depth. Also, reflection losses on the output can be calculated analogically to those on the input, by which I obtained the output electric field $E_{out}(t)$.

Auxiliary parameters obtained by calculation of electric field propagation through Z-hex

Since the described calculations in the previous subsubsection are quite complicated, I wanted to recalculate the response function as few times as possible. That is why for propagation from 0 μm depth, I did not use the response function obtained for 0 μm depth but those corresponding to a higher depth. The parameters used in the calculation are in Tab. 7.1. For example, one can see that using parameter 0.82 for propagation from 0 to 20 μm is verified by subsequent obtaining of 0.84 for 20 μm. Further check revealed that the parameter used for propagation from 0 to 20 μm has anyway a minor effect on the

parameter determined for 20 μm depth.

The resulting transmission, as displayed in Fig. 5.3 in green, is then calculated using $E_{out}(t)$ and the reference signal by standard procedures. (Alternatively, it can be also calculated directly in the Fourier space by multiplying the partial transmissions through the material and through surfaces of the sample.) The model does not include internal reflections, as pointed out in Chapter 5.

7.6 Determination of experimental statistical errors

Statistical uncertainty of the transmission amplitude was determined based on set of time traces which were later averaged for further evaluation. Every time trace was separately Fourier-Transformed and the statistical error was calculated separately for each point in the Fourier (frequency) space for the real and imaginary part of the Fourier-Transformed signal. From these data, the error of the transmission function is evaluated as an error of division of two quantities—transmission through the sample and transmission through a free space.

7.7 Spectra history of Y-hex

The history of the Y-hex crystal was the following: Linear THz spectra were measured on a 191 μm-thick sample, whose temperature and magnetic-field history is not fully clear, so one may suspect both ALC as well as TC magnetic structures at low temperature. The crystal was then thinned down to 87 μm for the TeraFERMI experiment. Afterward, it was heated to 450 K and the linear THz spectra were then measured in the zero-field-cooled ALC phase.

Since the thickness of the sample changed, I do not compare transmission amplitude but rather the imaginary part of the refractive index (κ), which is a material-specific parameter independent on the sample thickness. In Fig. 7.3(a), I compare linear spectra before and after the experiment at TeraFERMI together with the highest-intensity spectrum at TeraFERMI. Note that the statistical errors of the linear experiment are very low, and their comparison to the errors at TeraFERMI were discussed in Chapter 5, so I do not display any errorbars here.

Despite remarkable differences between the two linear spectra, both of them exhibit remarkably higher κ in 1.4–1.5 THz range than the TeraFERMI spectrum does. Therefore, I can conclude that within statistical errors, the lower absorption at 1.4 THz for the TeraFERMI experiment is likely to be related to physics of the sample.

I yet discuss differences between the two linear spectra: While the spectrum taken before the TeraFERMI experiment exhibits a double-peak shape, the spectrum taken after shows rather a broad single peak. First explanation is that the spectrum before the TeraFERMI experiment does not correspond to the single-phase ALC structure, and the second peak corresponds to the TC structure. The TeraFERMI experiment could still start in the ALC structure, because the sample was heated to $\approx$ 400 K when being thinned down, which should be enough to reach the ALC structure in the subsequent zero-field cooling. The second explanation is based on the assumption of inhomogeneity of the crystal, implying that the thinner sample has, in average, different chemical composition,

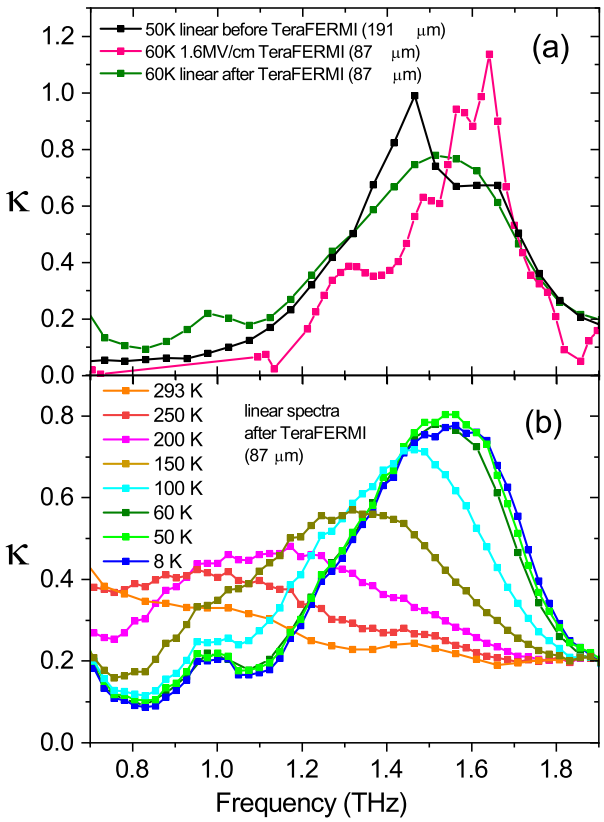

Figure 7.3: (a) Effect of intense THz radiation from TeraFERMI and history effect on the electromagnon in Y-hex. Black and olive are spectra of the imaginary part of the refractive index (κ) before and after the experiment at TeraFERMI, respectively. Their difference is much bigger than the statistical error. The spectra from TeraFERMI are displayed in pink. The small difference in temperatures (50 K vs. 60 K) has a minor effect, as seen from panel (b), showing temperature dependence linear THz spectra of Y-hex.

so the magnetic structure. Alternatively, any other chemical composition change could have happened during thinning down. The third explanation assumes permanent changes of the intense THz radiation beyond the picture based on static magnetic structures. This might include some irreversible changes of the chemical composition, which would in turn influence the magnetic structures.

Altogether, I stress that the sample history may have a crucial importance. This accounts for temperature, magnetic field, and possibly also the history of the THz radiation. It is always optimal to start with a sample in a well defined magnetic structure (either ALC or TC in this case) before each experiment to better track spectral differences from the pristine state. In my case, I cannot guarantee that the original experiment represents the pure ALC state, because I am not sure about the magnetic-temperature history which could have influenced the magnetic structure in the past.

7.8 Temperature dependence spectra of Y-hex

Typical cumulative heating effect is very small at TeraFERMI due to its low repetition rate (50 Hz) [252]. Nevertheless, I can directly exclude a possibility that the observed blue-shift in Y-hex is ascribed to heating by investigating temperature dependence of the linear spectra. Indeed, in Fig. 7.3(a), I display temperature dependence spectra of Y-hex which show red-shift upon heating, similarly as similar electromagnons in Y-hexaferrites [180, 207]. Therefore, the observed blue-shift cannot be described to sample heating.

7.9 Calculation of strength of the maximum internal THz magnetic field at TeraFERMI

As mentioned in the Tab. 2.2 and Sec. 7.1, the maximum external THz electric field incoming to the sample, $E_{ext}(t)$, displayed in Fig. 5.2(a), reaches 1.6 MV/cm. According to the Fresnel formula for reflection losses, I calculated the internal spectral amplitude $E_{0\mu\mathrm{m}}(\omega)$ and subsequently the internal electric field $E_{0\mu\mathrm{m}}(t)$, as mentioned in Sec. 7.5. My task is to determine the corresponding internal magnetic field, $B_{0\mu\mathrm{m}}(t)$.

Inside the material, the relation between magnitudes of the electric and magnetic fields is $B = E/v$, while $v = c/n$ is the velocity of radiation in the material, n being the real part of the refractive index. From my linear spectroscopy experiment, I can approximate the real part of the refractive index as $n \approx 5$, thus getting $B_{0\mu\mathrm{m}}(t)$. The peak of this function reaches as high as 0.9 T, which is maximal THz magnetic field in the sample.

7.10 Magnetization curve of Y-hex

Fig. 7.4 shows magnetization curve of a zero-field-cooled Y-hex at 10 K for $\boldsymbol{H} \| ab$-plane. After zero-field cooling, the sample is in the ALC phase, while the application of the in-plane field drives the magnetic structure to the TC phase [189]. The question is how large field is necessary to drive the system to the TC phase, and compare this static field to the THz magnetic field from TeraFERMI.

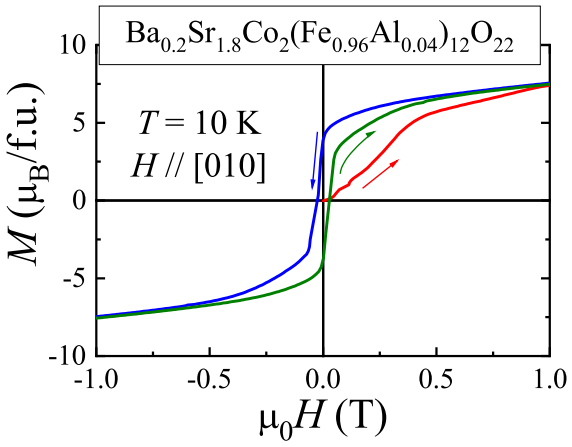

Figure 7.4: Magnetization curve of zero-field-cooled Y-hex at 10 K for $\boldsymbol{H} \parallel ab$-plane. Red is the virgin curve, while blue and green are curves after application +6 T and -6 T, respectively.

The virgin curve (red) matches the hysteretic ones at and above 1 T, meaning that after application of this field, all volume of the sample is in the TC phase. Nevertheless, the kink of the virgin curve at 0.5 T signs that most of the volume is in the TC phase already at this field, and some fraction of the sample is in the TC phase already for few hundreds of mT. This can be well compared to the THz magnetic field which is of the same order—as calculated in Sec. 7.9, the peak THz magnetic field reaches 0.9 T. Therefore, if I assume that the magnetic THz field of the same magnitude can act a similar way as the static magnetic field, I can expect that it transformed a part of the sample from the ALC to the TC phase.

Acknowledgments

At first, I would like to thank both of my supervisors, Stanislav Kamba and Sándor Bordács. I was very lucky to collaborate with such outstanding scientists in a field of multiferroics. I am indebted to Stanislav for introducing me the field of multiferroics and for his kindness and permanent support during my complicated Ph.D. studies. To Sándor, I am grateful for showing me how rigorous scientific investigation should be performed, and for his kindness and patience with me, since his intellect and performance highly exceeded mine.

I would like to thank several of my collaborators, without whom this Ph.D. work could not be done. At the Institute of Physics in Prague, these were mainly Christelle Kadlec and Filip Kadlec, who introduced me into THz spectroscopy and enormously helped me with measurements and manuscripts preparation. I also have to thank Petr Kužel, who built the THz lab and developed a unique program, without which I cannot imagine THz spectra evaluation. Further, I thank Dalibor Repček, Fedir Borodavka and Jan Drahokoupil for helping with THz, Raman and x-ray diffraction measurements, respectively. My work based in Budapest University of Technology and Economics stands on top of shoulders of four ”giants”, who did enormous amount of work, while my small contribution continued on top of it. These are István Kézsmárki, Sándor Bordács, Dávid Szaller and Vilmos Kocsis, who developed formalism for optical directional anisotropy effects, and performed several experiments on the crystals I investigated in this thesis. I thank all of them for numerous enlightening discussions. Importantly, both in Prague and in Budapest, I was extremely lucky to be in friendly communities of supportive colleagues, with whom sharing workplace was motivating and joyful.

I would like to thank colleagues from several collaborating groups. At the National Institute of Chemical Physics and Biophysics in Tallinn, it was a great fun to collaborate with tough nordic guys – Urmas Nagel, Toomas Rõõm, Laur Peedu, Johan Viirok and Kirill Amelin from THz laboratory on their outstanding spectrometer. Indispensable theoretical support came from Karlo Penc, Judith Romhányi and Péter Balla, for which I cannot be grateful enough since I cannot imagine how mentally difficult it is to work as a theoretical physicist. I am very indebted to Alexej Pashkin who prepared a THz spectroscopy setup at FELBE, HZDR just for the purpose of my research, and enormously helped me during several exhausting measurements.

Next, I would like to thank sample suppliers, first of all Vilmos Kocsis, who not only grew high-quality single crystals with help of Yusuke Tokunaga, but he characterized them as well. I was lucky to discuss with Yi Sheng Chai, who provided me hexaferrites crystals together with Kun Zhai, and he also gave me a deep knowledge about these complicated compounds. Next hexaferrite crystals were provided by Chang Bae Park and Kee Hoon Kim, to whom I also thank for providing additional data. For providing me hexaferrite

ceramics I thank Josef Buršík and Róbert Uhrecký.

I would like to thank many people who helped me during exhausting experiments at facilities providing intense THz radiation. At TeraFERMI in Trieste, I got an extensive help from Andrea Perucchi, Paola Di Pietro, Nidhi Adhlakha and Federica Piccirilli. At TELBE in Dresden-Rossendorf, I got non-stop help during the experiments from Sergey Kovalev, Jan-Christoph Deinert, Michael Gensch, Nilesh Awari, Min Chen, Zhe Wang, Bertram Green, Semyon Germanskyi, Igor Ilyakov and Mohammed Bawatna.

Next category of people who helped me are those who contributed by a little help, which was, however, extremely valuable. For instance, Sae Hwan Chun provided me details about his model, without which I would not be able to do any calculations. Furthermore, Titusz Fehér helped me with understanding magnetic resonances, and Dávid Szaller provided me LaTeX code of his dissertation. Jiří Fryštacký and Miloslav Krejza helped me by sample cutting in Prague, while Béla Horváth and Márton Hajdú provided me a technical support in Budapest.

Further, I would like to thank several people who helped me with different kinds of measurement: Jan Prokleška, Petr Proschek, Vladimír Tkáč, Martin Míšek, Michal Dušek, Veronica Goian, Maxim Savinov, Karel Jurek, Štěpán Huber, John Michael Klopf, Rakesh Rana, Bálint Fülöp, Zoltán Scherübl, Zoltán Kovács-Krausz, Botond Sánta and others, whom I apologize for not mentioning them here explicitly.

Yet, I have to thank numerous people for transferring me knowledge via lectures or discussions, including inspiring people I met at several conferences. Instead of mentioning numerous names and omitting those whose names I do not remember, I would like to highlight just one name as an example – my university teacher, legendary Štefan Zajac, whom I am grateful for his outstanding lectures about solid state physics and magnetism during my undergraduate studies. Moreover, I thank him for his empathy and care about my studies, and traveling from Prague to Budapest to be a committee member at my final exam.

Last, but not least, I would like to thank my closest persons in my life. First of all, to my parents for their full support. Special thanks I have towards my sister Linda, who motivated my by her outstanding ambitious life story, my cousin David, who inspired me to study physics, and especially joint PhD program, my grandfather Vladimír, who always cared about my progress and gave me positive energy, and my friend David Krause, whose unconventional comments helped me to wash my brain during mentally exhausting times. I would also like to thank two of my girlfriends I had during my PhD studies, Michelle Greenough and Tinkara Troha, with whom I could share most intimate stories of my Ph.D. life.

Bibliography

[1] R. Ramesh and L. W. Martin, "Electric field control of magnetism: multiferroics and magnetoelectrics," *La Rivista del Nuovo Cimento*, vol. 44, pp. 251–289, May 2021.

[2] R. Ramesh and S. Manipatruni, "Electric field control of magnetism," *Proceedings of the Royal Society A: Mathematical, Physical and Engineering Sciences*, vol. 477, no. 2251, p. 20200942, 2021.

[3] M. Bibes and A. Barthélémy, "Multiferroics: towards a magnetoelectric memory.," *Nature Materials*, vol. 7, pp. 425–6, 2008.

[4] Y. H. Chu, L. W. Martin, M. B. Holcomb, M. Gajek, S. jen Han, Q. He, N. Balke, C.-H. Yang, D. Lee, W. Hu, Q. Zhan, P. Yang, A. Fraile-Rodríguez, A. Scholl, S. X. Wang, and R. Ramesh, "Electric-field control of local ferromagnetism using a magnetoelectric multiferroic.," *Nature materials*, vol. 76, pp. 478–482, 2008.

[5] A. S. Logginov, G. A. Meshkov, A. V. Nikolaev, E. P. Nikolaeva, A. P. Pyatakov, and A. K. Zvezdin, "Room temperature magnetoelectric control of micromagnetic structure in iron garnet films," *Applied Physics Letters*, vol. 93, no. 18, p. 182510, 2008.

[6] L. D. Barron, *Molecular Light Scattering and Optical Activity*. Cambridge University Press, 2 ed., 2004.

[7] I. Kezsmarki, D. Szaller, S. Bordacs, H. Murakawa, Y. Tokura, H. Engelkamp, T. Room, and U. Nagel, "One-way transparency of four-coloured spin-wave excitations in multiferroic materials," *Nature Commun.*, vol. 5, p. 3203, 2014.

[8] I. Kézsmárki, U. Nagel, S. Bordács, R. S. Fishman, J. H. Lee, H. T. Yi, S.-W. Cheong, and T. Rõõm, "Optical diode effect at spin-wave excitations of the room-temperature multiferroic $BiFeO_3$," *Phys. Rev. Lett.*, vol. 115, p. 127203, Sep 2015.

[9] I. Kézsmárki, N. Kida, H. Murakawa, S. Bordács, Y. Onose, and Y. Tokura, "Enhanced directional dichroism of terahertz light in resonance with magnetic excitations of the multiferroic $Ba_2CoGe_2O_7$ oxide compound," *Phys. Rev. Lett.*, vol. 106, p. 057403, Feb 2011.

[10] S. Kimura, M. Matsumoto, and H. Tanaka, "Electrical switching of the nonreciprocal directional microwave response in a triplon Bose-Einstein condensate," *Phys. Rev. Lett.*, vol. 124, p. 217401, May 2020.

[11] J. Vít, J. Viirok, L. Peedu, T. Rõ om, U. Nagel, V. Kocsis, Y. Tokunaga, Y. Taguchi, Y. Tokura, I. Kézsmárki, P. Balla, K. Penc, J. Romhányi, and S. Bordács, "In situ electric-field control of THz nonreciprocal directional dichroism in the multiferroic

$Ba_2CoGe_2O_7$," *Phys. Rev. Lett.*, vol. 127, p. 157201, Oct 2021.

[12] C. D. Stanciu, F. Hansteen, A. V. Kimel, A. Kirilyuk, A. Tsukamoto, A. Itoh, and T. Rasing, "All-optical magnetic recording with circularly polarized light," *Phys. Rev. Lett.*, vol. 99, p. 047601, Jul 2007.

[13] A. Kirilyuk, A. V. Kimel, and T. Rasing, *All-Optical Switching of Magnetization*, ch. 10, pp. 80–107. CRC Press, 2019.

[14] P. Curie, "Sur la symétrie dans les phénomènes physiques, symétrie d'un champ électrique et d'un champ magnétique," *J. Phys. Theor. Appl.*, vol. 3, pp. 393–415, 1894.

[15] F. E. Neumann, *Vorlesungen über die Theorie der Elastizität der festenKörper und des Lichtäthers*. Leipzig: B. G.Teubner-Verlag, 1885.

[16] L. D. Landau and E. M. Lifshitz, *Electrodynamics of Continuous Media*. Gostekhizdat, 1957.

[17] R. R. Birss, *Symmetry and Magnetism*, vol. 3, ch. 4, pp. 136–140. North-Holland publishing company, 1964.

[18] N. Astrov, "The magnetoelectric effect in antiferromagnetics," *JETP*, vol. 38, pp. 984–985, Sept. 1960.

[19] I. E. Dzyaloshinskii, "On the magneto-electrical effect in antiferromagnets," *JETP*, vol. 37, pp. 881–882, 1959.

[20] W. F. Brown, R. M. Hornreich, and S. Shtrikman, "Upper bound on the magnetoelectric susceptibility," *Phys. Rev.*, vol. 168, pp. 574–577, Apr 1968.

[21] V. J. Folen, G. T. Rado, and E. W. Stalder, "Anisotropy of the magnetoelectric effect in Cr_2O_3," *Phys. Rev. Lett.*, vol. 6, pp. 607–608, Jun 1961.

[22] D. N. Astrov, "Magnetoelectric effect in chromium oxide," *Sov. Phys. JETP*, vol. 13, pp. 729–733, Oct. 1961.

[23] G. T. Rado, "Mechanism of the magnetoelectric effect in an antiferromagnet," *Phys. Rev. Lett.*, vol. 6, pp. 609–610, Jun 1961.

[24] T. R. McGuire, E. J. Scott, and F. H. Grannis, "Antiferromagnetism in a Cr_2O_3 crystal," *Phys. Rev.*, vol. 102, pp. 1000–1003, May 1956.

[25] L. Néel, "Nobel lecture," NobelPrize.org. Nobel Prize Outreach, 1970.

[26] H. Schmid, "Multi-ferroic magnetoelectrics," *Ferroelectrics*, vol. 162, no. 1, pp. 317–338, 1994.

[27] N. A. Spaldin, S. Cheong, and R. Ramesh, "Multiferroics: Past, present, and future," *Physics Today*, vol. 63, pp. 38–43, 2010.

[28] N. A. Hill, "Why are there so few magnetic ferroelectrics?," *The Journal of Physical Chemistry B*, vol. 104, no. 29, pp. 6694–6709, 2000.

[29] P. Ravindran, R. Vidya, A. Kjekshus, H. Fjellvåg, and O. Eriksson, "Theoretical investigation of magnetoelectric behavior in $BiFeO_3$," *Phys. Rev. B*, vol. 74, p. 224412, Dec 2006.

[30] I. Sosnowska, T. P. Neumaier, and E. Steichele, "Spiral magnetic ordering in bismuth ferrite," *Journal of Physics C: Solid State Physics*, vol. 15, pp. 4835–4846,

aug 1982.

[31] H. Schmid, "On a magnetoelectric classification of materials," *International journal of magnetism*, vol. 4, no. 4, pp. 337–361, 1973.

[32] D. I. Khomskii, "Classifying multiferroics: Mechanisms and effects," *Physics*, vol. 2, p. 20, 2009.

[33] A. Kania, S. Miga, E. Talik, I. Gruszka, M. Szubka, M. Savinov, J. Prokleška, and S. Kamba, "Dielectric and magnetic properties, and electronic structure of multiferroic perovskite $PbFe_{0.5}Ta_{0.5}O_3$ and incipient ferroelectric pyrochlore $Pb_2Fe_{0.34}Ta_{1.84}O_{7.11}$ single crystals and ceramics," *Journal of the European Ceramic Society*, vol. 36, no. 14, pp. 3369–3381, 2016.

[34] B. B. V. Aken, T. T. Palstra, A. Filippetti, and N. A. Spaldin, "The origin of ferroelectricity in magnetoelectric $YMnO_3$," *Nature Materials*, vol. 3, pp. 164–170, feb 2004.

[35] N. A. Spaldin, M. Fechner, E. Bousquet, A. Balatsky, and L. Nordström, "Monopole-based formalism for the diagonal magnetoelectric response," *Physical Review B*, vol. 88, p. 094429, sep 2013.

[36] N. A. Spaldin, M. Fiebig, and M. V. Mostovoy, "The toroidal moment in condensed-matter physics and its relation to the magnetoelectric effect*," *Journal of Physics: Condensed Matter*, vol. 20, p. 434203, 2008.

[37] C. Ederer and N. A. Spaldin, "Towards a microscopic theory of toroidal moments in bulk periodic crystals," *Physical Review B*, vol. 76, p. 214404, Dec 2007.

[38] R. D. King-Smith and D. Vanderbilt, "Theory of polarization of crystalline solids," *Physical Review B*, vol. 47, pp. 1651–1654, jan 1993.

[39] A. Planes, T. Castán, and A. Saxena, "Recent progress in the thermodynamics of ferrotoroidic materials," *Multiferroic Materials*, vol. 1, jan 2015.

[40] V. Kocsis, S. Bordács, Y. Tokunaga, J. Viirok, L. Peedu, T. Rõõm, U. Nagel, Y. Taguchi, Y. Tokura, and I. Kézsmárki, "Magnetoelectric spectroscopy of spin excitations in $LiCoPO_4$," *Phys. Rev. B*, vol. 100, p. 155124, Oct 2019.

[41] B. B. V. Aken, J.-P. Rivera, H. Schmid, and M. Fiebig, "Observation of ferrotoroidic domains," *Nature*, vol. 449, pp. 702–705, oct 2007.

[42] M. Mercier, J. Gareyte, and E. Bertaut, "Une nouvelle famille de corps magnetoelectriques-$LiMnPO_4$ (M= Mn, Co, Ni)," *Comptes Rendus Hebdomadaires Des Seances De L Academie Des Sciences Serie B*, vol. 264, no. 13, p. 979, 1967.

[43] K. Kimura, P. Babkevich, M. Sera, M. Toyoda, K. Yamauchi, G. S. Tucker, J. Martius, T. Fennell, P. Manuel, D. D. Khalyavin, R. D. Johnson, T. Nakano, Y. Nozue, H. M. Rønnow, and T. Kimura, "Magnetodielectric detection of magnetic quadrupole order in $Ba(TiO)Cu_4(PO_4)_4$ with Cu_4O_{12} square cupolas," *Nature Communications*, vol. 7, oct 2016.

[44] P. Wang, X. Lu, X. Gong, and H. Xiang, "Microscopic mechanism of spin-order induced improper ferroelectric polarization," *Comp. Mat. Science*, vol. 112, pp. 448 – 458, 2016.

[45] M. Matsumoto, K. Chimata, and M. Koga, "Symmetry analysis of spin-dependent

electric dipole and its application to magnetoelectric effects," *J. Phys. Soc. Japan*, vol. 86, no. 3, p. 034704, 2017.

[46] C. Jia, S. Onoda, N. Nagaosa, and J. H. Han, "Bond electronic polarization induced by spin," *Phys. Rev. B*, vol. 74, p. 224444, Dec 2006.

[47] H. Katsura, N. Nagaosa, and A. V. Balatsky, "Spin current and magnetoelectric effect in noncollinear magnets," *Phys. Rev. Lett.*, vol. 95, p. 057205, Jul 2005.

[48] Y. Tokura, S. Seki, and N. Nagaosa, "Multiferroics of spin origin," *Rep. Prog. Phys.*, vol. 77, no. 7, p. 076501, 2014.

[49] I. A. Sergienko and E. Dagotto, "Role of the Dzyaloshinskii-Moriya interaction in multiferroic perovskites," *Phys. Rev. B*, vol. 73, p. 094434, Mar 2006.

[50] I. E. Dzyaloshinskii, "A thermodynamic theory of "weak" ferromagnetism of antiferromagnetics," *J. Phys. Chem. Solids*, vol. 4, pp. 241–255, 1958.

[51] T. Moriya, "New mechanism of anisotropic superexchange interaction," *Phys. Rev. Lett.*, vol. 4, pp. 228–230, Mar 1960.

[52] T. Moriya, "Anisotropic superexchange interaction and weak ferromagnetism," *Phys. Rev.*, vol. 120, pp. 91–98, Oct 1960.

[53] Y. S. Chai, S. Kwon, S. H. Chun, I. Kim, B.-G. Jeon, K. H. Kim, and S. Lee, "Electrical control of large magnetization reversal in a helimagnet," *Nature Commun.*, vol. 5, p. 4208, 2014.

[54] T. A. Kaplan and S. D. Mahanti, "Canted-spin-caused electric dipoles: A local symmetry theory," *Phys. Rev. B*, vol. 83, p. 174432, May 2011.

[55] M. Mostovoy, "Helicoidal ordering in iron perovskites," *Physical Review Letters*, vol. 94, p. 137205, apr 2005.

[56] I. A. Sergienko, C. Şen, and E. Dagotto, "Ferroelectricity in the magnetic E-phase of orthorhombic perovskites," *Phys. Rev. Lett.*, vol. 97, no. 22, p. 227204, 2006.

[57] L. Bulaevskii, "Theory of non-uniform antiferromagnetic spin chains," *Sov. Phys. JETP*, vol. 17, pp. 684–687, 1963.

[58] J. C. Bonner and M. E. Fisher, "Linear magnetic chains with anisotropic coupling," *Phys. Rev.*, vol. 135, pp. A640–A658, Aug 1964.

[59] C. N. Yang and C. P. Yang, "One-Dimensional Chain of Anisotropic Spin-Spin Interactions. I. Proof of Bethe's Hypothesis for Ground State in a Finite System," *Phys. Rev.*, vol. 150, pp. 321–327, Oct 1966.

[60] J. W. Bray, L. V. Interrante, I. S. Jacobs, and J. C. Bonner, *The Spin-Peierls Transition*, pp. 353–415. Boston, MA: Springer US, 1983.

[61] S.-P. Shen, X.-Z. Liu, Y.-S. Chai, A. Studer, K. Rule, K. Zhai, L.-Q. Yan, D.-S. Shang, F. Klose, Y.-T. Liu, D.-F. Chen, and Y. Sun, "Hidden spin-order-induced room-temperature ferroelectricity in a peculiar conical magnetic structure," *Phys. Rev. B*, vol. 95, p. 094405, Mar 2017.

[62] H. J. Xiang, E. J. Kan, Y. Zhang, M.-H. Whangbo, and X. G. Gong, "General theory for the ferroelectric polarization induced by spin-spiral order," *Phys. Rev. Lett.*, vol. 107, p. 157202, Oct 2011.

[63] A. Malashevich and D. Vanderbilt, "First principles study of improper ferroelectricity in $TbMnO_3$," *Phys. Rev. Lett.*, vol. 101, p. 037210, Jul 2008.

[64] A. Malashevich and D. Vanderbilt, "Dependence of electronic polarization on octahedral rotations in $TbMnO_3$ from first principles," *Phys. Rev. B*, vol. 80, p. 224407, Dec 2009.

[65] H. C. Walker, F. Fabrizi, L. Paolasini, F. de Bergevin, J. Herrero-Martin, A. T. Boothroyd, D. Prabhakaran, and D. F. McMorrow, "Femtoscale magnetically induced lattice distortions in multiferroic $TbMnO_3$," *Science*, vol. 333, no. 6047, pp. 1273–1276, 2011.

[66] H. J. Xiang, P. S. Wang, M.-H. Whangbo, and X. G. Gong, "Unified model of ferroelectricity induced by spin order," *Phys. Rev. B*, vol. 88, p. 054404, Aug 2013.

[67] X. Wu, D. Vanderbilt, and D. R. Hamann, "Systematic treatment of displacements, strains, and electric fields in density-functional perturbation theory," *Phys. Rev. B*, vol. 72, p. 035105, Jul 2005.

[68] C. W. Swartz and X. Wu, "Modeling functional piezoelectricity in perovskite superlattices with competing instabilities," *Phys. Rev. B*, vol. 85, p. 054102, Feb 2012.

[69] R. Kubo, "Statistical-mechanical theory of irreversible processes. I. General theory and simple applications to magnetic and conduction problems," *Journal of the Physical Society of Japan*, vol. 12, no. 6, pp. 570–586, 1957.

[70] S. Miyahara and N. Furukawa, "Nonreciprocal directional dichroism and toroidal-magnons in helical magnets," *Journal of the Physical Society of Japan*, vol. 81, no. 2, p. 023712, 2012.

[71] S. Bordács, I. Kézsmárki, D. Szaller, L. Demko, N. Kida, H. Murakawa, Y. Onose, R. Shimano, T. Rõõm, U. Nagel, S. Miyahara, N. Furukawa, and Y. Tokura, "Chirality of matter shows up via spin excitations," *Nature Physics*, vol. 8, pp. 734–738, 2012.

[72] R. de L. Kronig, "On the theory of dispersion of x-rays," *J. Opt. Soc. Am.*, vol. 12, pp. 547–557, Jun 1926.

[73] H. A. Kramers, "La diffusion de la lumière par les atomes," *Atti Cong. Intern. Fisici, (Transactions of Volta Centenary Congress) Como.*, vol. 2, pp. 545–557, 1927.

[74] D. Szaller, S. Bordács, V. Kocsis, T. Rõõm, U. Nagel, and I. Kézsmárki, "Effect of spin excitations with simultaneous magnetic- and electric-dipole character on the static magnetoelectric properties of multiferroic materials," *Phys. Rev. B*, vol. 89, p. 184419, May 2014.

[75] D. Szaller, S. Bordács, and I. Kézsmárki, "Symmetry conditions for nonreciprocal light propagation in magnetic crystals," *Phys. Rev. B*, vol. 87, p. 014421, Jan 2013.

[76] E. Ascher, "Some properties of spontaneous currents," *Helv. Phys. Acta*, vol. 39, pp. 40–48, 1966.

[77] G. L. J. A. Rikken and E. Raupach, "Observation of magneto-chiral dichroism," *Nature*, vol. 390, pp. 493–494, 1997.

[78] G. Rikken, E. Raupach, and T. Roth, "Recent advances in magneto-optics," *Physica*

B: Condensed Matter, vol. 294-295, pp. 1–4, 2001. Proceedings of the Sixth International Symposium on Research in High Magnetic Fields.

[79] C. Koerdt, G. Düchs, and G. L. J. A. Rikken, "Magnetochiral anisotropy in Bragg scattering," *Phys. Rev. Lett.*, vol. 91, p. 073902, Aug 2003.

[80] G. L. J. A. Rikken, J. Fölling, and P. Wyder, "Electrical magnetochiral anisotropy," *Phys. Rev. Lett.*, vol. 87, p. 236602, Nov 2001.

[81] V. Krstić, S. Roth, M. Burghard, K. Kern, and G. L. J. A. Rikken, "Magnetochiral anisotropy in charge transport through single-walled carbon nanotubes," *The Journal of Chemical Physics*, vol. 117, no. 24, pp. 11315–11319, 2002.

[82] G. L. J. A. Rikken and P. Wyder, "Magnetoelectric anisotropy in diffusive transport," *Phys. Rev. Lett.*, vol. 94, p. 016601, Jan 2005.

[83] K. Zakeri, Y. Zhang, J. Prokop, T.-H. Chuang, N. Sakr, W. X. Tang, and J. Kirschner, "Asymmetric Spin-Wave Dispersion on Fe(110): Direct Evidence of the Dzyaloshinskii-Moriya Interaction," *Phys. Rev. Lett.*, vol. 104, p. 137203, Mar 2010.

[84] Y. Iguchi, S. Uemura, K. Ueno, and Y. Onose, "Nonreciprocal magnon propagation in a noncentrosymmetric ferromagnet $LiFe_5O_8$," *Phys. Rev. B*, vol. 92, p. 184419, Nov 2015.

[85] S. Seki, Y. Okamura, K. Kondou, K. Shibata, M. Kubota, R. Takagi, F. Kagawa, M. Kawasaki, G. Tatara, Y. Otani, and Y. Tokura, "Magnetochiral nonreciprocity of volume spin wave propagation in chiral-lattice ferromagnets," *Phys. Rev. B*, vol. 93, p. 235131, Jun 2016.

[86] Y. Iguchi, Y. Nii, M. Kawano, H. Murakawa, N. Hanasaki, and Y. Onose, "Microwave nonreciprocity of magnon excitations in the noncentrosymmetric antiferromagnet $Ba_2MnGe_2O_7$," *Phys. Rev. B*, vol. 98, p. 064416, Aug 2018.

[87] J. Heil, B. Lüthi, and P. Thalmeier, "Nonreciprocal surface-acoustic-wave propagation in aluminum," *Phys. Rev. B*, vol. 25, pp. 6515–6517, May 1982.

[88] R. Sasaki, Y. Nii, Y. Iguchi, and Y. Onose, "Nonreciprocal propagation of surface acoustic wave in $Ni/LiNbO_3$," *Phys. Rev. B*, vol. 95, p. 020407, Jan 2017.

[89] T. Nomura, X.-X. Zhang, S. Zherlitsyn, J. Wosnitza, Y. Tokura, N. Nagaosa, and S. Seki, "Phonon magnetochiral effect," *Physical Review Letters*, vol. 122, p. 145901, apr 2019.

[90] Y. Tokura and N. Nagaosa, "Nonreciprocal responses from non-centrosymmetric quantum materials," *Nature Communications*, vol. 9, sep 2018.

[91] J. J. Hopfield and D. G. Thomas, "Photon momentum effects in the magneto-optics of excitons," *Phys. Rev. Lett.*, vol. 4, pp. 357–359, Apr 1960.

[92] T. Roth and G. L. J. A. Rikken, "Observation of magnetoelectric linear birefringence," *Phys. Rev. Lett.*, vol. 88, p. 063001, Jan 2002.

[93] M. Kubota, T. Arima, Y. Kaneko, J. P. He, X. Z. Yu, and Y. Tokura, "X-ray directional dichroism of a polar ferrimagnet," *Phys. Rev. Lett.*, vol. 92, p. 137401, Mar 2004.

[94] J. H. Jung, M. Matsubara, T. Arima, J. P. He, Y. Kaneko, and Y. Tokura, "Optical

magnetoelectric effect in the polar $GaFeO_3$ ferrimagnet," *Phys. Rev. Lett.*, vol. 93, p. 037403, Jul 2004.

[95] N. Kida, Y. Kaneko, J. P. He, M. Matsubara, H. Sato, T. Arima, H. Akoh, and Y. Tokura, "Enhanced optical magnetoelectric effect in a patterned polar ferrimagnet," *Phys. Rev. Lett.*, vol. 96, p. 167202, Apr 2006.

[96] M. Saito, K. Taniguchi, and T.-h. Arima, "Gigantic optical magnetoelectric effect in CuB_2O_4," *Journal of the Physical Society of Japan*, vol. 77, no. 1, p. 013705, 2008.

[97] M. Saito, K. Ishikawa, K. Taniguchi, and T. Arima, "Magnetic control of crystal chirality and the existence of a large magneto-optical dichroism effect in CuB_2O_4," *Phys. Rev. Lett.*, vol. 101, p. 117402, Sep 2008.

[98] Y. Takahashi, R. Shimano, Y. Kaneko, H. Murakawa, and Y. Tokura, "Magnetoelectric resonance with electromagnons in a perovskite helimagnet," *Nature Physics*, vol. 8, pp. 121–125, 2012.

[99] Y. Takahashi, Y. Yamasaki, and Y. Tokura, "Terahertz magnetoelectric resonance enhanced by mutual coupling of electromagnons," *Phys. Rev. Lett.*, vol. 111, p. 037204, Jul 2013.

[100] S. Kibayashi, Y. Takahashi, S. Seki, and Y. Tokura, "Magnetochiral dichroism resonant with electromagnons in a helimagnet.," *Nature communications*, vol. 5, p. 4583, 2014.

[101] A. M. Kuzmenko, V. Dziom, A. Shuvaev, A. Pimenov, M. Schiebl, A. A. Mukhin, V. Y. Ivanov, I. A. Gudim, L. N. Bezmaternykh, and A. Pimenov, "Large directional optical anisotropy in multiferroic ferroborate," *Phys. Rev. B*, vol. 92, p. 184409, Nov 2015.

[102] S. Bordács, V. Kocsis, Y. Tokunaga, U. Nagel, T. Rõ om, Y. Takahashi, Y. Taguchi, and Y. Tokura, "Unidirectional terahertz light absorption in the pyroelectric ferrimagnet $CaBaCo_4O_7$," *Phys. Rev. B*, vol. 92, p. 214441, Dec 2015.

[103] Y. Takahashi, S. Kibayashi, Y. Kaneko, and Y. Tokura, "Versatile optical magnetoelectric effects by electromagnons in $MnWO_4$ with canted spin-spiral plane," *Phys. Rev. B*, vol. 93, p. 180404, May 2016.

[104] H. Narita, Y. Tokunaga, A. Kikkawa, Y. Taguchi, Y. Tokura, and Y. Takahashi, "Observation of nonreciprocal directional dichroism via electromagnon resonance in a chiral-lattice helimagnet $Ba_3NbFe_3Si_2O_{14}$," *Phys. Rev. B*, vol. 94, p. 094433, Sep 2016.

[105] V. Kocsis, K. Penc, T. Rõõm, U. Nagel, J. Vít, J. Romhányi, Y. Tokunaga, Y. Taguchi, Y. Tokura, I. Kézsmárki, and S. Bordács, "Identification of antiferromagnetic domains via the optical magnetoelectric effect," *Phys. Rev. Lett.*, vol. 121, p. 057601, Aug 2018.

[106] T. Sato, N. Abe, S. Kimura, Y. Tokunaga, and T.-h. Arima, "Magnetochiral dichroism in a collinear antiferromagnet with no magnetization," *Phys. Rev. Lett.*, vol. 124, p. 217402, May 2020.

[107] S. Yu, B. Gao, J. W. Kim, S.-W. Cheong, M. K. L. Man, J. Madéo, K. M. Dani, and D. Talbayev, "High-temperature terahertz optical diode effect without magnetic

order in polar $FeZnMo_3O_8$," *Phys. Rev. Lett.*, vol. 120, p. 037601, Jan 2018.

[108] S. Rezende, *Fundamentals of Magnonics*. Springer Nature Switzerland AG, First Edition, 2020.

[109] M. Matsumoto and M. Koga, "Longitudinal spin-wave mode near quantum critical point due to uniaxial anisotropy," *Journal of the Physical Society of Japan*, vol. 76, no. 7, p. 073709, 2007.

[110] M. Matsumoto, H. Kuroe, T. Sekine, and T. Masuda, "Transverse and longitudinal excitation modes in interacting multispin systems," *Journal of the Physical Society of Japan*, vol. 79, no. 8, p. 084703, 2010.

[111] K. Penc, J. Romhányi, T. Rõõm, U. Nagel, A. Antal, T. Fehér, A. Jánossy, H. Engelkamp, H. Murakawa, Y. Tokura, D. Szaller, S. Bordács, and I. Kézsmárki, "Spin-stretching modes in anisotropic magnets: Spin-wave excitations in the multiferroic $Ba_2CoGe_2O_7$," *Phys. Rev. Lett.*, vol. 108, p. 257203, Jun 2012.

[112] M. Matsumoto, "Electromagnon as a probe of Higgs (longitudinal) mode in collinear and noncollinear magnetically ordered states," *Journal of the Physical Society of Japan*, vol. 83, no. 8, p. 084704, 2014.

[113] M. Matsumoto, T. Sakurai, Y. Hirao, H. Ohta, Y. Uwatoko, and H. Tanaka, "First ESR detection of Higgs amplitude mode and analysis with extended spin-wave theory in dimer system $KCuCl_3$," *Applied Magnetic Resonance*, vol. 52, pp. 523–564, Apr 2021.

[114] M. P. V. Stenberg and R. de Sousa, "Sinusoidal electromagnon in $RMnO_3$: Indication of anomalous magnetoelectric coupling," *Phys. Rev. B*, vol. 85, p. 104412, Mar 2012.

[115] L. Peedu, V. Kocsis, D. Szaller, J. Viirok, U. Nagel, T. Rõ om, D. G. Farkas, S. Bordács, D. L. Kamenskyi, U. Zeitler, Y. Tokunaga, Y. Taguchi, Y. Tokura, and I. Kézsmárki, "Spin excitations of magnetoelectric $LiNiPO_4$ in multiple magnetic phases," *Phys. Rev. B*, vol. 100, p. 024406, Jul 2019.

[116] Y. T. Rebane, "Faraday effect produced in the residual ray region by the magnetic moment of an optical phonon in an ionic crystal," *Zh. Eksp. Teor. Fiz*, vol. 84, p. 2323, 1983.

[117] D. M. Juraschek, M. Fechner, A. V. Balatsky, and N. A. Spaldin, "Dynamical multiferroicity," *Phys. Rev. Materials*, vol. 1, p. 014401, Jun 2017.

[118] L. Allen, M. W. Beijersbergen, R. J. C. Spreeuw, and J. P. Woerdman, "Orbital angular momentum of light and the transformation of Laguerre-Gaussian laser modes," *Phys. Rev. A*, vol. 45, pp. 8185–8189, Jun 1992.

[119] A. A. Sirenko, P. Marsik, C. Bernhard, T. N. Stanislavchuk, V. Kiryukhin, and S.-W. Cheong, "Terahertz vortex beam as a spectroscopic probe of magnetic excitations," *Phys. Rev. Lett.*, vol. 122, p. 237401, Jun 2019.

[120] T. F. Nova, A. Cartella, A. Cantaluppi, M. Foerst, D. Bossini, R. V. Mikhaylovskiy, A. V. Kimel, R. Merlin, and A. Cavalleri, "An effective magnetic field from optically driven phonons," *Nature Physics*, vol. 13, pp. 132–136, 2017.

[121] S. Tauchert, M. Volkov, D. Ehberger, D. Kazenwadel, M. Evers, H. Lange,

A. Donges, A. Book, W. Kreuzpaintner, U. Nowak, and P. Baum, "Polarized phonons carry angular momentum in ultrafast demagnetization.," *Nature*, vol. 602 7895, pp. 73–77, 2022.

[122] R. Sasaki, Y. Nii, and Y. Onose, "Magnetization control by angular momentum transfer from surface acoustic wave to ferromagnetic spin moments," *Nature Commun.*, vol. 12, p. 2599, 2021.

[123] A. Rückriegel, S. Streib, G. E. W. Bauer, and R. A. Duine, "Angular momentum conservation and phonon spin in magnetic insulators," *Phys. Rev. B*, vol. 101, p. 104402, Mar 2020.

[124] C. Dornes, Y. Acremann, M. Savoini, M. Kubli, M. Neugebauer, E. Abreu, L. Huber, G. Lantz, C. A. F. Vaz, H. T. Lemke, E. M. Bothschafter, M. Porer, V. J. Esposito, L. Rettig, M. Buzzi, A. Alberca, Y. W. Windsor, P. Beaud, U. Staub, D. Zhu, S. Song, J. M. Glownia, and S. L. Johnson, "The ultrafast Einstein–de Haas effect," *Nature*, vol. 565, pp. 209–212, 2019.

[125] D. M. Juraschek and N. A. Spaldin, "Orbital magnetic moments of phonons," *Phys. Rev. Materials*, vol. 3, p. 064405, Jun 2019.

[126] D. M. Juraschek, T. c. v. Neuman, and P. Narang, "Giant effective magnetic fields from optically driven chiral phonons in $4f$ paramagnets," *Phys. Rev. Research*, vol. 4, p. 013129, Feb 2022.

[127] A. Baydin, F. G. G. Hernandez, M. Rodriguez-Vega, A. K. Okazaki, F. Tay, G. T. Noe, I. Katayama, J. Takeda, H. Nojiri, P. H. O. Rappl, E. Abramof, G. A. Fiete, and J. Kono, "Magnetic control of soft chiral phonons in PbTe," *Phys. Rev. Lett.*, vol. 128, p. 075901, Feb 2022.

[128] Y. Ren, C. Xiao, D. Saparov, and Q. Niu, "Phonon magnetic moment from electronic topological magnetization," *Phys. Rev. Lett.*, vol. 127, p. 186403, Oct 2021.

[129] S. Pal, N. Strkalj, C.-J. Yang, M. C. Weber, M. Trassin, M. Woerner, and M. Fiebig, "Origin of terahertz soft-mode nonlinearities in ferroelectric perovskites," *Phys. Rev. X*, vol. 11, p. 021023, Apr 2021.

[130] B. Cheng, T. Schumann, Y. C. Wang, X. S. Zhang, D. Barbalas, S. Stemmer, and N. P. Armitage, "A large effective phonon magnetic moment in a Dirac semimetal.," *Nano letters*, vol. 20, pp. 5991–5996, 2020.

[131] C. Hauf, A.-A. H. Salvador, M. Holtz, M. Woerner, and T. Elsaesser, "Soft-mode driven polarity reversal in ferroelectrics mapped by ultrafast x-ray diffraction," *Structural Dynamics*, vol. 5, p. 024501, 2018.

[132] T. Kimura, T. Goto, H. Shintani, K. Ishizaka, T. hisa Arima, and Y. Tokura, "Magnetic control of ferroelectric polarization," *Nature*, vol. 426, pp. 55–58, 2003.

[133] A. M. Shuvaev, V. D. Travkin, V. Y. Ivanov, A. A. Mukhin, and A. Pimenov, "Evidence for electroactive excitation of the spin cycloid in $TbMnO_3$," *Phys. Rev. Lett.*, vol. 104, p. 097202, Mar 2010.

[134] R. Saint-Martin and S. Franger, "Growth of $LiCoPO_4$ single crystals using an optical floating-zone technique," *Journal of Crystal Growth*, vol. 310, no. 4, pp. 861–864, 2008.

[135] H. Murakawa, Y. Onose, S. Miyahara, N. Furukawa, and Y. Tokura, "Comprehensive study of the ferroelectricity induced by the spin-dependent d-p hybridization mechanism in $Ba_2XGe_2O_7$ (X = Mn, Co, and Cu)," *Phys. Rev. B*, vol. 85, p. 174106, May 2012.

[136] N. Momozawa, M. Mita, and H. Takei, "Single crystal growth of $(Ba_{1-x}Sr_x)_2Zn_2Fe_{12}O_{22}$ from high temperature solution," *J. Cryst. Growth*, vol. 83, no. 3, pp. 403 – 409, 1987.

[137] Y. Chai, S. H. Chun, S. Y. Haam, Y. S. Oh, I. Kim, and K. H. Kim, "Low-magnetic-field control of dielectric constant at room temperature realized in $Ba_{0.5}Sr_{1.5}Zn_2Fe_{12}O_{22}$," *New Journal of Physics*, vol. 11, p. 073030, 2009.

[138] F. Kadlec, C. Kadlec, J. Vít, F. Borodavka, M. Kempa, J. Prokleška, J. Buršík, R. Uhrecký, S. Rols, Y. S. Chai, K. Zhai, Y. Sun, J. Drahokoupil, V. Goian, and S. Kamba, "Electromagnon in the Z-type hexaferrite $(Ba_xSr_{1-x})_3Co_2Fe_{24}O_{41}$," *Phys. Rev. B*, vol. 94, p. 024419, Jul 2016.

[139] V. Skoromets, H. Němec, V. Goian, S. Kamba, and P. Kužel, "Performance Comparison of Time-Domain Terahertz, Multi-terahertz, and Fourier Transform Infrared Spectroscopies," *Journal of Infrared, Millimeter, and Terahertz Waves*, vol. 39, pp. 1249–1263, oct 2018.

[140] F. Gervais, *Infrared and Millimeter Waves*.

[141] S. L. Dexheimer, ed., *Terahertz Spectroscopy*. CRC Press, dec 2017.

[142] M. Born, E. Wolf, A. B. Bhatia, P. C. Clemmow, D. Gabor, A. R. Stokes, A. M. Taylor, P. A. Wayman, and W. L. Wilcock, *Principles of Optics: Electromagnetic Theory of Propagation, Interference and Diffraction of Light*. Cambridge University Press, 7 ed., 1999.

[143] N. Vieweg, F. Rettich, A. Deninger, H. Roehle, R. J. B. Dietz, T. Göbel, and M. Schell, "Terahertz-time domain spectrometer with 90 dB peak dynamic range," *Journal of Infrared, Millimeter, and Terahertz Waves*, vol. 35, pp. 823–832, 2014.

[144] T. C. Damen, S. P. S. Porto, and B. Tell, "Raman effect in zinc oxide," *Phys. Rev.*, vol. 142, pp. 570–574, Feb 1966.

[145] "Free-Electron Lasers at the ELBE - Center for High-Power Radiation Sources at the HZDR in Dresden-Rossendorf, https://www.hzdr.de/db/Cms?pOid=10234pNid=471," Aug 2022.

[146] "Telbe: High-field high-repetition-rate terahertz facility @ elbe, https://www.hzdr.de/db/cms?poid=34100pnid=2609," Aug 2022.

[147] B. Green, S. Kovalev, V. Asgekar, G. Geloni, U. Lehnert, T. Golz, M. Kuntzsch, C. Bauer, J. Hauser, J. Voigtländer, B. Wustmann, I. Koesterke, M. Schwarz, M. Freitag, A. Arnold, J. Teichert, M. Justus, W. Seidel, C. Ilgner, N. Awari, D. Nicoletti, S. Kaiser, Y. Laplace, S. Rajasekaran, L. Zhang, S. Winnerl, H. Schneider, G. Schay, I. Lorincz, A. Rauscher, I. Radu, S. Maehrlein, T. Kim, J. Lee, T. Kampfrath, S. Wall, J. Heberle, A. Málnási-Csizmadia, A. Steiger, A. Müller, M. Helm, U. Schramm, T. Cowan, P. Michel, A. Cavalleri, A. Fisher, N. Stojanovic, and M. Gensch, "High-Field High-Repetition-Rate Sources for the Coherent THz Control of Matter," *Scientific Reports*, vol. 6, 2016.

[148] S. Kovalev, B. Green, T. Golz, S. Maehrlein, N. Stojanovic, A. Fisher, T. Kampfrath, and M. Gensch, "Probing ultra-fast processes with high dynamic range at 4th-generation light sources: Arrival time and intensity binning at unprecedented repetition rates," *Structural Dynamics*, vol. 4, p. 024301, 2017.

[149] A. Perucchi, S. D. Mitri, G. Penco, E. Allaria, and S. Lupi, "The TeraFERMI terahertz source at the seeded FERMI free-electron-laser facility.," *The Review of scientific instruments*, vol. 84 2, p. 022702, 2013.

[150] P. D. Pietro, N. Adhlakha, F. Piccirilli, L. Capasso, C. Svetina, S. D. Mitri, M. Veronese, F. Giorgianni, S. Lupi, and A. Perucchi, "TeraFERMI: A Super-radiant Beamline for THz Nonlinear Studies at the FERMI Free Electron Laser Facility," *Synchrotron Radiation News*, vol. 30, no. 4, pp. 36–39, 2017.

[151] J.-P. Rivera, "The linear magnetoelectric effect in $LiCoPO_4$ revisited," *Ferroelectrics*, vol. 161, no. 1, pp. 147–164, 1994.

[152] T. Sato, T. Masuda, and K. Uchinokura, "Magnetic property of $Ba_2CoGe_2O_7$," *Physica B: Condensed Matter*, vol. 329-333, pp. 880–881, 2003. Proceedings of the 23rd International Conference on Low Temperature Physics.

[153] A. Zheludev, T. Sato, T. Masuda, K. Uchinokura, G. Shirane, and B. Roessli, "Spin waves and the origin of commensurate magnetism in $Ba_2CoGe_2O_7$," *Phys. Rev. B*, vol. 68, p. 024428, Jul 2003.

[154] H. T. Yi, Y. J. Choi, S. Lee, and S.-W. Cheong, "Multiferroicity in the square-lattice antiferromagnet of $Ba_2CoGe_2O_7$," *Applied Physics Letters*, vol. 92, no. 21, p. 212904, 2008.

[155] M. Akaki, J. Tozawa, D. Akahoshi, and H. Kuwahara, "Gigantic magnetoelectric effect caused by magnetic-field-induced canted antiferromagnetic-paramagnetic transition in quasi-two-dimensional $Ca_2CoSi_2O_7$ crystal," *Applied Physics Letters*, vol. 94, p. 212904, May 2009.

[156] M. Akaki, J. Tozawa, D. Akahoshi, and H. Kuwahara, "Magnetic and dielectric properties of $A_2CoSi_2O_7$ (A = Ca, Sr, Ba) crystals," *Journal of Physics: Conference Series*, vol. 150, p. 042001, mar 2009.

[157] H. Murakawa, Y. Onose, and Y. Tokura, "Electric-field switching of a magnetic propagation vector in a helimagnet," *Phys. Rev. Lett.*, vol. 103, p. 147201, Sep 2009.

[158] H. Murakawa, Y. Onose, S. Miyahara, N. Furukawa, and Y. Tokura, "Ferroelectricity induced by spin-dependent metal-ligand hybridization in $Ba_2CoGe_2O_7$," *Phys. Rev. Lett.*, vol. 105, p. 137202, Sep 2010.

[159] S. Miyahara and N. Furukawa, "Theory of magnetoelectric resonance in two-dimensional S = 3/2 antiferromagnet $Ba_2CoGe_2O_7$ via spin-dependent metal-ligand hybridization mechanism," *Journal of the Physical Society of Japan*, vol. 80, no. 7, p. 073708, 2011.

[160] J. M. Perez-Mato and J. L. Ribeiro, "On the symmetry and the signature of atomic mechanisms in multiferroics: the example of $Ba_2CoGe_2O_7$," *Acta Crystallographica Section A*, vol. 67, pp. 264–268, May 2011.

[161] P. Toledano, D. D. Khalyavin, and L. C. Chapon, "Spontaneous toroidal moment and field-induced magnetotoroidic effects in $Ba_2CoGe_2O_7$," *Phys. Rev. B*, vol. 84, p. 094421, Sep 2011.

[162] V. Hutanu, A. Sazonov, H. Murakawa, Y. Tokura, B. Náfrádi, and D. Chernyshov, "Symmetry and structure of multiferroic $Ba_2CoGe_2O_7$," *Phys. Rev. B*, vol. 84, p. 212101, Dec 2011.

[163] K. Yamauchi, P. Barone, and S. Picozzi, "Theoretical investigation of magnetoelectric effects in $Ba_2CoGe_2O_7$," *Phys. Rev. B*, vol. 84, p. 165137, Oct 2011.

[164] J. Romhányi, M. Lajkó, and K. Penc, "Zero- and finite-temperature mean field study of magnetic field induced electric polarization in $Ba_2CoGe_2O_7$: Effect of the antiferroelectric coupling," *Phys. Rev. B*, vol. 84, p. 224419, Dec 2011.

[165] M. Akaki, H. Iwamoto, T. Kihara, M. Tokunaga, and H. Kuwahara, "Multiferroic properties of an åkermanite $Sr_2CoSi_2O_7$ single crystal in high magnetic fields," *Phys. Rev. B*, vol. 86, p. 060413(R), Aug 2012.

[166] J. Romhányi and K. Penc, "Multiboson spin-wave theory for $Ba_2CoGe_2O_7$: A spin-3/2 easy-plane néel antiferromagnet with strong single-ion anisotropy," *Phys. Rev. B*, vol. 86, p. 174428, Nov 2012.

[167] V. Hutanu, A. Sazonov, M. Meven, H. Murakawa, Y. Tokura, S. Bordács, I. Kézsmárki, and B. Náfrádi, "Determination of the magnetic order and the crystal symmetry in the multiferroic ground state of $Ba_2CoGe_2O_7$," *Phys. Rev. B*, vol. 86, p. 104401, Sep 2012.

[168] M. Akaki, T. Tadokoro, T. Kihara, M. Tokunaga, and H. Kuwahara, "High magnetic field dependence of magnetodielectric properties in $Sr_2CoSi_2O_7$ crystal," *Journal of Low Temperature Physics*, vol. 170, pp. 291–295, 2013.

[169] M. Soda, M. Matsumoto, M. Månsson, S. Ohira-Kawamura, K. Nakajima, R. Shiina, and T. Masuda, "Spin-nematic interaction in the multiferroic compound $Ba_2CoGe_2O_7$," *Phys. Rev. Lett.*, vol. 112, p. 127205, Mar 2014.

[170] V. Hutanu, A. P. Sazonov, M. Meven, G. Roth, A. Gukasov, H. Murakawa, Y. Tokura, D. Szaller, S. Bordács, I. Kézsmárki, V. K. Guduru, L. C. J. M. Peters, U. Zeitler, J. Romhányi, and B. Náfrádi, "Evolution of two-dimensional antiferromagnetism with temperature and magnetic field in multiferroic $Ba_2CoGe_2O_7$," *Phys. Rev. B*, vol. 89, p. 064403, Feb 2014.

[171] M. Akaki, H. Kuwahara, A. Matsuo, K. Kindo, and M. Tokunaga, "Successive magnetic transitions of $Ca_2CoSi_2O_7$ in high magnetic fields," *Journal of the Physical Society of Japan*, vol. 83, no. 9, p. 093704, 2014.

[172] T. Nakajima, Y. Tokunaga, V. Kocsis, Y. Taguchi, Y. Tokura, and T.-h. Arima, "Uniaxial-stress control of spin-driven ferroelectricity in multiferroic $Ba_2CoGe_2O_7$," *Phys. Rev. Lett.*, vol. 114, p. 067201, Feb 2015.

[173] M. Soda, S. Hayashida, B. Roessli, M. Månsson, J. S. White, M. Matsumoto, R. Shiina, and T. Masuda, "Continuous control of local magnetic moment by applied electric field in multiferroics $Ba_2CoGe_2O_7$," *Phys. Rev. B*, vol. 94, p. 094418, Sep 2016.

[174] A. Sazonov, V. Hutanu, M. Meven, G. Roth, I. Kézsmárki, H. Murakawa, Y. Tokura, and B. Náfrádi, "The low-temperature crystal structure of the multiferroic melilite $Ca_2CoSi_2O_7$," *Acta Crystallographica Section B*, vol. 72, pp. 126–132, Feb 2016.

[175] M. Akaki, D. Yoshizawa, A. Okutani, T. Kida, J. Romhányi, K. Penc, and M. Hagiwara, "Direct observation of spin-quadrupolar excitations in $Sr_2CoGe_2O_7$ by high-field electron spin resonance," *Phys. Rev. B*, vol. 96, p. 214406, Dec 2017.

[176] J. Viirok, U. Nagel, T. Rõõm, D. G. Farkas, P. Balla, D. Szaller, V. Kocsis, Y. Tokunaga, Y. Taguchi, Y. Tokura, B. Bernáth, D. L. Kamenskyi, I. Kézsmárki, S. Bordács, and K. Penc, "Directional dichroism in the paramagnetic state of multiferroics: A case study of infrared light absorption in $Sr_2CoSi_2O_7$ at high temperatures," *Phys. Rev. B*, vol. 99, p. 014410, Jan 2019.

[177] W. D. Horrocks and D. A. Burlone, "Toward a theory of the spectral and magnetic properties of transition metal ions occupying low-symmetry sites in metalloproteins. Application of the angular overlap model to distorted tetrahedral tetrachlorocobaltate(2-) ions," *Journal of the American Chemical Society*, vol. 98, no. 21, pp. 6512–6516, 1976.

[178] P. C. Hohenberg and W. F. Brinkman, "Sum rules for the frequency spectrum of linear magnetic chains," *Phys. Rev. B*, vol. 10, pp. 128–131, Jul 1974.

[179] J. W. Kim, S. Khim, S. H. Chun, Y. Jo, L. Balicas, H. T. Yi, S.-W. Cheong, N. Harrison, C. D. Batista, J. Hoon Han, and K. Hoon Kim, "Manifestation of magnetic quantum fluctuations in the dielectric properties of a multiferroic," *Nature Communications*, vol. 5, p. 4419, Jul 2014.

[180] J. Vít, F. Kadlec, C. Kadlec, F. Borodavka, Y. S. Chai, K. Zhai, Y. Sun, and S. Kamba, "Electromagnon in the Y-type hexaferrite $BaSrCoZnFe_{11}AlO_{22}$," *Physical Review B*, vol. 97, p. 134406, Apr 2018.

[181] R. C. Pullar, "Hexagonal ferrites: A review of the synthesis, properties and applications of hexaferrite ceramics," *Progress in Materials Science*, vol. 57, no. 7, pp. 1191–1334, 2012.

[182] T. Kimura, "Magnetoelectric hexaferrites," *Annu. Rev. Cond. Matt. Phys.*, vol. 3, pp. 93–110, 2012.

[183] *Ferrites*, Philips Technical Library, Eindhoven, 1959.

[184] G. Albanese, M. Carbucicchio, A. Deriu, G. Asti, and S. Rinaldi, "Influence of the cation distribution on the magnetization of Y-type hexagonal ferrites," *Applied physics*, vol. 7, pp. 227–238, Jul 1975.

[185] S. Utsumi, D. Yoshiba, and N. Momozawa, "Superexchange interactions of $(Ba_{1-x}Sr_x)_2Zn_2Fe_{12}O_{22}$ system studied by neutron diffraction," *Journal of the Physical Society of Japan*, vol. 76, no. 3, p. 034704, 2007.

[186] N. Momozawa, Y. Yamaguchi, H. Takei, and M. Mita, "Magnetic structure of $(Ba_{1-x}Sr_x)_2Zn_2Fe_{12}O_{22}$ (x= 0–1.0)," *J. Phys. Soc. Japan*, vol. 54, no. 2, pp. 771–780, 1985.

[187] E. Gorter, "Saturation magnetization of some ferrimagnetic oxides with hexagonal crystal structures," *Proceedings of the IEE-Part B: Radio and Electronic*

Engineering, vol. 104, no. 5S, pp. 255–260, 1957.

[188] S. H. Chun, Y. S. Chai, B.-G. Jeon, H. J. Kim, Y. S. Oh, I. Kim, H. Kim, B. J. Jeon, S. Y. Haam, J.-Y. Park, S. H. Lee, J.-H. Chung, J.-H. Park, and K. H. Kim, "Electric field control of nonvolatile four-state magnetization at room temperature," *Phys. Rev. Lett.*, vol. 108, p. 177201, Apr 2012.

[189] C. B. Park, K. W. Shin, S. H. Chun, J. H. Lee, Y. S. Oh, S. M. Disseler, C. A. Heikes, W. D. Ratcliff, W.-S. Noh, J.-H. Park, and K. H. Kim, "Control of magnetoelectric coupling in the Co_2Y-type hexaferrites," *Phys. Rev. Materials*, vol. 5, p. 034412, Mar 2021.

[190] V. Kocsis, T. Nakajima, M. Matsuda, A. Kikkawa, Y. Kaneko, J. Takashima, K. Kakurai, T. Arima, Y. Tokunaga, Y. Tokura, and Y. Taguchi, "Stability of multiferroic phase and magnetization-polarization coupling in Y-type hexaferrite crystals," *Physical Review B*, vol. 101, p. 075136, 2020.

[191] S.-P. Shen and Y. Sun, "Magnetoelectric multiferroicity and quantum paraelectricity in hexaferrites," *Science China Physics, Mechanics & Astronomy*, vol. 62, p. 47501, Nov 2018.

[192] T. Nakajima, Y. Tokunaga, M. Matsuda, S. Dissanayake, J. Fernandez-Baca, K. Kakurai, Y. Taguchi, Y. Tokura, and T.-h. Arima, "Magnetic structures and excitations in a multiferroic Y-type hexaferrite $BaSrCo_2Fe_{11}AlO_{22}$," *Phys. Rev. B*, vol. 94, p. 195154, Nov 2016.

[193] T. Kimura, G. Lawes, and A. P. Ramirez, "Electric polarization rotation in a hexaferrite with long-wavelength magnetic structures," *Phys. Rev. Lett.*, vol. 94, p. 137201, 2005.

[194] V. Kocsis, T. Nakajima, M. Matsuda, A. Kikkawa, Y. Kaneko, J. Takashima, K. Kakurai, T. Arima, F. Kagawa, Y. Tokunaga, Y. Tokura, and Y. Taguchi, "Magnetization-polarization cross-control near room temperature in hexaferrite single crystals," *Nature Communications*, vol. 10, 2019.

[195] S. Shen, L. Yan, Y. Chai, J. Cong, and Y. Sun, "Magnetic field reversal of electric polarization and magnetoelectric phase diagram of the hexaferrite $Ba_{1.3}Sr_{0.7}Co_{0.9}Zn_{1.1}Fe_{10.8}Al_{1.2}O_{22}$," *Appl. Phys. Lett.*, vol. 104, no. 3, 2014.

[196] S. H. Chun, Y. S. Chai, Y. S. Oh, D. Jaiswal-Nagar, S. Y. Haam, I. Kim, B. Lee, D. H. Nam, K.-T. Ko, J.-H. Park, J.-H. Chung, and K. H. Kim, "Realization of giant magnetoelectricity in helimagnets," *Phys. Rev. Lett.*, vol. 104, p. 037204, Jan 2010.

[197] K. Zhai, Y. Wu, S. Shen, W. Tian, H. Cao, Y. Chai, B. C. Chakoumakos, D. Shang, L. Yan, F. Wang, and Y. Sun, "Giant magnetoelectric effects achieved by tuning spin cone symmetry in Y-type hexaferrites," *Nature Commun.*, vol. 8, p. 519, 2017.

[198] Y. Kitagawa, Y. Hiraoka, T. Honda, T. Ishikura, H. Nakamura, and T. Kimura, "Low-field magnetoelectric effect at room temperature," *Nature Mat.*, vol. 9, pp. 797–802, 2010.

[199] Y. S. Chai, S. H. Chun, J. Z. Cong, and K. H. Kim, "Magnetoelectricity in multiferroic hexaferrites as understood by crystal symmetry analyses," *Phys. Rev. B*, vol. 98, p. 104416, Sep 2018.

[200] L. Wang, D. Wang, Q. Cao, Y. Zheng, H. Xuan, J. Gao, and Y. Du, "Electric control of magnetism at room temperature," *Scientific Reports*, vol. 2, 2012.

[201] K. Okumura, T. Ishikura, M. Soda, T. Asaka, H. Nakamura, Y. Wakabayashi, and T. Kimura, "Magnetism and magnetoelectricity of a U-type hexaferrite $Sr_4Co_2Fe_{36}O_{60}$," *Applied Physics Letters*, vol. 98, no. 21, p. 212504, 2011.

[202] Y. Q. Song, Y. Fang, L. Y. Wang, W. P. Zhou, Q. Q. Cao, D. H. Wang, and Y. W. Du, "Spin reorientation transition and near room-temperature multiferroic properties in a W-type hexaferrite $SrZn_{1.15}Co_{0.85}Fe_{16}O_{27}$," *Journal of Applied Physics*, vol. 115, no. 9, p. 093905, 2014.

[203] S. Shen, X. Liu, Y. Chai, A. J. Studer, C. He, S. Wang, and Y. Sun, "Reversibility of spin-induced electric polarization in multiferroic hexaferrites," *Phys. Rev. B*, vol. 100, p. 134433, Oct 2019.

[204] N. Kida, D. Okuyama, S. Ishiwata, Y. Taguchi, R. Shimano, K. Iwasa, T. Arima, and Y. Tokura, "Electric-dipole-active magnetic resonance in the conical-spin magnet $Ba_2Mg_2Fe_{12}O_{22}$," *Phys. Rev. B*, vol. 80, p. 220406(R), 2009.

[205] N. Kida, S. Kumakura, S. Ishiwata, Y. Taguchi, and Y. Tokura, "Gigantic terahertz magnetochromism via electromagnons in the hexaferrite magnet $Ba_2Mg_2Fe_{12}O_{22}$," *Phys. Rev. B*, vol. 83, p. 064422, Feb 2011.

[206] T. Nakajima, Y. Takahashi, S. Kibayashi, M. Matsuda, K. Kakurai, S. Ishiwata, Y. Taguchi, Y. Tokura, and T.-h. Arima, "Electromagnon excitation in the field-induced noncollinear ferrimagnetic phase of $Ba_2Mg_2Fe_{12}O_{22}$ studied by polarized inelastic neutron scattering and terahertz time-domain optical spectroscopy," *Phys. Rev. B*, vol. 93, p. 035119, Jan 2016.

[207] H. Shishikura, Y. Tokunaga, Y. Takahashi, R. Masuda, Y. Taguchi, Y. Kaneko, and Y. Tokura, "Electromagnon resonance at room temperature with gigantic magnetochromism," *Phys. Rev. Applied*, vol. 9, p. 044033, Apr 2018.

[208] S. H. Chun, K. W. Shin, H. J. Kim, S. Jung, J. Park, Y.-M. Bahk, H.-R. Park, J. Kyoung, D.-H. Choi, D.-S. Kim, G.-S. Park, J. F. Mitchell, and K. H. Kim, "Electromagnon with sensitive terahertz magnetochromism in a room-temperature magnetoelectric hexaferrite," *Phys. Rev. Lett.*, vol. 120, p. 027202, Jan 2018.

[209] S. Kamba, F. Borodavka, F. Kadlec, C. Kadlec, Y. S. Chai, K. Zhai, J. Buršík, and J. Vít, "Vibrational spectra of multiferroics with Y- and Z-type hexaferrite structures," *Ferroelectrics*, vol. 532, no. 1, pp. 208–220, 2018.

[210] H. B. Lee, Y.-S. Song, J.-H. Chung, S. H. Chun, Y. S. Chai, K. H. Kim, M. Reehuis, K. Prokeš, and S. Mat'aš, "Field-induced incommensurate-to-commensurate phase transition in the magnetoelectric hexaferrite $Ba_{0.5}Sr_{1.5}Zn_2(Fe_{1-x}Al_x)_{12}O_{22}$," *Phys. Rev. B*, vol. 83, p. 144425, Apr 2011.

[211] S. Hirose, K. Haruki, A. Ando, and T. Kimura, "Mutual control of magnetization and electrical polarization by electric and magnetic fields at room temperature in y-type $BaSrCo_{2-x}Zn_xFe_{11}AlO_{22}$ ceramics," *Applied Physics Letters*, vol. 104, no. 2, p. 022907, 2014.

[212] H. Shishikura, S. Ishiwata, Y. Taguchi, Y. Tokura, and Y. Takahashi, "Role of spin-spiral period for anomalous magnetic-field-induced spectral variation of elec-

tromagnon resonance in multiferroic $Ba_2Mg_2Fe_{12}O_{22}$," *Journal of the Physical Society of Japan*, vol. 91, no. 3, p. 033701, 2022.

[213] S. Kamba, V. Goian, M. Savinov, E. Buixaderas, D. Nuzhnyy, M. Maryško, M. Kempa, V. Bovtun, J. Hlinka, K. Knížek, P. Vaněk, P. Novák, J. Buršík, Y. Hiraoka, T. Kimura, K. Kouřil, and H. Štěpánková, "Dielectric, magnetic, and lattice dynamics properties of Y-type hexaferrite $Ba_{0.5}Sr_{1.5}Zn_2Fe_{12}O_{22}$: Comparison of ceramics and single crystals," *J. Appl. Phys.*, vol. 107, no. 10, p. 104109, 2010.

[214] S. Skiadopoulou, V. Goian, C. Kadlec, F. Kadlec, X. F. Bai, I. C. Infante, B. Dkhil, C. Adamo, D. G. Schlom, and S. Kamba, "Spin and lattice excitations of a $BiFeO_3$ thin film and ceramics," *Phys. Rev. B*, vol. 91, p. 174108, 2015.

[215] J. Buhot, C. Toulouse, Y. Gallais, A. Sacuto, R. De Sousa, D. Wang, L. Bellaiche, M. Bibes, A. Barthélémy, A. Forget, *et al.*, "Driving spin excitations by hydrostatic pressure in $BiFeO_3$," *Phys. Rev. Lett.*, vol. 115, no. 26, p. 267204, 2015.

[216] U. Nagel, R. S. Fishman, T. Katuwal, H. Engelkamp, D. Talbayev, H. T. Yi, S.-W. Cheong, and T. Rõõm, "Terahertz spectroscopy of spin waves in multiferroic $BiFeO_3$ in high magnetic fields," *Phys. Rev. Lett.*, vol. 110, p. 257201, Jun 2013.

[217] J. H. Lee, I. Kézsmárki, and R. S. Fishman, "First-principles approach to the dynamic magnetoelectric couplings for the non-reciprocal directional dichroism in $BiFeO_3$," *New J. Phys.*, vol. 18, no. 4, p. 043025, 2016.

[218] P. Fleury and R. Loudon, "Scattering of light by one-and two-magnon excitations," *Phys. Rev.*, vol. 166, no. 2, p. 514, 1968.

[219] N. Kida, Y. Takahashi, J. Lee, R. Shimano, Y. Yamasaki, Y. Kaneko, S. Miyahara, N. Furukawa, T. Arima, and Y. Tokura, "Terahertz time-domain spectroscopy of electromagnons in multiferroic perovskite manganites [invited]," *J. Opt. Soc. Am. B*, vol. 26, no. 9, pp. A35–A51, 2009.

[220] A. J. Hearmon, R. D. Johnson, T. A. W. Beale, S. S. Dhesi, X. Luo, S.-W. Cheong, P. Steadman, and P. G. Radaelli, "Magnetic fan structures in $Ba_{0.5}Sr_{1.5}Zn_2Fe_{12}O_{22}$ hexaferrite revealed by resonant soft x-ray diffraction," *Phys. Rev. B*, vol. 88, p. 174413, Nov 2013.

[221] H. Ueda, Y. Tanaka, Y. Wakabayashi, and T. Kimura, "Soft x-ray resonant diffraction study of magnetic structure in magnetoelectric Y-type hexaferrite," *Physica B: Condensed Matter*, 2018. in press.

[222] A. P. Cracknell, "Scattering matrices for the Raman effect in magnetic crystals," *Journal of Physics C: Solid State Physics*, vol. 2, pp. 500–511, mar 1969.

[223] K. C. Erb and J. Hlinka, "Vector and bidirector representations of magnetic point groups," *Phase Transitions*, vol. 93, no. 1, pp. 1–42, 2020.

[224] D. Talbayev, S. A. Trugman, A. V. Balatsky, T. Kimura, A. J. Taylor, and R. D. Averitt, "Detection of coherent magnons via ultrafast pump-probe reflectance spectroscopy in multiferroic $Ba_{0.6}Sr_{1.4}Zn_2Fe_{12}O_{22}$," *Phys. Rev. Lett.*, vol. 101, p. 097603, Aug 2008.

[225] J. Vít, D. Repček, C. Kadlec, F. Kadlec, N. Adhlakha, P. Di Pietro, F. Piccirilli, S. Kovalev, J.-C. Deinert, I. Ilyakov, N. Awari, M. Chen, J. Buršík, C. B. Park, K. H.

Kim, M. Gensch, A. Perucchi, and S. Kamba, "Search for nonlinear thz absorption by electromagnons in multiferroic hexaferrites," *Journal of the Physical Society of Japan*, vol. 91, no. 10, p. 104703, 2022.

[226] S. Schlauderer, C. Lange, S. Baierl, T. Ebnet, C. Schmid, D. Valovcin, A. K. Zvezdin, A. Kimel, R. Mikhaylovskiy, and R. Huber, "Temporal and spectral fingerprints of ultrafast all-coherent spin switching," *Nature*, vol. 569, pp. 383–387, 2019.

[227] D. Afanasiev, J. R. Hortensius, B. A. Ivanov, A. Sasani, E. Bousquet, Y. M. Blanter, R. V. Mikhaylovskiy, A. V. Kimel, and A. D. Caviglia, "Ultrafast control of magnetic interactions via light-driven phonons," *Nature Materials*, vol. 20, pp. 607–611, May 2021.

[228] K. Jhuria, J. Hohlfeld, A. Pattabi, E. Martin, A. Y. Arriola Córdova, X. Shi, R. Lo Conte, S. Petit-Watelot, J. C. Rojas-Sánchez, G. Malinowski, S. Mangin, A. Lemaitre, M. Hehn, J. Bokor, R. Wilson, and J. Gorchon, "Spin–orbit torque switching of a ferromagnet with picosecond electrical pulses," *Nature Electronics*, vol. 3, pp. 680–686, 2020.

[229] A. Kimel, B. Ivanov, R. V. Pisarev, P. A. Usachev, A. Kirilyuk, and T. Rasing, "Inertia-driven spin switching in antiferromagnets," *Nature Physics*, vol. 5, pp. 727–731, 2009.

[230] I. Radu, K. Vahaplar, C. Stamm, T. Kachel, N. Pontius, H. Dürr, T. Ostler, J. Barker, R. Evans, R. Chantrell, A. Tsukamoto, A. Itoh, A. Kirilyuk, T. Rasing, and A. Kimel, "Transient ferromagnetic-like state mediating ultrafast reversal of antiferromagnetically coupled spins," *Nature*, vol. 472, pp. 205–208, 2011.

[231] S. Baierl, M. Hohenleutner, T. Kampfrath, A. K. Zvezdin, A. Kimel, R. Huber, and R. Mikhaylovskiy, "Nonlinear spin control by terahertz-driven anisotropy fields," *Nature Photonics*, vol. 10, pp. 715–718, 2016.

[232] A. Kimel, A. Kirilyuk, P. A. Usachev, R. Pisarev, A. Balbashov, and T. Rasing, "Ultrafast non-thermal control of magnetization by instantaneous photomagnetic pulses," *Nature*, vol. 435, pp. 655–657, 2005.

[233] K. Olejník, T. Seifert, Z. Kašpar, V. Novák, P. Wadley, R. P. Campion, M. Baumgartner, P. Gambardella, P. Němec, J. Wunderlich, J. Sinova, P. Kužel, M. Müller, T. Kampfrath, and T. Jungwirth, "Terahertz electrical writing speed in an antiferromagnetic memory," *Science Advances*, vol. 4, no. 3, 2018.

[234] K. Yamaguchi, M. Nakajima, and T. Suemoto, "Coherent control of spin precession motion with impulsive magnetic fields of half-cycle terahertz radiation," *Phys. Rev. Lett.*, vol. 105, p. 237201, Dec 2010.

[235] T. Kampfrath, A. Sell, G. Klatt, A. Pashkin, S. Mahrlein, T. Dekorsy, M. Wolf, M. Fiebig, A. Leitenstorfer, and R. Huber, "Coherent terahertz control of antiferromagnetic spin waves," *Nature Photonics*, vol. 5, pp. 31–34, 2011.

[236] T. Kubacka, J. A. Johnson, M. C. Hoffmann, C. Vicario, S. de Jong, P. Beaud, S. Grübel, S.-W. Huang, L. Huber, L. Patthey, Y.-D. Chuang, J. J. Turner, G. L. Dakovski, W.-S. Lee, M. P. Minitti, W. Schlotter, R. G. Moore, C. P. Hauri, S. M. Koohpayeh, V. Scagnoli, G. Ingold, S. L. Johnson, and U. Staub, "Large-amplitude

spin dynamics driven by a THz pulse in resonance with an electromagnon," *Science*, vol. 343, no. 6177, pp. 1333–1336, 2014.

[237] S. Baierl, J. H. Mentink, M. Hohenleutner, L. Braun, T.-M. Do, C. Lange, A. Sell, M. Fiebig, G. Woltersdorf, T. Kampfrath, and R. Huber, "Terahertz-driven nonlinear spin response of antiferromagnetic nickel oxide," *Phys. Rev. Lett.*, vol. 117, p. 197201, Nov 2016.

[238] Y. Takahashi, N. Kida, Y. Yamasaki, J. Fujioka, T. Arima, R. Shimano, S. Miyahara, M. Mochizuki, N. Furukawa, and Y. Tokura, "Evidence for an electric-dipole active continuum band of spin excitations in multiferroic $TbMnO_3$.," *Phys. Rev. Lett.*, vol. 101 18, p. 187201, 2008.

[239] M. Mochizuki and N. Nagaosa, "Theoretically predicted picosecond optical switching of spin chirality in multiferroics," *Phys. Rev. Lett.*, vol. 105, p. 147202, Sep 2010.

[240] Private communication with S.H. Chun, who provided us details of the spin model elaborated in Ref. [208].

[241] J. Lu, X. Li, H. Y. Hwang, B. K. Ofori-Okai, T. Kurihara, T. Suemoto, and K. A. Nelson, "Coherent two-dimensional terahertz magnetic resonance spectroscopy of collective spin waves," *Phys. Rev. Lett.*, vol. 118, p. 207204, May 2017.

[242] R. Santoro, D. Segal, and R. Newnham, "Magnetic properties of $LiCoPO_4$ and $LiNiPO_4$," *Journal of Physics and Chemistry of Solids*, vol. 27, no. 6, pp. 1192–1193, 1966.

[243] D. Vaknin, J. L. Zarestky, L. L. Miller, J.-P. Rivera, and H. Schmid, "Weakly coupled antiferromagnetic planes in single-crystal $LiCoPO_4$," *Phys. Rev. B*, vol. 65, p. 224414, May 2002.

[244] W. Tian, J. Li, J. W. Lynn, J. L. Zarestky, and D. Vaknin, "Spin dynamics in the magnetoelectric effect compound $LiCoPO_4$," *Phys. Rev. B*, vol. 78, p. 184429, Nov 2008.

[245] I. Kornev, M. Bichurin, J.-P. Rivera, S. Gentil, H. Schmid, A. G. M. Jansen, and P. Wyder, "Magnetoelectric properties of $LiCoPO_4$ and $LiNiPO_4$," *Phys. Rev. B*, vol. 62, pp. 12247–12253, Nov 2000.

[246] A. S. Zimmermann, D. Meier, and M. Fiebig, "Ferroic nature of magnetic toroidal order," *Nature Communications*, vol. 5, p. 4796, Sep 2014.

[247] V. Kocsis, Y. Tokunaga, Y. Tokura, and Y. Taguchi, "Switching of antiferromagnetic states in $LiCoPO_4$ as investigated via the magnetoelectric effect," *Phys. Rev. B*, vol. 104, p. 054426, Aug 2021.

[248] *Beam Optics*, ch. 3, pp. 80–107. John Wiley & Sons, Ltd, 1991.

[249] H. B. Lee, S. H. Chun, K. W. Shin, B.-G. Jeon, Y. S. Chai, K. H. Kim, J. Schefer, H. Chang, S.-N. Yun, T.-Y. Joung, and J.-H. Chung, "Heliconical magnetic order and field-induced multiferroicity of the Co_2Y-type hexaferrite $Ba_{0.3}Sr_{1.7}Co_2Fe_{12}O_{22}$," *Phys. Rev. B*, vol. 86, p. 094435, Sep 2012.

[250] N. Momozawa, "Neutron diffraction study of helimagnet $(Ba_{1-x}Sr_x)_2Zn_2Fe_{12}O_{22}$," *Journal of the Physical Society of Japan*, vol. 55, no. 11, pp. 4007–4013, 1986.

[251] W.-S. Noh, K.-T. Ko, S. H. Chun, K. H. Kim, B.-G. Park, J.-Y. Kim, and J.-H. Park, "Magnetic origin of giant magnetoelectricity in doped Y-type hexaferrite $Ba_{0.5}Sr_{1.5}Zn_2(Fe_{1-x}Al_x)_{12}O_{22}$," *Phys. Rev. Lett.*, vol. 114, p. 117603, Mar 2015.

[252] F. Novelli, C. Y. Ma, N. Adhlakha, E. M. Adams, T. Ockelmann, D. Das Mahanta, P. Di Pietro, A. Perucchi, and M. Havenith, "Nonlinear terahertz transmission by liquid water at 1 THz," *Applied Sciences*, vol. 10, no. 15, 2020.